



HAL
open science

Numerical modeling of the physical processes causing the reawakening of a magmatic chamber and of the associated geophysical signals

Alexandre Carrara

► **To cite this version:**

Alexandre Carrara. Numerical modeling of the physical processes causing the reawakening of a magmatic chamber and of the associated geophysical signals. Volcanology. Université Grenoble Alpes, 2019. English. NNT: 2019GREAU031 . tel-02497014

HAL Id: tel-02497014

<https://theses.hal.science/tel-02497014>

Submitted on 3 Mar 2020

HAL is a multi-disciplinary open access archive for the deposit and dissemination of scientific research documents, whether they are published or not. The documents may come from teaching and research institutions in France or abroad, or from public or private research centers.

L'archive ouverte pluridisciplinaire **HAL**, est destinée au dépôt et à la diffusion de documents scientifiques de niveau recherche, publiés ou non, émanant des établissements d'enseignement et de recherche français ou étrangers, des laboratoires publics ou privés.

THÈSE

Pour obtenir le grade de

DOCTEUR DE LA COMMUNAUTE UNIVERSITE GRENOBLE ALPES

Spécialité : **Terre Solide (CETSOL)**

Arrêté ministériel : 25 mai 2016

Présentée par

Alexandre CARRARA

Thèse dirigée par **Alain BURGISSER**, CNRS – Université Savoie Mont-Blanc
codirigée par **Philippe LESAGE**, Université Savoie Mont-Blanc

préparée au sein de **L'Institut des Sciences de la Terre**
dans l'école doctorale **Terre, Univers, Environnement (TUE)**

Modélisations numériques des processus de réveil d'une chambre magmatique et des signaux géophysiques associés

Numerical modeling of the physical processes causing the reawakening of a magmatic chamber and of the associated geophysical signals

Thèse soutenue publiquement le **16 Décembre 2019**,

devant le jury composé de :

Monsieur Alain BURGISSER

Chargé de recherche, CNRS Université Savoie Mont-Blanc, Directeur de thèse

Monsieur Philippe LESAGE

Maitre de conférence, Université Savoie Mont-Blanc, Co-Directeur de thèse

Monsieur Olivier BACHMANN

Professeur, ETH Zürich, Rapporteur

Monsieur Luca CARICCHI

Professeur, Université de Genève, Rapporteur

Monsieur Frederic DONZE

Professeur, Université Grenoble Alpes, Examineur, Président

Madame Valérie VIDAL

Chargée de recherche, CNRS ENS Lyon, Examinatrice



Acknowledgements

This thesis represents three years of work and would not have been possible without the help of several people. First of all, I would like to thank Olivier Bachmann and Luca Caricchi, who both accepted to review this manuscript and to evaluate my research work. Thanks also to Valerie Vidal and Frederic Donze who accepted to be part of the jury.

Foremost, I am deeply grateful to my advisors Alain Burgisser and Philippe Lesage, for their continued support, patience, and for sharing their friendships. Their guidance helped me a lot during my research and the writing of this manuscript. Especially, I would like to thank Alain for everything he brought me (especially for sharing with me the secret of his famous Swiss fondue), for having initiated a further career in earth science, and sending me worldwide. Our journey in Izu-Oshima remains one of my favorite moments during this thesis. I thanks Philippe for all the constructive suggestions and insightful comments that helped me a lot in understanding the physics of wave propagation in magmas. Chapter 6 benefits deeply from his tremendous advices. I could not imagine having better advisors and mentors for my PhD.

Beside my advisors, I would like to express my special gratitude to George Bergantz (the most French of all Americans) for his contributions and support during this thesis, which benefits enormously from his persistent help and meticulous comments. Thanks to his enthusiasm and kindness, my visits to Seattle have always been great pleasures. Thank also to Jillian Schleicher and Zach McIntire for their warm welcome and help on the Seattle campus.

I wish to express my deep appreciation to the rest of the members of my thesis committee (with my advisors): Virginie Pinel and Valerie Vidal. These annual meetings and insightful comments or questions have helped me a lot in moving my ideas forward. I take this opportunity to acknowledge more deeply Virginie Pinel for mentorship and advices during my two master projects that brought me to this thesis.

I am also grateful to Alison Rust and Mark Gilbertson for their time and help during my visit in Bristol. Although this work does not appear directly in this manuscript, it helped me to improve my understanding of the physics of granular materials, which greatly benefited my research.

In addition to my doctoral scholarship, this thesis and participation in conferences, were partially funded by grant AO7bis-International 2017 Labex OSUG@2020 (Investissements d'avenir – ANR10 LABX56), grant ChaMaFo from the University Savoie Mont Blanc (attributed to Alain Burgisser), and a mobility grant provided by the TUE doctorate school. I take this opportunity to acknowledge the TUE doctoral school for their financial support and advices during the thesis. All the numerical simulations presented in this manuscript were computed using the CIMENT infrastructure (<https://ciment.ujf-grenoble.fr>), which is supported by the Rhône-Alpes region (GRANT CPER07_13 CIRA: <http://www.ci-ra.org>).

I benefited from the participation in four summer–winter schools: The TEC21 in Grenoble, the short course on magmas in Perugia, the GRANITE I summer school in Orléans, and the CIDER 2019 in Berkeley. I would like to thank the organizers, lecturers, and participants of these trainings for the enlightening discussions and the good times shared there. I acknowledge the CIDER program for providing me the onsite support in Berkeley and to the TUE doctorate school for taking charged of the trip.

During this thesis I benefited from the encouragement and advices for the members of ISTerre Chambéry. I would like to thanks everyone who has helped me improve my knowledge in earth sciences, and especially the members of volcano geophysics team. I thanks my fellow students in ISTerre Chambéry (Abdellali, les Antoinnes, Cedric, Delphine, Grace, Hervé, Laure, Léa, Marceau, Sandrine, Timothé, Zenlu), and to the master students. I am grateful to Fabien Massot for all his critical support concerning administrative tasks (even if he is a fan of the RCT).

Finally, this thesis represents the end of my student life, which would not have been the same without several people. Thanks to my friends and especially the old ones (Cecile, Flo, Julie, Luc, Rachel, Simon, Thibaut,...) for your craziness and the wonderful moments. My deepest gratitude goes to my family. To my parents, Françoise and Olivier, and my sister, Marine, for their kindness, unconditional support, and the inspiring courage they have shown during the recent years. To my grandparents, whose success has always inspired me. I would also to thank Anaïs for her love and encouragements throughout this thesis, and especially for her support during the writing of this manuscript. My last but not least thanks goes to Newton, many of the ideas presented in this manuscript are the result of our walks.

Abstract:

The reawakening of volcanoes asleep since hundreds or thousands years (ex. Komagatake, 1640; Pinatubo, 1991) is a mysterious phenomenon. Volcanic eruptions are the surface expressions of processes occurring in the underlying magmatic systems. Long-lived magmatic reservoirs located in the upper crust have been shown to result from the accumulation of intrusions of new magmas, and spend most of their dwelling time as mush. A mush is a magma that is cooled and crystallized, in which the crystals are touching each other to form a rigid framework, that inhibit its ability to flow. The generation of eruptible conditions requires destabilizing the force chains link crystals in contact. Such destabilization is often thought to be triggered by the recharge of the mush with new magma. A better understanding of the physical processes occurring in magmatic reservoirs by the emplacement of new magma is required to identify the conditions that primer in volcanic eruptions. The characterization of the effects of the intrusion on the physical conditions of the magmatic reservoir and on the associated geophysical signals is necessary to best mitigate volcanic hazards.

This thesis explores first the physical processes controlling the motions of the crystals in magmas and mush. Previous studies have not considered the presence of lubrication forces. These hydrodynamic forces are opposed to the relative motions between neighboring crystals. By developing scaling relationships of the importance of the forces controlling the motion of the solids, and numerical simulations using a Discrete Element Method coupled with a Computational Fluid Dynamic approach (CFD-DEM), we constrained the effects of lubrication on magmas and defined a dimensionless number able to predict lubrication importance. Results show that lubrication is opposed to the onset or the arrest of motions within the mush. Neglecting lubrication results in underestimating the duration of transient dynamics, but does not affect the quantification of steady-state dynamics.

We then used CFD-DEM simulations to explore the emplacement mechanisms of mobile magmas within mush and their effects on the magmatic reservoir. Results show that the behavior of the intrusion is controlled by the injection velocity and by the density contrast between the two melt phases of the resident mush and the intruded material. Under most natural conditions, simulations suggest that the intruded magma is expected to pond at the base of the mush and to be

emplaced as a horizontal layer. This scenario does not lead to a high degree of mixing nor to conditions for which an eruption may be triggered rapidly. The recharge in new magmas, however, generates conditions propitious for the extraction of eruptible magmas from the mush. It appears that the unfolding of a recharge event depends on the evolution of the density contrast between the mush interstitial melt and the intruded melt and on the thermal exchanges following the intrusion.

The detection of volumes composed by eruptible magmas from seismic signals requires knowledge of their seismic properties, which are yet poorly constrained. We used the coupled phase approach to compute the propagation velocities and attenuation coefficients of seismic waves in magmas. This approach is based on the linearization of the continuum conservation equations that control the motions of the fluid and the solids. Results show that, in crystal-bearing magmas, the propagation velocity of compressional waves is mainly controlled by the crystal volume fraction. The measure of the intrinsic attenuation coefficient is required to distinguish the chemical composition of the magmas. The joint monitoring in time of seismic waves velocities and intrinsic attenuation coefficients seems the most suitable method to detect the initiation of an eruption from a magmatic reservoir.

Keywords:

Numerical model, volcanology, magma, geophysics

Résumé:

Le réveil de volcans endormis depuis de nombreuses années (ex. Komagatake, 1640; Pinatubo, 1991) est un phénomène qui reste mystérieux. Les éruptions volcaniques sont les expressions de surface de processus prenant place dans le système magmatique sous-jacent. Les réservoirs magmatiques situés dans la croûte supérieure sont formés par des injections répétées de magmas mobiles, et résident la plupart du temps à l'état de mush. Un mush est un magma refroidi et cristallisé, où les cristaux se touchent et forment un squelette rigide qui inhibe sa capacité à s'écouler. Les chaînes de forces liant ces cristaux en contact doivent être déstabilisées afin de générer des conditions pouvant mener à une éruption. Une telle déstabilisation est souvent considérée comme le résultat de la recharge du réservoir. Une meilleure compréhension des processus physiques liés à la recharge d'un mush est donc nécessaire afin d'identifier les conditions qui favorisent le déclenchement d'une éruption volcanique. La caractérisation de l'effet d'une intrusion sur les conditions physiques du réservoir et sur les signaux géophysiques associés, est nécessaire pour permettre la détection des dynamiques menant à une éruption, et de gérer au mieux les risques associés.

Cette thèse explore dans un premier temps les processus physiques qui contrôlent le mouvement des cristaux dans les magmas et les mush. Les études précédentes ne considéraient pas les forces de lubrification. Ces forces hydrodynamiques sont opposées au mouvement relatif entre deux cristaux voisins. A l'aide de lois d'échelle quantifiant l'importance des différentes forces contrôlant le mouvement des cristaux et de simulations numériques utilisant la méthode des éléments discrets, couplée à la modélisation dynamique de la phase fluide (CFD-DEM), nous avons contraint l'effet de la lubrification et défini un nombre sans dimension indiquant son importance. Les résultats montrent que la lubrification s'oppose à l'initiation ou l'arrêt de mouvements dans le mush. La négliger sous-estime la durée des phases transitoires mais n'affecte pas la quantification de l'état stationnaire de l'écoulement.

Nous avons utilisé des simulations CFD-DEM afin d'explorer les mécanismes d'emplacement de magmas mobiles dans un mush. Les résultats montrent que le comportement de l'intrusion est contrôlé par la vitesse d'injection et le contraste de densité entre la phase fondue du mush et celle du magma mis en place. Dans la plupart des conditions naturelles, les simulations

montrent que le magma injecté se met en place sous forme d'une couche horizontale à la base du mush. Cette situation ne résulte ni en un mélange efficace entre mush et intrusion, ni en des dynamiques permettant de générer immédiatement une éruption. En revanche, la recharge du mush génère des conditions qui peuvent mener à la génération et à l'extraction de volumes de magmas possédant une éruptivité. Il apparaît que le déroulement d'un événement de recharge dépend de l'évolution de la densité relative entre la phase fondue du mush et celle du magma mis en place et de l'évolution thermique qui suit l'intrusion.

La détection de volumes de magmas possédant une éruptivité à partir de données sismiques requiert une connaissance de leurs propriétés sismiques. Ces propriétés sont à ce jour mal contraintes. En utilisant une approche de phases couplées basée sur la linéarisation des équations conservatives contrôlant le mouvement des phases fluide et solide, nous avons calculé les vitesses de propagation et facteurs d'atténuation des ondes sismiques dans les magmas. Les résultats montrent que, dans les magmas chargés en cristaux, la vitesse des ondes dépend principalement du contenu en cristaux. Distinguer des magmas de différentes compositions chimiques nécessite de mesurer l'atténuation intrinsèque. Le suivi des évolutions conjointes de ces deux observables semble être l'approche la plus à même de détecter des dynamiques magmatiques menant à une éruption.

Mots clés:

Modèle numérique, volcanologie, magma, géophysique

TABLE OF CONTENTS:

Acknowledgments	i
Abstract	iii
Résumé	v
Table of contents	vii
Chapter 1 : General introduction	1
1.1 Motivations	1
1.2 The physical processes of mush reawakening	6
1.3 Imaging unrest events and seismic properties of eruptible magmas	10
1.4 Manuscript organization and scientific questions	13
Chapter 2 : CFD-DEM Model	19
2.1 Introduction	19
2.2 Governing equations of the fluid phase	25
2.2.1 Mass conservation	25
2.2.2 Momentum conservation	25
2.2.3 Energy equation	26
2.2.4 State equations	27
2.2.5 Effect of the presence of the solid phase	28
2.3 Governing equations of the solids	30
2.3.1 Constitutive equations	30
2.3.2 Contact Model	31
2.3.2.a Collisional interactions	32
2.3.2.b Frictional interactions	34
2.3.3 Heat transfer between the solids	35
2.3.3.a Solid-Solid conduction	36
2.3.3.b Solid-Fluid-Solid conduction	37
2.3.3.c Relative importance of the two conduction modes	38
2.4 Couplings between the phases	39

2.4.1 Momentum coupling	39
2.4.2 Thermal coupling	41
2.5 Numerical solver	42
2.5.1 Overview of the SIMPLE algorithm	42
2.5.2 DEM solver.....	44
2.5.3 Interpolation schemes.....	48
2.5.3.a Particle side.....	48
2.5.3.b Fluid side.....	50
2.5.4 Boundary conditions.....	50
2.5.5 Dimensionless numbers	51
Chapter 3 : Effects of lubrication on mush dynamics	57
3.1 Introduction	57
3.2 Method.....	60
3.2.1 Formulation of the BBO equation	60
3.2.2 CFD-DEM Model.....	63
3.3 Results	63
3.3.1 Grains scale	63
3.2.1.a Scaling of the relative importance of the forces exerted on a particle.....	63
3.2.1.b Dimensionless formulation	65
3.3.2 Macroscopic scale	66
3.2.2.a Experiment 1 : Rayleigh-Taylor instabilities.....	66
3.2.2.b Experiment 2 : Injection of a fresh magma into a mush	72
3.3.3 Interpretation.....	75
3.4 Discussion.....	76
3.4.1 Influence of the crystals size and shape.....	76
3.4.2 Comparison with other studies	77
3.4.3 Implication on magma rheology and magmatic system dynamics.....	78
3.4 Conclusion	81
Supplementary section S3.1	84

Supplementary section S3.2	85
Supplementary section S3.3	89
Supplementary section S3.4	90
Supplementary section S3.5	92
Chapter 4 : CFD-DEM modeling of recharge events within mush	95
4.1 Introduction	95
4.2 Method.....	98
4.2.1 Numerical method	98
4.2.2 Numerical setup and experiments	100
4.2.3 Dimensionless parameters	101
4.3 Results	104
4.3.1 Effect of buoyancy and viscosity	104
4.3.2 Injection velocity.....	110
4.3.3 Results summary.....	113
4.4 Discussion.....	114
4.4.1 Model limitations.....	114
4.4.2 Implication on mush dynamics and on the modeling of crystal-bearing magmas.....	116
4.5 Conclusion	118
Supplementary section S4.1	121
Supplementary section S4.2	124
Supplementary section S4.3	127
Chapter 5 : Numerical simulations of the mixing caused by a magma intruding a resident mush.....	129
5.1 Introduction	129
5.2 Method.....	131
5.1 Results	135
5.2 Discussion.....	140
5.1 Conclusion.....	146
Chapter 6 : The seismic properties of eruptible magmas.....	149
6.1 Introduction	149

6.2 Theoretical assumptions.....	152
6.3 Method.....	153
6.3.1 Conservative equations of the phases	153
6.3.2 Fluid-solid and solid-solid couplings.....	154
6.3.3 Calculation of the acoustical properties of the suspension.....	156
6.3.4 Magmas under consideration.....	157
6.4 Results	158
6.4.1 Magmas physical properties.....	158
6.4.2 Fluid-solid momentum coupling.....	160
6.4.3 Solids-solids momentum coupling.....	161
6.4.4 Wave velocities and attenuation coefficients in suspensions	163
6.4.4.a Compressional waves	163
6.4.4.b Shear waves.....	165
6.4.5 Compressional waves in suspensions.....	166
6.4.6 Shear waves in suspensions.....	171
6.4.7 Application to magmas	171
6.5 Discussion.....	173
6.5.1 Limitations.....	173
6.5.2 Model validation	177
6.5.3 Implications for magmas	178
6.5 Conclusion.....	181
Supplementary section S6.1	185
Chapter 7 : General conclusions.....	187
Manuscript references	194

Chapter 1: General introduction

1.1 Motivations

The reawakening of volcanoes that have been dormant for several hundreds or thousands of years (e.g. Komagatake, 1640; Tambora 1812; Krakatoa 1883; Lassen peak, 1914; Bezymianny, 1955; Pinatubo, 1991; Chaitén 2008) remains a mysterious phenomenon challenging our ability to predict eruptions and mitigate volcanic hazards. Volcanoes and eruptions are the surface signatures of processes occurring throughout the underlying magmatic systems, including melt generation, crystallization, differentiation, migration, accumulation, and mixing. In this thesis manuscript, following terminologies given recently (e.g. Bachmann and Bergantz, 2008; Sparks et al., 2019), we use *magma chamber* to characterize a volume composed by mobile and *eruptible magmas*, which is below a critical crystallinity (~50 % crystal volume fraction). In these regions, the melt is the continuous phase and crystals (and possibly exsolved volatiles) are the suspended phases. Above this critical volume fraction in solids, the term *mush* is used to characterize the volumes dominated by the presence of the crystals, which are touching each other to form a semi-rigid continuous framework with interstitial and interconnected melt. The domain of *rocks* encompasses two sub-domains: the *supersolidus* or *partially molten rocks*, in which unconnected melt pocket are present and the *subsolidus rocks* characterized by the absence of a molten phase. The boundary between the mush and rock domains is defined as the melt connectivity transition (Sparks et al., 2019). The boundary between the domains of mush and eruptible magmas is defined at the jamming transition (transition between jammed and unjammed states) which occurs either at the random close or loose packings, depending on the friction coefficient of the crystals (Bergantz et al., 2017). By combining several of these concepts, we can also define the domains of the *magmatic reservoir* that includes all the regions in which melt is present, and the *magmatic system*, which is composed by all the volumes affected by heat or mass transfers, and stress induced by the magmatic activity (Fig. 1.1).

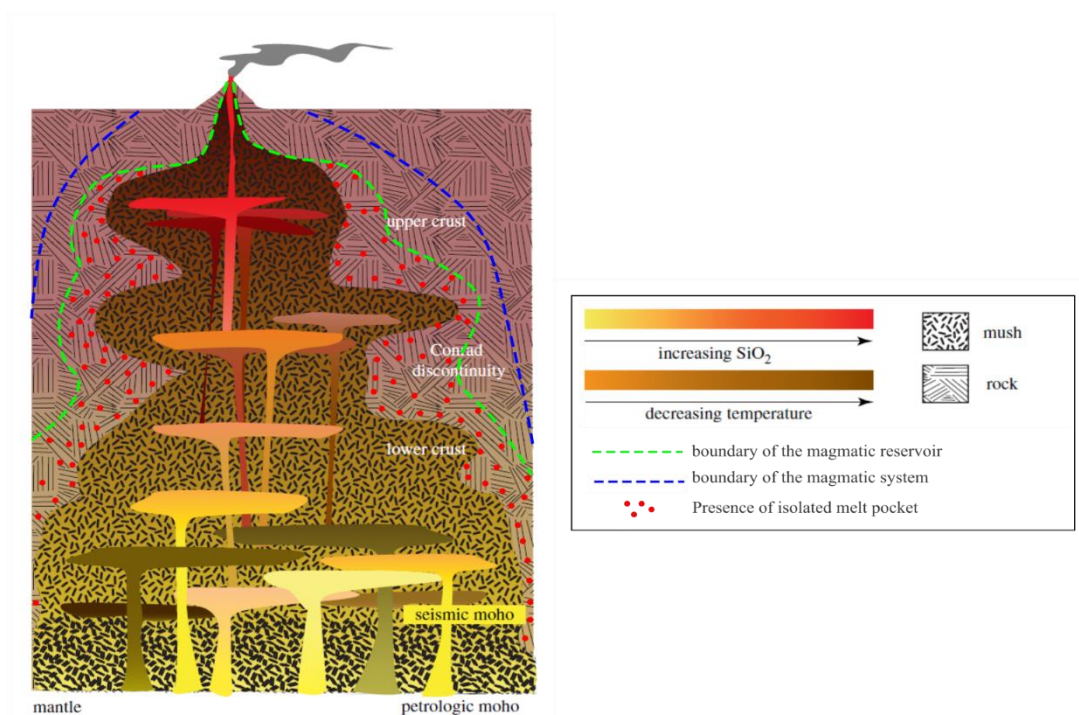


Figure 1.1: Schematic image of a magmatic system. The figure displays a crustal section of a magmatic system going from the top of the mantle to the surface. The boundaries of the magmatic system is indicated with a dashed blue curve. The green dashed curve indicates the limits of the magmatic reservoir in which the red dots indicate the presence of partially molten rocks. The rest of the magmatic system is composed by mush and magma chambers. The mush location is indicated with rectangular glyphs. The color within the magma chambers depends on the concentration in SiO_2 of the melt phase, going from yellow for more primitive magmas to red for more evolved ones. Modified after Cashman et al., 2017

Magmatic reservoirs are inferred to be formed by the repeated injections of small sheets of hot and mobile magmas within the crust (e.g. Annen et al., 2015, 2006; Annen and Sparks, 2002; Gelman et al., 2013; Karakas et al., 2017). The condition to generate a long-lived magma reservoir is to advect more heat (emplacement of new magma sheets) than the amount lost by conduction into the host crust (Annen et al., 2015; Sparks et al., 2019). The critical emplacement rate depends on the host crust temperature, intrusion geometries (which depends itself on injected material temperature, composition and physical properties) (Annen et al., 2015). If the advection rate is below the critical one, individual sheets have enough time to solidify before a new intrusion occurs (Fig. 1.2A). If the recharge frequency is sufficient, the incubation time needed to develop a long-lived magmatic reservoir may be reached (Fig. 1.2B). Because the critical emplacement rate depends on the crust thermal structure, it is easier to form and maintain a magma reservoir in the hotter lower crust than in the colder upper crust (Annen et al., 2006). Most of the magma differentiation is likely to occur within the lower crust reservoir, leading to the accumulation of

differentiated magmas in the upper crust (Annen et al., 2006). The longevity of such upper reservoirs depends on the maturation state of the lower crust. When the lower reservoir is relatively young and weakly developed, the upper crust remains cold and high advection rates are required to maintain temperatures above the solidus ($> \sim 10^{-2} \text{ km}^3 \text{ yr}^{-1}$) disfavoring the formation of large mushy reservoirs. Contrariwise, the presence of a mature and long-lived lower magmatic reservoir affects the thermal structure of the upper crust and favors the accumulation of large and long lived volumes of magmas with lower critical intrusion rates ($> \sim 10^{-4} \text{ km}^3 \text{ yr}^{-1}$) (Karakas et al., 2017). The injection rate in the upper reservoir also have critical control on the frequency and volume of eruption (Caricchi et al., 2014). These reservoirs are more likely to produce eruptions and this manuscript will focus on the processes occurring within these upper crustal magmatic reservoirs.

During the past decades, there were numerous pieces of evidence that upper crustal magmatic reservoirs spend most of their time as mush (Bachmann and Huber, 2016; Caricchi and Blundy, 2015a; Cashman et al., 2017; Edmonds et al., 2019). A convincing proof arises from the modeling of their thermal evolution. As explained above, magmatic reservoirs are likely formed by repeated recharge of hot and mobile magmas (Fig. 1.2), which cool and crystallize because of the conduction of their heat into the crust. The efficiency of conduction depends on the temperature gradient between the intrusion and its host, which is initially high. As the intrusion is mobile, it

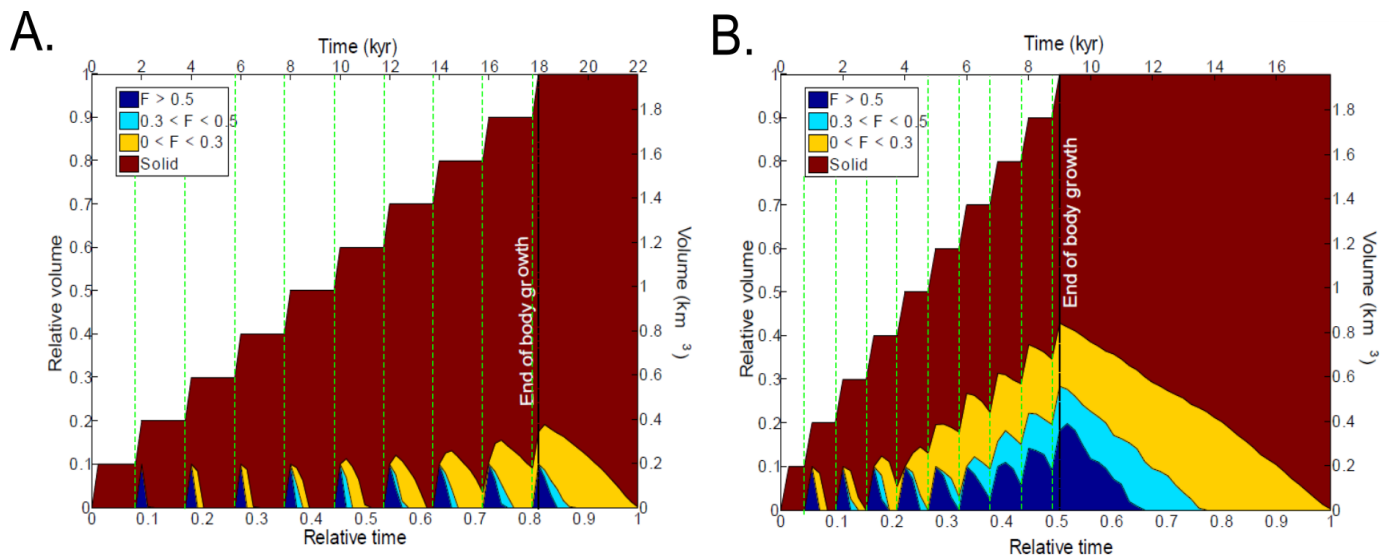


Figure 1.2: Results of numerical simulations showing how the rate of incremental building of magma bodies influences the size and longevity of the magmatic reservoir. Both cartoons are simulations performed with the same initial temperature of the host rock, in which ten 100m thick sills are emplaced with frequencies of [A] 2 kyrs and, [B] 1 kyrs. On each plot, the periods of sill emplacements are indicated with vertical dashed green lines. Modified after Annen et al., 2015.

may also convect, which tends to concentrate the temperature gradient at the intruder margins and enhanced its cooling rate (Bachmann and Huber, 2016). It leads to its rapid crystallization until the magma/mush transition is reached (Fig. 1.3). This transition induces large changes in the magma chemical composition and rheology (see next paragraph), which cancel convections and thus decrease the temperature gradients (Huber et al., 2009). This effect, in addition to the release of the latent heat of crystallization, decreases the cooling rate of the intruded material once this rheological transition is reached (Fig. 1.3) (Huber et al., 2009). Another evidence arises from the eruption of crystal-rich magmas such as the Fish Canyon Tuff (Bachmann et al., 2002), the AD 1640 Hokkaido-Komagatake eruption (Takahashi and Nakagawa, 2013), the AD 1991 Mt Pinatubo eruption (Pallister et al., 1992), or the AD 1995 Montserrat eruption (Murphy et al., 1998), which attests for the presence of magmatic reservoirs dominated by crystal-bearing magmas. Finally, seismic tomographies often show low-seismic velocity anomalies in the upper crust beneath volcanoes (e.g. Indrastuti et al., 2019; Lees, 1992; Miller and Smith, 1999; Paulatto et al., 2012; Waite and Moran, 2009). These anomalies are usually interpreted as resulting from the presence partially melted rocks and mush, but do not evidence the presence of large accumulations of mobile magmas.

As the upper magmatic reservoir is dominated by mush and crystal bearing magmas, the rheology of such magmatic mixtures have a critical control on their dynamics (Caricchi et al.,

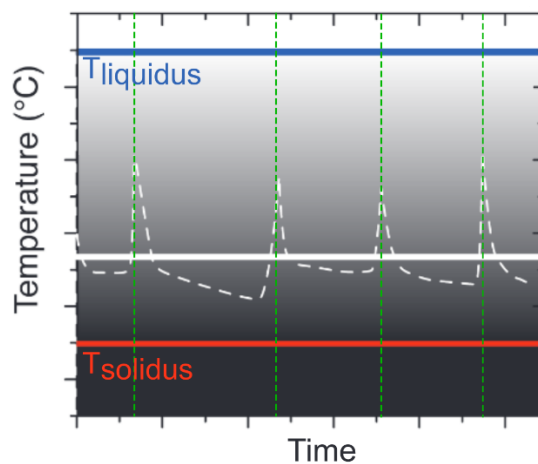


Figure 1.3: Evolution of the temperature in the central and hotter part of a magmatic body function of time. The period of emplacement of the repeated injections that increase the temperature of the reservoir are indicated with vertical green dashed lines. The temperature of the hotter part of the magma body is displayed with a white dashed curve. Blue, red, and white thick horizontal lines correspond to the temperatures of the liquidus, solidus and magma/mush transition respectively. Modified after Bachmann and Huber, 2016.

2007; Cordonnier et al., 2012; Lavallée et al., 2007; Sparks, 2003) and may also influence eruptive styles (Karlstrom et al., 2012). The transition between magmas and mush is linked to profound changes in the rheology, with an increase of several orders of magnitude of the effective viscosities. It is also marked by the onset of non-Newtonian behaviors characterized by shear thinning (decrease of the effective viscosity with the increase of the strain rate), and possibly the onset of a yield stress (Caricchi et al., 2007; Costa et al., 2009; Lavallée et al., 2012; Mader et al., 2013; Petford, 2009). These non-linear relationships between stress and strain result from the initiation of frictional contacts between crystals and the formation of force chains (Bergantz et al., 2017). Force chains are interconnected networks formed by the frictional contact between the particles, showing regions of high and low stresses. Their strengths depend on the local organization of the crystals and applied stresses. Because of the lock-up generated by the force chains, mushes are not eruptible (Marsh, 1981) and must be rejuvenated (destabilization of the forces chains and inhibition of the crystals friction) prior to eruptions. Accurate modeling of these mush dynamics is difficult because of the complex rheologies of magmatic mixtures. First attempts to model magmatic reservoir dynamics were performed with a combination of laboratory and numerical experiments (e.g. Bergantz and Ni, 1999; Huppert et al., 1984; Jellinek et al., 1999; Snyder and Tait, 1996) where the magma was considered as a fluid having effective properties function of the crystallinity and temperature. However, rheological laws that attempt to index the effective viscosity as a function of the crystal volume fraction (e.g. Krieger-Dougherty law) fail to recover non-Newtonian effects because they only take into account the hydrodynamic effects related to the presence of the crystals and neglect their frictional contacts. The approach chosen in this work is to use advanced physical modeling of crystal-bearing magmas. The core tool used herein is called Computational-Fluid-Dynamic and Discrete-Element-Method (CFD-DEM) numerical simulations (Bergantz et al., 2015; Schleicher et al., 2016; Schleicher and Bergantz, 2017), which will be explained in detail in Chapter 2. Despite their computational costs, CFD-DEM numerical simulations are particularly suitable to study mush dynamics because they do not rely on such rheological laws, and rather solve explicitly the motions of each grain and the stresses generated by its frictional contacts. However, the pioneering CFD-DEM simulations have been carried out at relatively low melt viscosities (0.2 Pa s) that are not relevant of evolved magmas ($>10^3$ Pa s), which prevents the simple extrapolation of their results to long-lived and dormant magmatic systems.

The evidence of mush dominated magma bodies challenges our ability to predict eruptions, and mitigate volcanic hazards. It is accepted that recharge events are ubiquitous in nature and may trigger volcanic eruptions (see next section). Understanding in which conditions such events may lead, or not, to an eruption is critical. This is why the comprehension of the magmas and mush rheologies, their evolutions during unrest events, and their associated physical processes at the grain scales is important. Finally, the geophysical detection of such event, estimations of the eruptible volumes, and physical properties of the materials is one of the key to better comprehend volcanic hazard. This thesis thus aims at improving our understanding of the grain scale physics, time scales and dynamics of unrest event. It also targets at improving our knowledge of the seismic properties of eruptible magmas in order to increase our ability to interpret results of seismic tomography images in terms of material properties of the eruptible magmas.

1.2 The physical processes of mush reawakening

The rejuvenation of magmatic mush prior to eruption requires the destabilization of the force chains and the generation of eruptible magmas. Different scenarios have been proposed in the literature. Some of them involved the injection of hot and mobile magma whereas others not. Here, we focus on mush reawakening scenarios in which the triggering event is the recharge in new magma, as highlighted in several eruptions (e.g. Murphy et al., 2000; Pallister et al., 1992; Takahashi and Nakagawa, 2013; Tomiya and Takeuchi, 2009). Thus, we do not consider scenarios that do not involve the input of enthalpy and momentum by new injection such as vibro-agitation (Davis et al., 2007), deep fragmentation (Gottsmann et al., 2009), syn-eruptive processes (Cashman and Giordano, 2014; Karlstrom et al., 2012), or relevant of cases where an eruptible magma chamber is already formed (e.g. Girona et al., 2015).

Bachmann and Bergantz (2006) proposed a scenario named *gas sparging* in which a hot and wet intruder emplaces at the base of the mush and reheats it without mass transfer of melt or crystals. The heat is transferred through conduction and advection by percolation of exsolved volatiles released during the second boiling of the intruded magma, which induces an upward flow

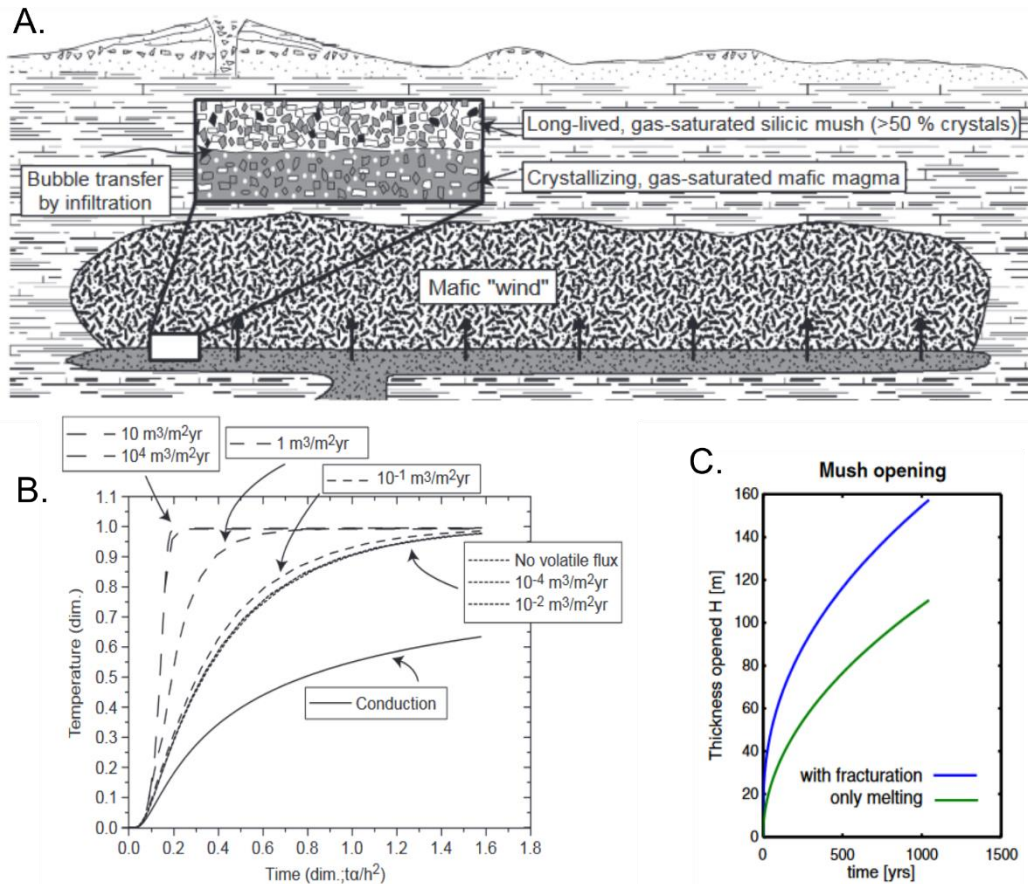


Figure 1.4: The sparging rejuvenation model (Bachmann and Bergantz, 2006). [A] Conceptual model. The cartoon displays a section of the upper crust in which a mush body is emplaced. A mafic intrusion is stalled at the base of the mush transferring heat by conduction, and advection of the exsolved volatiles released by the second boiling of the intruded magma. The inset show a zoom of the interface between the host mush and intruder. After Bachmann and Bergantz, 2006. [B] Evolution of the mush rejuvenation function volatiles flux. The abscissa is a dimensionless diffusive time and the ordinate is a dimensionless temperature. After Bachmann and Bergantz, 2006. [C] Evolution of the thickness of the remobilized layer function of the presence of absence of microfracturation. The blue curve corresponds to the case with fracturation and the green one without. After Huber et al., 2011.

of the host melt (Fig 1.4A). A significant upward flux in volatiles decreases the reactivation time (Fig 1.4B) and increases the accumulated volume of eruptible magma. However, the effectiveness of this advection process is limited to a narrow range of crystallinity at which crystal repacking occurs and channels of exsolved volatiles may be formed (Bachmann and Huber, 2019; Parmigiani et al., 2016, 2014). The *thermomechanical* model from Huber et al., 2011, extends the gas sparging one and considers sequences of microfracturing of the locked mush above the remobilization front to release the local overpressure generated by the partial melting of the crystals. This phenomenon accelerates and enhances the rejuvenation of mush (Fig 1.4C) by destabilization of the force chains. These two models consider the progressive rejuvenation of the mush without gravitational

instability (stable front remobilization) and require relatively long reactivation times (thousands of years for large systems).

Other models consider the occurrence of gravitational instabilities between the rejuvenated and locked part of the mush. The rejuvenation of the mush is also initiated by the advection of heat from a mobile magma stalled at the floor of the mushy reservoir (Burgisser and Bergantz, 2011; Couch et al., 2001). The *unzipping* model from Burgisser and Bergantz, 2011, and the *self-mixing* one from Couch et al. (2001), rely on the formation of a growing mobile layer at the interface between the host and the intruder by the melting of the crystals. This thermal boundary layer becomes less dense than the overlying mush and unstable. In the *self-mixing* model, this instability generates Rayleigh-Taylor instabilities that advect heat and mix with the host mush (Fig 1.5A). In the *unzipping* model, once the mobile layer reaches a critical thickness, it starts to convect internally. As this convective layer continues to grow, it becomes unstable and forms a larger buoyant instability by merging of adjacent convective cells, which leads to the overturn of the mush (Fig 1.5B). The two scenarios postulate the fluid-like behavior of the mush, which is consistent for weak mush just below the jamming transition (Bergantz et al., 2015). However, the scenario of unzipping appears more probable than that of self-mixing because the apparent viscosity contrast between the mush and mobile layer prevents the formation of simple convection (Burgisser and Bergantz, 2011). The unzipping model presents a rapid mechanism to rejuvenate a mush on timescales ranging from several months to decades after the emplacement of the hot mush layer (Fig 1.5C–D).

All of these models concentrate on specific processes of the mush remobilization, but rely on the assumption that the triggering event is the emplacement of a hot magma sill at the base of the mush without exchange of melt or solids. However, recent CFD-DEM numerical simulations focused on basaltic mush dynamics have shown that when injected, a crystal-free melt may fluidize and ascent through the mush (Bergantz et al., 2017, 2015; Schleicher et al., 2016; Schleicher and Bergantz, 2017). In these mafic simulations, the presence of granular soft faults delimits a region called the mixing bowl, in which mechanical mixing between the host and injected melts occurs. It raises the question of the behavior of injections in the context of evolved magmatic mush, which may influence their remobilization dynamics. It shows the necessity to extend these mafic studies to conditions relevant of evolved magmatic reservoirs and incorporate the effects of the difference in compositions and temperature between the host and intruded magma, which may impose a strong

contrast between their apparent viscosities and densities. Understanding and predicting the emplacement dynamics of new magma into a mush is of critical importance for our insight of mush remobilization processes.

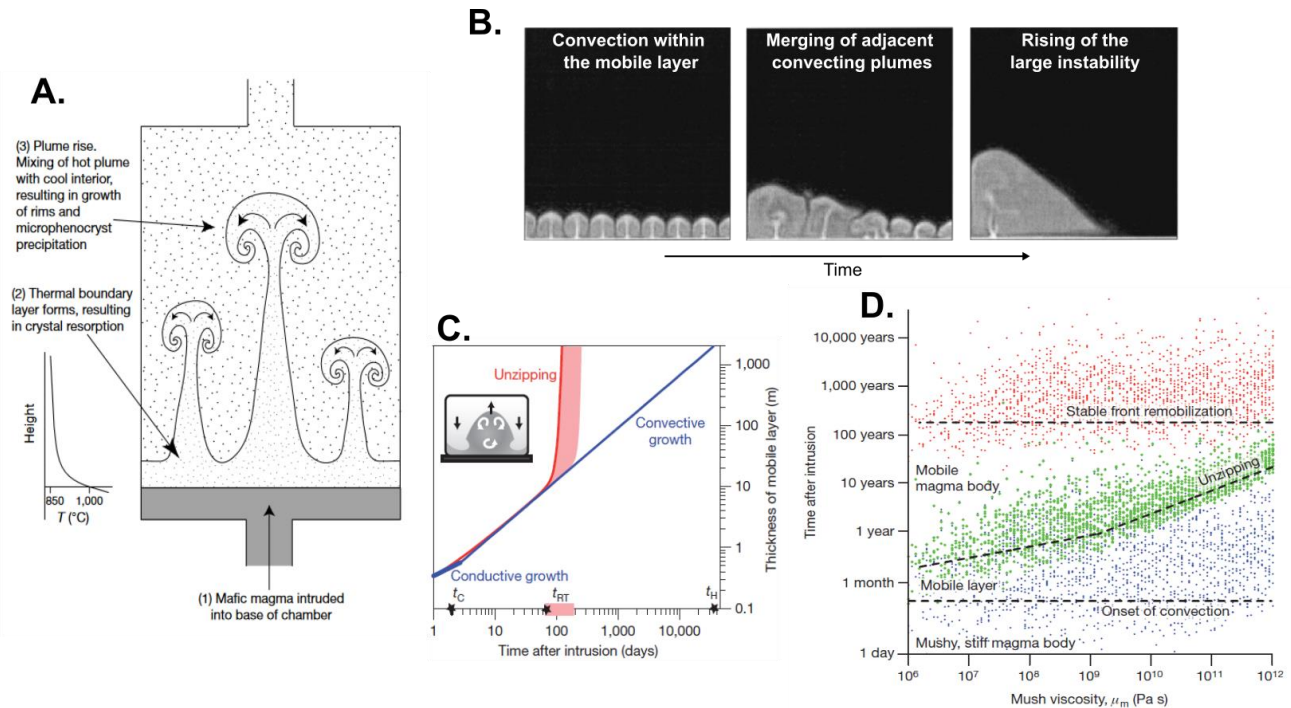


Figure 1.5: Remobilization of mush with gravitational instabilities. [A] Principle of the ‘self-mixing’ model (Couch et al., 2001). The intrusion of a mafic magma stalls at the base of the mush and reheats it, forming a mobile layer due to the decrease in the crystallinity. This thermal boundary layer becomes buoyant and unstable, producing rising plumes within the mush that mix with it. After Couch et al., 2001. [B] Snapshots of a numerical experiment showing the formation of plumes in a fluid with a strong temperature dependent viscosity, illustrating the unzipping scenario (Ke and Solomatov, 2004). In the three snapshots, the color of the fluid depends on its viscosity. Black colors indicate a very viscous fluid, and grey ones lower viscosities. The time increases to the left. In this experiment, the medium is heated by a plate located at the base of the tank. Modified after Ke and Solomatov, 2004. [C] Principle of the ‘unzipping’ model (Burgisser and Bergantz, 2011). The abscissa is the time and the ordinate the thickness of the mobile layer with logarithmic scales. The occurrence of the gravitational instability leads to the overturn of the mush (red curve) that significantly accelerates the reawakening process compared to a stable front remobilization (blue curve). After Burgisser and Bergantz, 2011. [D] Results of a Monte-Carlo simulations with the unzipping model. The axes are the mush effective viscosity in abscissa and the time in ordinate, both with logarithmic scales. For each simulation, three dots are displayed, indicating the onset of convections within the mobile layer (blue dots), the remobilization time with unzipping (green dots) and the reawakening time with a stable front remobilization (red dots). These results illustrate the efficiency of the unzipping to rapidly remobilize a magmatic mush. After Burgisser and Bergantz, 2011.

1.3 Imaging unrest events and seismic properties of eruptible magmas

The monitoring of unrest events with seismic tomography images relies to our ability to detect and image fluid dominated regions across magmatic systems. This method is based on the inversion of seismic signals travelling through the magmatic systems from active or natural sources. Upper crustal magma reservoirs usually show the presence of low seismic velocity anomalies (e.g. Indrastuti et al., 2019; Lees, 1992; Miller and Smith, 1999; Paulatto et al., 2012; Waite and Moran, 2009). These low velocities zones are usually interpreted as indicating the presence of partially molten rocks and mush (Fig 1.6). Furthermore, the presence of high ratio between compressional and shear waves velocities (V_p/V_s) beneath volcanoes also suggests the presence of a fluid phase (e.g. Chiarabba and Moretti, 2006; Kiser et al., 2016; Nakajima et al., 2001). However, the finite values of these ratios indicate that shear waves can travel across these upper crustal magmatic reservoirs, which does not support the presence of large accumulation of eruptible magmas. If detectable, these batches of magmas must be characterized by a zero velocity zone for the S waves and a sharp decrease of the P wave velocity at natural frequencies (Caricchi, 2008), as observed across the East Pacific ridge (Singh et al., 1998). The lack of evidence of melt dominated regions by seismic imaging can be explain by the episodically presence of magma chambers that rapidly reach a mushy state (Fig. 1.3), the averaging and smoothing effects of seismic tomography, or the fact that magma chambers may be hidden by the crystal mush because of the attenuation of wave in the mush. Tomographic images are computed with the first waves arrivals, that correspond to the fastest way between the source and the stations, which may be outside the magmatic system because of the low seismic velocity in magmatic system compared to the host crust. It results in the decrease of our ability to image magma bodies characterized by low velocities with such method based on wave travel times.

During the past decades, the seismic wave attenuation tomography has shown to be a promising tool to image subsurface structures (e.g. Prudencio et al., 2018) and magmatic plumbing systems (e.g. De Siena et al., 2014; Gori et al., 2005). Two types of attenuation exist, the scattering one related to geometric dispersion generated by rough heterogeneities, and the intrinsic attenuation related to the absorption and dissipation of the seismic energy by the medium in which the wave is travelling. Within magmatic systems, the presence of high attenuations are usually

interpreted as evidencing the presence of partially molten bodies, whereas low attenuation anomalies are linked to the presence of fully crystallized magma bodies. Quantitative interpretation of these results in terms of magma physical properties bears on our poor knowledge of the seismic properties of eruptible magmas and especially of their intrinsic attenuation. Few theoretical works and experiments have been performed to study the seismic properties of magmas. Most of these works focused on the properties of partially molten rocks (e.g. Mavko, 1980), or measured experimentally the velocities of both P and S waves at high frequencies before extrapolating them to seismic one (e.g. Caricchi et al., 2008). Other models predict the attenuation of seismic waves generated by the presence of melt filled crack but have to assume an intrinsic attenuation coefficient of the magma contained in this cracks (e.g. Kumagai and Chouet, 2000). Thanks to thermodynamic models, the materials properties (bulk modulus, density, viscosity, and heat conductivity/capacity) of the melt, which control the velocities and attenuations of waves in pure melt, can be easily predicted as a function of its composition, temperature, and pressure (Ghiorso, 2004; Ghiorso and Kress, 2004; Giordano et al., 2008). However the presence of particles in a suspension can greatly affect the wave velocities and attenuation as shown in experimental studies (e.g. Kuster and Toksoz, 1974b). Thus, it is necessary to have a physical model able to link the materials properties and concentration of the constituents of a magmatic mixture, to their velocities and attenuation coefficients in order to interpret the results of seismic tomographies with quantitative (amount of eruptible magma accumulated), and qualitative (physical properties of this magma) assessments.

Different theoretical models were proposed to predict wave velocities and attenuation coefficients in suspensions as a function of the constituent properties and concentrations. Two main approaches are used to predict the effective elastic and anelastic properties of suspensions: the *scattering theory* (e.g. Berryman, 1980; Kuster and Toksöz, 1974a) and the *coupled phase theory* (e.g. Atkinson and Kytömaa, 1992; Evans and Attenborough, 1997; Harker and Temple, 1988). The first approach models the scattering of an incident plane wave by immobile spherical inclusions and decomposes it in harmonics. This approach presents the advantage to be valid at any frequencies. The second is restricted to low frequencies but is able to take into account the relative motions between the phases and can explicitly incorporate mechanisms of momentum, heat and mass transfers between the constituents. Its applicability is limited to the long wavelength

assumption for which the seismic wavelengths have to be much larger than characteristic size of suspended phase. This assumption is valid at natural frequencies for magmas because the crystal sizes are very small compared to the seismic wavelengths, which makes this method particularly suitable to be applied to eruptible magmas. However, applying the coupled phase approach to eruptible magmas requires novel modifications of the constitutive equations in order to incorporate the viscous dissipation in the melt phase and the lubricated interactions between close crystals when approaching to the magma-mush transition.

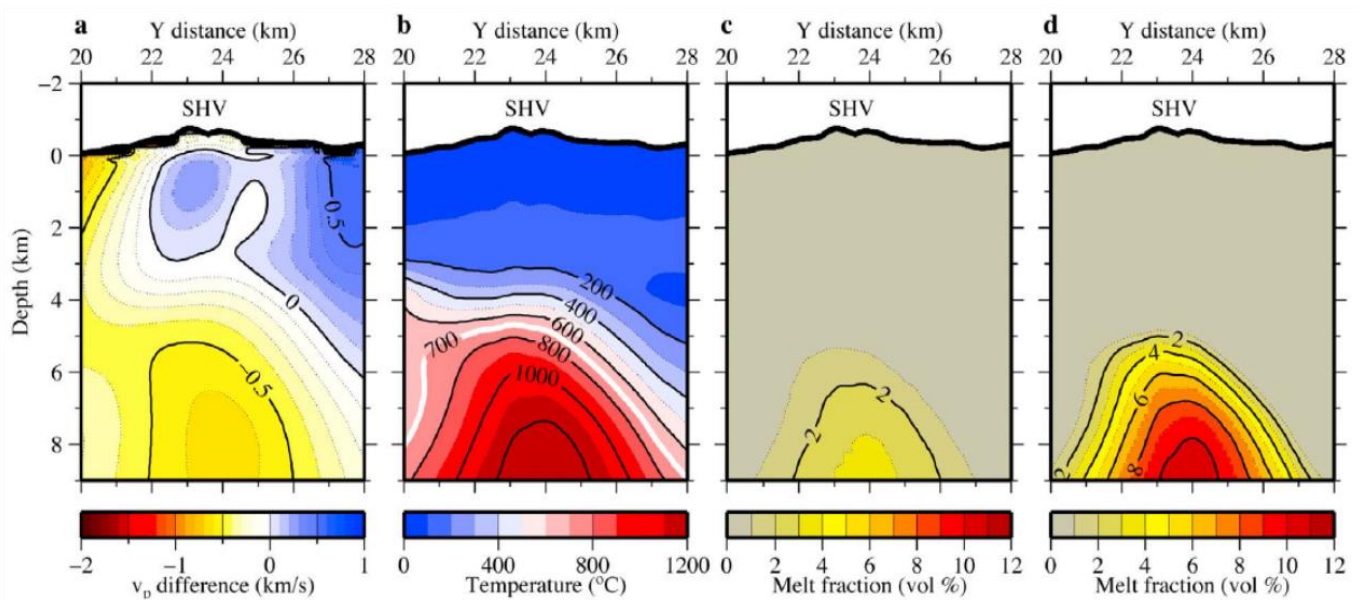


Figure 1.6 : Results and interpretations of V_p tomography at Soufriere Hill Volcano (SVH), Monsterrat Island (Paulatto et al., 2012). [A] Measured seismic anomalies in km s^{-1} . [B] Computed temperatures related to the seismic anomalies assuming that no melt is present. [C] Estimation of the melt volume fraction assuming a constant temperature (700°C) and considering the melt pocket as interconnected thin lenses. [D] Estimation of the melt volume fraction assuming a constant temperature (700°C) and considering the melt pocket as isolated spheres. All after Paulatto et al., 2012.

1.4 Manuscript organization and scientific questions

The rest of this manuscript is organized in six chapters. The first one (chapter 2) presents basic concepts of fluid mechanics required in the next chapters, and the theory of the software and code, MFIX (Multiphase Flow with Interphases eXchange), which is used in chapters 3, 4, and 5. In chapter 3, we constrain the importance and effects of lubrication on the dynamics of mush. Chapters 4 and 5 explore the dynamics of a magmatic mush and aim at determining the physical mechanisms that promote the reawakening of a magmatic mush. The last chapter explores the seismic properties of eruptible magmas.

In more details, chapter 3 examines what are the relevant forces that control the motion of crystals in a mush. Contact, buoyancy, pressure and drag forces were considered in previous simulations (Bergantz et al., 2015; Schleicher et al., 2016; Schleicher and Bergantz, 2017). However, lubrication (forces arising from the relative motion between close crystals) have not been incorporated yet. The magnitude of these forces is proportional to the surrounding melt viscosity and inversely proportional to the distance between the edges of neighboring crystals. In the context of evolved magmas, close the rheological lock-up, the importance and effect of these forces must be addressed. It implies to find what are the non-dimensional numbers that are the most relevant to discriminate which forces controls the motion of an individual crystal. CFD-DEM numerical simulations that include these lubrication forces are performed to explore their effects on mush macroscopic dynamics. The main objectives in this chapter is to determine the effects of lubrication forces on the macroscopic dynamic of crystals bearing magmas and mush. For that it required to define the relevant dimensionless numbers that scale the importance of each force controlling the motion of individual mush crystals at the grain scale and implement lubrication forces in the MFIX CFD-DEM model.

Chapter 4 explores the intrusion mechanisms of mobile magmas within weak mush and aims at identifying which conditions promote the most the rejuvenation of a magmatic mush. It extends studies performed during the last half decade (Bergantz et al., 2015; Schleicher et al., 2016; Schleicher and Bergantz, 2017) in order to study evolved mush dynamics. The effects induced by the presence of viscosity and buoyancy contrasts on the emplacement of new magmas must also be characterized before discussing the implications of the mechanics of magma intrusion on the

reawakening of mushy reservoirs. Here the main objective is to constrain the short-term behavior of an intrusion within a mush. In this way, the CFD-DEM model has to be adapted to replicate conditions relevant of chemically evolved magmas without unrealistic increase of the computational cost. It also requires to identify the relevant dimensionless parameters that are helpful to predict the behavior of the intruder.

Chapter 5 aims at exploring the interactions and mixing between intruded magma and resident mush and the effects of the intrusion on the physical properties of the host. It uses the results of Chapter 4 to constrain simulations mimicking conditions that are shared by many magmatic reservoirs. In particular, thermal processes may play an important role in the interactions between the mush and the intrusion and they have to be considered in the simulations. It requires to implement the temperature dependence of density and viscosity of the melt and to simulate the dynamics of the mush after intrusion emplacement. The description of the interactions between the intrusion and its host also calls for the quantification of the efficiency and the localization of mixing.

The sixth chapter goal is to predict the seismic properties (velocity and attenuation) of eruptible magmas, which are poorly understood. Chapter 6 uses the coupled phase approach, which presents the advantage of accounting for different physical processes and coupling between the phases. This allows us to explore the relative importance of different dissipative mechanisms and to give quantitative predictions of attenuation coefficients. However, it necessitates the modification of the constitutive equations in order to be applicable to magmas. The aims of this chapter is to predict the P waves velocities and attenuation coefficients in eruptible magma, which requires to adapt the couple phase approach to conditions relevant of magmas and identify the main attenuation mechanisms.

References:

- Annen, C., Blundy, J.D., Leuthold, J., Sparks, R.S.J., 2015. Construction and evolution of igneous bodies: Towards an integrated perspective of crustal magmatism. *Lithos* 230, 206–221. <https://doi.org/10.1016/j.lithos.2015.05.008>
- Annen, C., Blundy, J.D., Sparks, R.S.J., 2006. The Genesis of Intermediate and Silicic Magmas in Deep Crustal Hot Zones. *J. Petrol.* 47, 505–539. <https://doi.org/10.1093/ptrology/egi084>
- Annen, C., Sparks, R.S.J., 2002. Effects of repetitive emplacement of basaltic intrusions on thermal evolution and melt generation in the crust. *Earth Planet. Sci. Lett.* 203, 937–955. [https://doi.org/10.1016/S0012-821X\(02\)00929-9](https://doi.org/10.1016/S0012-821X(02)00929-9)
- Atkinson, C.M., Kytömaa, H.K., 1992. Acoustic wave speed and attenuation in suspensions. *Int. J. Multiph. Flow* 18, 577–592. [https://doi.org/10.1016/0301-9322\(92\)90053-J](https://doi.org/10.1016/0301-9322(92)90053-J)
- Bachmann, O., Bergantz, G., 2008. The Magma Reservoirs That Feed Supereruptions. *Elements* 4, 17–21. <https://doi.org/10.2113/GSELEMENTS.4.1.17>
- Bachmann, O., Bergantz, G.W., 2006. Gas percolation in upper-crustal silicic crystal mushes as a mechanism for upward heat advection and rejuvenation of near-solidus magma bodies. *J. Volcanol. Geotherm. Res.* 149, 85–102. <https://doi.org/10.1016/j.jvolgeores.2005.06.002>
- Bachmann, O., Dungan, M.A., Lipman, P.W., 2002. The Fish Canyon Magma Body, San Juan Volcanic Field, Colorado: Rejuvenation and Eruption of an Upper-Crustal Batholith. *J. Petrol.* 43, 1469–1503. <https://doi.org/10.1093/ptrology/43.8.1469>
- Bachmann, O., Huber, C., 2019. The Inner Workings of Crustal Distillation Columns; the Physical Mechanisms and Rates Controlling Phase Separation in Silicic Magma Reservoirs. *J. Petrol.* 60, 3–18. <https://doi.org/10.1093/ptrology/egy103>
- Bachmann, O., Huber, C., 2016. Silicic magma reservoirs in the Earth's crust. *Am. Mineral.* 101, 2377–2404. <https://doi.org/10.2138/am-2016-5675>
- Bergantz, G.W., Ni, J., 1999. A numerical study of sedimentation by dripping instabilities in viscous fluids. *Int. J. Multiph. Flow* 25, 307–320. [https://doi.org/10.1016/S0301-9322\(98\)00050-0](https://doi.org/10.1016/S0301-9322(98)00050-0)
- Bergantz, G.W., Schleicher, J.M., Burgisser, A., 2017. On the kinematics and dynamics of crystal-rich systems. *J. Geophys. Res. Solid Earth* 122, 2017JB014218. <https://doi.org/10.1002/2017JB014218>
- Bergantz, G.W., Schleicher, J.M., Burgisser, A., 2015. Open-system dynamics and mixing in magma mushes. *Nat. Geosci.* 8, 793–796. <https://doi.org/10.1038/ngeo2534>
- Berryman, J.G., 1980. Long-wavelength propagation in composite elastic media I. Spherical inclusions. *J. Acoust. Soc. Am.* 68, 1809–1819. <https://doi.org/10.1121/1.385171>
- Burgisser, A., Bergantz, G.W., 2011. A rapid mechanism to remobilize and homogenize highly crystalline magma bodies. *Nature* 471, 212–215. <https://doi.org/10.1038/nature09799>
- Caricchi, L., Annen, C., Blundy, J., Simpson, G., Pinel, V., 2014. Frequency and magnitude of volcanic eruptions controlled by magma injection and buoyancy. *Nat. Geosci.* 7, 126–130. <https://doi.org/10.1038/ngeo2041>
- Caricchi, L., Blundy, J., 2015. The temporal evolution of chemical and physical properties of magmatic systems. *Geol. Soc. Lond. Spec. Publ.* 422, 1–15. <https://doi.org/10.1144/SP422.11>
- Caricchi, L., Burlini, L., Ulmer, P., 2008. Propagation of P and S-waves in magmas with different crystal contents: Insights into the crystallinity of magmatic reservoirs. *J. Volcanol. Geotherm. Res., Evolution, Transfer and Release of Magmas and Volcanic Gases* 178, 740–750. <https://doi.org/10.1016/j.jvolgeores.2008.09.006>
- Caricchi, L., Burlini, L., Ulmer, P., Gerya, T., Vassalli, M., Papale, P., 2007. Non-Newtonian rheology of crystal-bearing magmas and implications for magma ascent dynamics. *Earth Planet. Sci. Lett.* 264, 402–419. <https://doi.org/10.1016/j.epsl.2007.09.032>
- Cashman, K.V., Giordano, G., 2014. Calderas and magma reservoirs. *J. Volcanol. Geotherm. Res.* 288, 28–45. <https://doi.org/10.1016/j.jvolgeores.2014.09.007>
- Cashman, K.V., Sparks, R.S.J., Blundy, J.D., 2017. Vertically extensive and unstable magmatic systems: A unified view of igneous processes. *Science* 355, eaag3055. <https://doi.org/10.1126/science.aag3055>
- Chiarabba, C., Moretti, M., 2006. An insight into the unrest phenomena at the Campi Flegrei caldera from Vp and Vp/Vs tomography. *Terra Nova* 18, 373–379. <https://doi.org/10.1111/j.1365-3121.2006.00701.x>
- Cordonnier, B., Caricchi, L., Pistone, M., Castro, J., Hess, K.-U., Gottschaller, S., Manga, M., Dingwell, D.B., Burlini, L., 2012. The viscous-brittle transition of crystal-bearing silicic melt: Direct observation of magma rupture and healing. *Geology* 40, 611–614. <https://doi.org/10.1130/G3914.1>
- Costa, A., Caricchi, L., Bagdassarov, N., 2009. A model for the rheology of particle-bearing suspensions and partially molten rocks. *Geochem. Geophys. Geosystems* 10. <https://doi.org/10.1029/2008GC002138>
- Couch, S., Sparks, R.S.J., Carroll, M.R., 2001. Mineral disequilibrium in lavas explained by convective self-mixing in open magma chambers. *Nature* 411, 1037–1039. <https://doi.org/10.1038/35082540>
- Davis, M., Koenders, M.A., Petford, N., 2007. Vibro-agitation of chambered magma. *J. Volcanol. Geotherm. Res., Large Silicic Magma Systems* 167, 24–36. <https://doi.org/10.1016/j.jvolgeores.2007.07.012>
- De Siena, L., Thomas, C., Waite, G.P., Moran, S.C., Klemme, S., 2014. Attenuation and scattering tomography of the deep plumbing system of Mount St. Helens. *J. Geophys. Res. Solid Earth* 119, 8223–8238. <https://doi.org/10.1002/2014JB011372>

- Edmonds, Cashman Katharine V., Holness Marian, Jackson Matthew, 2019. Architecture and dynamics of magma reservoirs. *Philos. Trans. R. Soc. Math. Phys. Eng. Sci.* 377, 20180298. <https://doi.org/10.1098/rsta.2018.0298>
- Evans, J.M., Attenborough, K., 1997. Coupled phase theory for sound propagation in emulsions. *J. Acoust. Soc. Am.* 102, 278–282. <https://doi.org/10.1121/1.419745>
- Gelman, S.E., Gutiérrez, F.J., Bachmann, O., 2013. On the longevity of large upper crustal silicic magma reservoirs. *Geology* 41, 759–762. <https://doi.org/10.1130/G34241.1>
- Ghiorso, M.S., 2004. An equation of state for silicate melts. I. Formulation of a general model. *Am. J. Sci.* 304, 637–678. <https://doi.org/10.2475/ajs.304.8-9.637>
- Ghiorso, M.S., Kress, V.C., 2004. An equation of state for silicate melts. II. Calibration of volumetric properties at 105 Pa. *Am. J. Sci.* 304, 679–751. <https://doi.org/10.2475/ajs.304.8-9.679>
- Giordano, D., Russell, J.K., Dingwell, D.B., 2008. Viscosity of magmatic liquids: A model. *Earth Planet. Sci. Lett.* 271, 123–134. <https://doi.org/10.1016/j.epsl.2008.03.038>
- Girona, T., Costa, F., Schubert, G., 2015. Degassing during quiescence as a trigger of magma ascent and volcanic eruptions. *Sci. Rep.* 5, 18212. <https://doi.org/10.1038/srep18212>
- Gori, P.D., Chiarabba, C., Patanè, D., 2005. Qp structure of Mount Etna: Constraints for the physics of the plumbing system. *J. Geophys. Res. Solid Earth* 110. <https://doi.org/10.1029/2003JB002875>
- Gottsmann, J., Lavallée, Y., Martí, J., Aguirre-Díaz, G., 2009. Magma–tectonic interaction and the eruption of silicic batholiths. *Earth Planet. Sci. Lett.* 284, 426–434. <https://doi.org/10.1016/j.epsl.2009.05.008>
- Harker, A.H., Temple, J.A.G., 1988. Velocity and attenuation of ultrasound in suspensions of particles in fluids. *J. Phys. Appl. Phys.* 21, 1576–1588. <https://doi.org/10.1088/0022-3727/21/11/006>
- Huber, C., Bachmann, O., Dufek, J., 2011. Thermo-mechanical reactivation of locked crystal mushes: Melting-induced internal fracturing and assimilation processes in magmas. *Earth Planet. Sci. Lett.* 304, 443–454. <https://doi.org/10.1016/j.epsl.2011.02.022>
- Huber, C., Bachmann, O., Manga, M., 2009. Homogenization processes in silicic magma chambers by stirring and mushification (latent heat buffering). *Earth Planet. Sci. Lett.* 283, 38–47. <https://doi.org/10.1016/j.epsl.2009.03.029>
- Huppert, H.E., Stephen, R., Sparks, J., Turner, J.S., 1984. Some effects of viscosity on the dynamics of replenished magma chambers. *J. Geophys. Res. Solid Earth* 89, 6857–6877. <https://doi.org/10.1029/JB089iB08p06857>
- Indrastuti, N., Nugraha, A.D., McCausland, W.A., Hendrasto, M., Gunawan, H., Kusnandar, R., Kasbani, Kristianto, 2019. 3-D Seismic Tomographic study of Sinabung Volcano, Northern Sumatra, Indonesia, during the inter-eruptive period October 2010–July 2013. *J. Volcanol. Geotherm. Res.* <https://doi.org/10.1016/j.jvolgeores.2019.03.001>
- Jellinek, A.M., Kerr, R.C., Griffiths, R.W., 1999. Mixing and compositional stratification produced by natural convection: 1. Experiments and their application to Earth's core and mantle. *J. Geophys. Res. Solid Earth* 104, 7183–7201. <https://doi.org/10.1029/1998JB900116>
- Karakas, O., Degruyter, W., Bachmann, O., Dufek, J., 2017. Lifetime and size of shallow magma bodies controlled by crustal-scale magmatism. *Nat. Geosci.* 10, 446–450. <https://doi.org/10.1038/ngeo2959>
- Karlstrom, L., Rudolph, M.L., Manga, M., 2012. Caldera size modulated by the yield stress within a crystal-rich magma reservoir. *Nat. Geosci.* 5, 402–405. <https://doi.org/10.1038/ngeo1453>
- Kiser, E., Palomeras, I., Levander, A., Zelt, C., Harder, S., Schmandt, B., Hansen, S., Creager, K., Ulberg, C., 2016. Magma reservoirs from the upper crust to the Moho inferred from high-resolution Vp and Vs models beneath Mount St. Helens, Washington State, USA. *Geology* 44, 411–414. <https://doi.org/10.1130/G37591.1>
- Kumagai, H., Chouet, B.A., 2000. Acoustic properties of a crack containing magmatic or hydrothermal fluids. *J. Geophys. Res. Solid Earth* 105, 25493–25512. <https://doi.org/10.1029/2000JB900273>
- Kuster, G., Toksöz, M., 1974a. Velocity and attenuation of seismic waves in two-phase media: part i. theoretical formulations. *GEOPHYSICS* 39, 587–606. <https://doi.org/10.1190/1.1440450>
- Kuster, G.T., Toksoz, M.N., 1974b. Velocity and attenuation of seismic waves in two-phase media; Part II, Experimental results. *Geophysics* 39, 607–618. <https://doi.org/10.1190/1.1440451>
- Lavallée, Y., Hess, K.-U., Cordonnier, B., Dingwell, D.B., 2007. Non-Newtonian rheological law for highly crystalline dome lavas. *Geology* 35, 843–846. <https://doi.org/10.1130/G23594A.1>
- Lavallée, Y., Varley, N., Alatorre-Ibargüenoiia, M., Hess, K.-U., Kueppers, U., Mueller, S., Richard, D., Scheu, B., Spieler, O., Dingwell, D., 2012. Magmatic architecture of dome-building eruptions at Volcán de Colima, Mexico. *Bull. Volcanol.* 74, 249–260.
- Lees, J.M., 1992. The magma system of Mount St. Helens: non-linear high-resolution P-wave tomography. *J. Volcanol. Geotherm. Res.* 53, 103–116. [https://doi.org/10.1016/0377-0273\(92\)90077-Q](https://doi.org/10.1016/0377-0273(92)90077-Q)
- Marsh, B.D., 1981. On the crystallinity, probability of occurrence, and rheology of lava and magma. *Contr. Mineral. and Petrol.* 78, 85–98. <https://doi.org/10.1007/BF00371146>
- Mader, H.M., Llewellyn, E.W., Mueller, S.P., 2013. The rheology of two-phase magmas: A review and analysis. *J. Volcanol. Geotherm. Res.* 257, 135–158. <https://doi.org/10.1016/j.jvolgeores.2013.02.014>
- Mavko, G.M., 1980. Velocity and attenuation in partially molten rocks. *J. Geophys. Res. Solid Earth* 5173–5189. [https://doi.org/10.1029/JB085iB10p05173@10.1002/\(ISSN\)2169-9356.STANFORD1](https://doi.org/10.1029/JB085iB10p05173@10.1002/(ISSN)2169-9356.STANFORD1)
- Miller, D.S., Smith, R.B., 1999. P and S velocity structure of the Yellowstone volcanic field from local earthquake and controlled-source tomography. *J. Geophys. Res. Solid Earth* 104, 15105–15121. <https://doi.org/10.1029/1998JB900095>
- Murphy, M.D., Sparks, R.S.J., Barclay, J., Carroll, M.R., Brewer, T.S., 2000. Remobilization of Andesite Magma by Intrusion of Mafic Magma at the Soufriere Hills Volcano, Montserrat, West Indies. *J. Petrol.* 41, 21–42.

-
- Murphy, M.D., Sparks, R.S.J., Barclay, J., Carroll, M.R., Lejeune, A.-M., Brewer, T.S., Macdonald, R., Black, S., Young, S., 1998. The role of magma mixing in triggering the current eruption at the Soufriere Hills Volcano, Montserrat, West Indies. *Geophys. Res. Lett.* 25, 3433–3436. <https://doi.org/10.1029/98GL00713>
- Nakajima, J., Matsuzawa, T., Hasegawa, A., Zhao, D., 2001. Three-dimensional structure of Vp, Vs, and Vp/Vs beneath northeastern Japan: Implications for arc magmatism and fluids. *J. Geophys. Res. Solid Earth* 106, 21843–21857. <https://doi.org/10.1029/2000JB000008>
- Pallister, J.S., Hoblitt, R.P., Reyes, A.G., 1992. A basalt trigger for the 1991 eruptions of Pinatubo volcano? *Nature* 356, 426–428. <https://doi.org/10.1038/356426a0>
- Parmigiani, A., Faroughi, S., Huber, C., Bachmann, O., Su, Y., 2016. Bubble accumulation and its role in the evolution of magma reservoirs in the upper crust. *Nature* 532, 492–495. <https://doi.org/10.1038/nature17401>
- Parmigiani, A., Huber, C., Bachmann, O., 2014. Mush microphysics and the reactivation of crystal-rich magma reservoirs. *J. Geophys. Res. Solid Earth* 119, 6308–6322. <https://doi.org/10.1002/2014JB011124>
- Paulatto, M., Annen, C., Henstock, T.J., Kiddle, E., Minshull, T.A., Sparks, R.S.J., Voight, B., 2012. Magma chamber properties from integrated seismic tomography and thermal modeling at Montserrat. *Geochem. Geophys. Geosystems* 13. <https://doi.org/10.1029/2011GC003892>
- Petford, N., 2009. Which effective viscosity? *Mineral. Mag.* 73, 167–191. <https://doi.org/10.1180/minmag.2009.073.2.167>
- Prudencio, J., Manga, M., Taira, T., 2018. Subsurface Structure of Long Valley Caldera Imaged With Seismic Scattering and Intrinsic Attenuation. *J. Geophys. Res. Solid Earth* 123, 5987–5999. <https://doi.org/10.1029/2017JB014986>
- Schleicher, J.M., Bergantz, G.W., 2017. The Mechanics and Temporal Evolution of an Open-system Magmatic Intrusion into a Crystal-rich Magma. *J. Petrol.* 58, 1059–1072. <https://doi.org/10.1093/petrology/egx045>
- Schleicher, J.M., Bergantz, G.W., Breidenthal, R.E., Burgisser, A., 2016. Time scales of crystal mixing in magma mushes. *Geophys. Res. Lett.* 43, 1543–1550. <https://doi.org/10.1002/2015GL067372>
- Singh, S.C., Kent, G.M., Collier, J.S., Harding, A.J., Orcutt, J.A., 1998. Melt to mush variations in crustal magma properties along the ridge crest at the southern East Pacific Rise. *Nature* 394, 874–878. <https://doi.org/10.1038/29740>
- Snyder, D., Tait, S., 1996. Magma mixing by convective entrainment. *Nature* 379, 529–531. <https://doi.org/10.1038/379529a0>
- Sparks, R.S.J., 2003. Forecasting volcanic eruptions. *Earth Planet. Sci. Lett.* 210, 1–15. [https://doi.org/10.1016/S0012-821X\(03\)00124-9](https://doi.org/10.1016/S0012-821X(03)00124-9)
- Sparks, R.S.J., Annen, C., Blundy, J.D., Cashman, K.V., Rust, A.C., Jackson, M.D., 2019. Formation and dynamics of magma reservoirs. *Philos. Trans. R. Soc. A.* <https://doi.org/10.1098/rsta.2018.0019>
- Takahashi, R., Nakagawa, M., 2013. Formation of a Compositionally Reverse Zoned Magma Chamber: Petrology of the ad 1640 and 1694 Eruptions of Hokkaido-Komagatake Volcano, Japan. *J. Petrol.* 54, 815–838. <https://doi.org/10.1093/petrology/egs087>
- Tomiya, A., Takeuchi, S., 2009. Two-Stage Magma Mixing and Initial Phase of the 1667 Plinian Eruption of Tarumai Volcano. AGU Fall Meet. Abstr. 51.
- Waite, G.P., Moran, S.C., 2009. VP Structure of Mount St. Helens, Washington, USA, imaged with local earthquake tomography. *J. Volcanol. Geotherm. Res.* 182, 113–122. <https://doi.org/10.1016/j.jvolgeores.2009.02.009>

Chapter 2: CFD-DEM model

2.1 Introduction

Modeling multiphase flows in volcanology is challenging because of the strong feedbacks existing between the dynamics of the different phases. Several approaches have been used to model volcanic fluid flows in which a discrete phase is present (solids here). In the Eulerian *single phase pseudo-fluid* approach, the fluid and solids are assumed to move together and are approximated as a pseudo-fluid having effective properties function of the constituents individual properties and concentrations (e.g. Dufek and Bergantz, 2005; Kelfoun and Druitt, 2005; Longo et al., 2012, 2006; Montagna et al., 2015). In this approach, the multiphase flow is described with one set of constitutive equations. The *two-fluid model* (TFM) is an Eulerian-Eulerian approach that considers the two phases as interpenetrating continuums experiencing coupling between their respective motions and temperatures. The discrete phase is averaged in space and described by constitutive equations similar to those of the fluid phase (e.g. Bergantz, 2000; Bergantz and Ni, 1999; Dufek and Bachmann, 2010; Molina et al., 2012; Ruprecht et al., 2008). This approach can be extended to account of the presence of a gaz phase (Keller and Suckale, 2019). The *Lattice-Boltzmann Model* (LBM) can be applied to either two-phases (e.g. Huber et al. 2008) or three-phases (e.g. Parmigiani et al 2014). This method solve the discrete Boltzmann equation instead of the Navier-Stokes equations and is based on streaming and collision processes able to reproduce complex behaviors in fluids. The *Discrete-Element-Method* (DEM) approach is a Lagrangian approach that considers the discrete phase as particles. It was used to study different phenomena in volcanology as for example, mush and magma dynamics, pyroclastic density currents, or stability of volcanic edifices (e.g. Bergantz et al., 2017, 2015; Breard et al., 2018; Holohan et al., 2017; Lube et al., 2019; McIntire et al., 2019; Morgan and McGovern, 2005; Qin et al., 2019; Schleicher et al., 2016; Schleicher and Bergantz, 2017; Suckale et al., 2012).

The *single phase pseudo-fluid* and *two-fluid model* present the advantage to be applicable to large scales and are able to model the dynamic of entire magmatic reservoirs. Continuum models also present the advantage to be able to account of reacting flows (e.g. Keller and Suckale 2019), which may play a great role on how magmatic materials evolved chemically during their transport

through the crust. However, they cannot fully describe the complex couplings between the constituents. The *single phase pseudo-fluid* method does not account of the relative motion between the particles and the fluid. The effect of the presence of solids on the mixture rheology may be approximated with rheological law that indexes the effective viscosity of the suspension to the solid volume fraction (e.g Einstein-Roscoe or Krieger-Dougherty laws). However, these laws only capture the hydrodynamic effects and cannot account of non-Newtonian behaviors related to frictional and/or collisional contacts between the solids. The *TFM* considers two sets of constitutive equations for each phase and is able to account for phase relative motions and coupling interactions. In this approach, the particle dynamic is averaged in space, and particle rotations are neglected. The particle-particle interactions are expressed in the solid stress tensor that depends on the solid volume fraction. At small concentrations, the stress tensor is collisional. However, it is not able to model complex particles flows (e.g. crossing flows; Chen and Wang, 2014) or solid–solid unmixing such as size and/or density segregation because of the averaging in space of the solid phase. For dense suspensions, the stress tensor is frictional and depends on the effective friction coefficient of the mixture. This coefficient may be predicted with constitutive equations based on viscous numbers (e.g. Boyer et al., 2011). However, this approach cannot capture local and nonlinear effects related to the presence of the frictional force chains. The *LBM* may be applied either to pore scale (Parmigiani et al 2011, Parmigiani et al. 2014) or reservoir scale processes (Huber et al, 2008) and present the advantage to be able to account of reacting flows and surface tension between the liquid and gas phases as well as wetting and non-wetting interactions between the solids and fluid phases. However, the actual *LBM* approaches in volcanology impose that the solid phase is immobile (e.g Huber et al. 2008; Parmigiani et al. 2011) which restrict their application in the present study. The *DEM* approach is able to fully capture the stresses generated by the frictional contacts between the solids, making it particularly suitable to study magmatic mush dynamics. It also presents the advantage to obtain particle trajectories, force distribution, and the organization of the force chains to describe and characterize the dynamics. However, this method is computationally expensive and is limited by the number of particles it can handle, restricting its application to small-scale setups. Thus, the *DEM* model must be used to study specific and complex physical processes of mush dynamics and cannot model the entire magmatic reservoir.

When using a discrete model for the solids, two approaches exist to model the fluid. The *Direct Numerical Simulation* (DNS-DEM) is a method in which the fluid is fully resolved, which

means that the fluid grid cells are smaller than the size of the particles (e.g. Qin et al., 2019; Suckale et al., 2012). This method presents the advantage to model explicitly the flow of the fluid around the particles and to not rely on averaged drag laws to manage the coupling between the fluid and the solids. However, because of the large number of fluid elements, it is restricted in the number of particles it can handle, which limits it to study dynamics at the pore scale. The approach chosen here is *Computational-Fluid-Dynamics and Discrete-Element-Method* (CFD-DEM) which represents a compromise between the DNS-DEM model and larger scale approaches. The fluid grid size is larger than that of the particle (a fluid element contains a few particles), which increases significantly the number of particles which can be handled in the simulation. The CFD-DEM model is able to manage computational domains up to a few meters, allowing it to access the macroscopic effects of the complex coupling processes occurring at the grain scale. The modeling of the coupling between the solids and the fluid necessitates to average in space the particle properties, and interpolate the fluid properties at the particle positions. Then the drag forces are computed with parameterized laws. This approach is not able to capture the rotation of the spherical particles under fluid shear or the turbulence of the fluid between the particles. However, for magmatic mush, the particle Reynolds numbers are small, indicating that the fluid creeps around the solids and that the characteristic length scales of the mixture flow are much larger than the solid sizes. Thereby, CFD-DEM approaches are ideal to study complex mush dynamics at the macroscopic scale.

There is petrological (Wallace, 2005) and field (Wallace, 2001) evidences that large silicic magma bodies contain a free gas phase while stored at upper crustal depths. This magmatic volatile phase is most likely present as bubbles in melt-rich regions and as elongated channels in crystal-rich regions (Parmigiani et al., 2014). Even in melt-rich area, it could account for as much as 10 vol% of a magma chamber (Wallace, 2005). The presence of bubbles may affect how magmatic reservoirs respond mechanically to the input of new magma. Exsolved volatiles increase the compressibility of the materials constituting the reservoir, which dampens the increase of pressure associated with the injection of new magma and how the host reservoir and surrounding crust accommodates it. According to authors, it can drive magma mixing and significantly affect convective regimes (Ruprecht et al., 2008). However, magma mixing does not always involve a gas phase, At Vesuvius, for instance, mixing occurred with undersaturated magmas (Cioni et al., 1995). Among others Pistone et al. (2012) have conducted exploratory experiments on the behavior

of crystal-bearing bubbly magmas, and found out that the three-phase magma response to shear is complex with a combination of shear localization, crystal breakage, and bubble migration due to crystal rotation. When two phases are not lumped together (Suckale et al., 2016), modeling of such three-phase interactions is currently only possible within small computational volumes ($<10^2$ particles) under restricted conditions such as deformable bubbles with immobile but polyhedral crystals (e.g. Parmigiani et al., 2017) or mobile but spherical crystals (Qin and Suckale, 2017). Because these inspirational studies struggle to find appropriate validation experiments (e.g. Oppenheimer et al., 2015), three-phase modeling is currently a very high gain endeavor but also a very risky one.

The present chapter aims at presenting the theory and some numerical aspects of the MFIX CFD-DEM model used in the chapters 3, 4, and 5. These chapters focus on the controls exerted by the solid phase on the mush dynamics and have not required modification of the MFIX approach for the fluid phase. During this thesis, a particular attention was paid to the modeling of the discrete solid phase. Thereby, the main focus of the present chapter is dedicated to the modeling of the solid phase. The fluid phase conservative equations and numerical approach are quickly presented. For a complete presentations, see Syamlal (1998), and Syamlal et al. (1993). For a presentation of the derivation of the fluid phase constitutive equations, see Crowe et al. (1997), and Ishii and Hibiki (2011). The presentation of the DEM model covers the MFIX-2016 implementation. The changes implemented in the models during this thesis are presented in the corresponding chapters. For verifications and validations of MFIX-DEM, see Garg et al. (2012), and Li et al. (2012). In the present chapter, the first part introduces the fluid phase constitutive equations. The second part presents the solid constitutive equations and particle-particle coupling phenomena. The third part details the coupling interactions between the solids and the surrounding fluid. The fourth part gives an overview of the numerical methods. The key points of the fluid solver are presented. A presentation of the DEM solver follows and its stability conditions are detailed. The last part presents briefly the dimensionless numbers used during this thesis.

Symbol (unit)	Definition
C_D	Particle drag coefficient
C_{pf} (J K ⁻¹)	Fluid heat capacity
C_{ps} (J K ⁻¹)	Particle heat capacity
d_p (m)	Particle diameter

Symbol (unit)	Definition
$D_{i,j}$ (m)	Distance between particle center of mass
E (Pa)	Particle young modulus
$e_n ; e_t$	Normal and tangential restitution coefficients
\vec{f} (kg m s ⁻²)	Fluid body forces
F_R	Froude number
\vec{F}_B (kg m s ⁻²)	Basset force
\vec{F}_C (kg m s ⁻²)	Contact force
$\vec{F}_C^{\vec{n}}$ (kg m s ⁻²)	Normal contact force
$\vec{F}_C^{\vec{t}}$ (kg m s ⁻²)	Tangential contact force
$\vec{F}_S^{\vec{n}}$ (kg m s ⁻²)	Normal contact spring force
$\vec{F}_S^{\vec{t}}$ (kg m s ⁻²)	Tangential contact spring force
\vec{F}_D (kg m s ⁻²)	Drag force
$\vec{F}_D^{\vec{n}}$ (kg m s ⁻²)	Normal contact dashpot force
$\vec{F}_D^{\vec{t}}$ (kg m s ⁻²)	Tangential contact dashpot force
\vec{F}_{fs} (kg m s ⁻²)	Fluid solid momentum transfer force
\vec{F}_P (kg m s ⁻²)	Pressure force force
\vec{F}_{VM} (kg m s ⁻²)	Virtual mass force
G (Pa)	Particle shear modulus
\vec{g} (m s ⁻²)	Gravitational acceleration vector
H_{fs} (W)	Fluid-solid heat transfer
$H_{i,j}$ (W m ⁻² K ⁻¹)	Solid-fluid-solid effective conductance
h (m)	Distance between particle edges
h_t	Coefficient of fluid-solid heat transfer
I_s (kg m ²)	Particle inertial moment
\vec{J}_{fs} (kg m s ⁻¹)	Fluid-solids momentum transfer
K_f (Pa)	Fluid bulk modulus
K_v	Generic kernel of the control volume
k_f (W m ⁻¹ K ⁻¹)	Fluid heat conductivity
k_t (Pa)	Tangential spring coefficient
k_n (Pa)	Normal spring coefficient
k_s (W m ⁻¹ K ⁻¹)	Particle heat conductivity
k_f (W m ⁻¹ K ⁻¹)	Fluid heat conductivity
L (m)	Distance between the particle center of mass and contact point
L_e	Leighton number
m_{eff} (kg)	Particles effective mass
m_s (kg)	Particle mass
Nu	Nusselt number
P (Pa)	Fluid pressure
P^* (Pa)	Initial pressure field during the iteration
P' (Pa)	Fluid pressure correction
Pe	Peclet number
P_R	Prandtl number
Q_{fs} (w m ⁻²)	Fluid-solids heat flux

Symbol (unit)	Definition
Q_{sfs} (w m ⁻²)	Solids-fluid-solids heat flux
Q_{ss} (w m ⁻²)	Solids-solids heat flux
R^* (m)	Contact area effective radius
R_{eff} (m)	Particles effective radius
Re	Reynolds number
Re_p	Particle Reynolds number
St	Stokes number
T_f (K)	Fluid temperature
T_s (K)	Particle temperature
\vec{T}_C (kg m ² s ⁻²)	Contact Torque
t (s)	Time
$\vec{t}_{i,j}$	Tangential contact unit vector
V_f (m ³)	Volume of fluid contain in the volume v
\vec{V}_s (m s ⁻¹)	Total particle relative velocity
\vec{v}_f (m s ⁻¹)	Fluid velocity
v_{fx}^* (m s ⁻¹)	Fluid uncorrected velocity in x direction
v_{fy}^* (m s ⁻¹)	Fluid uncorrected velocity in y direction
v_{fz}^* (m s ⁻¹)	Fluid uncorrected velocity in z direction
v_{fx}' (m s ⁻¹)	Fluid velocity correction in x direction
v_{fy}' (m s ⁻¹)	Fluid velocity correction in y direction
v_{fz}' (m s ⁻¹)	Fluid velocity correction in z direction
\vec{v}_s (m s ⁻¹)	Particle velocity
\vec{X} (m)	Particle position vector
\vec{X}_f (m)	Fluid grid node position
α_c	Contact stability coefficient
α_f (K ⁻¹)	Fluid thermal expansion coefficient
α_{sfs} (rad)	Solid-fluid-solid heat transfer effective angle
α_v	Viscous stability coefficient
β_{sfs} (rad)	Solid-solid heat transfer effective angle
β_{fs}	Fluid-particle momentum transfer coefficient
$\dot{\gamma}$ (s ⁻¹)	Shear rate
$\Delta\rho$ (kg m ⁻³)	Density contrast between fluid and particles
Δt (s)	Fluid time step
Δt_{solid} (s)	Solid time step
$\Delta t_{contact}$ (s)	Maximum contact time step
Δt_{drag} (s)	Maximum drag time step
Δx (m)	Grid size in x direction
Δy (m)	Grid size in y direction
Δz (m)	Grid size in z direction
δ_{ij}	Kronecker delta or Unit tensor
$\vec{\delta}_t$ (m)	Tangential displacement
δ_n (m)	Particle overlap
$\vec{\epsilon}_f$ (s ⁻¹)	Strain rate tensor
ϵ (m)	Particle roughness

Symbol (unit)	Definition
ζ (m)	Thermal fluid lens length
η (Pa s)	Fluid dynamic viscosity
η_b (Pa s)	Fluid bulk viscosity
η_n	Normal contact damping coefficient
η_t	Tangential contact damping coefficient
$\vec{\eta}_{i,j}$ (Pa s)	Normal vector between the particle center of mass
λ (Pa s)	Fluid volume viscosity
μ_s	Particle friction coefficient
ρ_p (kg m ⁻³)	Particle density
ρ_f (kg m ⁻³)	Fluid density
σ	Particle Poisson ratio
$\overline{\sigma}_f$ (kg m ⁻¹ s ⁻²)	Fluid stress tensor
σ_n (kg m ⁻¹ s ⁻²)	Normal load
$\overline{\sigma}_v$ (kg m ⁻¹ s ⁻²)	Viscous stress tensor
τ_s (s)	Particle response time
v (m ³)	Fluid cell volume
Φ	Particle volume fraction
$\vec{\omega}_s$ (rad s ⁻¹)	Particle rotation vector
ω (rad s ⁻¹)	Oscillatory flow angular frequency

Table 2.1: List of the chapters symbols

2.2 Governing equations of the fluid phase

2.2.1 Mass conservation

The mass conservation, or equation of continuity, states that within a control volume, the rate of mass accumulation is balanced by the mass fluxes through its surfaces. Neglecting mass sources, it is expressed by a differential form as (Ishii and Hibiki, 2011):

$$\frac{\partial \rho_f}{\partial t} + \nabla \cdot (\rho_f \vec{v}_f) = 0, \quad (2.1)$$

where ρ_f is the fluid density and \vec{v}_f is the fluid velocity (see table 2.1 for a list of the chapter variables). The first term in Eq. (2.1) describes the rate of internal mass change in the control volume and the second one, the total amount of mass exchanged at its boundaries. For many applications, it is valid to consider the fluid as incompressible and to use the Boussinesq approximation (density gradient neglected excepted in the buoyancy term of the momentum equation). Applying these assumptions to Eq. (2.1) yields:

$$\nabla \cdot \vec{v}_f = 0, \quad (2.2)$$

which expresses that the flow of an incompressible fluid in a control volume is solenoidal.

2.2.2 Momentum conservation

The momentum balance or equation of motion, links the evolution of the fluid momentum within the control volume to the internal and external forces applied to it. In its differential form, it reads (Ishii and Hibiki, 2011):

$$\frac{D \rho_f \vec{v}_f}{Dt} = \nabla \cdot \overline{\overline{\sigma}}_f + \rho_f \vec{f}. \quad (2.3)$$

In equation (2.3), the left hand side is the material derivative of the product of the fluid density and velocity¹. On the right hand side, the first term is the divergence of the fluid stress tensor, $\overline{\overline{\sigma}}_f$, which corresponds to the fluid internal forces. The second term corresponds to the body forces applied to

¹ $\frac{D \rho_f \vec{v}_f}{Dt} = \frac{\partial \rho_f \vec{v}_f}{\partial t} + \nabla \cdot (\rho_f \vec{v}_f \otimes \vec{v}_f)$

the control volume. This force may be reduced to the gravitational forces ($\vec{f} = \vec{g}$). The fluid stress tensor can be split in pressure and viscous contributions as:

$$\overline{\overline{\sigma}}_f = -P \delta_{ij} + \overline{\overline{\sigma}}_v, \quad (2.4)$$

where P is the fluid pressure, δ_{ij} is the unit tensor, and $\overline{\overline{\sigma}}_v$ is the viscous stress. For a Newtonian fluid (linear relationship between the fluid strain rate and stress), the viscous stress tensor may be expressed by:

$$\overline{\overline{\sigma}}_v = 2 \eta \overline{\overline{\epsilon}}_f + \lambda \text{tr}(\overline{\overline{\epsilon}}_f) \delta_{ij}. \quad (2.5)$$

On the right hand side of Eq. (2.5), the first term corresponds to the shear contribution to the stress tensor, whereas the second term refers to the volumetric part. The symbols η , λ , and $\overline{\overline{\epsilon}}_f$, represent the fluid dynamic viscosity, volume viscosity, and strain rate tensor, respectively. Neglecting the rotation of the fluid, the strain rate tensor may be expressed as a function of the fluid velocity as:

$$\overline{\overline{\epsilon}}_f = \frac{1}{2} \left(\nabla \vec{v}_f + (\nabla \vec{v}_f)^T \right). \quad (2.6)$$

Considering the fluid as incompressible², and applying the Boussinesq approximation, the combination of Eqs. (2.3), (2.4), and (2.5) results in the incompressible momentum balance:

$$\rho_f \frac{D \vec{v}_f}{Dt} = -\nabla \cdot P + 2 \nabla \cdot \eta \left(\overline{\overline{\epsilon}}_f - \frac{1}{3} \text{tr}(\overline{\overline{\epsilon}}_f) \delta_{ij} \right) + \rho_f \vec{g}. \quad (2.7)$$

2.2.3 Energy balance

The thermal energy balance expresses that the variation of the internal thermal energy within a control volume depends on the heat exchanged at its boundaries. Neglecting radiative heat transfer, it may be expressed in its differential form as (Ishii and Hibiki, 2011):

$$\frac{\partial \rho_f c_{pf} T_f}{\partial t} + \vec{v}_f \cdot \nabla (\rho_f c_{pf} T_f) = -\nabla \cdot (k_f \nabla T_f), \quad (2.8)$$

² $\eta_b = \lambda + \frac{2}{3}\eta = 0$ (η_b = bulk viscosity)

where C_{pf} is the fluid heat capacity, T_f is the fluid temperature, and k_f is fluid the heat conductivity. The first term in the left hand side of Eq. (2.8) is the temporal variation of the internal energy within the control volume. The second one is the advection term corresponding to the energy transported by the fluid flow. The term in the right-hand side quantifies the amount of energy transferred by conduction at the control volume boundaries. Neglecting the spatial and temporal variations of both the fluid conductivity and heat capacity, and considering an incompressible fluid under the Boussinesq approximation, Eq. (2.8) may be simplified:

$$\rho_f C_{pf} \frac{\partial T_f}{\partial t} + \rho_f C_{pf} \vec{v}_f \cdot \nabla (T_f) = -k_f \nabla^2 T_f. \quad (2.9)$$

2.2.4 State equations

In order to close the set of transport equations, a state equation is required. This equation links the variations of fluid temperature and pressure to its density. The fluid thermal expansion expresses the density variation of the fluid as a function of its temperature and allows the system to convect. Similarly, the bulk modulus of the fluid phase links the evolution of the fluid pressure to its density and controls the velocity of pressure waves. Incorporating these two effects, with the assumption of first order variations (no pressure and temperature dependences of the fluid bulk modulus and thermal expansion coefficient) the state equation may be formulated as:

$$\frac{\partial \rho_f}{\partial t} = K_f \frac{\partial P}{\partial t} + \alpha_f \frac{\partial T}{\partial t}, \quad (2.10)$$

where, K_f is the fluid bulk modulus, and α_f is the thermal expansion coefficient of the fluid. When the fluid is incompressible, eq. (2.10) may be reduced to:

$$\frac{\partial \rho_f}{\partial T} = \alpha_f. \quad (2.11)$$

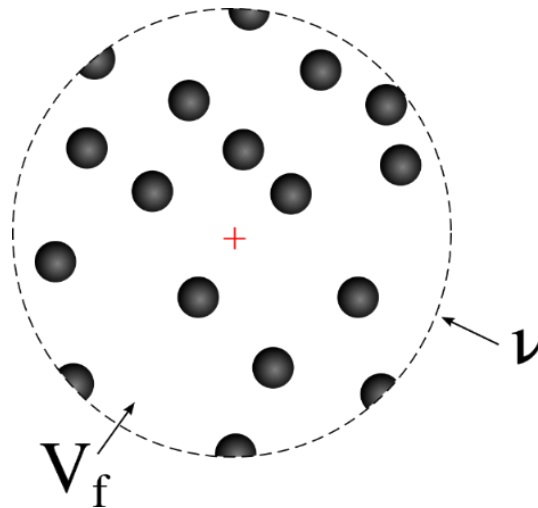


Figure 2.1: Concept of volume averaging. The figure displays particles in a section of a spherical control volume. The dashed black circle is the edge of the control volume, ν , in which the volume average procedure is performed. Within this sphere, the white color indicates the presence the volume of fluid, V_f . The red cross indicates the point at which the fluid averaged values are assigned. Modified from Crowe et al. (1997).

2.2.5 Effect of the presence of a solid phase

For multiphase systems the presence of a dispersed phase, even in small concentrations, may significantly modified the dynamics of fluid flow. Contrary to the DNS approach, the CFD-DEM one requires to average the fluid properties over the control volumes. In this way, an averaging procedure is applied to the fluid constitutive equations to account for the presence of the particles. Several Eulerian averaging approaches exist, such as the area, ensemble, line, statistical, time, or volume averaging procedures (see Ishii and Hibiki, 2011, pp. 55-66). In MFIX, because of the numerical method employed to solve the fluid constitutive equations, a volume averaging is used. It consists in averaging the particle properties at a given time over a control volume and assigning these computed values to a position in the fluid field (Fig. 2.1). In the following, the principle of the method is described and the averaged fluid constitutive equations are introduced. For a more complete presentation of the averaging procedure of the fluid constitutive equations and the vector operators, see Crowe et al. (1997), pp 427-449.

The volume average of the fluid constitutive equations requires to average the fluid properties (for example here the fluid density ρ_f) in a control volume, v , as:

$$\overline{\rho_f} = \frac{1}{v} \int_v (\rho_f dv), \quad (2.12)$$

where $\overline{\rho_f}$ is the volume-averaged fluid density. The average of the fluid density over the volume of fluid, V_f , contained in the control volume v is the fluid macroscopic density, $\langle \rho_f \rangle$. Replacing the volume integral of the fluid density by the macroscopic fluid density and volume V_f yields:

$$\overline{\rho_f} = \frac{V_f}{v} \langle \rho_f \rangle. \quad (2.13)$$

The ratio of the fluid volume other the total volume of the representative elementary element is expressed by the solid volume fraction, Φ , as:

$$\overline{\rho_f} = (1 - \Phi) \langle \rho_f \rangle. \quad (2.14)$$

Applying this procedure to Eqs. (2.2), (2.7), and (2.9) gives the fluid constitutive equations used in MFIX for the fluid phase (for simplicity, the symbols indicating the macroscopic averages are omitted):

$$\frac{\partial (1-\Phi)}{\partial t} + \nabla \cdot ((1 - \Phi) \vec{v}_f) = 0, \quad (2.15)$$

$$\rho_f \frac{D (1-\Phi) \vec{v}_f}{Dt} = -\nabla \cdot ((1 - \Phi)P) + \nabla \cdot \overline{\sigma}_v + (1 - \Phi)\rho_f \vec{g} + \vec{I}_{fs}, \quad (2.16)$$

$$\rho_f C_{pf} \left(\frac{\partial (1-\Phi) T_f}{\partial t} + \vec{v}_f \cdot \nabla ((1 - \Phi) T_f) \right) = -k_f \cdot \nabla^2 ((1 - \Phi) T_f) + H_{fs}, \quad (2.17)$$

$$\overline{\sigma}_v = 2 \eta (1 - \Phi) \overline{\epsilon}_f + \lambda (1 - \Phi) tr(\overline{\epsilon}_f) \delta_{ij}. \quad (2.18)$$

In equations 2.16 and 2.17, the symbols \vec{I}_{fs} and H_{fs} are the coupling terms and corresponds to the momentum and heat transferred from solids to the fluid (see section 2.6).

2.3 Governing equations of the solids

2.3.1 Constitutive equations

To define the constitutive equations, we consider a granular immersed medium in a jammed state and focus on one particle, labeled i (Fig. 2.2). This particle is in contact with N neighbor particles and is close to, but separated from, M particles. The equations controlling its motion are the Newton's second laws of motions. For translational and rotational motions, they give:

$$m_s(i) \frac{d\vec{v}_s(i)}{dt} = \sum_{j=1}^N \left(\vec{F}_C(i, j) \right) + \vec{F}_{fs}(i) + m_s \vec{g}, \quad (2.19)$$

$$I_s(i) \frac{d\vec{\omega}_s}{dt} = \sum_{j=1}^N \left(\vec{T}_C(i, j) \right), \quad (2.20)$$

where m_s is the particle mass, \vec{v}_s is the solid velocity vector, \vec{F}_C is the contact force, and \vec{F}_{fs} is the force exerted by the fluid on the particles. In Eq. (2.20), I_s moment of inertia³, is the, $\vec{\omega}_s$ is the rotation vector, and \vec{T}_C is the torque generated by the frictional contacts. The first term in the right hand side of Eq. (2.19) corresponds to the momentum coupling between the solids. It is the sum of all the collisional and frictional interactions formed by the particle i with its N neighbors. The second one corresponds to the momentum transferred from the fluid to the particles. The last one is the gravitational force. The right hand side of Eq. (2.20) is the sum of all the different contact torques that the particle i experienced with its N neighbors. The torque generated by the fluid-solid momentum coupling is neglected.

The temperature evolution of the solids may be expressed in the following equation:

$$m_s(i) C_{Ps}(i) \frac{\partial T_s(i)}{\partial t} = Q_{fs}(i) + \sum_{j=1}^N \left(Q_{ss}(i, j) + Q_{sfs}(i, j) \right) + \sum_{j=1}^M \left(Q_{sfs}(i, j) \right), \quad (2.21)$$

where C_{Ps} is the particle heat capacity. Q_{fs} , Q_{ss} , and Q_{sfs} are the fluid-solid, solid-solid, and the solid-fluid-solid heat fluxes (the radiative heat transfer between the particles is neglected). The fluid-solid heat flux corresponds to the energy exchanged at the interface between the solid and the fluid. The solid-solid contribution is a conductive heat transfer between particles in contacts. The

³ $I_s(i) = \frac{\pi \rho_s(i) d_p(i)^3}{6}$

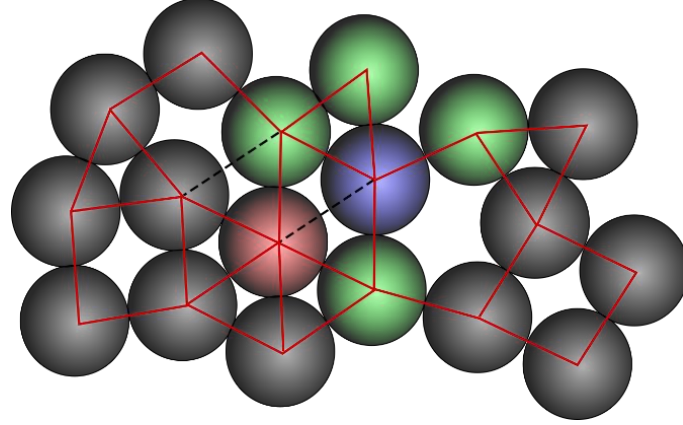


Figure 2.2: Conceptual granular medium. The considered medium is composed by discrete spherical particles in a jammed condition, forming a crystal framework. The force chains between particles in contact are indicated with red lines. The blue particle corresponds to the one considered to express the equation of motion and temperature evolution. The ones in green are the particles in contact with the blue one, exchanging momentum by collisional and frictional interactions. The red particle is separate from the blue one but is close enough to exchange heat by condition through the fluid film between them (particle-fluid-particle heat transfer). The dashed line between these two particles indicates this interaction.

solid-fluid-solid term is a conductive heat flux between two close but separated particle edges through the thin fluid layer that separates them.

2.3.2 Contact model

Let's consider the interaction between two particles in contact, labeled as i and j (Fig. 2.3 A). The contacts are modeled with a soft sphere approach (Tsuji et al., 1993), which is a spring-dashpot model, meaning that only a part of the energy is conserved whereas the rest is dissipated during the contact. The total contact force may be split in normal (collision), $\overline{F_C^n}$, and tangential (friction) components, $\overline{F_C^t}$ (Fig 2.3 B). The total translational contact force, $\overline{F_C}(i, j)$, is then expressed as:

$$\overline{F_C}(i, j) = \overline{F_C^n}(i, j) + \overline{F_C^t}(i, j). \quad (2.22)$$

The collisional torque involves the distance between each particle center of mass and contact point⁴, L :

$$\overline{T_C}(i) = L(i) \overline{\eta}_{i,j} \wedge \overline{F_C^t}(i, j) \quad (2.23)$$

⁴ $L(i) = \frac{4 \|\vec{x}(j) - \vec{x}(i)\|^2 + d_p(i)^2 - d_p(j)^2}{8 \|\vec{x}(j) - \vec{x}(i)\|}$; $L(j) = \|\vec{x}(j) - \vec{x}(i)\| - L(i)$

$$\vec{T}_C(j) = L(j) \vec{\eta}_{i,j} \wedge \vec{F}_C^t(i,j) \quad (2.24)$$

where $\vec{\eta}_{i,j}$ is the unit vector going from the center of mass of particle i to the one of particle j ⁵.

2.3.2.a Collisional interactions

The normal contact force between the particles i and j may be expressed as:

$$\vec{F}_C^n(i,j) = \vec{F}_S^n(i,j) + \vec{F}_D^n(i,j). \quad (2.25)$$

The first term in the right hand side of Eq. (2.25) is the conservative part of the contact force (spring), and the second one the dissipative part (dashpot). The conservative part is function of the overlap distance between the two particles, δ_n , and of the spring coefficient, k_n , as:

$$\vec{F}_S^n(i) = -\vec{F}_S^n(j) = -k_n(i,j) \delta_n(i,j) \vec{\eta}_{i,j}, \quad (2.26)$$

The overlap distance is computed as a function of the distance between the two particles center of mass, $D(i,j)$, and their respective diameters:

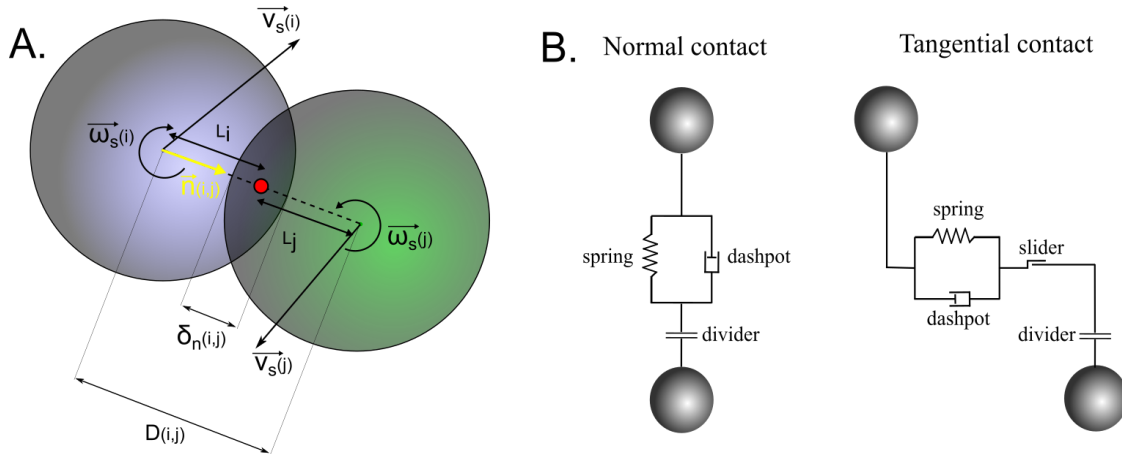


Figure 2.3: The soft sphere contact model. [A] system of two particles producing a contact by overlapping. The two straight arrows starting from the particles centers are the velocity vectors. The curved ones indicates the rotation vectors. The red dot represents the theoretical contact point [B] Conceptual model used for the normal and tangential contact forces. The normal contact contains a spring and a dashpot. The divider indicates that no cohesive forces are accounted. The tangential contact model is similar to the normal one but also includes a slider to express that frictional slipping are consider. Modified from Garg et al., 2010.

⁵ $\vec{\eta}_{i,j} = \frac{\vec{x}(j) - \vec{x}(i)}{\|\vec{x}(j) - \vec{x}(i)\|}$

$$\delta_n(i, j) = \frac{d_p(i) + d_p(j)}{2} - D(i, j). \quad (2.27)$$

The normal dissipative contact contribution depends on the normal dashpot coefficient between the two particles, η_n , and the normal relative velocity between the particles, which is computed by projecting the total relative velocity between the two particles at the contact point, \vec{V}_s , on the unit vector $\vec{\eta}_{i,j}$:

$$\overline{F}_D^n(i, j) = \eta_n(i, j) \left(\vec{V}_s(i, j) \cdot \vec{\eta}_{i,j} \right) \vec{\eta}_{i,j}. \quad (2.28)$$

The total relative velocity at the contact point incorporates the effects of both translational and rotational relative motions between the particles, and may be expressed as:

$$\vec{V}_s(i, j) = \vec{v}_s(i) - \vec{v}_s(j) + \left(L(i) \vec{\omega}(i) + L(j) \vec{\omega}(j) \right) \wedge \vec{\eta}_{i,j}. \quad (2.29)$$

To compute the spring and dashpot coefficients, the Hertzian contact model is used. In this model, the normal spring coefficient, k_n , is computed as a function of the particles Young modulus, E , Poisson ratios, σ , and normal overlap distance (Hertz, 1896):

$$k_n(i, j) = \frac{4}{3} \frac{E(i) E(j) \sqrt{R_{eff}(i, j)}}{E(j) (1 - \sigma(i)^2) + E(i) (1 - \sigma(j)^2)} \delta_n(i, j)^{\frac{1}{2}}, \quad (2.30)$$

where R_{eff} is the effective radius of the particles⁶. Finally, the normal dashpot coefficient is expressed as (Silbert et al., 2001):

$$\eta_n(i, j) = \frac{2 \sqrt{m_{eff}(i, j) k_n(i, j) \ln(e_n)}}{\sqrt{\pi^2 + \ln(e_n)^2}} \delta_n(i, j)^{\frac{1}{4}}, \quad (2.31)$$

where m_{eff} , is the effective mass⁷ of the two particles, and e_n is the normal restitution coefficient of the contact. This last parameter controls the relative importance of the conservative and dissipative parts of the contact force. When $e_n = 1$, the contact is purely elastic and all the energy

⁶ $R_{eff}(i, j) = \frac{d_p(i) d_p(j)}{2 (d_p(i) + d_p(j))}$

⁷ $m_{eff}(i, j) = \frac{m(i) m(j)}{m(i) + m(j)}$

is conserved. On the contrary, when $e_n = 0$, all the energy dissipates during the contact and no rebound occurs.

2.3.2.b Frictional interactions

Similarly to the normal contacts, the tangential force may be split into a conservative and a dissipative term.

$$\overrightarrow{F_C^t} = \overrightarrow{F^t_S} + \overrightarrow{F^t_D}. \quad (2.32)$$

The first term in the right hand side of equation is the conservative part of the tangential contact force (spring), and the second one the dissipative part. For the tangential spring, two expressions exist depending on the frictional state of the particle contact, which can be either static or dynamic. The static friction spring term is:

$$\overrightarrow{F^t_S} = -k_t \overrightarrow{\delta_t}, \quad (2.33)$$

where k_t is the tangential spring coefficient, and $\overrightarrow{\delta_t}$ is the accumulated tangential displacement. The cumulated tangential displacement is computed during the ‘static’ frictional contact as:

$$\overrightarrow{\delta_t}(i, j) = \int_{static} \frac{\partial \overrightarrow{\delta_t}(i, j)}{\partial t} dt. \quad (2.34)$$

To track the occurrence of tangential sliding (dynamic friction), a Mohr-Coulomb criterion is used. It assumes that the sliding occurs when the magnitude of the static tangential forces overcomes a threshold, which depends on the normal contact force $\overrightarrow{F_n}$ and particles friction coefficient, μ_s . The sliding is assumed to occur when:

$$\left\| \overrightarrow{F^t_S}(i, j) \right\| > \mu_s \left\| \overrightarrow{F_C^n}(i, j) \right\|. \quad (2.35)$$

During the dynamic slide, the tangential force is given by:

$$\overrightarrow{F^t_S}(i, j) = \mu_s \left\| \overrightarrow{F_C^n}(i, j) \right\| \overrightarrow{t_{i,j}}, \quad (2.36)$$

where, $\vec{t}_{i,j}$ is the tangential unit vector⁸. When the sliding occurs, the incremental evolution of the tangential displacement is reset to:

$$\vec{\delta}_t(i,j) = \frac{\mu_s k_n \delta_n}{k_t} \vec{t}_{i,j}. \quad (2.37)$$

As for the normal contact forces, the Hertz contact model is used to compute the spring constant. For tangential contacts, it depends on the particles shear modulus⁹, G , the Poisson coefficients and tangential displacement (Hertz, 1896):

$$k_t(i,j) = \frac{16}{3} \frac{G(i) G(j) \sqrt{R_{eff}(i,j)}}{G(j) (2-\sigma(i)) + G(i) (2-\sigma(j))} \|\vec{\delta}_t(i,j)\|^{\frac{1}{2}}. \quad (2.38)$$

Finally, the tangential dashpot contribution is:

$$\vec{F}_D^t(i,j) = \eta_t(i,j) (\vec{V}_s(i,j) - (\vec{V}_s(i,j) \cdot \vec{\eta}_{i,j}) \vec{\eta}_{i,j}), \quad (2.39)$$

with (Silbert et al., 2001):

$$\eta_t(i,j) = \frac{2 \sqrt{m_{eff}(i,j) k_t(i,j) \ln(e_t)}}{\sqrt{\pi^2 + \ln(e_t)^2}} \|\delta_t(i,j)\|^{\frac{1}{4}}, \quad (2.40)$$

where, e_t represents the tangential restitution coefficient having the same meaning as e_n .

2.3.3 Heat transfer between solids

In the model, two heat transfer modes occur between the solids: the conduction between particles in contact and heat conduction through the thin fluid lens between them (the radiative heat transfer is neglected). Here, two situations are considered to present the heat transfer between the particles (Fig 2.4). The first considers two separated particles (Fig 2.4 B). In this situation, the solid-fluid-solid heat transfer is the only mechanism able to transmit energy between the two

⁸ $\vec{t}_{i,j} = \frac{\vec{\delta}_t}{\|\vec{\delta}_t\|}$

⁹ $G(i) = \frac{E(i)}{2(1+\sigma(i))}$

particles. The second situation explores the situation where the two particles are in contact (Fig 2.4 A) for which both solid-solid and solid-fluid-solid heat transfers occur. The two next sub-sections present each mechanism separately. The relative importance of these mechanisms on the overall particle-to-particle heat transfer within a particle bed is discussed in the third sub-section.

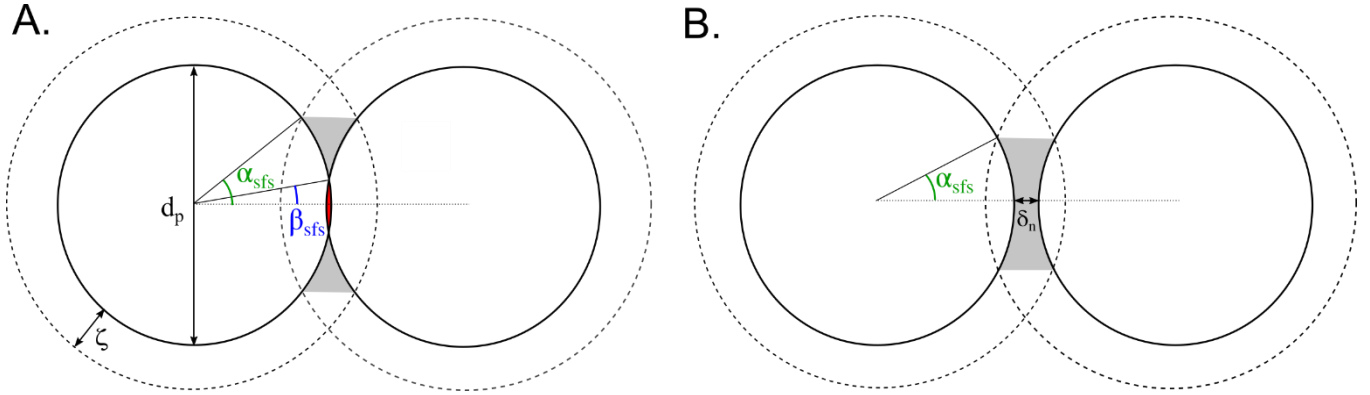


Figure 2.4: Particle-to-particle heat transfer modes. [A] The two spherical particles are in contacts. The solid circles correspond to the particles edges and the dashed ones to the boundary of the thermal boundary layers, ζ . The overlapping volume is indicated in red. The gray color indicates the effective area where solid-fluid-solid heat conduction occurs. The angle indicated with green and blue curves are the angles between the particle normal vector and edge of the solid-fluid-solid effective area and edge of the contact area. [B] Same as A for the case of two separated particles.

2.3.3.a Solid-Solid conduction

During the contact between two particles, a solid-solid conductive heat transfer may occur if a difference between their temperatures exists (here, the temperature is considered as uniform within a particle). Between two particles i and j , this heat flux reads (Batchelor and O'Brien, 1977):

$$Q_{SS}(i, j) = 2 k_s R^*(i, j) (T_s(i) - T_s(j)), \quad (2.41)$$

where $R^*(i, j)$ is the radius of the effective contact area between the two particles that depends on their radius and distance between their center of mass, $D(i, j)$, as:

$$R^*(i, j) = \frac{d_p(i)}{2} \sin \left(\cos^{-1} \frac{d_p(i)^2 + d_p(j)^2 + 4D(i, j)^2}{4 d_p(i) D(i, j)} \right). \quad (2.42)$$

2.3.3.b Solid-Fluid-Solid conduction

The solid-fluid-solid heat transfer occurs as well as when the particle are separated by a short distance or when they are in contact (Rong and Horio, 1999). For each particle, a fluid lens distance, ξ , is defined. It corresponds to a thermal boundary layer indicating the maximum distance at which the heat may be conducted efficiently within the fluid around the particle. As for the solid-solid heat transfer, the solid-fluid-solid heat flux depends on the effective area on which the heat is exchanged. This effective area depends on the overlapping between the thermal boundary layer around one particle and the physical edge of the other one (Fig. 2.4 B). This effective radius is accounted in the effective particles conductance, $H(i, j)$. The solid-fluid-solid heat flux is given by:

$$Q_{ssf}(i, j) = H(i, j) (T_s(i) - T_s(j)). \quad (2.43)$$

The value of the effective thermal conductance depends on the particle individual heat conductances:

$$H(i, j) = \frac{H(i)H(j)}{H(i)+H(j)}. \quad (2.44)$$

If the two particles are separated (Fig 2.4 B), the values of the particle individual heat conductance are computed as (Rong and Horio, 1999):

$$H(i) = -k_f \int_0^{\alpha_{ssf}} \left(\frac{\pi d_p(i) \sin \theta}{D_{ij} - d_p(i) \cos \theta} \right) d \left(\frac{d_p(i)}{2} \sin \theta \right), \quad (2.45)$$

where $d(d_p(i) \sin \theta / 2)$ is an incremental radius in the particle-fluid-particle effective area (θ is a incremental angle related to α_{ssf}). α_{ssf} is the angle between the particles normal vector and the position where the particle edge intersects the thermal boundary of its neighbor (Fig. 2.4 A–B).

When the particles are in contact (Fig 2.4 A), Eq. (2.45) transforms to:

$$H(i) = -k_f \int_{\beta_{ssf}}^{\alpha_{ssf}} \left(\frac{\pi d_p(i) \sin \theta}{D_{ij} - d_p(i) \cos \theta} \right) d \left(\frac{d_p(i)}{2} \sin \theta \right), \quad (2.46)$$

where β_{ssf} represents the angle between the normal vector and intersection of the two particle physical edges (Fig. 2.4 A).

2.3.3.c Relative importance of the two conduction modes

The relative importance of solid-solid and solid-fluid-solid modes on the amount of heat conducted between two particles is computed by considering the presence of two identical particles having a relative temperature of 10 K . Figure 2.5 displays the solid-solid, solid-fluid-solid, and total conductive heat fluxes as a function of the distance or overlap between the two particles. It shows that in a particle bed the dominant heat transfer mechanism is the solid-fluid-solid conduction. The relative importance of the solid-solid and solid-fluid-solid modes depends on the ratio between the solids and fluid heat conductivities. When this ratio is below ~ 100 , the solid-solid conduction have a weak control on the particle bed macroscopic heat transfer as observed in experiments (Delvosalle and Vanderschuren, 1985).

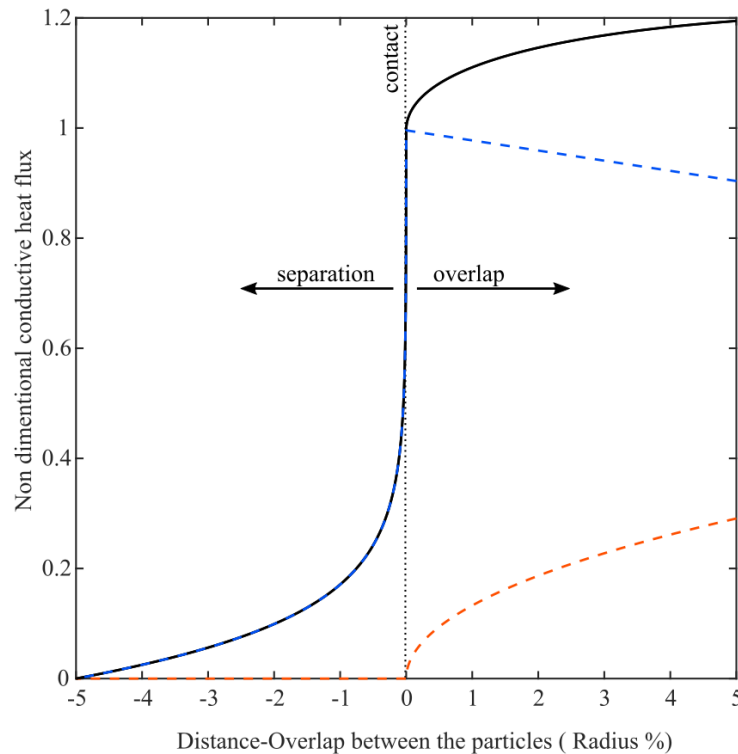


Figure 2.5: Relative contributions of the solid-solid and solids-fluid-solid heat transfers. The abscissa represents the overlap distance, in percent of the particles radius. The ordinate is a dimensionless conductive heat flux. Each curve is normalized by the value of the solid-fluid-solid heat flux when the two particles start to touch. The black thick curve is the total conductive heat flux between the particles. The blue dashed curve is the solid-fluid-solid heat flux. The orange dashed curve corresponds to the solid-solid contribution.

2.4 Coupling between the phases

2.4.1 Momentum coupling

The total force exerted by the motion of the fluid to the solids includes both steady and unsteady terms, and may be expressed as:

$$\overrightarrow{F_{fs}}(i) = \overrightarrow{F_P}(i) + \overrightarrow{F_D}(i) + \overrightarrow{F_{VM}}(i) + \overrightarrow{F_B}(i). \quad (2.47)$$

where, $\overrightarrow{F_P}$ is the pressure force, $\overrightarrow{F_D}$ is the viscous drag force, $\overrightarrow{F_{VM}}$ is the virtual mass force, and $\overrightarrow{F_B}$ is the Basset force. The first force describes the effect of the fluid pressure gradient. The drag expresses the steady viscous forces applied by the fluid on the particles (or vice versa) because of their relative motions. The two last forces are unsteady terms only important in transient dynamics that may be neglected for many applications. They both depend on the relative acceleration between the particles and the fluid. The virtual mass describes the effect of the force needed to move a volume of fluid when a particle is accelerating. The Basset term expresses the effect of the variation in the size of the viscous boundary layer (distance over which the fluid flow is affected by the presence of the particle). Neglecting the unsteady forces reduces the momentum transfer force to the drag and pressure terms and reads:

$$\overrightarrow{F_D}(i) = -\left(\frac{\pi}{6} d_p(i)^3\right) \nabla P(i) - \frac{\beta(i)}{(1-\phi(i))} \left(\frac{\pi}{6} d_p(i)^3\right) (\overrightarrow{v_s}(i) - \overrightarrow{v_f}(i)), \quad (2.48)$$

where $\beta(i)$ is the momentum transfer coefficient, and $\overrightarrow{v_f}(i)$ is the fluid velocity at the position of the particle i . The pressure gradient can be decomposed in its hydrostatic and dynamic components.

The hydrostatic pressure force is:

$$\overrightarrow{F_{P\ static}}(i) = -\frac{\pi}{6} d_p(i)^3 \rho_f \overrightarrow{g}, \quad (2.49)$$

which corresponds to the Archimedes force. The drag coefficient is computed with the Gidaspow drag model, which presents the advantage to be valid over a wide range of concentrations in solids:

$$\beta(i) = \begin{cases} \frac{3}{4} C_D(i) \frac{\rho_f \Phi(i)(1-\Phi(i)) \|\vec{v}_f(i) - \vec{v}_s(i)\|}{d_p(i)} (1 - \Phi(i))^{-2.65} & \text{if } \Phi(i) \leq 0.2 \\ \frac{150 \Phi(i)^2 \eta}{(1-\Phi(i)) d_p(i)^2} + \frac{1.75 \rho_f \Phi(i) \|\vec{v}_f(i) - \vec{v}_s(i)\|}{d_p(i)} & \text{if } \Phi(i) > 0.2 \end{cases}. \quad (2.50)$$

In equation (2.50), the upper line corresponds to the Wen-Yu drag coefficient and is valid for particle volume fractions below 0.2. Above 0.2, the Ergun law gives the coefficient of momentum transfer between the fluid and the particles. This last equation can be split into two terms. The first corresponds to the viscous part and is given by a Kozeny-Carman relationship describing the viscous flow at low particle Reynolds numbers, Re_p . The second is the inertial term, which depends on the relative velocity between the two phases and comes from a Burke-Plummer equation, describing the fluid kinetics at high Re_p . The Wen-Yu drag model requires to estimate the drag coefficient, C_D , for which empirical relationships exist with Re_p . The one used here is:

$$C_D(i) = \begin{cases} \frac{24}{Re_p(i)} (1 + 0.15 Re_p(i)^{0.687}), \\ 0.44 \end{cases}, \quad (2.51)$$

$$Re_p(i) = \frac{d_p(i) \|\vec{v}_f(i) - \vec{v}_s(i)\| \rho_f}{\eta}. \quad (2.52)$$

Because of the Newton's third law, the drag force exerted by the fluid on the particles must be taken into account within the interphases momentum transfer term in Eq. (2.16). The different numerical representations of the phases (Eulerian and Lagrangian) impose that the drag force at the particle scale must be averaged in space to the fluid scale. The fluid-solid momentum exchange term in Eq. 2.14 may be expressed as:

$$\vec{I}_{fs}(k) = \frac{1}{v} \sum_{i=1}^{N_p} \left(\frac{\beta(i) \left(\frac{\pi}{6} d_p(i)^3\right)}{(1-\Phi(i))} \left(\vec{v}_f(k) - \vec{v}_s(i) \right) K_v(\vec{X}(i), \vec{X}_f(k)) \right), \quad (2.53)$$

with K_v being a generic kernel indicating the contribution of a particle located at a position \vec{X} to a fluid grid node located at the position \vec{X}_f . N_p indicates the number of particles affecting the fluid at the position \vec{X}_f .

2.4.2 Thermal coupling

The transfer of heat between the two phases occurs by either conduction or advection of the heat at the boundary between the two mediums. The efficiency of fluid-solid heat transfer is expressed by the Nusselt number, Nu . From the discrete particle point of view, the heat flux between the two phases reads:

$$Q_{fs}(i) = \pi Nu(i) k_f (T_s(i) - T_f), \quad (2.54)$$

with,

$$Nu(i) = 2 + 0.6 Re_p(i)^{\frac{1}{2}} Pr^{\frac{1}{3}}. \quad (2.55)$$

Where Pr corresponds to the Prandtl number (See section 6 for details). Eq. (2.55) is a experimentally determined correlation of heat transfer (Ranz and Marshall, 1952; Rong and Horio, 1999). As for the momentum, computing the heat fluxes from the solid to the fluid requires to sum the heat exchanged with each individual particles through the fluid volume as:

$$H_{fs}(k) = \sum_{i=1}^{N_p} \left(Q_{fs}(i) K_v(\vec{X}(i), \vec{X}_f(k)) \right), \quad (2.56)$$

Further details about the momentum transfer and heat transfer interpolation and averaging are given in the next section.

2.5 Numerical solvers

2.5.1 Overview of the SIMPLE algorithm

To solve the fluid constitutive equations, MFI-X-DEM uses the SIMPLE (Semi-Implicit Method Linked Equations) algorithm (Patankar, 1980). It is an iterative method based on successive corrections of fluid velocities and pressure field. It uses a staggered grid in which fluid pressure and velocities are stored at different positions in order to avoid the convergence to checkerboard pressure fields (Fig 2.6). An overview of the algorithm steps is presented here. For a detailed presentation of the discretization of the constitutive equations and algorithm operations, see Patankar, 1980 and Syamlal, 1998. For each fluid time step, the algorithm operations are:

- i:** Update the fluid physical properties. The Eq. (2.11) is used to compute the new densities and, in some runs, the fluid viscosity, according to the fluid temperature field from the previous time step.
- ii.** The velocity and pressure gradients are computed from the results of the previous iteration or time step (for the first iteration).
- iii.** The momentum equation (Eq. 2.16) is solved to compute a new velocity field (v_{fx}^* , v_{fy}^* , v_{fz}^*) with the pressure field from the previous iteration, P^* (or a guessed one for the first solver's iteration). Note that the estimated velocity field does generally not respect the mass continuity (Eq. 2.15).
- iv.** The mass fluxes at each face of the control volumes are updated with the new fluid velocities field computed at step 3 (v_{fx}^* , v_{fy}^* , v_{fz}^*).
- v.** A fluid pressure correction P' is computed in order to obtain a pressure field $P = P^* + P'$ satisfying the continuity equation (Eq. 2.15).
- vi.** The fluid pressure field is updated with the pressure correction from step 5.
- vii.** A fluid velocity correction (v_{fx}' , v_{fy}' , v_{fz}') is computed from P' and applied according to the new pressure field.
- viii.** The temperature of the fluid is computed with Eq. (2.17) and the corrected fluid velocities computed at step 7.

ix. The total dynamic residual is computed by summing those of steps 3, 5 and the heat residual is obtained from step 8.

x. If both residuals are below a threshold, the time step is considered as having converged and the fluid velocity, pressure, and temperature fields are used to compute the solids dynamics in the DEM part. If the residuals are above the threshold and converges (i.e. is smaller than that of the previous iteration), the algorithm restarts from step 2 with the fluid properties computed during the present iteration. When any residual diverges, the fluid time increment, Δt , is reduced and the iteration is restarted from step 1 with the fluid properties from the previous time step.

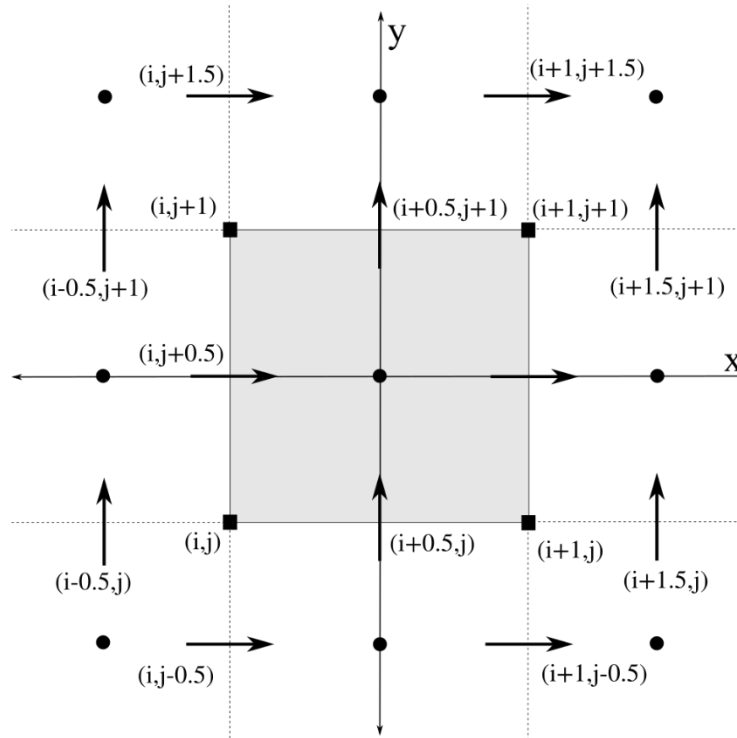


Figure 2.6: Representation of the staggered grid use to represent the fluid phase (in 2D here). The central control volume is indicated in gray. The dotted vertical and horizontal lines represent the edges of the neighbor control volumes. The black filled circles located at the centers of the cells represent the positions of the grid where the scalar quantities (volume fraction, pressure, density, or viscosity...) are stored. The vertical arrows represent the positions where the vertical fluid velocities (v_{fy}) are stored. Similarly, the horizontal arrows indicate where x fluid velocities (v_{fx}) are stored. The black filled squares correspond to the locations of the interpolation nodes (see section 2.4.6).

2.5.2 DEM solver

Computing the particle motion requires one to integrate in time their accelerations given by Eqs. (2.19) and (2.20) and ensuing velocities and positions. For that, a first-order Euler time integration scheme is used (Gear, 1971). The integral in time of the particles acceleration is approximated by:

$$\vec{v}_s(i) (t + \Delta t_{solid}) = \vec{v}_s(i) (t) + \frac{\sum_{j=1}^N (\vec{F}_C(i,j)) + \vec{F}_{fs}(i) + m_s \vec{g}}{m_s} \Delta t_{solid}. \quad (2.57)$$

The positions of the particles are updated as:

$$\vec{X}(i) (t + \Delta t_{solid}) = \vec{X}(i) (t) + \vec{v}_s(i) (t + \Delta t_{solid}), \quad (2.58)$$

where Δt_{solid} is the DEM time step. For the particle rotation, the Euler time integration is:

$$\vec{\omega}_s(i) (t + \Delta t_{solid}) = \vec{\omega}_s(i) (t) + \frac{\sum_{j=1}^N (\vec{T}_C(i,j))}{I_s(i)} \Delta t_{solid}. \quad (2.59)$$

Finally, the temperature evolution of the particles is computed as:

$$T_s^{(k)} (t + \Delta t_{solid}) = T_s^{(k)} (t) + \Delta t_{solid} \frac{Q_{fs}^{(k)} + \sum_{l=1}^{N_l^{(k)}} (Q_{ss}^{(k,l)}(t) + Q_{sfs}^{(k,l)}(t))}{m^{(k)} c_{p_s}}. \quad (2.60)$$

This time integration scheme is usually preferred to higher order ones (e.g. the second order Adams-Bashforth scheme; Sundaram and Collins, 1996), because with the short solid time step used, Δt_{solid} , this integration scheme is sufficient to ensure the reliability of the results with lower memory consumptions (Dziugys and Peters, 2001; Garg et al., 2010). The reliability and efficiency of the DEM approach is linked with the solid time step used. The smaller this time step is, the higher is the frequency at which the particle velocities are updated, and the more accurate the simulation is. However, the solids iterations are time consuming and too small a time step can lead to unrealistically long computation time. The solid time step used in the simulations has thus to be set to the appropriate value to ensure both the reliability and efficiency of the simulation.

To ensure the stability of the simulation, the time step has to be related to the duration of the physical processes occurring on the particles. Two phenomena must be considered here: the particle contacts and the drag acceleration. For each of these forces, a characteristic duration may

be defined. For the contact between two particles, it is its duration, defined as (here between two particles i and j):

$$t^{col}(i, j) = \pi \sqrt{\frac{k_n(i, j)}{m_{eff}(i, j)} - \frac{\eta_n(i, j)}{4 m_{eff}^2(i, j)}}. \quad (2.61)$$

Then the stability time step related to the particle contact is:

$$\Delta t_{contact} = \frac{\min(t_{col})}{\alpha_c}, \quad (2.62)$$

where α_c is the empirical contact stability coefficient, usually set to 50. This threshold is sufficient to ensure the reliability of the simulation for a purely granular simulation, or when the fluid has a relatively low viscosity. When the fluid has a high viscosity, the stability criterion related to the drag force needs to be accounted for as well. The drag stability time step is related to the particle response time, τ_s , which corresponds to the time for a particle to reach its terminal velocity with a constant acceleration. The particle response time is inversely proportional to the fluid viscosity:

$$\tau_s(i) = \frac{|\Delta\rho| d_p(i)^2}{18 \eta}, \quad (2.63)$$

where $\Delta\rho$ represents the density contrast between the fluid and solids. The drag maximum time step reads:

$$\Delta t_{drag} = \frac{\min(\tau_s)}{\alpha_v}, \quad (2.64)$$

where α_v is an empirical viscous stability constant. The simulation solid time step is given by:

$$\Delta t_{solid} = \min(\Delta t_{contact}, \Delta t_{drag}) \quad (2.65)$$

The imposed value α_c and α_v control the reliability of the simulation and have to be necessarily higher than one.

To illustrate the effect of these values on the reliability and stability of the simulations, let's consider an isolated particle immersed in a viscous fluid flowing in the x direction steadily at a velocity $v_f(x)$. The particle starts at rest and accelerates because of the viscous drag imposed by the fluid. Neglecting the effect of gravity, the particle equation of motion can be reduced to:

$$m_s \frac{d v_s(x)}{dt} = -3 \pi \eta d_p (v_s(x) - v_{fx}), \quad (2.66)$$

where the term in the right hand side of Eq. (2.66) is the Stokes drag law. The analytical solution of Eq. (2.66) is:

$$v_{s(x)}(t) = v_{f(x)} \left(1 - e^{-\frac{3\pi\eta d_p}{m_s} t} \right). \quad (2.67)$$

Figure 2.7 displays the comparison between the analytical solution of the particle motion (Eq. 2.67) and the results of a first order Euler integration with different values for the stability coefficient α_v . It shows that when $\alpha_v < 0.5$, the particle velocity diverges. When $0.5 < \alpha_v < 1$, the particle velocity oscillates around the expected velocity between successive time steps and converge to the

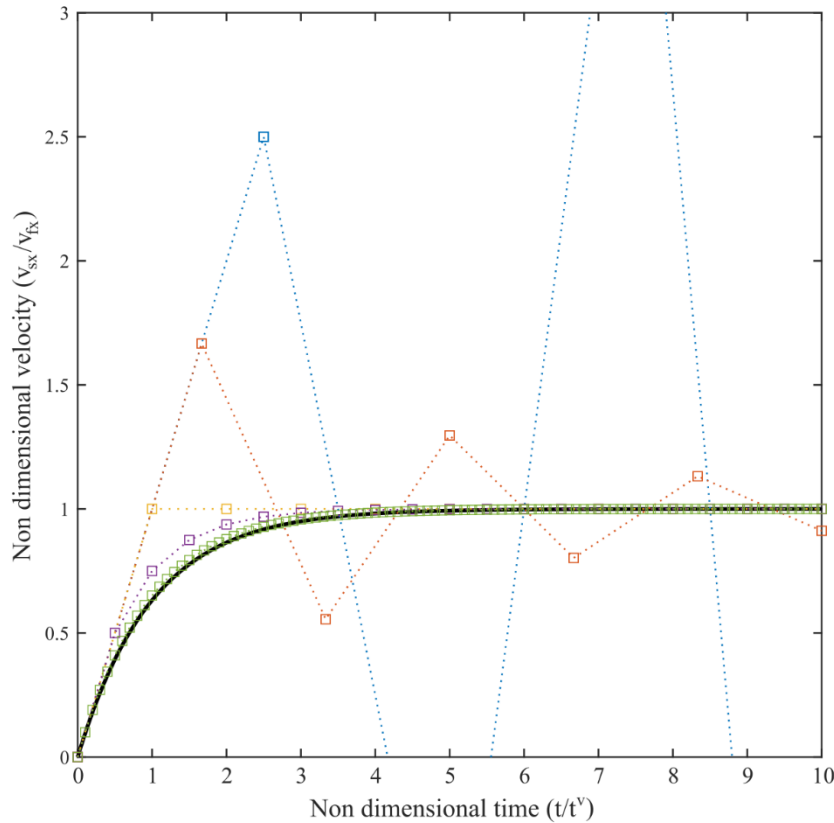


Figure 2.7: Acceleration of an isolated particle immersed in a fluid flowing with a uniform and constant velocity. The graph compares analytical solution and numerical approximations with different drag stability coefficients. The abscissa is a non-dimensional time defined as the ratio of the time and drag characteristic time. The ordinate is a non-dimensional velocity corresponding to the ratio of the particle velocity and fluid uniform velocity. The analytical solution of the particle equation of motion is indicated with a thick black curve. Dashed curves represent the numerical approximations using a first order Euler integration scheme. The open squares are the computed particle velocities at each time step. The blue, orange, yellow, purple, and green colors indicate that the drag stability coefficient used is 0.4, 0.6, 1, 2, and 10, respectively.

fluid velocity. At $\alpha_v = 1$, after one iteration the particle reaches its terminal velocity and the drag force is canceled. In this situation, the particle velocity terminal velocity is reproduced but the time to reach it is underestimated. When $\alpha_v > 1$, the evolution of the relative velocity between the particle and the surrounding fluid may be retrieved. The accuracy of the numerical solution is proportional to the stability coefficient. A good agreement between analytical and numerical solutions is generally obtained once $\alpha_v > 25$. For application to chemically evolved mush with high melt viscosity, this time step reach values of the 10^{-9} s, which is a strong limitation to the application of the CFD-DEM method with such a classical time integration scheme. This limitation will be lifted in section 4.2.1.

2.5.3 Interpolation schemes

An accurate description of the phase coupling in an Eulerian-Lagrangian framework requires one to interpolate the fluid properties at the particle locations and, conversely, the particles mean field to the fluid grid. This allows, for instance, the smooth calculation of the free fall of a single particle across several fluid cells. For that a second order accurate in space interpolation scheme is used (Garg et al., 2012). Here, we present the key points of the interpolation algorithms. For further details, readers are redirected to Garg et al., (2012 and 2007).

2.5.3.a Particle side

Because of the fluid staggered grid, the interpolation of the fluid properties at the particle locations is performed in two steps. Let's consider a control volume in 2D (Fig. 2.6). The pressure is known at the center of the control volume, fluid velocities in the x direction are known at the center of the left and right faces of the volume, and the y fluid velocity at the top and bottom faces. The first step consists in interpolating the x and y fluid velocities at the four corners of the control volume (Fig 2.6). For that, linear interpolations of the fluid velocities in each direction are performed for all the corners. For example, with an uniformly spaced grid at the position (i, j) , it gives:

$$v_{fx}(i, j) = \frac{v_{fx}(i, j+0.5) - v_{fx}(i, j-0.5)}{2}, \quad (2.68)$$

$$v_{fy}(i,j) = \frac{v_{fy}(i+0.5,j) - v_{fy}(i-0.5,j)}{2}. \quad (2.69)$$

In this way, each corner of the control volume is characterized by fluid velocities in all space directions. For the second step, we consider a particle located within the control volume at position $(i+x, j+y)$, where the spatial coordinate are given relative to the control volume reference point (the position $(0,0)$ is located at the bottom left corner) (Fig. 2.8 A). The fluid properties are interpolated at the particle location as a function of the values previously interpolated at the control volume corners. This second step is a quadratic interpolation given by:

$$v_{fx}(x,y) = v_{fx}(i,j) + \frac{v_{fx}(i+1,j) - v_{fx}(i,j)}{\Delta x} x + \frac{v_{fx}(i,j+1) - v_{fx}(i,j)}{\Delta y} y + \frac{v_{fx}(i,j) + v_{fx}(i+1,j+1) - v_{fx}(i+1,j) - v_{fx}(i,j+1)}{\Delta x \Delta y} x y, \quad (2.70)$$

where Δx and Δy are the grid spaces.

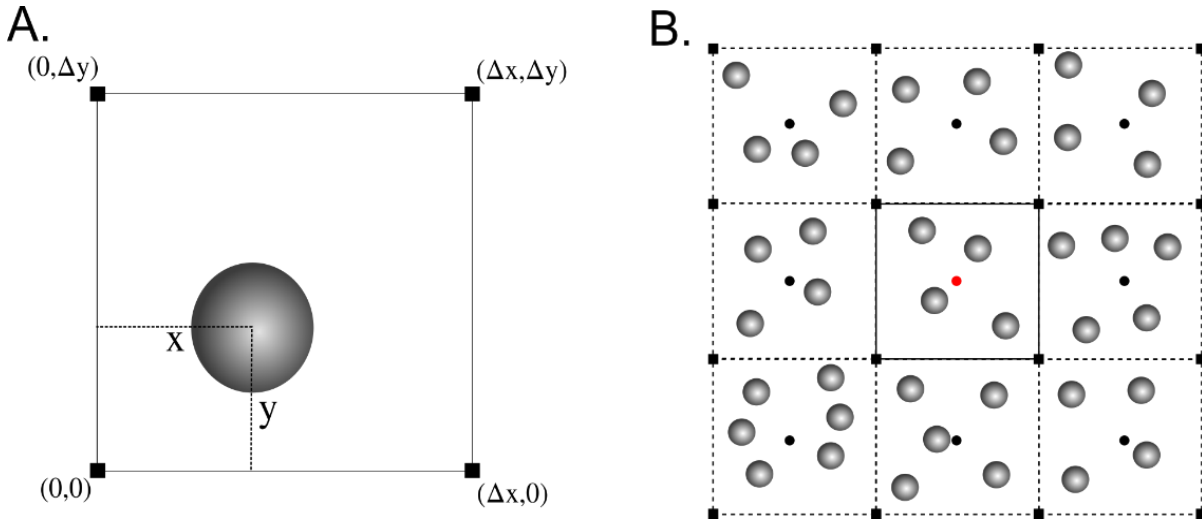


Figure 2.8: Lagrangian-Eulerian interpolation scheme (in 2D here). [A] Interpolation of the fluid properties at the particle location. The drawing represents a particle in a fluid cell. The black squares represent the locations where the fluid properties have been interpolated from the fluid staggered grid (Fig 2.6). [B] Interpolation of the particle properties on the fluid grid. Here, nine fluid cells are displayed. The red dot represents the point where the particle volume fraction and momentum exchange coefficient are interpolated and stored. The black ones are the interpolation nodes of the neighbor cells. The black squares indicate the positions where the particles properties are interpolated during the first step (see text). The interpolated properties at the red dot depends on the particles located in all the cells displayed on the drawing.

2.5.3.b Fluid side

The backward approximation of the particle properties at the fluid grid nodes (particle volume fraction, temperature, and drag force) uses a similar approach as the forward one. This computation is performed in two steps. First, for each cell, the contribution of the N_p particles contained in this volume is the sum at each corners of the cell (Fig 2.8 B). For example, the particle masses are summed using:

$$\langle m_s \rangle = \sum_{k=1}^{N_p} m_s \left(1 - \frac{x(i)}{\Delta x}\right) \left(1 - \frac{y(i)}{\Delta y}\right), \quad (2.71)$$

The particle concentration is then computed at the center of the cell (Fig 2.8 B) as a function of the value of the 8 control volume corners following:

$$\Phi_s = \frac{\sum_{k=1}^8 \langle m_s \rangle(k)}{v \rho_s}, \quad (2.72)$$

where k is the corner index. Other higher order and more expensive interpolation schemes exist (Garg et al., 2007). The second-order interpolation scheme is less accurate than other ones but presents the advantage to be less expensive. In the context of magmatic mush, the spatial variation of the fluid velocity and particle concentration do not varies greatly in space (low Re) and this approach is acceptable.

2.5.4 Boundary conditions

The boundary conditions implemented in the model are the following:

- The Non Slip Wall (NSW), where all the components of the fluid velocity are set to zero.
- The Free Slip Wall (FSW), where the walls are frictionless. The component of the fluid velocity that is normal to the wall is null, whereas for tangential components, the gradients of the fluid velocity are null.
- The mass flux boundary is used to impose an incoming flux of fluid in the computational domain. The jet is perpendicular to the boundary and can be either positive (inflow) or negative (outflow).

-
- The pressure outlet/inlet boundary corresponds to a boundary where the fluid can freely exit or enter into the computational domain at a constant pressure. The fluid velocity gradients are considered as null at this boundary.
 - The periodic boundaries are used to simulate an ‘infinite’ medium and correspond to cyclic flow through the boundary surfaces. The fluid that exits the domain by one side then enters it at the opposite surface.
 - The fixed heat flux is a boundary condition imposed to a wall where the heat flux is fixed and may be set to zero to simulate an isolating surface.
 - The fixed temperature boundary can be used with either wall or inlet/outlet and imposes the temperature at the boundary surface.

2.6 Dimensionless numbers

Reynolds numbers:

The Reynolds number, Re , characterizes the ratio of the fluid inertia and viscous force. It helps to describe the intensity of turbulence in fluid flows. Its general formulation is:

$$Re = \frac{\rho_f v_0 \delta_0}{\eta} \quad (2.73)$$

Its sense depends on the characteristic distance, δ_0 , and velocity, v_0 . If these two values are chosen to represent either the fluid or the mixture, it indicates the nature of the flow. At low (<1) Reynolds number, the fluid flow is laminar. At high Reynolds number, the fluid flow is turbulent.

When the particle diameter and relative velocity with the surrounding fluid are used as characteristic distance and velocity, respectively, this number is called the particle Reynolds number, Re_p (Eq. 2.51). It indicates how the fluid flows around the particle. At low Re_p , the fluid creeps around the particle. On the contrary, when $Re_p \gg 1$, the fluid flow creates a turbulent wake in the lee side of the particle.

The Reynolds number may also be used to characterize the effects of an oscillatory fluid flow on suspended particles. This number is given by:

$$Re_{\Omega} = \sqrt{\frac{\rho_f \omega d_p^2}{8 \eta}}, \quad (2.74)$$

where ω is the angular frequency of the oscillatory flow. When $Re_{\Omega} \ll 1$, particles motions are controlled by the steady viscous effects, whereas when $Re_{\Omega} \gg 1$, inertial unsteady effects dominate.

Stokes number:

The Stokes number, S_T , quantifies the amount of momentum coupling between the fluid and solids. It corresponds to the ratio of the particle inertia over the fluid viscous force. At low Reynolds number, it reads:

$$S_T = \frac{\rho_s d_p^2 v_0}{18 \eta \delta_0}, \quad (2.75)$$

where v_0 is a characteristic velocity, and δ_0 is a characteristic distance. At low Stokes numbers, the solids follow the fluid streamlines whereas at high S_T , the motion of both constituents are decoupled.

Peclet number:

In a fluid, the Peclet number, Pe , quantifies the ratio of the heat transferred by forced convection over conduction:

$$Pe = \frac{c_{Pf} \rho_f v_0 \delta_0}{\lambda_f}. \quad (2.76)$$

At low Pe , the heat transfer is dominated by conduction, whereas at high Pe , the energy is transported by advection. Pe corresponds to the product of the Reynolds and Prandtl numbers.

Nusselt number:

The Nusselt number indicates the efficiency of heat transfer by natural convection at the interface between a solid and fluid. It may be expressed as:

$$Nu = \frac{h_t \delta_0}{k_f}, \quad (2.77)$$

where h_t is the coefficient of heat transfer. This number is usually computed with empirical relationships such as Eq. 2.55 to estimate the heat transfer coefficient.

Froude number:

The particle Froude number is used here to quantify the importance of gravitational force on the acceleration of a particle. It may be defined as:

$$Fr^2 = \frac{\rho_f v_0^2}{\Delta\rho g \delta_0}. \quad (2.78)$$

When the Froude number is high, gravitational forces weakly affect the particle inertia. At low Fr , the motion due to buoyancy force dominates.

Prandtl number:

The Prandtl number quantifies the competition between momentum and heat diffusivities. It is defined as:

$$Pr = \frac{\eta C_{Pf}}{k_f}. \quad (2.79)$$

When $Pr \ll 1$, it indicates that hydrodynamic phenomena are negligible compared to heat conduction. It is the contrary at high Pr number.

Leighton number:

The Leighton number, Le , characterizes the transition from frictional to lubricated flow. It corresponds to the ratio of the lubrication forces and frictional forces:

$$Le = \frac{\eta h \dot{\gamma}}{\sigma_n \varepsilon}, \quad (2.80)$$

where $\dot{\gamma}$, is the shear rate, σ_n is the normal stress, and ε is the particle roughness. High Le indicates that the particles are separated by a viscous fluid film and have lubricated interactions. Low Le indicates that particles are in frictional contacts.

References:

- Batchelor, K.G., O'Brien, W.R., 1977. Thermal or electrical conduction through a granular material. *Proc. R. Soc. Lond. Math. Phys. Sci.* 355, 313–333. <https://doi.org/10.1098/rspa.1977.0100>
- Bergantz, G.W., 2000. On the dynamics of magma mixing by reintrusion: implications for pluton assembly processes. *J. Struct. Geol.* 22, 1297–1309. [https://doi.org/10.1016/S0191-8141\(00\)00053-5](https://doi.org/10.1016/S0191-8141(00)00053-5)
- Bergantz, G.W., Ni, J., 1999. A numerical study of sedimentation by dripping instabilities in viscous fluids. *Int. J. Multiph. Flow* 25, 307–320. [https://doi.org/10.1016/S0301-9322\(98\)00050-0](https://doi.org/10.1016/S0301-9322(98)00050-0)
- Bergantz, G.W., Schleicher, J.M., Burgisser, A., 2017. On the kinematics and dynamics of crystal-rich systems. *J. Geophys. Res. Solid Earth* 122, 2017JB014218. <https://doi.org/10.1002/2017JB014218>
- Bergantz, G.W., Schleicher, J.M., Burgisser, A., 2015. Open-system dynamics and mixing in magma mushes. *Nat. Geosci.* 8, 793–796. <https://doi.org/10.1038/ngeo2534>
- Boyer, F., Guazzelli, É., Pouliquen, O., 2011. Unifying Suspension and Granular Rheology. *Phys. Rev. Lett.* 107, 188301. <https://doi.org/10.1103/PhysRevLett.107.188301>
- Breard, E.C.P., Dufek, J., Lube, G., 2018. Enhanced Mobility in Concentrated Pyroclastic Density Currents: An Examination of a Self-Fluidization Mechanism. *Geophys. Res. Lett.* 45, 654–664. <https://doi.org/10.1002/2017GL075759>
- Chen, X., Wang, J., 2014. A comparison of two-fluid model, dense discrete particle model and CFD-DEM method for modeling impinging gas–solid flows. *Powder Technol.* 254, 94–102. <https://doi.org/10.1016/j.powtec.2013.12.056>
- Crowe, C.T., Schwarzkopf, J.D., Sommerfeld, M., Tsuji, Y., 1997. *Multiphase Flows with Droplets and Particles*. CRC Press.
- Cioni, R., Civetta, L., Marianelli, P., Metrich, N., Santacroce, R., Sbrana, A., 1995. Compositional layering and syn-eruptive mixing of a periodically refilled shallow magma chamber: the AD 79 Plinian eruption of Vesuvius. *Journal of Petrology* 36, 739–776.
- Delvosalle, C., Vanderschuren, J., 1985. Gas-to-particle and particle-to-particle heat transfer in fluidized beds of large particles. *Chem. Eng. Sci.* 40, 769–779. [https://doi.org/10.1016/0009-2509\(85\)85030-2](https://doi.org/10.1016/0009-2509(85)85030-2)
- Dufek, J., Bachmann, O., 2010. Quantum magmatism: Magmatic compositional gaps generated by melt-crystal dynamics. *Geology* 38, 687–690. <https://doi.org/10.1130/G30831.1>
- Dufek, J., Bergantz, G.W., 2005. Lower Crustal Magma Genesis and Preservation: a Stochastic Framework for the Evaluation of Basalt–Crust Interaction. *J. Petrol.* 46, 2167–2195. <https://doi.org/10.1093/petrology/egi049>
- Džiugys, A., Peters, B., 2001. An approach to simulate the motion of spherical and non-spherical fuel particles in combustion chambers. *Granul. Matter* 3, 231–266. <https://doi.org/10.1007/PL00010918>
- Garg, R., Galvin, J., Li, T., Pannala, S., 2012. Open-source MFIx-DEM software for gas–solids flows: Part I—Verification studies. *Powder Technol.* 220, 122–137.
- Garg, R., Galvin, J., Li, T., Pannala, S., 2010. Documentation of open-source MFIx-DEM software for gas-solids flows. URL <https://www.netl.doe.gov/documentation/demdoc2012-1> Pdf Accessed 31 March 2014.
- Garg, R., Narayanan, C., Lakehal, D., Subramaniam, S., 2007. Accurate numerical estimation of interphase momentum transfer in Lagrangian–Eulerian simulations of dispersed two-phase flows. *Int. J. Multiph. Flow* 33, 1337–1364. <https://doi.org/10.1016/j.ijmultiphaseflow.2007.06.002>
- Gear, C., 1971. Simultaneous Numerical Solution of Differential-Algebraic Equations. *IEEE Trans. Circuit Theory* 18, 89–95. <https://doi.org/10.1109/TCT.1971.1083221>

- Hertz, H., 1896. Miscellaneous papers by H. Hertz. Transl. Jones Schott GA MacMillan Co Ltd Lond. 146–183.
- Holohan, E.P., Sudhaus, H., Walter, T.R., Schöpfer, M.P.J., Walsh, J.J., 2017. Effects of Host-rock Fracturing on Elastic-deformation Source Models of Volcano Deflation. *Sci. Rep.* 7, 1–12. <https://doi.org/10.1038/s41598-017-10009-6>
- Huber, C., Parmigiani, A., Chopard, B., Manga, M., and Bachmann, O., 2008. Lattice Boltzmann model for melting with natural convection: *International Journal of Heat and Fluid Flow*, v. 29, no. 5, p. 1469-1480.
- Ishii, M., Hibiki, T., 2011. *Thermo-Fluid Dynamics of Two-Phase Flow*. Springer Science+Business Media , LLC .
- Kelfoun, K., Druitt, T.H., 2005. Numerical modeling of the emplacement of Socompa rock avalanche, Chile. *J. Geophys. Res. Solid Earth* 110. <https://doi.org/10.1029/2005JB003758>
- Keller, T., and Suckale, J., 2019, A continuum model of multi-phase reactive transport in igneous systems: *Geophysical Journal International*, v. 219, no. 1, p. 185-222.
- Li, T., Garg, R., Galvin, J., Pannala, S., 2012. Open-source MFIx-DEM software for gas-solids flows: Part II—Validation studies. *Powder Technol.* 220, 138–150.
- Longo, A., Papale, P., Vassalli, M., Saccorotti, G., Montagna, C.P., Cassioli, A., Giudice, S., Boschi, E., 2012. Magma convection and mixing dynamics as a source of Ultra-Long-Period oscillations. *Bull. Volcanol.* 74, 873–880. <https://doi.org/10.1007/s00445-011-0570-0>
- Longo, A., Vassalli, M., Papale, P., Barsanti, M., 2006. Numerical simulation of convection and mixing in magma chambers replenished with CO₂-rich magma. *Geophys. Res. Lett.* 33. <https://doi.org/10.1029/2006GL027760>
- Lube, G., Breard, E.C.P., Jones, J., Fullard, L., Dufek, J., Cronin, S.J., Wang, T., 2019. Generation of air lubrication within pyroclastic density currents. *Nat. Geosci.* 12, 381–386. <https://doi.org/10.1038/s41561-019-0338-2>
- McIntire, M.Z., Bergantz George W., Schleicher Jillian M., 2019. On the hydrodynamics of crystal clustering. *Philos. Trans. R. Soc. Math. Phys. Eng. Sci.* 377, 20180015. <https://doi.org/10.1098/rsta.2018.0015>
- Molina, I., Burgisser, A., Oppenheimer, C., 2012. Numerical simulations of convection in crystal-bearing magmas: A case study of the magmatic system at Erebus, Antarctica. *J. Geophys. Res. Solid Earth* 117. <https://doi.org/10.1029/2011JB008760>
- Montagna, C.P., Papale, P., Longo, A., 2015. Timescales of mingling in shallow magmatic reservoirs. *Geol. Soc. Lond. Spec. Publ.* 422, 131–140. <https://doi.org/10.1144/SP422.6>
- Morgan, J.K., McGovern, P.J., 2005. Discrete element simulations of gravitational volcanic deformation: 1. Deformation structures and geometries. *J. Geophys. Res. Solid Earth* 110. <https://doi.org/10.1029/2004JB003252>
- Oppenheimer, J., Rust, A.C., Cashman, K.V., Sandnes, B., 2015. Gas migration regimes and outgassing in particle-rich suspensions. *Frontiers in Physics* 3, 60.
- Patankar, S.V., 1980. *Numerical heat transfer and fluid flow*. Hemisphere Pub. Corp.
- Parmigiani, A., Degruyter, W., Leclaire, S., Huber, C., Bachmann, O., 2017. The mechanics of shallow magma reservoir outgassing. *Geochemistry, Geophysics, Geosystems* 18, 2887–2905. <https://doi.org/10.1002/2017GC006912>
- Parmigiani, A., Huber, C., Bachmann, O., 2014. Mush microphysics and the reactivation of crystal-rich magma reservoirs. *Journal of Geophysical Research: Solid Earth* 119, 6308–6322. <https://doi.org/10.1002/2014JB011124>
- Parmigiani, A., Huber, C., Bachmann, O., and Chopard, B., 2011, Pore-scale mass and reactant transport in multiphase porous media flows: *Journal of Fluid Mechanics*, v. 686, p. 40-76.
- Pistone, M., Caricchi, L., Ulmer, P., Burlini, L., Ardia, P., Reusser, E., Marone, F., Arbaret, L., 2012. Deformation experiments of bubble- and crystal-bearing magmas: Rheological and microstructural analysis. *Journal of Geophysical Research: Solid Earth* 117. <https://doi.org/10.1029/2011JB008986>
- Qin, Z., Suckale, J., 2017. Direct numerical simulations of gas–solid–liquid interactions in dilute fluids. *International Journal of Multiphase Flow* 96, 34–47
- Qin, Z., Alison, K., Suckale, J., 2019. Rotation matters - Direct numerical simulations of rectangular particles in suspensions at low to intermediate solid fraction. *ArXiv190308167 Phys*.
- Ranz, W.E., Marshall, W.R., 1952. Evaporation from droplets. *Chem. Eng. Prog.* 48, 141–146.
- Rong, D., Horio, M., 1999. DEM simulation of char combustion in a fluidized bed. *Second Int. Conf. CFD Miner. Process Ind.* CSIRO Melb. Aust. 1999 65–70.
- Ruprecht, P., Bergantz, G.W., Dufek, J., 2008. Modeling of gas-driven magmatic overturn: Tracking of phenocryst dispersal and gathering during magma mixing. *Geochem. Geophys. Geosystems* 9. <https://doi.org/10.1029/2008GC002022>
- Schleicher, J.M., Bergantz, G.W., 2017. The Mechanics and Temporal Evolution of an Open-system Magmatic Intrusion into a Crystal-rich Magma. *J. Petrol.* 58, 1059–1072. <https://doi.org/10.1093/petrology/egx045>
- Schleicher, J.M., Bergantz, G.W., Breidenthal, R.E., Burgisser, A., 2016. Time scales of crystal mixing in magma mushes. *Geophys. Res. Lett.* 43, 1543–1550. <https://doi.org/10.1002/2015GL067372>
- Silbert, L.E., Ertas, D., Grest, G.S., Halsey, T.C., Levine, D., Plimpton, S.J., 2001. Granular flow down an inclined plane: Bagnold scaling and rheology. *Phys. Rev. E* 64, 051302.
- Suckale, J., Sethian, J.A., Yu, J., Elkins-Tanton, L.T., 2012. Crystals stirred up: 1. Direct numerical simulations of crystal settling in nondilute magmatic suspensions. *J. Geophys. Res. Planets* 117. <https://doi.org/10.1029/2012JE004066>
- Suckale, J., Keller, T., Cashman, K.V., Persson, P.-O., 2016. Flow-to-fracture transition in a volcanic mush plug may govern normal eruptions at Stromboli. *Geophysical Research Letters* 43, 12,071-12,081
- Sundaram, S., Collins, L.R., 1996. Numerical Considerations in Simulating a Turbulent Suspension of Finite-Volume Particles. *J. Comput. Phys.* 124, 337–350. <https://doi.org/10.1006/jcph.1996.0064>
- Syamlal, 1998. MFIx documentation numerical technique (No. DOE/MC/31346-01). EG and G Technical Services of West Virginia, Inc., Morgantown, WV (United States). <https://doi.org/10.2172/656644>
- Syamlal, M., 1998. MFIx documentation numerical technique. EG and G Technical Services of West Virginia, Inc., Morgantown,

-
- Syamlal, M., Rogers, W., OBrien, T.J., 1993. MFIX documentation theory guide. USDOE Morgantown Energy Technology Center, WV (United States).
- Tsuji, Y., Kawaguchi, T., Tanaka, T., 1993. Discrete particle simulation of two-dimensional fluidized bed. *Powder Technol.* 77, 79–87. [https://doi.org/10.1016/0032-5910\(93\)85010-7](https://doi.org/10.1016/0032-5910(93)85010-7)
- Wallace, P.J., 2005. Volatiles in subduction zone magmas: concentrations and fluxes based on melt inclusion and volcanic gas data. *Journal of volcanology and Geothermal Research* 140, 217–240.
- Wallace, P.J., 2001. Volcanic SO₂ emissions and the abundance and distribution of exsolved gas in magma bodies. *Journal of Volcanology and Geothermal Research* 108, 85–106.

Chapter 3: Effects of lubrication forces on mush dynamics¹⁰

3.1. Introduction

Magma bodies residing in the crust are formed by repeated injections of mobile magma and are inferred to reside in a mushy state (Bachmann and Bergantz, 2004a; Cashman et al., 2017; Hildreth, 2004). A mush is magma with a high concentration of crystals (also called particles here). The rheology of mushes is one of most critical phenomenon controlling magma transport within volcanic systems (Caricchi et al., 2007; Cordonnier et al., 2012; Kendrick et al., 2013; Lavallée et al., 2012, 2007; Ryerson et al., 1988; Sparks, 2003), sometimes influencing eruptive styles (Karlstrom et al., 2012). However the transition between a mobile magma and the mush state is complex and poorly understood. Macroscopically, this transition is characterized by the emergence of non-Newtonian behaviors characterized by shear thinning and possibly continuous and/or discontinuous shear thickening (Lavallée et al., 2012, 2007; Petford, 2009; Mader et al., 2013 and references therein).

However, attempts to index crystal-rich rheology to the volume fraction of crystals, whether by a Krieger-Dougherty type power law or by a viscous number scaling relation (Bergantz et al., 2017; Deubelbeiss et al., 2011), fail to recover non-Newtonian behavior in the absence of inertia. These models can predict the correct volume fraction dependence at a fixed shear rate, but cannot capture shear rate dependence at fixed volume fraction (e.g., Mari et al., 2014). This is because there is only one stress scale associated with the Krieger-Dougherty relation: the one associated with hydrodynamics. And while the viscous number framing includes a gravitational stress scale, it cannot predict the transition to discontinuous shear thickening or differentiate between jamming occurring from steric or frictional effects. It is now apparent that these non-Newtonian processes arise by the initiation of normal and frictional tangential forces from particle contact, which can happen at particle volume fractions of 0.3 or less. The onset of friction introduces an additional

¹⁰ Published as : Carrara, A., Burgisser, A., Bergantz, G.W., 2019. Lubrication effects of lubrication on magmatic mush dynamics. *J. Volcanol. Geotherm. Res.* 380, 19–30. <https://doi.org/10.1016/j.jvolgeores.2019.05.008>

stress scale into the rheology that is not resolved in the traditional framing. Hence any process that influences the onset of frictional contacts, such as lubrication, can have a profound effect on the rheology of the mush.

Following Bergantz et al. (2017), we further develop the scaling relationships for lubrication with an emphasis on how lubrication influences the time-dependence of a system as it moves between locked or frictional states. When neighboring particles graze each other in a viscous fluid, the ensuing hydrodynamic interactions create tangential lubrication forces on the particles (Jeffrey and Onishi, 1984; Marzougui et al., 2015). Normal lubrication forces arise when particles approach or are separated from each other. In sheared suspensions, lubrication effects due to these two forces dominate over that caused by particle spinning (Marzougui et al., 2015). The relative motions required to squeeze or suck the fluid from the gap between their edges result in the dissipation of the particle kinetic energy, which depends mostly on the fluid viscosity and particle separation distance. The importance of lubrication forces on mush dynamics is not obvious because these forces can be viewed as either opposing, or promoting the fluidization of the dense suspension in response to the arrival of new magma (Bergantz et al., 2017). Lubrication also influences the path of individual crystals during remobilization and the time they have to respond to changes in their chemical environment. As a result, the residence time of crystals within magmatic systems is affected by the transient lubricated state, the effects of which cannot be ignored when reconstructing the thermal history of crystals (e.g., Cooper and Kent, 2014; Barboni et al., 2016).

Here we use computational fluid dynamics with discrete element modeling (CFD-DEM) to explore the role of lubrication in mush systems. CFD-DEM numerical simulations have proven to be a powerful tool to study magmatic mush dynamics (Bergantz et al., 2017, 2015; Schleicher et al., 2016). In such models, the behavior of the continuous fluid phase (silicate melt) is computed by solving Navier-Stokes equations on an Eulerian grid. Individual crystals are represented by spheres, the trajectories of which are computed in a Lagrangian framework with the Newton laws of motion. This representation of the solid phase allows the CFD-DEM framework to explicitly resolve solid/solid interactions such as contact and friction and the coupling with the surrounding fluid. Despite high computational costs, models based on CFD-DEM have been validated (Deen et al., 2007) and are often employed as benchmarks to validate other numerical approaches (e.g. Chen and Wang, 2014). Previous CFD-DEM models used to study mush dynamics include the micro-

scale physics of contact, drag, and buoyancy forces (Bergantz et al., 2017, 2015; McIntire et al., 2019; Schleicher et al., 2016) but do not explicitly consider lubrication forces.

Symbol (unit)	Definition
A	Lubrication parameter
C	Particle shape and roughness parameter
d_p (m)	Particle diameter
$e_n ; e_t$	Normal and tangential restitution coefficients
F_R	Froude number
g (m s ⁻²)	Gravitational acceleration
h (m)	Distance between particle edges
j	Ratio of the distance between particle edges and their radius
S_T	Stokes number
S_O	Sommerfeld number
t (s)	time
U_{inj} (m s ⁻¹)	Injection velocity
U_{mf} (m s ⁻¹)	Minimum fluidization velocity
U_T (m s ⁻¹)	Particle terminal velocity
v_{p_i} (m s ⁻¹)	i^{th} particle velocity
v_p (m s ⁻¹)	Relative velocity between two particles
v_f (m s ⁻¹)	Relative velocity between particle and fluid
v_{fluid} (m s ⁻¹)	Fluid velocity
v_0 (m s ⁻¹)	Fluid characteristic velocity
W (m)	3 rd dimension length
δ (m)	Fluid characteristic distance
α	Permeability parameter
β (°)	Incidence angle
$\Delta\rho$ (kg m ⁻³)	Density contrast between fluid and particles
ε (m)	Particle roughness
η_f (Pa s)	Fluid viscosity
ρ_p (kg m ⁻³)	Particle density
ρ_f (kg m ⁻³)	Fluid density
$\tau ; \tau_d ; \tau_l$ (s)	Characteristic times
Φ	Particle volume fraction
Φ_{max}	Particle maximum packing fraction

Table 3.1: List of symbols and their meaning

Our objective is to address the effects and importance of lubrication forces on the dynamic of magmas and mushes. We first propose a scaling of the relative importance of lubrication forces at the particle scale with a simplified expression of lubrication. We then focus on macroscopic scale dynamics by investigating with CFD-DEM simulations the effects of a more complete description of lubrication in two canonical cases of fluid dynamics relevant to magmatic systems, the sedimentation and the remobilization of a dense particle bed. Finally, the effect of lubrication forces on magma and mushes dynamics is discussed.

3.2. Method

3.2.1. Formulation of the BBO equation with lubrication forces

To scale the importance of lubrication forces on a dense granular suspension, we consider a system of smooth spheres arranged in a hexagonal lattice and immersed in a viscous fluid with a density contrast (i.e. $\rho_p \neq \rho_f$, where ρ_p is the sphere density and ρ_f is the fluid density) (Fig. 3.1 A; symbols are summarized in Table 3.1). The particles have the same diameter, d_p , and they are separated by a small but finite distance, h . The motion of a given particle in a magmatic viscous fluid can be described by the truncated Lagrangian Basset-Boussinesq-Oseen (BBO) equation (Bergantz et al., 2017). Following Marzougui et al. (2015), we neglect lubrication effects arising from rolling and twisting relative motions between the particles, which only produce marginal effects compared to normal and tangential lubrication (Fig. 10 in Marzougui et al., 2015). There are different formulations of the lubrication forces. At the particle scale, we use a simplification proposed by Marzougui et al. (2015) of the more complete expression of Jeffrey and Onishi (1984) because it is amenable to algebraic manipulations. In the CFD-DEM model (section 3.2.2), we use the formulation of Frankel and Acrivos (1967) because it does not feature the unphysical negative torques at large inter-particle distance of the particle-scale expression (Marzougui et al., 2015). Incorporating both normal¹¹ and tangential lubrications forces, the BBO equation can be expressed as:

¹¹ In Bergantz et al., (2017), the normal lubrication expression should be replaced by the form used here (Eqs. (1) and (3) with $\beta=0$) to take into account that contacts occur between two spheres and not between a sphere and a plate (Andreotti et al., 2013).

$$\frac{d \overline{v}_{p1}}{dt} = \frac{\Delta\rho \vec{g}}{\rho_p} - \frac{3 \eta_f \overline{v}_f}{2 \alpha \rho_p d_p^2} - \frac{3 \eta_f \overline{v}_p}{\rho_p d_p^2} A, \quad (3.1)$$

where \overline{v}_{p1} is the particle velocity, $\Delta\rho = \rho_p - \rho_f$, ρ_f is the fluid viscosity, t is the time, and \vec{g} is the gravitation acceleration. The left-hand side of Eq. (3.1) represents the acceleration of the particle considered and the first term on the right-hand side is the reduced buoyancy. The second term corresponds to the viscous drag exerted by the fluid on the particle due to the velocity difference between the particle and the surrounding fluid, $\overline{v}_f = \overline{v}_{p1} - \overline{v}_{fluid}$. The coefficient α refers to the permeability of the dense particle network, which is given by the Carman-Kozeny relationship (Bergantz et al., 2017):

$$\alpha = \frac{(1-\Phi)^3}{C \Phi^2}, \quad (3.2)$$

where Φ is the particle volume fraction and C is a constant depending on particle shape and roughness ($C = 44.4$ for smooth sphere, MacDonald et al., 1991). As pointed out by Bergantz et al. (2017) this drag law is only reliable for dense suspensions when $\alpha > 1/12$, which corresponds to $\Phi > \sim 0.3$. The last term on the right-hand side of Eq. (3.1) incorporates both normal and tangential lubrication forces due to the relative velocity between the particle and its neighbor (subscripts $p1$ and $p2$ respectively), $\overline{v}_p = \overline{v}_{p1} - \overline{v}_{p2}$. The relationship between normal and tangential forces is expressed in the A coefficient (Marzougui et al., 2015):

$$A = \frac{3 \cos(\beta)}{2j} - \ln(j) \sin(\beta), \quad (3.3)$$

where j is the ratio of the distance between the particle edges, h , over their diameter ($j = 2h/d_p$), and β is the incidence angle that corresponds to the angle between the relative velocity and the vector linking the particle pair centers (Fig. 3.1 B). In an hexagonal lattice, j can be linked to the ratio of the particle volume fraction over the maximum packing fraction (Ancy et al., 1999):

$$j = 1 - \left(\frac{\Phi}{\Phi_{max}} \right)^{\frac{1}{3}}. \quad (3.4)$$

The tangential lubrication force expression used in Eqs. (3.1) and (3.3) gives reliable results up to $j = 0.2$ (Fig. 3 in Marzougui et al., 2015). As a result, Eq. (3.1) is valid from $\Phi/\Phi_{max} < 1$

down to $\Phi/\Phi_{max} = 0.5$, which corresponds to $j = 0.2$. For a system of two particles (Fig. 3.1 B), the meaning of the incidence angle, β , is obvious and decomposes the relative velocity vector into normal and tangential components. For a multi-particle system (Fig. 3.1 A), each particle pair displays a different relative velocity and incidence angle with respect to the central particle. The motion of the central particle is affected by the resultant lubrication force caused by all neighboring particles, which means that \vec{v}_p and β must be viewed as representative relative particle velocity and incidence angle, respectively. The meaning of these two parameters in a multiparticle system is explored in the supplementary section S3.1.

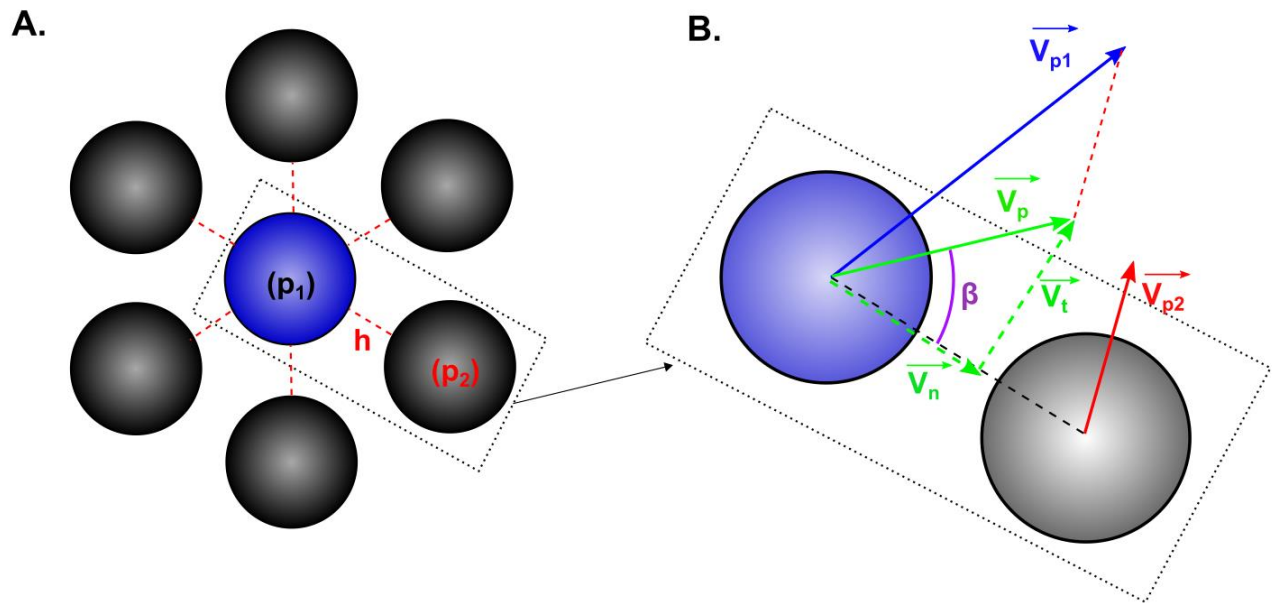


Figure 3.1: Conceptual model considered to scale the importance of lubrication forces. [A] The central target particle (p1) is in blue. Its six neighboring particles are indicated in black and are arranged in a hexagonal lattice. The minimum distance between the edges of particles pairs is indicated by red dashed lines and has been exaggerated for clarity. The black dashed box represents the region depicted in B. [B] Zoom on a particle pair. The blue particle represents the particle p1 and the black one represents p2. Their velocity vectors are represented by blue and red arrows, respectively. The green arrow represents the relative particle velocity seen by particle p1, \vec{v}_p . The two dashed green arrows indicate the decomposition of the relative velocity in its normal, \vec{v}_n , and tangential, \vec{v}_t , components. The angle between the vectors \vec{v}_p and \vec{v}_n , is called the incidence angle β (purple).

3.2.2 CFD-DEM model

We performed CFD-DEM numerical simulations by using the MFIX software (<https://mfix.netl.doe.gov/>). The equations are summarized in the supplementary section S3.2. Detailed explanations about the theory and implementation of the model can be found in Garg et al. (2010), Syamlal (1998), Syamlal et al. (1993), and validation of the DEM approaches in Garg et al. (2012) and Li et al. (2012). We included both normal and tangential lubrication forces into the model by implementing the formulas used by Marzougui et al. (2015). We emphasize that the drag and lubrication expressions used in the simulations are different from those used for in the scaling approach (i.e. the tangential lubrication force in Table A1 is the expression of Frankel and Acrivos (1967) and not that of Eqs. (3.1) and (3.3)) to ensure the consistency of the DEM modeling in dilute conditions.

Unfortunately, no simple analytical solution of the approach of two spheres exists because both \vec{v}_p and h that appear in the lubrication force vary with time. We validated instead our implementation of the lubrication forces by reproducing the particle bouncing experiment from Gondret et al. (2002). We obtain a good fit between the experimental results and our numerical simulation. Details and results of this validation are reported in the supplementary materials S3.3.

3.3. Results

3.3.1. Grains scale

3.3.1.a. Scaling of the relative importance of the forces exerted on a particle

To determine what parameters control most particle motion, we express the vectors involved in Eq. (3.1) by their magnitudes, which are always positive by definition. This allows us to quantify what are the dominant forces among buoyancy, viscous drag and lubrication. The importance of gravitational forces can be expressed by using the terminal fall velocity of the particle, which combines several variables involved in Eq. (3.1):

$$U_T = \frac{\Delta\rho g d_p^2}{3\eta_f}. \quad (3.5)$$

We introduce U_T in the drag and lubrication terms by multiplying each term by $1 = U_T/U_T = (\Delta\rho g dp^2)/(3\eta_f U_T)$. After rearranging, Eq. (3.1) becomes:

$$\frac{\rho_p}{\Delta\rho g} \frac{d v_{p1}}{dt} = 1 - \frac{v_f}{2\alpha U_T} - \frac{A v_p}{U_T}. \quad (3.6)$$

The left-hand side of Eq. (3.6) represents the non-dimensional gravitational acceleration of the particle (p1). The first term on the right-hand-side of Eq. (3.6) that equals unity expresses the fact that the gravitational acceleration of the particle is constant in time. The two last terms represents the non-dimensional drag and lubrication forces, respectively. The equality between drag and buoyancy forces occurs when $1 = v_f/(2\alpha U_T)$, which implies that :

$$v_f = 2\alpha U_T. \quad (3.7)$$

Similarly, the balance between buoyancy and lubrication is expressed by the equality $1 = A v_p / U_T$, which yields:

$$v_p = \frac{U_T}{A}. \quad (3.8)$$

Finally, equality between the drag and lubrication forces requires that $v_f/(2\alpha U_T) = A v_p / U_T$, which yields the following relationship between v_p and v_f :

$$v_f = 2\alpha A v_p. \quad (3.9)$$

The three forces balance each other when $\frac{v_f}{2\alpha U_T} = 1$ and $\frac{A v_p}{U_T} = 1$. Thus Eq. (3.7) is valid for $\frac{A v_p}{U_T} \leq 1$, Eq. (3.8) is valid for $\frac{v_f}{2\alpha U_T} \leq 1$, and Eq. (3.9) is valid for $\frac{A v_p}{U_T} \geq 1$ and $\frac{v_f}{2\alpha U_T} \geq 1$.

The three force domains and associated boundaries are summarized in Fig. 3.2. Predicting which forces control the motion of a particle requires to replace that particle in the force diagram. Its position depends on the ratio Φ/Φ_{max} , the angle β , and the two relative velocities v_p and v_f . The two first variables form the α and A coefficients. The influence of lubrication forces is maximum when the coefficient A is maximized, which means that it is possible to define an optimal angle, β_{opt} , that most promotes lubrication. This angle depends also on Φ/Φ_{max} and it corresponds to the point at which the derivative of A with respect to β is null:

$$\beta_{opt} = \tan^{-1} \left(-\frac{2j \ln(j)}{3} \right). \quad (3.10)$$

Conversely, we found that $\beta=90^\circ$ is most adverse to lubrication effects, which corresponds to pure tangential relative motion.

3.3.1.b. Dimensionless formulation

The dimensionless form of Eq. (3.1) is (see supplementary section S3.4):

$$\frac{d\widetilde{v}_{p1}}{d\tilde{t}} = \frac{1}{F_R^2} - \frac{\widetilde{v}_f}{S_T} - \frac{\widetilde{v}_p}{S_O}. \quad (3.11)$$

The three velocities \widetilde{v}_{p1} , \widetilde{v}_f , and \widetilde{v}_p correspond to the dimensionless forms of the velocities involved in Eq. (3.1) that are defined as $\widetilde{v}_{p1} = v_{p1}/v_0$, $\widetilde{v}_f = v_f/v_0$ and $\widetilde{v}_p = v_p/v_0$, where v_0 is the characteristic speed. The variable \tilde{t} is the dimensionless time defined as $\tilde{t} = t/\tau$, where τ is the characteristic time corresponding to the ratio of the characteristics length, δ , and speed, v_0 ($\tau = \delta/v_0$). The three terms F_R , S_T and S_O , are the dimensionless Froude, Stokes and Sommerfeld numbers, respectively. Both F_R and S_T were used previously by Burgisser et al. (2005) and

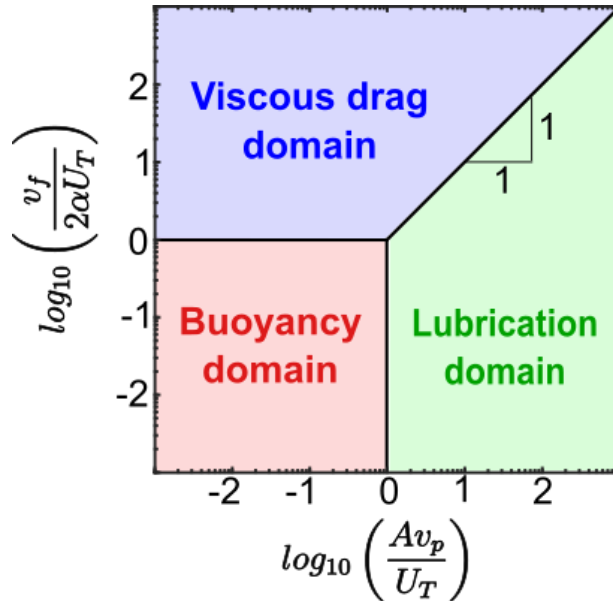


Figure 3.2: Force diagram summarizing scaling results. Axes have logarithmic scales with the ratios Av_p/U_T as abscissa and $v_f/2\alpha U_T$ as ordinate. The red, blue and green areas correspond to the domains where buoyancy, drag and lubrication dominate, respectively. Boundaries between the domains are reported with black lines corresponding to Eq. (3.7–3.9), respectively. Boundaries meet at a point where all forces have the same importance on particle motion.

Bergantz et al. (2017) to scale the controls of buoyancy and drag forces, respectively, and are expressed here as:

$$S_T = \frac{2\alpha \rho_p d_p^2 v_0}{3 \eta_f \delta} = \frac{\tau_d}{\tau}, \quad (3.12a)$$

$$F_R^2 = \frac{\rho_p v_0^2}{\Delta \rho g \delta}. \quad (3.12b)$$

The Stokes number characterizes the viscous drag coupling between the particle and the surrounding fluid, which corresponds to the ratio between the drag particle relaxation time ($\tau_d = d^2 \rho_p / 6 \alpha \eta_f$) and the characteristic time ($\tau = \delta / v_0$).

The Sommerfeld number characterizes the importance lubrication forces, and expresses the ratio between the lubrication particle relaxation time τ_l ($\tau_l = A d^2 \rho_p / 3 \eta_f$) and τ :

$$S_O = \frac{\rho_p d_p^2 v_0}{3 \eta_f A \delta} = \frac{\tau_l}{\tau}. \quad (3.13)$$

In the context of dense suspensions, the most appropriate characteristic distance is the gap between the particle edges, h . The relevant characteristic speed v_0 depends on the nature of the external forcing applied to the system. It could be, for instance, an externally imposed shear rate expressed as v_0/h .

3.3.2. Macroscopic scale

3.3.2.a Experiment 1: Rayleigh-Taylor instabilities

The first numerical experiment consists of a particle bed initially in a jammed state at the top of a tank filled with a viscous fluid. Simulations use non slip boundary conditions at the walls. The bed is initially at rest and simulations start when gravity is switched on. Due to the negative buoyancy of the particles, Rayleigh–Taylor-type instabilities are generated as shown by experimental (Michioka and Sumita, 2005) and numerical (Bergantz and Ni, 1999) experiments. To look at the effects of lubrication forces at the macroscopic scale of the settling bed, we performed the same simulation twice, once taking lubrication forces into account (simulation 1A) and once without lubrication forces (simulation 1B). A third simulation (simulation 1C) was run

without lubrication forces but mimicking lubrication by setting a low restitution coefficient (ratio of the kinetic energy conserved during the contact) as in Bergantz et al. (2015). Fluid and particle properties are indicated in Table 3.2 and taken from Michioka and Sumita (2005).

Figure 3.3 shows snapshots of the particle positions for the three runs 1A–C. Particle position maps show a clear difference between simulations 1A and 1B (Fig. 3.3). Run 1C presents a dynamics that is intermediate between those of 1A and 1B, so results of this approach to replicate lubrication forces are discussed in details in the supplementary section S3.5. Both simulations with (1A) and without (1B) lubrication start with the development of small Rayleigh–Taylor instabilities at the lower front of the particle bed, with a wavelength of ~ 3 mm that is consistent with that observed experimentally by Michioka and Sumita (2005) (Fig. 3.3 A–C). A small time delay in establishing the instabilities is observed for the simulation involving lubrication, 1A, compared to that without lubrication, 1B. Once the initial small particle plumes are formed, a larger instability is generated (Fig. 3.3 C–E). It is initiated by pure fluid that is buoyant relative to the suspended bed penetrating the left part of the bed. This rightward sweeping motion causes en masse bed sedimentation to produce a large particle plume encompassing most of the smaller plumes already sedimenting. We tested if the domain size controls the nature of the Rayleigh–Taylor instabilities observed in the experiments by varying the domain width, and observed the same kind of en masse bed sedimentation. It is always initiated by the opening of the particle bed in positions where the crystal network presents a lower particle volume fraction compared to the average random initial condition.

Run	η_f (Pa s)	d_p (m)	ρ_p (kg m ⁻³)	ρ_f (kg m ⁻³)	bed dimension (m × m)	e_n	e_t	lubrication
1A	0.2	$2.5 \pm 0.2 \cdot 10^{-4}$	2500	1250	0.03×0.005	0.7	0.35	yes
1B	0.2	$2.5 \pm 0.2 \cdot 10^{-4}$	2500	1250	0.03×0.005	0.7	0.35	no
1C	0.2	$2.5 \pm 0.2 \cdot 10^{-4}$	2500	1250	0.03×0.005	0.01	0.005	no

Table 3.2: Parameters used for the Rayleigh–Taylor instabilities experiment. The value of normal and tangential restitutions coefficient is the same between simulations 1A and 1B. These two values are artificially decreased to $e_n = 0.01$ and $e_t = 0.005$ in simulation 1C in an attempt to reproduce the effect of lubrication forces (see supplementary section S3.5).

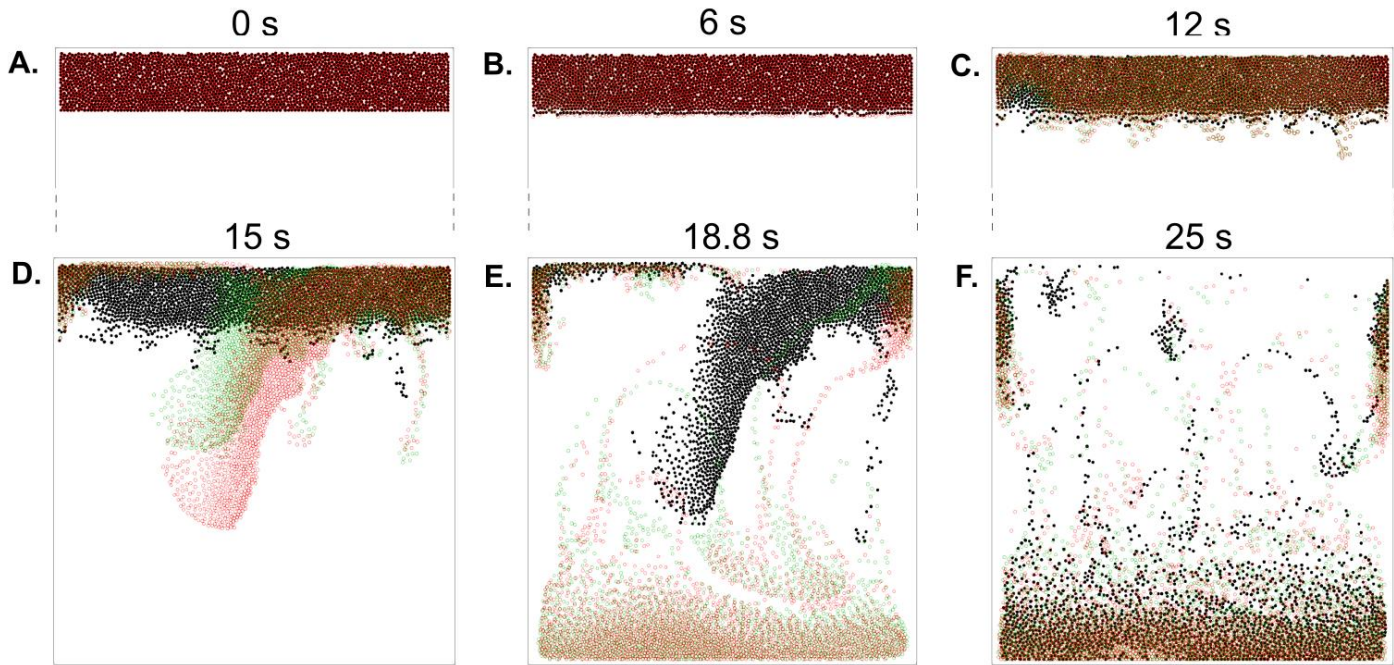


Figure 3.3: Snapshots from simulations 1A-C after 0 s [A], 6 s [B], 12 s [C], 15 s [D], 18.8 s [E] and 25 s [F]. Snapshots [A]-[C] are truncated and snapshots [D]-[F] represent the entire simulation domain. Filled and open circles represent the particles. Black disks represent the simulation involving lubrication forces (1A). Open red circles correspond to the simulation without lubrication (1B). The green open circles represent the run mimicking lubrication by reducing the restitution coefficients (1C).

All simulations display large plumes of similar shapes (Fig. 3.3 D–E), except that the plume of run 1A is slightly more narrow and of higher density than that of run 1B. The main effect of lubrication forces is on the duration of the development of the large instability responsible for en masse bed sedimentation. In run 1B, the large plume starts after 12 s (Fig. 3.3 C), and the plume reaches half of the tank height after 15 s (Fig. 3.3 D), whereas these steps are observed after 15 s and 18.8 s in run 1A, respectively (Fig. 3.3 D–E).

We selected in simulation 1A a group of neighboring particles within the large plume and tracked the time evolution of their individual relative velocities with the surrounding fluid, v_f , and of their relative velocities, v_p . The local particle volume fraction, Φ , is computed on the continuous grid (i.e. in each fluid computational cell) and is interpolated at each particle location. For each particle, the representative velocity relative to the neighboring particles is the magnitude of the sum of all the relative velocity vectors between that particle and its neighbors. The representative incidence angle is the average of all the pairwise angles between a given particle and its neighbors.

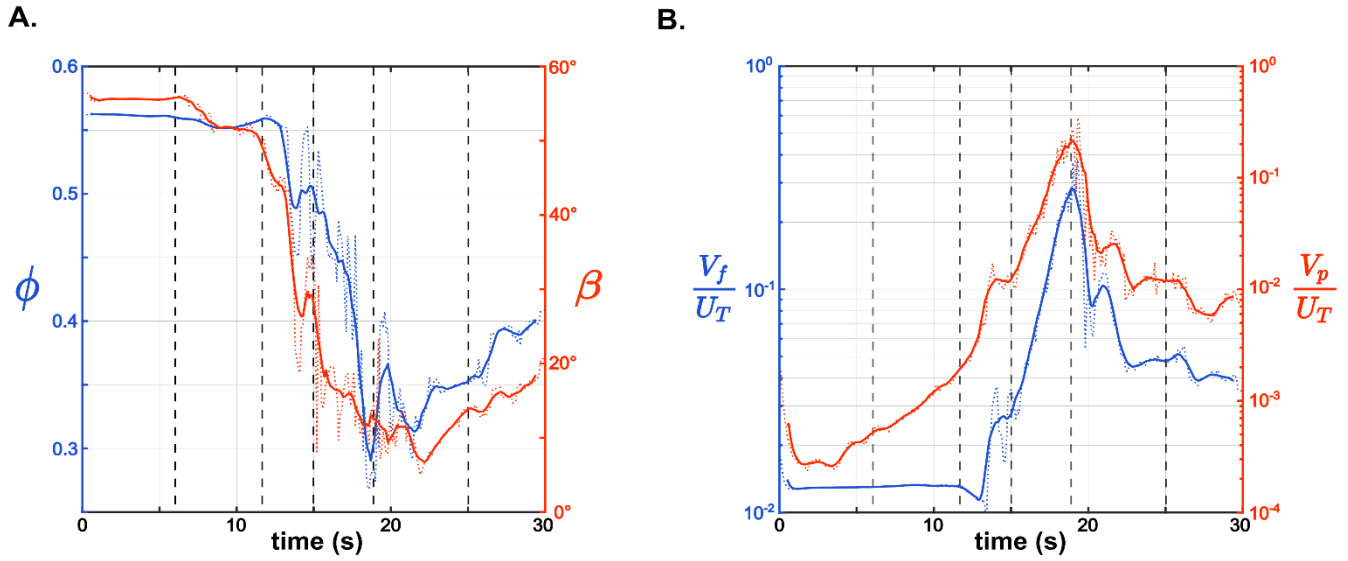


Figure 3.4: Temporal evolution of the physical parameters encountered by the group of tracked particles. [A] The graph has two ordinate axes. The blue axis and curve represent the local particle volume fraction averaged over the group of particle, Φ . The red axis and curve represent the average incidence angle, β . [B] The graph has two ordinate axes. The blue axis and curve represent the ratio between the particle–fluid relative velocity and the terminal fall velocity, V_f/U_T . The red axis and curve represent the ratio between the particles edges relative velocity and the terminal fall velocity, V_p/U_T . Vertical dashed lines represent the times at which the snapshots of Fig. 3 were taken.

Both relative velocities, β , and Φ were averaged over the group of particles and their time evolution was smoothed by performing a zero-phase moving average (Fig. 3.4). These smoothed parameters can be used to calculate the force balance, and Fig. 3.5 F shows snapshots of the locations of the selected particle group alongside their positions on the force diagram of Fig. 3.2.

At the start of the simulation, the particles are in a jammed state and undergo a slow dilation, as highlighted by the slight decrease of the particle volume fraction and the increase of v_p up to 12 s (Fig. 3.4 B). The entire bed is falling slowly under the influence of gravity without becoming deformed as shown by the constant value of v_f (Fig. 3.4 B) and by the pure fluid layer that forms atop the bed (Fig. 3.5 A). During this process, the buoyancy and drag forces felt by the particles are in equilibrium (Fig. 3.5 F) until the bed reaches its terminal fall velocity while keeping the same shape. The buoyant fluid is thus transported by porous flow through the pack of selected particles. At 12 s, lubrication forces become dominant (Fig. 3.5 F) because the particle relative velocity increases while the particle volume fraction is still close to its maximum. This point also corresponds to the time when the largest delay occurs between simulations 1A and 1B. After 15 s, when the large instability forms on the left part of the bed, v_f increases again (Fig. 3.4 B) and the

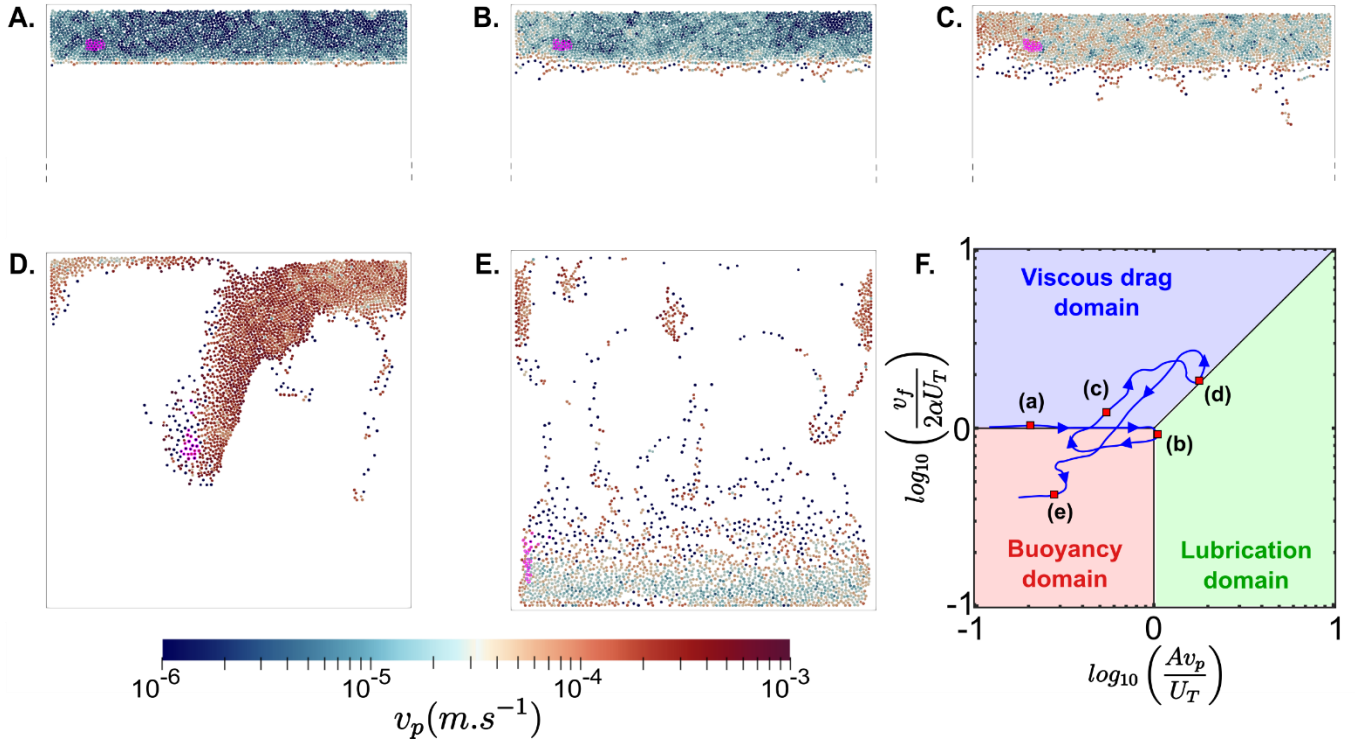


Figure 3.5: Analysis of the results of the simulation involving lubrication (1A) with the scaling summarized in Fig. 2. Plots [A], [B], [C], [D], and [E] represent snapshots of simulation 1A after 6 s, 12 s, 15 s, 18.8 s, and 25 s, respectively. Particles are represented by disks, the color of which depends on the value of the average relative velocity between a particle and its neighbors. The group of tracked particles is indicated by purple circles. Graph [F] displays the position of the group of tracked particles on the force scaling graph. The red, blue, and green areas represent the domain where buoyancy, drag, or lubrication dominates, respectively. The positions of the tracked particles at time steps [A]-[E] are indicated by red squares and depend on the average parameters reported in Fig. 4. The blue curve represents the dynamic history of the tracked particles.

viscous drag tends to control particles motion (Fig. 3.5 F). This suggests that the large plume is formed by the viscous entrainment of the fluid rather than by the net weight of the particles. During the large plume unfolding and sedimentation, v_p and v_f increase (Fig. 3.4 B) and equilibrium between fluid drag and lubrication occurs (Fig. 3.5 F). When the plume reaches the bottom of the tank, v_p and v_f decrease, Φ slowly increases and particle settling is controlled by their buoyancy. Our results show a good correlation between both relative velocities after the initial bed expansion (Fig. 4 B). Furthermore, v_f and v_p appear to be inversely proportional to the local solid volume fraction (Fig. 4 A), which suggests that they are not coupled directly, but that the coupling occurs through to the local particle concentration. Decreasing particle concentration results in a joint increase of the distance between particle edges and of bed permeability. As for magmas, the characteristic Stokes numbers of the simulation are small ($10^{-4} < S_T < 10^{-2}$), which indicates a strong coupling between fluid and particles. The relative velocity v_f is thus strongly controlled by

fluid–particle drag. As particle volume fraction decreases, so does the drag force, and higher relative fluid velocities are possible within the dense suspension. The same mechanism holds for v_p because of the monotonic relationship between lubrication forces and particle concentration. At low concentrations, particles can achieve higher relative velocities before lubrication forces dissipate the particles kinetic energy. We expect that the observed correlation between v_f and v_p breaks down for flows featuring high Stokes numbers, such as pyroclastic flows.

The 2D geometry used in these simulations has been shown to affect the results obtained by both numerical (e.g. Li et al., 2014; Peirano et al., 2001) and experimental studies on dense suspension dynamics (e.g., Courrech du Pont et al., 2003). It reduces the degrees of freedom that particles have to move relative to each other, which can potentially increase the particle relative velocities compared to the 3D case. To test the influence of the 2D geometry, we ran partial simulations of the settling runs 1A and 1B with a 3D geometry by imposing a width to the tank, W , of ten particle diameters ($W \approx 10 d_p$), with the same boundary conditions as the 2D simulations. Figure 3.6 displays snapshots of these simulations captured after 22s of sedimentation. The 3D results do not exhibit the en masse bed sedimentation associated with the formation of a large plume that characterizes the 2D simulations. Sedimentation is instead characterized by multiple thinner plumes, which is more consistent with the experimental results of Michioka and Sumita (2005). This is probably due to the third spatial dimension involved, which smooths the local particle volume fraction and hinders the emergence of the fluid-rich gaps that characterize 2D simulations. The time delay observed between the run involving lubrication (Fig. 3.6 A) and the one neglecting it (Fig. 3.6 B) is less pronounced than the lag observed with the 2D simulations. This suggests that the effect of lubrication forces is overestimated with a 2D geometry.

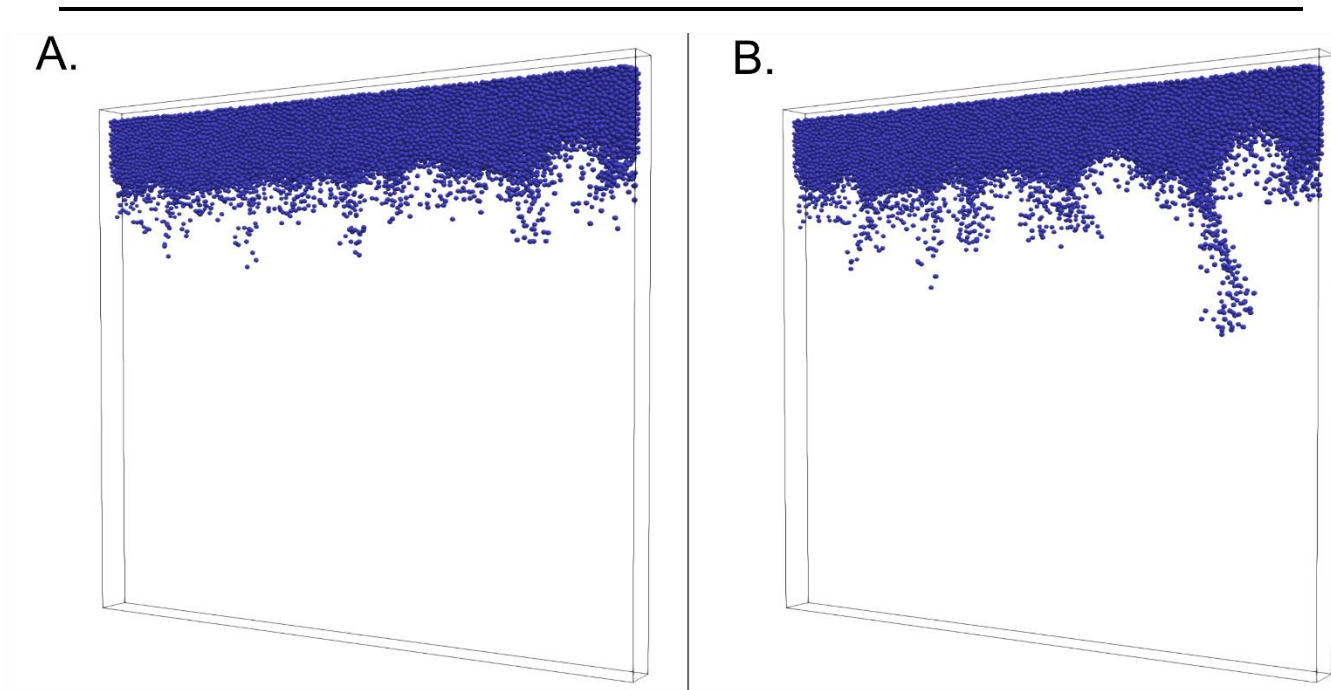


Figure 3.6: Snapshots at identical times (22 s) of the Rayleigh-Taylor simulations 1A and 1B performed in 3D. Black lines indicate the computational domain boundaries and blue spheres are particles. [A] Run with lubrication forces. [B] Run where lubrication forces are neglected.

3.3.2.b Experiment 2: Injection of a fresh magma into a mush

Previous studies (Bergantz et al., 2017, 2015; Schleicher et al., 2016; Schleicher and Bergantz, 2017) have shown that the local injection of a crystal-free magma inside a mush produces a localized fluidized area delimited by soft faults called the mixing bowl where mixing between injected and resident melts occurs within the resident crystal cargo. To test the role of lubrication forces in such a situation, we performed numerical simulations that keep the same particle and fluid properties these authors used (see Table 3.3). The dimensions of the bed and injection width were, however, reduced to limit computation duration. We conserved the same ratio between the injection velocity, U_{inj} , and the minimum fluidization velocity, U_{mf} , predicted by (Cui et al., 2014) as the one they used ($U_{inj} = 21.2 U_{mf}$). We performed two simulations that are summarized in Table 3.3. Simulation 2A took into account both normal and tangential lubrication forces. Simulation 2B did not involve lubrication, and thus corresponds to the original case explored by Bergantz et al. (2015) with higher coefficients of restitution. Two additional simulations that mimic lubrication by using low restitution coefficients identical to those of Bergantz et al. (2015) have a behavior intermediate to those of 2A and 2B and are discussed in details in the supplementary material S3.5.

Overall, simulations 2A and 2B exhibit the same kind of differences as observed in experiment 1. Both runs have very similar kinematics and dynamics during the ascent of the injected magma. They both start with the initial growth of a cavity just above the inlet. We did not observe any difference between the simulations up to this point. An instability then forms at the top of the cavity once the cavity area is large enough, and the cavity rises through the mush. Figure 3.7 displays snapshots of the simulations after 9.8 s of injection when the cavity reaches the top of the bed in run 2B. Each simulation ends with the establishment of a pulsating quasi-steady chimney between two counter-rotating 'granular vortices'. Run 2A presents a delay compared to run 2B because of lubrication forces (Fig. 7 A–B). The delay between runs 2A and 2B increases during the rise of the unstable cavity within the mush. An accumulated time difference of 1.1 s is observed between the two simulations when the injected magma reaches the top of the mush bed.

Run	η_f (Pa s)	d_p (m)	ρ_p (kg m ⁻³)	ρ_f (kg m ⁻³)	bed dimension (m × m)	e_n	e_t	Injection velocity (m s ⁻¹)	lubrication
2A	0.2	$4 \pm 0.2 \cdot 10^{-3}$	3300	2650	0.96×0.040	0.7	0.35	0.023	yes
2B	0.2	$4 \pm 0.2 \cdot 10^{-3}$	3300	2650	0.96×0.040	0.7	0.35	0.023	no

Table 3.3: Parameters used for the simulations involving the injection of crystal-free basalt inside a basaltic mush.

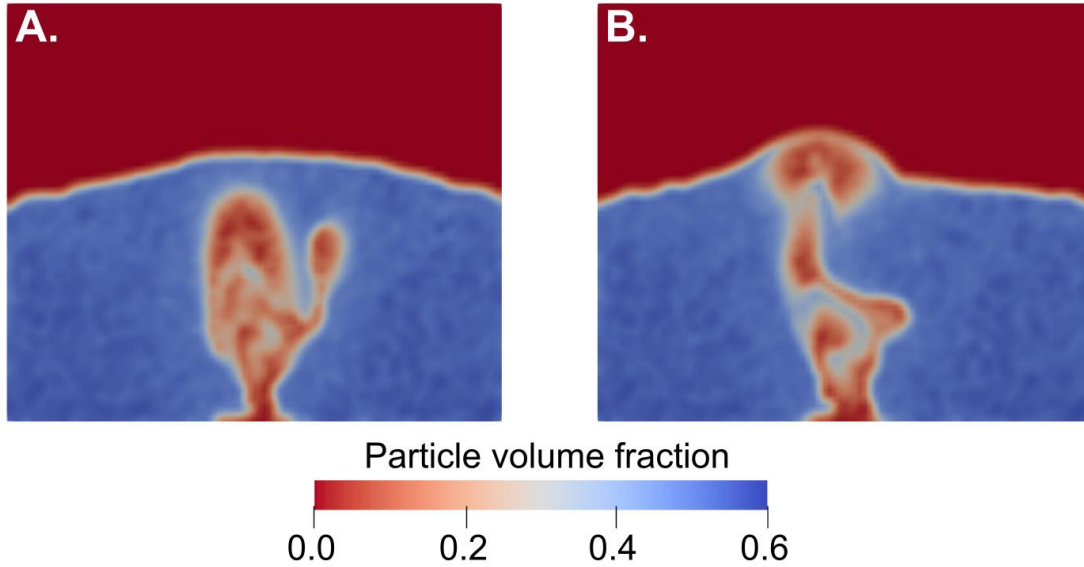


Figure 3.7: Snapshots of experiment 2 simulations. All simulations are displayed at the same time step, after 9.8 s of injection. The color code indicates the local particle volume fraction, which is in blue at its maximum and red when the cell only contains fluid. [A] Simulation involving lubrication (2A). [B] Simulation without lubrication (2B).

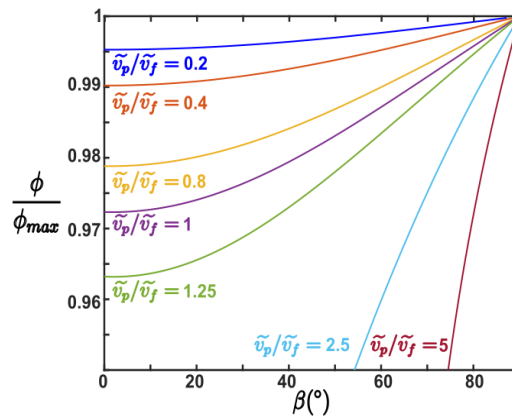


Figure 3.8: Evolution of the critical relative particle concentration as functions of the angle β and the ratio v_p/v_f . All curves correspond to the values of the critical concentration at which $S_T v_p / S_0 v_f = 1$. Their colors depend of the imposed ratio v_p/v_f . Each curve presents a minimum critical concentration when the relative motion of the particle is nearly normal ($\beta \rightarrow 0$), and a maximum at a relative particle concentration of ~ 1 when the relative motion is purely tangential ($\beta = 90^\circ$).

3.3.3. Interpretation

Figure 3.2 shows that the scaling relationships we propose can discriminate under which conditions lubrication forces are important. Their importance in controlling the dynamics of a dense suspension depends on the interplay of hydrodynamic stress exerted by the carrier phase, the velocity fluctuations among the solids, and the local particle concentration. The importance of drag and lubrication forces are inversely proportional to S_T and S_O , respectively. In general, when $S_T \ll 1$ and $S_O \ll 1$, the buoyancy force is negligible. This is usually the case for magmatic mixtures, which are characterized by high viscosities and small crystal sizes. The relative importance of lubrication forces over the drag force is expressed in the ratios S_T/S_O and \tilde{v}_p/\tilde{v}_f . Our simulations show that \tilde{v}_p and \tilde{v}_f coevolve when $S_T \ll 1$, and that $\sim 0.1 < \tilde{v}_p/\tilde{v}_f < \sim 1$ (Fig. 3.4 B). This ratio does not vary significantly with the particle volume fraction. On the contrary, the ratio S_T/S_O depends on the particle volume fraction and tends to infinity when approaching maximum packing. The ratio $S_T \tilde{v}_p / S_O \tilde{v}_f$ is equal to $2\alpha A \frac{\tilde{v}_p}{\tilde{v}_f}$, which is a function of the solid concentration and the incidence angle β . Figure 3.8 displays curves of critical particle concentrations at which the transition between dynamics dominated by the drag or lubrication forces occurs ($S_T \tilde{v}_p / S_O \tilde{v}_f = 1$). Above the critical concentration, lubrication forces have a larger magnitude than the drag force, and produce an apparent strain hardening at the onset, or at the end, of motion within the crystal network. Below the critical concentration, lubrication forces have a lower magnitude than the drag force and have only a marginal effect on dynamics as highlighted in our simulations (Fig. 3.3).

3.4. Discussion

3.4.1 Influence of crystals size and shape

We represent crystals as spheres with a unimodal size distribution. This is not the case in magmatic systems, where crystal size distributions (CSD) are polydisperse and often polymodal, and crystals are not spherical (Higgins, 2006; Higgins and Roberge, 2003; Marsh, 1988; Picard et al., 2011). The particle aspect ratio affects the rheology of crystal-bearing magmas (Cimarelli et al., 2011; Mueller et al., 2011, 2010; Picard et al., 2011; Mader et al., 2013; Moitra and Gonnermann, 2015). Both drag and lubrication forces become non-uniform around the crystals and depend on the orientations of the elongated particles (Bergantz et al., 2017). The relationship between particle shape and drag also influences their terminal fall velocity (Dellino et al., 2005). This last effect can be added into the numerical simulations by introducing a shape factor on the drag expression (Dioguardi et al., 2014). Some methods also exist to incorporate the particles shape within lubrication expressions, but they require additional iterations to find the minimum gap position and principal curvature direction between two elongated particles (Claeys and Brady, 1993; Janoschek et al., 2013). This calculation needs to be performed at each DEM time step and for each particle pair, which increases the computational cost of the simulations. Contact forces are not included within our scaling but are nevertheless present in nature and within the simulations. For non-spherical particles, the contact torques between non-spherical particles depend on the contact position and orientation (Bergantz et al., 2017). Our results and conclusions are therefore valid for spherical particles and are to be extended with caution to natural systems.

We employed three distinct but close particle sizes in order to avoid artificial shape 'crystallization'. This cannot be viewed as representative of the polydispersity present in natural systems. The CSD is an important parameter that controls the dynamic of the particles because each force and dimensionless number we considered depends on particle diameter. CSD also affects the maximum packing fraction that a dense suspension can reach. Maximum packing increases when the suspension is polydisperse, and, Apollonian packing aside, it is maximal when the CSD is bimodal with ~25% of fine particles and ~75% coarse particles (Ouchiyama and Tanaka, 2002; Farr and Groot, 2009; Faroughi and Huber, 2014). The effect of polydispersity on the force balance is not obvious because a high degree of polydispersity decreases particle bed permeability but increases the coordination number and thus the number density of lubricated bridges.

3.4.2. Comparison with other studies

Relationships exist to scale the competition between lubrication and friction in dense suspensions (Coussot and Ancey, 1999; Fernandez et al., 2013; Ness and Sun, 2015). These works motivated Bergantz et al. (2017) to scale the transition between dynamic regimes dominated by either friction or lubrication in magmas (we call here the dimensionless number characterizing the lubrication/friction transition the Leighton number, Le , to distinguish it from the Sommerfeld number we propose). At low Le , particles are in direct contact and at large Le , particles are separated by a lubrication film. This number is proportional to the distance between particle edges and fails to properly measure the importance of lubrication when particles tend to be far away from each other (Fernandez et al., 2013). It is thus unable to capture the transition between dynamic regimes where crystal motions are governed by either the lubricated film or melt motions that are further afield. In our formulation, however, lubrication is inversely proportional to S_O and to the distance between the particles. It thus properly scales the transition between lubricated and hydrodynamic regimes but fails to predict the onset of frictional behavior. The two scaling numbers are thus complementary to describe all the regime transitions that can be encountered in magmatic mush.

Our observations on the effect of lubrication on the macroscopic dynamics of a magmatic mush fit well with the results of Mutabaruka et al. (2014) on the initiation of motion in immersed granular avalanche. They observed the formation of a strain hardening followed by relaxation associated with dilation of the solid network when the initial particle concentration tends towards its maximum. At the initiation of the granular avalanche, they observed bed expansion when the initial particle concentration is higher than ~ 0.59 . This corresponds to ratios $\Phi/\Phi_{max} > 0.92$ with $\Phi_{max} = 0.64$. This illustrates well the importance of lubrication forces at the onset of motion of dense suspensions.

3.4.3 Implication on magma rheology and magmatic system dynamics

As in our experiments, magmatic mixtures are characterized by low Stokes numbers, $S_T \ll 1$, which indicates strong coupling between crystals and melt (Burgisser et al., 2005). Because of this dynamic similarity, we expect that our simulations illuminate the role of lubrication forces on mush dynamics and rheology. The rheology of magmas and mushes is now often studied by shearing or uniaxial compression experiments under high temperature and high confining pressure (e.g. Caricchi et al., 2007; Champallier et al., 2008; Laumonier et al., 2014, 2013; Lavallée et al., 2013, 2007). Capturing lubrication in such experiments, however, is challenging for several reasons. Our results show that lubrication effects appear when the crystal network is free to expand in response to deformation. Experiments involving water-bearing melts (e.g., Caricchi et al., 2007), however, feature a metal jacket that encloses the sample and prevents such dilation. This suggests that jacket-free experiments typical of uniaxial apparatus (e.g., Lavallée et al., 2007) have better chances to evidence lubrication. Bulk viscosities are determined using experimental data acquired when an apparent steady state is reached, which leaves out the initial transient response to the imposed constraint. Our results show that lubrication forces under quasi-steady state are weaker than other hydrodynamic micro-scale processes. It is not the case, however, when deformation is transient. This suggests that lubrication could be captured in shearing or compression experiments performed on samples near maximum packing during the initiation of shearing or during an abrupt change of the imposed shear rate. Initial non-linear increases in the stresses and apparent viscosities are well documented (Caricchi et al., 2007; Champallier et al., 2008; Lavallée et al., 2007). As these effects are observed for all particle concentrations (Champallier et al., 2008), they are inferred to reflect the combined effects of the elastic response of the experimental apparatus and of the initial reorganization of the particles in the pre-compacted sample (Lavallée et al., 2007). Our results suggest that these early non-linear stress responses and those following changes in applied strain rates might contain yet unexploited information on lubrication.

To identify which degrees of freedom control lubrication under magmatic conditions, we performed a Monte-Carlo analysis by varying the variables present in Eq. (3.1) over possible ranges encountered in magmas and mushes (Table 3.4). Figure 3.9 A displays the results in a format that recovers the same phase-space as that of Figure 3.2. We report in Fig. 3.9 B–F the probability

density distribution of the variables involved in the realizations where lubrication is the dominant force. Lubrication effects are expected to appear more often with small crystals rather than large ones (Fig. 3.9 B). It is not surprising because lubrication forces depend linearly on crystal diameter whereas the terminal velocity depends on the square of it (Eq. 3.5). The dependence on the melt viscosity shows that highly viscous melt are more likely to be in lubricated conditions (Fig. 3.9 C). As expected from our scaling, the two main parameters that control the importance of lubrication are the relative velocities between the crystals and the surrounding melt (Fig. 3.9 D and F). These two parameters may be very difficult to measure during experiments on magma rheology as they are dynamical properties. This is a reminder that the rheology of magmas and mushes depends greatly on such dynamic properties in addition to materials properties, which are the only ones often reported and used in studies treating magma rheology as a single fluid. The relative velocities between crystals and melt affects the time crystals have to respond to changes in chemical environment during mush unlocking. Owing to experimental limitations and to the strong tendency that multiphase suspensions have to foster particle gathering and dispersal when subjected to shear, such transient motions are difficult to appraise. Their understanding is nevertheless crucial to fully describe magma rheology and to predict the rate and duration of dynamic remobilization processes within magmatic systems.

Silicic magma bodies are thought to be formed by several increments of injected magma (Annen and Sparks, 2002) that cool, degas, and crystallize to reach a mushy state (Bachmann and Bergantz, 2004). In such systems, several scenarios have been evoked to explain eruption triggering. One is the rejuvenation of the magmatic mush associated with the injection of crystal-poor magmas (e.g. Pallister et al., 1992; Tomiya and Takeuchi, 2009). Another is the reactivation of the magmatic mush resulting from the emplacement of a hot batch of magma at the base of the crystal mush, which heats it up and melts the mush crystals to produce a mobile layer that eventually becomes unstable and ascends through the mush (Burgisser and Bergantz, 2011). Yet another scenario is crustal faulting that causes deep fragmentation of mush materials (Gottsmann et al., 2009). Each of these scenarios requires the initiation of motion within the mush. Our simulations have shown that lubrication forces produce strain hardening followed by softening during such event (Fig. 3.5). These forces likely play an important role in controlling the ascent rates and timescales of magmas within the crust. Neglecting them could result in underestimating

the resistance of the mush to the arrival of mobile magma. For instance, a magma batch ascending through a mush needs to continuously initiate the motion of the overlying crystals in order to open and penetrate the mush. Lubrication forces are opposed to this process and therefore slow down the ascent of the magma batch. In addition, the ascending magma batch is expected to form a fluidized chimney in its wake (e.g. Girard and Stix, 2009). Our results show that lubrication forces are important when the crystal-bearing magma is approaching jamming, a result consistent with other numerical and experimental results. These forces oppose the closing and clogging of the fluidized chimney, which tends to maintain the feeding system of the ascending batch. The overall effect of lubrication forces on such phenomena is thus a complex combination of both effects that needs further exploration because it bears on our capability to accurately predict timescales of magmatic mushes dynamics.

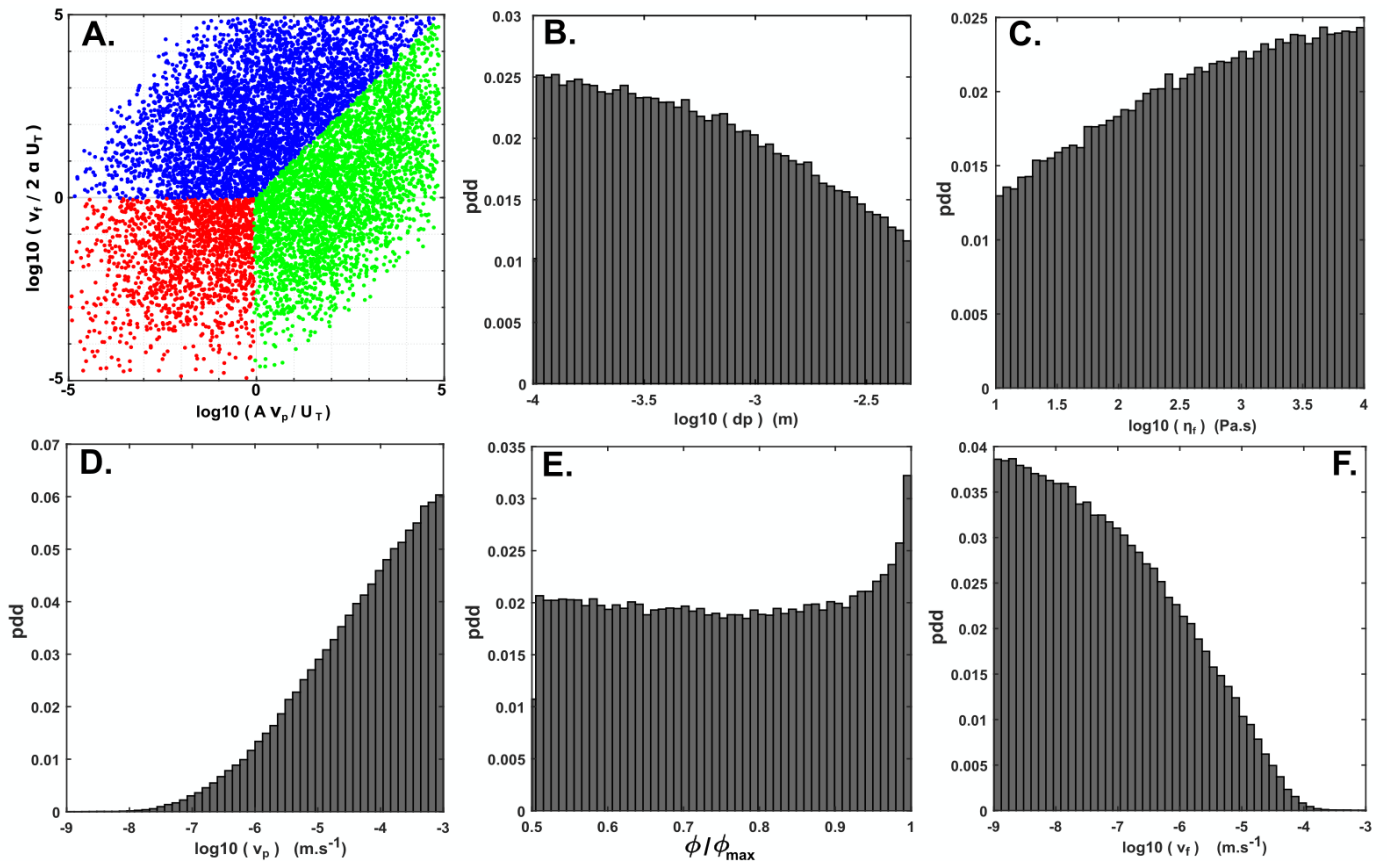


Figure 3.9: Exploration of the importance of lubrication in magmatic context. (a). Results of the Monte-Carlo analysis. Results are reported on logarithmic scales with the ratios $A v_p / U_T$ as abscissa and $v_f / 2 \alpha U_T$ as ordinate. We report only 10^4 of the 10^6 total realizations for clarity. Each dot corresponds to a realization and its color depends on the force with the highest magnitude. Realizations dominated by buoyancy, drag, or lubrication are indicated by red, blue, or green dots, respectively. [B–F] Probability density distributions (pdd) of the parameters involved in realizations where the lubrication forces dominate the others. We only reported the distributions of crystal diameter [B], fluid viscosity [C], particle relative velocity [D], the ratio of the particle volume fraction [E], and the relative velocity between the particle and the fluid [F].

Parameter	Lower bound	Upper bound
ρ_p (kg m ⁻³)	2700	3300
ρ_f (kg m ⁻³)	2450	3300
d_p (m)	10 ⁻⁴	5.10 ⁻³
η_f (Pa s)	10 ¹	10 ⁴
φ/φ_{max}	0.5	0.99999
β (°)	0	90
v_p (m s ⁻¹)	10 ⁻⁶	10 ⁻¹
v_f (m s ⁻¹)	10 ⁻⁶	10 ⁻¹

Table 3.4: Parameter ranges used for the Monte-Carlo analysis. Ranges were chosen to represent possible conditions encountered in magmatic systems while remaining in the validity domain of our analysis.

3.5. Conclusion

Using numerical simulation, we demonstrate that lubrication forces cannot be neglected when a magmatic mush exits or enters a jammed state. Our numerical experiments of sedimentation and remobilization of packed particle beds notably show that an apparent bulk strain hardening is produced by lubrication forces, which results in belated dynamics. We propose scaling relationships that highlight the dominant role of lubrication forces as the cause of the strain hardening and softening observed. This scaling leads us to propose a new formulation of the Sommerfeld number to scale the transition between hydrodynamic and lubricated regimes. Our formulation is complementary to that previously used in the literature aimed at capturing the transition between frictional and lubricated regimes. The two formulations can predict the overall transitions in dynamic regimes that a magmatic mush can be subjected to. Understanding lubrication has implications on the timescales of magmatic mush processes that control crystal thermal histories.

References:

- Ancey, C., Coussot, P., Evesque, P., 1999. A theoretical framework for granular suspensions in a steady simple shear flow. *J. Rheol.* 43, 1673–1699. <https://doi.org/10.1122/1.551067>
- Andreotti, B., Forterre, Y., Pouliquen, O., 2013. *Granular Media: Between Fluid and Solid*. Cambridge University Press.
- Annen, C., Sparks, R.S.J., 2002. Effects of repetitive emplacement of basaltic intrusions on thermal evolution and melt generation in the crust. *Earth Planet. Sci. Lett.* 203, 937–955. [https://doi.org/10.1016/S0012-821X\(02\)00929-9](https://doi.org/10.1016/S0012-821X(02)00929-9)
- Bachmann, O., Bergantz, G.W., 2004. On the origin of crystal-poor rhyolites: extracted from batholithic crystal mushes. *J. Petrol.* 45, 1565–1582.
- Barboni, M., Boehnke, P., Schmitt, A.K., Harrison, T.M., Shane, P., Bouvier, A.-S., Baumgartner, L., 2016. Warm storage for arc magmas. *Proc. Natl. Acad. Sci.* 201616129. <https://doi.org/10.1073/pnas.1616129113>

- Bergantz, G.W., Ni, J., 1999. A numerical study of sedimentation by dripping instabilities in viscous fluids. *Int. J. Multiph. Flow* 25, 307–320. [https://doi.org/10.1016/S0301-9322\(98\)00050-0](https://doi.org/10.1016/S0301-9322(98)00050-0)
- Bergantz, G.W., Schleicher, J.M., Burgisser, A., 2017. On the kinematics and dynamics of crystal-rich systems. *J. Geophys. Res. Solid Earth* 122, 2017JB014218. <https://doi.org/10.1002/2017JB014218>
- Bergantz, G.W., Schleicher, J.M., Burgisser, A., 2015. Open-system dynamics and mixing in magma mushes. *Nat. Geosci.* 8, 793–796. <https://doi.org/10.1038/ngeo2534>
- Burgisser, A., Bergantz, G.W., 2011. A rapid mechanism to remobilize and homogenize highly crystalline magma bodies. *Nature* 471, 212–215. <https://doi.org/10.1038/nature09799>
- Burgisser, A., Bergantz, G.W., Breidenthal, R.E., 2005. Addressing complexity in laboratory experiments: the scaling of dilute multiphase flows in magmatic systems. *J. Volcanol. Geotherm. Res.* 141, 245–265. <https://doi.org/10.1016/j.jvolgeores.2004.11.001>
- Caricchi, L., Burlini, L., Ulmer, P., Gerya, T., Vassalli, M., Papale, P., 2007. Non-Newtonian rheology of crystal-bearing magmas and implications for magma ascent dynamics. *Earth Planet. Sci. Lett.* 264, 402–419. <https://doi.org/10.1016/j.epsl.2007.09.032>
- Cashman, K.V., Sparks, R.S.J., Blundy, J.D., 2017. Vertically extensive and unstable magmatic systems: A unified view of igneous processes. *Science* 355, eaag3055. <https://doi.org/10.1126/science.aag3055>
- Champallier, R., Bystricky, M., Arbaret, L., 2008. Experimental investigation of magma rheology at 300 MPa: From pure hydrous melt to 76 vol.% of crystals. *Earth Planet. Sci. Lett.* 267, 571–583. <https://doi.org/10.1016/j.epsl.2007.11.065>
- Chen, X., Wang, J., 2014. A comparison of two-fluid model, dense discrete particle model and CFD-DEM method for modeling impinging gas–solid flows. *Powder Technol.* 254, 94–102. <https://doi.org/10.1016/j.powtec.2013.12.056>
- Cimarelli, C., Costa, A., Mueller, S., Mader, H.M., 2011. Rheology of magmas with bimodal crystal size and shape distributions: Insights from analog experiments. *Geochem. Geophys. Geosystems* 12. <https://doi.org/10.1029/2011GC003606>
- Claeys, I.L., Brady, J.F., 1993. Suspensions of prolate spheroids in Stokes flow. Part 1. Dynamics of a finite number of particles in an unbounded fluid. *J. Fluid Mech.* 251, 411–442. <https://doi.org/10.1017/S0022112093003465>
- Cooper, K.M., Kent, A.J.R., 2014. Rapid remobilization of magma crystals kept in cold storage. *Nature* 506, 480–483.
- Cordonnier, B., Caricchi, L., Pistone, M., Castro, J., Hess, K.-U., Gottschaller, S., Manga, M., Dingwell, D.B., Burlini, L., 2012. The viscous-brittle transition of crystal-bearing silicic melt: Direct observation of magma rupture and healing. *Geology* 40, 611–614. <https://doi.org/10.1130/G3914.1>
- Courrech du Pont, S., Gondret, P., Perrin, B., Rabaud, M., 2003. Wall effects on granular heap stability. *EPL Europhys. Lett.* 61, 492. <https://doi.org/10.1209/epl/i2003-00156-5>
- Coussot, P., Ancey, C., 1999. Rheophysical classification of concentrated suspensions and granular pastes. *Phys. Rev. E* 59, 4445–4457. <https://doi.org/10.1103/PhysRevE.59.4445>
- Cui, X., Li, J., Chan, A., Chapman, D., 2014. Coupled DEM–LBM simulation of internal fluidisation induced by a leaking pipe. *Powder Technol.* 254, 299–306. <https://doi.org/10.1016/j.powtec.2014.01.048>
- Deubelbeiss, Y., Kaus, B.J.P., Connolly, J.A.D., Caricchi, L., 2011. Potential causes for the non-Newtonian rheology of crystal-bearing magmas. *Geochemistry Geophys. Geosystems* 12, Q05007
- Deen, N.G., Annaland, M. van S., Hoef, M.A. van der, Kuipers, J. a. M., 2007. Review of discrete particle modeling of fluidized beds. *Chem. Eng. Sci.* 62, 28–44-. <https://doi.org/10.1016/j.ces.2006.08.014>
- Dellino, P., Mele, D., Bonasia, R., Braia, G., Volpe, L.L., Sulpizio, R., 2005. The analysis of the influence of pumice shape on its terminal velocity. *Geophys. Res. Lett.* 32. <https://doi.org/10.1029/2005GL023954>
- Dioguardi, F., Dellino, P., Mele, D., 2014. Integration of a new shape-dependent particle–fluid drag coefficient law in the multiphase Eulerian–Lagrangian code MFIx-DEM. *Powder Technol.* 260, 68–77. <https://doi.org/10.1016/j.powtec.2014.03.071>
- Faroughi, S.A., Huber, C., 2014. Crowding-based rheological model for suspensions of rigid bimodal-sized particles with interfering size ratios. *Phys. Rev. E* 90, 052303.
- Farr, R.S., Groot, R.D., 2009. Close packing density of polydisperse hard spheres. *J. Chem. Phys.* 131, 244101.
- Fernandez, N., Mani, R., Rinaldi, D., Kadau, D., Mosquet, M., Lombois-Burger, H., Cayer-Barrioz, J., Herrmann, H.J., Spencer, N.D., Isa, L., 2013. Microscopic Mechanism for Shear Thickening of Non-Brownian Suspensions. *Phys. Rev. Lett.* 111, 108301. <https://doi.org/10.1103/PhysRevLett.111.108301>
- Frankel, N.A., Acrivos, A., 1967. On the viscosity of a concentrated suspension of solid spheres. *Chem. Eng. Sci.* 22, 847–853. [https://doi.org/10.1016/0009-2509\(67\)80149-0](https://doi.org/10.1016/0009-2509(67)80149-0)
- Garg, R., Galvin, J., Li, T., Pannala, S., 2012. Open-source MFIx-DEM software for gas–solids flows: Part I—Verification studies. *Powder Technol.* 220, 122–137.
- Garg, R., Galvin, J., Li, T., Pannala, S., 2010. Documentation of open-source MFIx-DEM software for gas–solids flows. URL <https://mfix-netl.doe.gov/documentation/demdoc2012-1> Pdf Accessed 31 March 2014.
- Girard, G., Stix, J., 2009. Buoyant replenishment in silicic magma reservoirs: Experimental approach and implications for magma dynamics, crystal mush remobilization, and eruption. *J. Geophys. Res. Solid Earth* 114, B08203. <https://doi.org/10.1029/2008JB005791>
- Gondret, P., Lance, M., Petit, L., 2002. Bouncing motion of spherical particles in fluids. *Phys. Fluids* 14, 643–652. <https://doi.org/10.1063/1.1427920>
- Gottsmann, J., Lavallée, Y., Martí, J., Aguirre-Díaz, G., 2009. Magma–tectonic interaction and the eruption of silicic batholiths. *Earth Planet. Sci. Lett.* 284, 426–434. <https://doi.org/10.1016/j.epsl.2009.05.008>
- Higgins, M.D., 2006. Verification of ideal semi-logarithmic, lognormal or fractal crystal size distributions from 2D datasets. *J. Volcanol. Geotherm. Res., Modern Trends in Petrography*: 154, 8–16. <https://doi.org/10.1016/j.jvolgeores.2005.09.015>

- Higgins, M.D., Roberge, J., 2003. Crystal Size Distribution of Plagioclase and Amphibole from Soufrière Hills Volcano, Montserrat: Evidence for Dynamic Crystallization–Textural Coarsening Cycles. *J. Petrol.* 44, 1401–1411. <https://doi.org/10.1093/petrology/44.8.1401>
- Hildreth, W., 2004. Volcanological perspectives on Long Valley, Mammoth Mountain, and Mono Craters: several contiguous but discrete systems. *J. Volcanol. Geotherm. Res.* 136, 169–198.
- Janoschek, F., Harting, J., Toschi, F., 2013. Accurate lubrication corrections for spherical and non-spherical particles in discretized fluid simulations. ArXiv13086482 Cond-Mat Physicsphysics.
- Jeffrey, D.J., Onishi, Y., 1984. The forces and couples acting on two nearly touching spheres in low-Reynolds-number flow. *Z. Für Angew. Math. Phys. ZAMP* 35, 634–641. <https://doi.org/10.1007/BF00952109>
- Karlstrom, L., Rudolph, M.L., Manga, M., 2012. Caldera size modulated by the yield stress within a crystal-rich magma reservoir. *Nat. Geosci.* 5, 402–405.
- Kendrick, J.E., Lavallée, Y., Hess, K.-U., Heap, M.J., Gaunt, H.E., Meredith, P.G., Dingwell, D.B., 2013. Tracking the permeable porous network during strain-dependent magmatic flow. *J. Volcanol. Geotherm. Res.* 260, 117–126. <https://doi.org/10.1016/j.jvolgeores.2013.05.012>
- Laumonier, M., Scaillet, B., Arbaret, L., Champallier, R., 2014. Experimental simulation of magma mixing at high pressure. *Lithos* 196–197, 281–300. <https://doi.org/10.1016/j.lithos.2014.02.016>
- Laumonier, M., Scaillet, B., Pichavant, M., Champallier, R., Andújar, J., Arbaret, L., 2013. On the conditions of magma mixing and its bearing on andesite production in the crust. *Nat. Commun.* 5, 12 p. <https://doi.org/10.1038/ncomms6607>
- Lavallée, Y., Benson, P.M., Heap, M.J., Hess, K.-U., Flaws, A., Schillinger, B., Meredith, P.G., Dingwell, D.B., 2013. Reconstructing magma failure and the degassing network of dome-building eruptions. *Geology* 41, 515–518. <https://doi.org/10.1130/G33948.1>
- Lavallée, Y., Hess, K.-U., Cordonnier, B., Dingwell, D.B., 2007. Non-Newtonian rheological law for highly crystalline dome lavas. *Geology* 35, 843–846. <https://doi.org/10.1130/G23594A.1>
- Lavallée, Y., Varley, N., Alatorre-Ibargüenogitia, M., Hess, K.-U., Kueppers, U., Mueller, S., Richard, D., Scheu, B., Spieler, O., Dingwell, D., 2012. Magmatic architecture of dome-building eruptions at Volcán de Colima, Mexico. *Bull. Volcanol.* 74, 249–260.
- Li, T., Garg, R., Galvin, J., Pannala, S., 2012. Open-source MFI-X-DEM software for gas-solids flows: Part II—Validation studies. *Powder Technol.* 220, 138–150.
- Li, T., Pannala, S., Shahnam, M., 2014. Reprint of "CFD simulations of circulating fluidized bed risers, part II, evaluation of differences between 2D and 3D simulations. *Powder Technol., Selected Papers from the 2012 NETL Multiphase Flow Workshop* 265, 13–22. <https://doi.org/10.1016/j.powtec.2014.04.007>
- MacDonald, M.J., Chu, C.-F., Guilloit, P.P., Ng, K.M., 1991. A generalized Blake-Kozeny equation for multisized spherical particles. *AIChE J.* 37, 1583–1588.
- Mader, H.M., Llewellyn, E.W., Mueller, S.P., 2013. The rheology of two-phase magmas: A review and analysis. *J. Volcanol. Geotherm. Res.* 257, 135–158. <https://doi.org/10.1016/j.jvolgeores.2013.02.014>
- Mari, R., Seto, R., Morris, J.F., Denn, M.M., 2014. Shear thickening, frictionless and frictional rheologies in non-Brownian suspensions. *J. Rheol.* 58, 1693–1724. <https://doi.org/10.1122/1.4890747>
- Marsh, B.D., 1988. Crystal size distribution (CSD) in rocks and the kinetics and dynamics of crystallization. *Contrib. Mineral. Petrol.* 99, 277–291. <https://doi.org/10.1007/BF00375362>
- Marzougui, D., Chareyre, B., Chauchat, J., 2015. Microscopic origins of shear stress in dense fluid–grain mixtures. *Granul. Matter* 17, 297–309. <https://doi.org/10.1007/s10035-015-0560-6>
- McIntire Michael Z., Bergantz George W., Schleicher Jillian M., 2019. On the hydrodynamics of crystal clustering. *Philos. Trans. R. Soc. Math. Phys. Eng. Sci.* 377, 20180015. <https://doi.org/10.1098/rsta.2018.0015>
- Michioka, H., Sumita, 2005. Rayleigh-Taylor instability of a particle packed viscous fluid: Implications for a solidifying magma. *Geophys. Res. Lett.* 32. <https://doi.org/10.1029/2004GL021827>
- Moitra, P., Gonnermann, H.M., 2015. Effects of crystal shape- and size-modality on magma rheology. *Geochem. Geophys. Geosystems* 16, 1–26. <https://doi.org/10.1002/2014GC005554>
- Mueller, S., Llewellyn, E.W., Mader, H.M., 2011. The effect of particle shape on suspension viscosity and implications for magmatic flows. *Geophys. Res. Lett.* 38. <https://doi.org/10.1029/2011GL047167>
- Mueller, S., Llewellyn, E.W., Mader, H.M., 2010. The rheology of suspensions of solid particles. *Proc. R. Soc. Lond. Math. Phys. Eng. Sci.* 466, 1201–1228. <https://doi.org/10.1098/rspa.2009.0445>
- Mutabaruka, P., Delenne, J.-Y., Soga, K., Radjai, F., 2014. Initiation of immersed granular avalanches. *Phys. Rev. E* 89, 052203. <https://doi.org/10.1103/PhysRevE.89.052203>
- Ness, C., Sun, J., 2015. Flow regime transitions in dense non-Brownian suspensions: Rheology, microstructural characterization, and constitutive modeling. *Phys. Rev. E* 91, 012201. <https://doi.org/10.1103/PhysRevE.91.012201>
- Ouchiyama, N., Tanaka, T., 2002. Porosity estimation for random packings of spherical particles [WWW Document]. <https://doi.org/10.1021/i100016a019>
- Pallister, J.S., Hoblitt, R.P., Reyes, A.G., 1992. A basalt trigger for the 1991 eruptions of Pinatubo volcano? *Nature* 356, 426–428. <https://doi.org/10.1038/356426a0>
- Peirano, E., Delloume, V., Leckner, B., 2001. Two- or three-dimensional simulations of turbulent gas–solid flows applied to fluidization. *Chem. Eng. Sci.* 56, 4787–4799. [https://doi.org/10.1016/S0009-2509\(01\)00141-5](https://doi.org/10.1016/S0009-2509(01)00141-5)
- Petford, N., 2009. Which effective viscosity? *Mineral. Mag.* 73, 167–191. <https://doi.org/10.1180/minmag.2009.073.2.167>

-
- Picard, D., Arbaret, L., Pichavant, M., Champallier, R., Launeau, P., 2011. Rheology and microstructure of experimentally deformed plagioclase suspensions. *Geology* 39, 747–750. <https://doi.org/10.1130/G32217.1>
- Ryerson, F.J., Weed, H.C., Piwinski, A.J., 1988. Rheology of subliquidus magmas: 1. Picritic compositions. *J. Geophys. Res. Solid Earth* 93, 3421–3436. <https://doi.org/10.1029/JB093iB04p03421>
- Schleicher, J.M., Bergantz, G.W., 2017. The Mechanics and Temporal Evolution of an Open-system Magmatic Intrusion into a Crystal-rich Magma. *J. Petrol.* 58, 1059–1072. <https://doi.org/10.1093/petrology/egx045>
- Schleicher, J.M., Bergantz, G.W., Breidenthal, R.E., Burgisser, A., 2016. Time scales of crystal mixing in magma mushes. *Geophys. Res. Lett.* 43, 1543–1550. <https://doi.org/10.1002/2015GL067372>
- Sparks, R.S.J., 2003. Forecasting volcanic eruptions. *Earth Planet. Sci. Lett.* 210, 1–15. [https://doi.org/10.1016/S0012-821X\(03\)00124-9](https://doi.org/10.1016/S0012-821X(03)00124-9)
- Syamlal, M., 1998. MFIK documentation numerical technique. EG and G Technical Services of West Virginia, Inc., Morgantown, WV (United States).
- Syamlal, M., Rogers, W., O'Brien, T.J., 1993. MFIK documentation theory guide. USDOE Morgantown Energy Technology Center, WV (United States).
- Tomoya, A., Takeuchi, S., 2009. Two-Stage Magma Mixing and Initial Phase of the 1667 Plinian Eruption of Tarumai Volcano. AGU Fall Meet. Abstr. 51.

Supplementary Section S3.1:

This Supplementary section discusses the meaning of the particle relative velocity, v_p , and the incidence angle, β , for a multiparticle system.

Neither drag nor buoyancy depends directly on the topology of neighboring particles dynamics. The total lubrication force for a given particle, however, is the sum of all the pair interactions between that particle and its neighbors. Each particle pair is characterized by its own relative velocity, v_p , and incidence angle, β . The representative v_p of a particle corresponds to the difference between the particle velocity and the average velocity of its neighbors. It represents the velocity unsteadiness within the solids phase and corresponds to a measure of the energy fluctuation within the granular phase, which is often referred to as granular temperature (Andreotti et al., 2013; Goldhirsch, 2008). Formally, the parameter v_p we use corresponds to the square root of the classical definition of granular temperature, which suggests that lubrication effects could be taken into account in continuum models based on kinetic theory.

The physical meaning of the representative incidence angle β is less obvious. This angle varies between 0° for pure normal motion to 90° for pure tangential motion. It does not indicate the orientation of the particle relative motion and it thus cannot be used to gather information on the microstructural organization of the solids like, for instance, the contact fabric tensor (e.g. Bergantz et al., 2017). The importance of the angle β on the position of the point where all the forces are equal on the force diagram is weak except when this angle tends to be purely tangential (Fig. 3.8). This situation never happens in our simulations because average β ranges from

approximately 55° and 8° (Fig. 3.4 A). This variation of β had a negligible influence on the relative importance of lubrication forces as quantified by our scaling.

Supplementary Section S3.2: List of the model equations

This Supplementary section includes two tables summarizing the equation system solved in our numerical simulations (Tables S3.2.1–S3.2.2).

Table S3.2.1: List of the equations implemented in the CFD-DEM model

Equation names	Equations	Ref.	Experiments
Fluid constitutive equations (continuous formulation)			
Mass conservation	$\frac{\partial \varepsilon_f}{\partial t} + \nabla \cdot (\varepsilon_f \vec{v}_f) = 0$	1	[1, 2]
Momentum conservation	$\rho_f \left(\frac{\partial}{\partial t} (\varepsilon_f \vec{v}_f) + \nabla \cdot (\varepsilon_f \vec{v}_f \otimes \vec{v}_f) \right) = \nabla \cdot (\bar{\sigma}_f) + \varepsilon_f \rho_f \vec{g} + \vec{I}_f$	1	[1, 2]
Stress tensor	$\bar{\sigma}_f = P_f \delta_{ij} + \frac{2}{3} \eta_f \text{tr}(\bar{\varepsilon}_f) \delta_{ij} + 2 \eta_f \bar{\varepsilon}_f$	1	[1, 2]
DEM: solids time evolution integration (Discrete formulation)			
For each k^{th} particle of the system			
Euler velocity integration	$\vec{v}_p^{(k)}(t + \Delta t) = \vec{v}_p^{(k)}(t) + \frac{\vec{F}_D^{(k)}(t) + \sum_{l=1}^{N_l^{(k)}} \left(\vec{F}_c^{N^{(k,l)}}(t) + \vec{F}_c^{T^{(k,l)}}(t) \right)}{m^{(k)}} + \vec{g}$	2	[1, 2]
Euler displacement integration	$\vec{X}_p^{(k)}(t + \Delta t) = \vec{X}_p^{(k)}(t) + \Delta t \vec{v}_p^{(k)}(t + \Delta t)$	2	[1, 2]
Euler rotation integration	$\vec{\omega}_p^{(k)}(t + \Delta t) = \vec{\omega}_p^{(k)}(t) + \Delta t \frac{\sum_{l=1}^{N_l^{(k)}} \left(\vec{T}_c^{N^{(k,l)}} + \vec{T}_c^{L^{(k,l)}}(t) \right)}{I^{(k)}}$	2	[1, 2]
DEM: solids-solids interactions			
Interactions considered between two particles i and j ($d_i > d_j$)			
Normal contact force	$\vec{F}_c^N^{(i,j)}(t) = \left(-k_n^{(i,j)}(t) \delta_n^{(i,j)}(t) + \eta_n^{(i,j)}(t) \Delta V_p^N^{(i,j)}(t) \right) \vec{n}_{ij}$	2 5	[1, 2]
Tangential contact force	$\vec{F}_c^T^{(i,j)}(t) = -k_t^{(i,j)}(t) \delta_t^{(i,j)}(t) + \eta_t^{(i,j)}(t) \Delta V_p^T^{(i,j)}(t)$	2 5	[1, 2]
Collisional torque	$\vec{T}_c^{(i,j)}(t) = \frac{d_p^{(i)} - \delta_n^{(i,j)}(t)}{2} \vec{F}_c^T^{(i,j)}(t) ; \vec{T}_c^{(j,i)}(t) = \frac{d_p^{(j)} - \delta_n^{(i,j)}(t)}{2} \vec{F}_c^T^{(i,j)}(t)$	2	[1, 2]

Equation names	Equations	Ref.	Experiments
normal spring (Hertzian model)	$k_n^{(i,j)}(t) = \frac{4}{3} \frac{E^{(i)} E^{(j)} \sqrt{R_{eff}^{(i,j)}}}{E^{(i)} (1 - \sigma^{(i)^2}) + E^{(j)} (1 - \sigma^{(j)^2})} \delta_n^{(i,j)\frac{1}{2}}(t)$	2	[1, 2]
tangential spring (Hertzian model)	$k_t^{(i,j)}(t) = \frac{16}{3} \frac{G^{(i)} G^{(j)} \sqrt{R_{eff}^{(i,j)}}}{G^{(i)} (2 - \sigma^{(i)}) + G^{(j)} (2 - \sigma^{(j)})} \delta_t^{(i,j)\frac{1}{2}}(t)$	2	[1, 2]
Elastic modulus	$G = \frac{E}{2(1 + \sigma)}$	2	[1, 2]
Normal damping coefficient	$\eta_n^{(i,j)}(t) = \frac{2 \sqrt{m_{eff}^{(i,j)} k_n^{(i,j)}(t) \ln e_n }}{\sqrt{\pi^2 + \ln^2 e_n}} \delta_n^{(i,j)}(t)^{\frac{1}{4}}$	2 5	[1, 2]
Tangential damping coefficient	$\eta_t^{(i,j)} = \frac{2 \sqrt{m_{eff}^{(i,j)} k_t^{(i,j)}(t) \ln e_t }}{\sqrt{\pi^2 + \ln^2 e_t}} \delta_t^{(i,j)}(t)^{\frac{1}{4}}$	2 5	[1, 2]
effective radius	$R_{eff}^{(i,j)} = \frac{2(d_p^{(i)} + d_p^{(j)})}{d_p^{(i)} d_p^{(j)}}$	2	[1, 2]
Effective mass	$m_{eff}^{(i,j)} = \frac{m^{(i)} + m^{(j)}}{m^{(i)} m^{(j)}}$	2	[1, 2]
Normal lubrication force component	$F_L^N{}^{(i,j)}(t) = \frac{2 \pi \eta_f (d^{(i)} + d^{(j)})^2}{32 (h^{(i,j)}(t) + \varepsilon)} v_n(t)$	6	
Tangential lubrication force component	$F_L^T{}^{(i,j)}(t) = \frac{\pi \eta_f}{2} \left[-\frac{(d^{(i)} + d^{(j)})}{2} + \left(\frac{(d^{(i)} + d^{(j)})}{2} + (h^{(i,j)}(t) + \varepsilon) \right) \ln \left(\frac{(d^{(i)} + d^{(j)}) + 2(h^{(i,j)}(t) + \varepsilon)}{2(h^{(i,j)}(t) + \varepsilon)} \right) \right] v_t(t)$	6	
Total lubrication force	$F_L^{tot (i)}(t) = -F_L^{tot (j)}(t) = F_L^N{}^{(i,j)}(t) + F_L^T{}^{(i,j)}(t)$	6	
Total lubrication torque	$T_L^{(i)}(t) = -T_L^{(j)}(t) = \frac{d^{(i)} + (h^{(i,j)}(t) + \varepsilon)}{2} F_L^T{}^{(i,j)}(t)$	6	
DEM: Fluid-solids coupling (Discrete formulation)			
For each particle of the system			
Solids/Fluid momentum exchange on REV	$\vec{I}_f(t) = \frac{1}{v_{REV}} \sum_{k=1}^{N_k} \vec{F}_D^{(k)}(t) K_{REV}(X_p^{(k)})$	2	[1, 2]
Drag forces	$\vec{F}_D^{(k)}(t) = -\nabla P_f(t) \left(\frac{\pi}{6} d_p^{(k)3} \right) + \frac{\beta_{fs}^{(k)}(t)}{(1 - \varepsilon_f(t))} \left(\frac{\pi}{6} d_p^{(k)3} \right) (\vec{v}_f(t) - \vec{v}_p^{(k)}(t))$	2	[1, 2]

Equation names	Equations	Ref.	Experiments
Local fluid/solid momentum transfer	$\beta_{fs}^{(k)}(t) = \begin{cases} \frac{3}{4} C_D^{(k)}(t) \frac{\rho_f \varepsilon_f(t) (1 - \varepsilon_f)}{d_p^{(k)}} \ \vec{v}_f - \vec{v}_s^{(k)}\ \varepsilon_f^{-2.65} & \varepsilon_f \geq 0.8 \\ \frac{150 (1 - \varepsilon_f(t))^2 \eta_f}{\varepsilon_f(t) d_p^{(k)^2} + \frac{1.75 \rho_f (1 - \varepsilon_f(t)) \ \vec{v}_f(t) - \vec{v}_s^{(k)}(t)\ }{d_p^{(k)}}} & \varepsilon_f < 0.8 \end{cases}$	3 4	[1, 2]
Drag coefficient	$C_D^{(k)}(t) = \begin{cases} \frac{24}{Re^{(k)}(t)(1 + 0.15 Re^{(k)}(t)^{0.687})} & Re^{(k)}(t) < 1000 \\ 0.44 & Re^{(k)}(t) \geq 1000 \end{cases}$	3 4	[1, 2]
Dimensionless number			
Reynolds number	$Re^{(k)}(t) = \frac{d_m^{(k)} \ \vec{v}_f(t) - \vec{v}_s^{(k)}(t)\ \rho_f}{\eta_f}$	3	[1, 2]

¹ Syamlal et al., (1993)

² Garg et al., (2010)

³ Benyahia et al., (2012)

⁴ Gidaspow, (1986)

⁵ MFIx code

⁶ Marzougui et al., (2015)

Symbol	Definition
$C_D^{(k)}$	Drag coefficient of the k th particle
$d_p^{(i)}$	i th particle diameter
e_n	Particle normal restitution coefficient
e_t	Particle tangential restitution coefficient
$E^{(i)}$	i th particle Young modulus
$\vec{F}_c^{N(k,l)}$	Normal contact force between k th particle and its l th neighbor
$\vec{F}_c^{T(k,l)}$	Tangential contact forces between k th particle and its l th neighbor
$\vec{F}_D^{(k)}$	Drag force on k th particle
\vec{g}	Gravitational vector (m s ⁻²)
$G^{(k)}$	k th particle shear moduli
$h^{(i,j)}$	Distance between i th and j th particles edges
\vec{I}_f	Fluid-solid momentum exchange
$I^{(k)}$	k th particle moment of inertia
K_{REM}	Generic kernel to determine the influence of a particle located at $\vec{X}_p^{(k)}$ on the REV
$k_n^{(i,j)}$	Normal spring coefficient between i th and j th particles contact

$k_t^{(i,j)}$	Tangential spring coefficient between i^{th} and j^{th} particles contact
l	Neighbors index
$m^{(k)}$	k^{th} particle mass
$m_{eff}^{(i,j)}$	i^{th} and j^{th} particles effective radius
$N_l^{(k)}$	Number of neighbors of the k^{th} particle
N_k	Number of particles
$\overline{n}_{i,j}$	Normal vector between i^{th} and j^{th} particles
P_f	Fluid pressure (Pa)
REV	Representative elementary volume
$Re^{(k)}$	i^{th} particle Reynolds number
$R_{eff}^{(i,j)}$	i^{th} and j^{th} particles effective radius
$R_*^{(i,j)}$	Contact area radius between i^{th} and j^{th} particles
$\overline{T}_C^{(k,l)}$	Contact torque between k^{th} particle and its l^{th} neighbor
$\overline{T}_L^{(k,l)}$	Lubrication torque between k^{th} particle and its l^{th} neighbor
\vec{v}_f	Fluid velocity vector (m s ⁻¹)
$\overline{v}_p^{(k)}$	k^{th} particle velocity vector (m s ⁻¹)
$\overline{X}_p^{(k)}$	k^{th} particle position (m)
$\beta_{fs}^{(k)}$	k^{th} particle – fluid momentum transfer coefficient
$\Delta V_p^N(i,j)$	Normal relative velocity between i^{th} and j^{th} particles
$\Delta V_p^T(i,j)$	Tangential relative velocity between i^{th} and j^{th} particles
δ_{ij}	Kronecker tensor
$\delta_n^{(i,j)}$	Normal overlap between i^{th} and j^{th} particles
$\delta_t^{(i,j)}$	Tangential displacement during the contact between i^{th} and j^{th} particles contact
ε	Roughness distance below which lubrication is ineffective (m)
ε_f	Fluid volume fraction
ε_f	Fluid strain rate tensor
η_f	Fluid viscosity (Pa s)
$\eta_n^{(i,j)}$	Normal damping coefficient between i^{th} and j^{th} particles
$\eta_t^{(i,j)}$	Tangential damping coefficient between i^{th} and j^{th} particles
v	Domain volume (m ³)
ρ_f	Fluid density (kg m ⁻³)
$\sigma^{(i)}$	i^{th} particle Poisson coefficient
σ_f	Fluid stress tensor
$\overline{\omega}_p^{(k)}$	k^{th} particle rotation vector (rad s ⁻¹)
∇	Nabla operator
\otimes	Outer product

Table S3.2.2 : Symbols used in Table S1.

Supplementary Section S3.3:

This Supplementary section presents the validation experience and results to validate our implementation of lubrication forces.

The CFD-DEM approach is a parameterized method, in which the fluid cells are larger than particle sizes and the forces exerted by the fluid depend on fluid properties interpolated at the particle location. Our additions to this parameterized approach need to be validated to ensure results reliability. We validated our implementation of lubrication into MFIX by reproducing particle rebound experiments performed by Gondret et al. (2002). The experiments consisted of a sphere immersed in a viscous fluid and falling under the effect of gravity until it rebounds on a flat surface. The authors calculated the effective restitution coefficient of each rebound, which corresponds to the ratio of the particle velocity just before and after the contact occurring in wet condition normalized by the dry restitution coefficient. Results are sorted as a function of the collisional Stokes number used by the authors, $St = (\rho_p d_p v) / (18 \eta_f)$. When $St > 1$, the particle motion is controlled by its inertia whereas for $St < 1$, the surrounding fluid tends to dominate particle trajectory and behavior (Burgisser et al., 2005). Experimental results of Gondret et al. (2002) show that the effective restitution coefficient is affected by the presence of fluid when $St < 10^3$ (Fig. S1). When $St < 10$, the fluid effect is so important that no rebound was measurable. We performed numerical experiments with the particles and fluid properties from Gondret et al. (2002). Each case was run twice, the first one with lubrication and the second one without. Results show that our model outputs match the experimental data (Fig. S3.3.1). This validates our implementation of lubrication forces and shows that the model reproduces realistic contacts between particles immersed in a fluid.

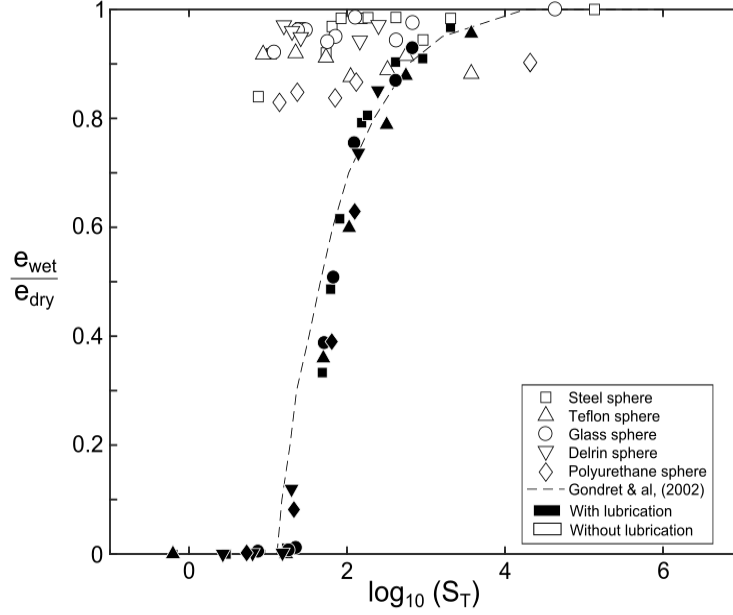


Figure S3.3.1: Validation of the lubrication forces implementation by reproducing experiments from Gondret et al. (2002). The abscissa is the decimal logarithm of the collisional Stokes number. The ordinate is the effective restitution coefficient defined as the ratio of the measured restitution coefficient in wet condition over the dry restitution coefficient. Each glyph represents a numerical simulation. The symbol shape depends on the sphere material, the black filling indicates the run with lubrication and the white filling the run without. A fit of the experimental results obtained by Gondret et al., (2002) is displayed as a dashed curve.

Supplementary Section S3.4:

This Supplementary section presents the steps to transform Eq. (3.1) to Eq. (3.11)

The dimensional Lagrangian BBO equation, which describes the motion of a particle in a dense suspension, is expressed in Eq. (3.1). We introduce in it the following dimensionless quantities:

$$\widetilde{v}_{p1} = \frac{v_{p1}}{v_0}; \quad \widetilde{v}_f = \frac{v_f}{v_0}; \quad \widetilde{v}_p = \frac{v_p}{v_0}; \quad \widetilde{\Delta\rho} = \frac{\Delta\rho}{\rho_0}; \quad \widetilde{\rho}_p = \frac{\rho_p}{\rho_0}; \quad \widetilde{t} = \frac{t}{\tau}; \quad \widetilde{d}_p = \frac{d_p}{\delta}; \quad \widetilde{\eta}_f = \frac{\eta_f}{\eta_0}; \quad \widetilde{g} = \frac{g}{g_0} \quad (\text{S3.4.1})$$

where \widetilde{v}_{p1} , \widetilde{v}_f and \widetilde{v}_p correspond to the dimensionless forms of the velocities involved in Eq. (3.1). Variables $\widetilde{\Delta\rho}$, $\widetilde{\rho}_p$, \widetilde{t} , \widetilde{d}_p , $\widetilde{\eta}_f$, and \widetilde{g} are the dimensionless density contrast, particle density, time, particle diameter, fluid viscosity and gravitational acceleration, respectively. Variables v_0 , ρ_0 , δ , τ , η_0 , and g_0 represent the characteristic speed, density, distance, time, viscosity and gravitational acceleration, respectively. Introducing the dimensionless variables into Eq. (3.1) yields:

$$\frac{v_0^2}{\delta} \frac{d \widetilde{v}_{p1}}{d \widetilde{t}} = \frac{\widetilde{\Delta\rho} \rho_0 \widetilde{g} g_0}{\widetilde{\rho}_p \rho_0} - \frac{3 \widetilde{\eta}_f \eta_0 \widetilde{v}_f v_0}{2 \alpha \widetilde{\rho}_p \rho_0 \widetilde{d}_p^2 \delta^2} - \frac{3 \widetilde{\eta}_f \eta_0 \widetilde{v}_p v_0 A}{\widetilde{\rho}_p \rho_0 \widetilde{d}_p^2 \delta^2}. \quad (\text{S3.4.2})$$

Defining $\rho_0 = \rho_p$, $\tau = \delta/v_0$, $\eta_0 = \eta_f$, and $g_0 = g$, gives:

$$\widetilde{\Delta\rho} = \frac{\Delta\rho}{\rho_p} ; \widetilde{\rho_p} = 1 ; \widetilde{t} = \frac{t v_0}{\delta} ; \widetilde{\eta_f} = 1 ; \widetilde{g} = 1, \quad (\text{S3.4.3})$$

and

$$\frac{v_0^2}{\delta} \frac{d \widetilde{v_{p1}}}{d \widetilde{t}} = \frac{\Delta\rho g}{\rho_p} - \frac{3 \eta_f \widetilde{v_f} v_0}{2 \alpha \rho_p \widetilde{d_p}^2 \delta^2} - \frac{3 \eta_f \widetilde{v_p} v_0 A}{\rho_p \widetilde{d_p}^2 \delta^2}. \quad (\text{S3.4.4})$$

Replacing $\widetilde{d_p}^2 \delta^2$ by d_p^2 and moving the term v_0^2/δ from the right-hand side to the left-hand side yields:

$$\frac{d \widetilde{v_{p1}}}{d \widetilde{t}} = \frac{\Delta\rho g \delta}{\rho_p v_0^2} - \frac{3 \eta_f \widetilde{v_f} \delta}{2 \alpha \rho_p d_p^2 v_0} - \frac{3 \eta_f \widetilde{v_p} \delta A}{\rho_p d_p^2 v_0}. \quad (\text{S3.4.5})$$

Equation (S3.4.5) can also be expressed as:

$$\frac{d \widetilde{v_{p1}}}{d \widetilde{t}} = \frac{1}{F_R^2} - \frac{\widetilde{v_f}}{S_T} - \frac{\widetilde{v_p}}{S_O}, \quad (\text{S3.4.6})$$

with:

$$F_R^2 = \frac{\rho_p v_0^2}{\Delta\rho g \delta}, \quad (\text{S3.4.7a})$$

$$S_T = \frac{2 \alpha \rho_p d_p^2 v_0}{3 \eta_f \delta}, \quad (\text{S3.4.7b})$$

$$S_O = \frac{\rho_p d_p^2 v_0}{3 \eta_f A \delta}. \quad (\text{S3.4.7c})$$

Supplementary Section S3.5:

This Supplementary section explores the possibility to resolve implicitly lubrication interactions in CFD-DEM models.

Previous CFD-DEM works involving dense suspensions have taken lubrication effects into account by artificially decreasing the dry contact restitution coefficients (i.e. the proportion of the kinetic energy conserved during contact) between particles to unrealistic low values (typical below 0.1) (Bergantz et al., 2015; Schleicher et al., 2016; Schleicher and Bergantz, 2017). Our results indicate that lubrication forces affect the simulation dynamics when the solids are close to jamming. The strongest lubrication effects are produced by the resistance of the carrier phase to the expansion of the discrete solid phase. This process does not involve any contacts, so one can expect that lowering the contact restitution coefficients would poorly mimic the effect of having explicit lubrication forces. We tested this assumption by running both experiments 1 and 2 with low restitution coefficients. Surprisingly, results show that time delays of bed sedimentation and bed remobilization caused by the presence of lubrication forces are also present with low restitution coefficients (Fig. 3.3 and S3.5.1). We tested the relationship between delay and restitution coefficients by running two simulations similar to simulation 2A except that lubrications forces were mimicked by two distinct low restitution coefficients (Table S3.1). The delays are inversely proportional to the value of the restitution coefficients (Fig. S3.5.1 B–C).

The initial expansion produced by either the injection (experiment 1) or the return flow of the fluid (experiment 2) imposes an additional stress on the surrounding particle bed. We observed that this stress is distributed within the particle bed thanks to particle contacts and the loading of contact force chains (Fig S3.5.2). When restitution coefficients are decreased, contact durations are longer, and force chains can accommodate more stress before any strain occurs. This mechanism is the most likely cause of the delays observed in the runs with low restitutions coefficients. Our results indicate that, in the case explored herein, lowering restitution coefficients is a valid approach to mimic the belated initiation of motion of the particle bed caused by lubrication. The generality of this approach must be tested for other applications.

Run	η_f (Pa s)	d_p (m)	ρ_p (kg m ⁻³)	ρ_f (kg m ⁻³)	bed size (m × m)	e_n	e_t	injection width (m)	injection velocity (m s ⁻¹)	lubricatio n
2A	0.2	$4 \pm 0.2 \cdot 10^{-3}$	3300	2650	0.96×0.40	0.7	0.35	0.16	0.023	yes
SEA	0.2	$4 \pm 0.2 \cdot 10^{-3}$	3300	2650	0.96×0.40	0.01	0.005	0.16	0.023	No
SEB	0.2	$4 \pm 0.2 \cdot 10^{-3}$	3300	2650	0.96×0.40	0.1	0.05	0.16	0.023	No

Table S3: Parameters used for the simulations involving the injection of a crystal-free basalt inside a basaltic mush.

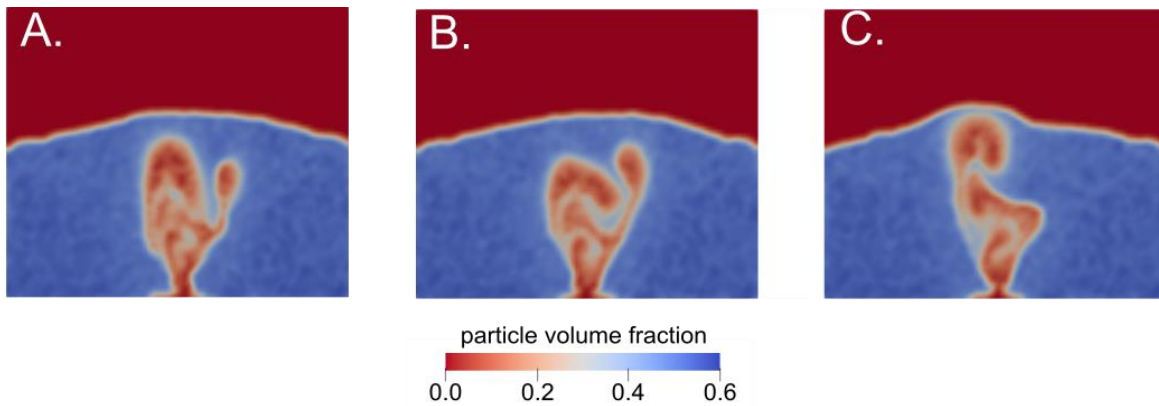


Figure S3.5.1: Snapshots of experiment 2A simulations with lubrication and two simulations that mimic it. All simulations are displayed at the same time step after 9.8 s of injection. The color code indicates the local particle volume fraction. [A] Simulation involving lubrication (2A) [B] – [C] Simulations that mimic lubrication by reducing restitution coefficients to $e_n = 0.01$ (run SEA) and $e_n = 0.1$ (run SEB), respectively.

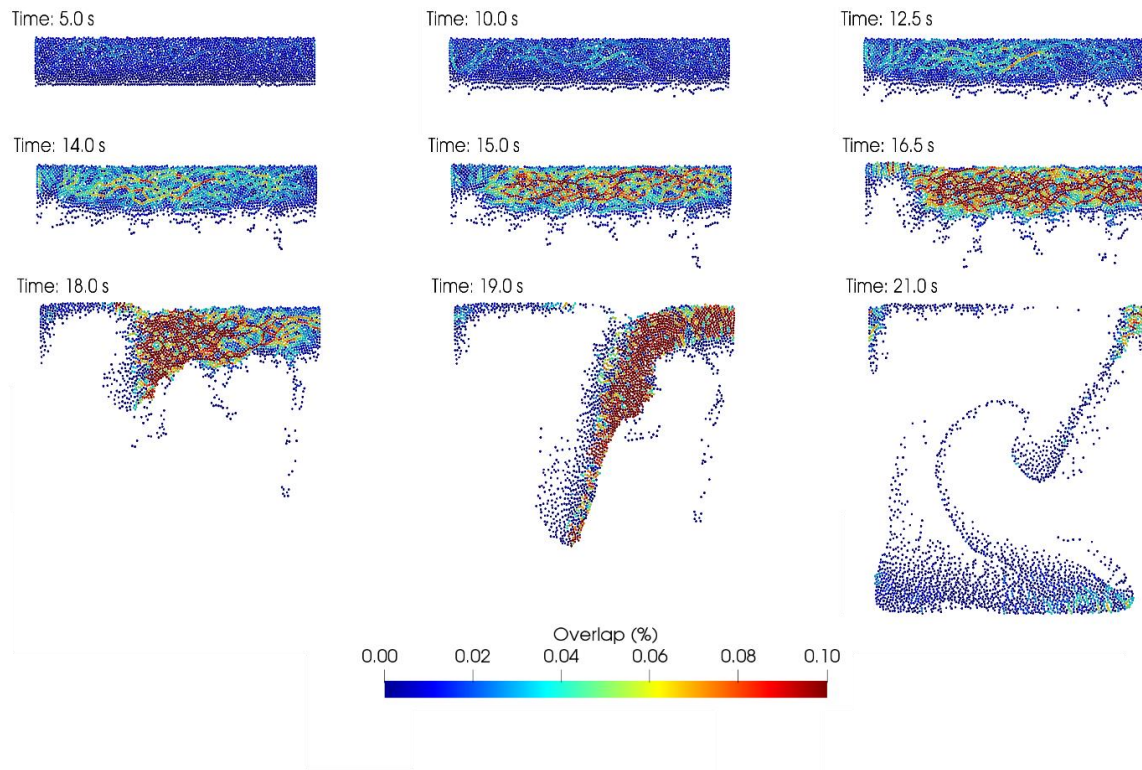


Figure S3.5.2: Evolution of the particle overlaps. Each disk represents a particle on run 1A. The color depends on the maximum overlap between the particle and its neighbors. The maximum overlap percentage indicates the loading applied to the particles force chains. For each particle the percentage of overlap is taken as the maximum overlap distance between the particle and its neighbors divided by the particle diameter ($= 100 (\max(\delta_n) / d_p)$).

Additional references:

- Benyahia, S., Syamlal, M., O'Brien, T.J., 2012. Summary of MFIx equations 2012-1. URL https://mfix.netl.doe.gov/download/mfix/mfix_current_documentation/MFIFEquations2012-1.pdf. Accessed 31 August 2018.
- Gidaspow, D., 1986. Hydrodynamics of Fluidization and Heat Transfer: Supercomputer Modeling. *Appl. Mech. Rev.* 39, 1–23. <https://doi.org/10.1115/1.3143702>
- Goldhirsch, I., 2008. Introduction to granular temperature. *Powder Technol., Granular Temperature* 182, 130–136. <https://doi.org/10.1016/j.powtec.2007.12.002>

Chapter 4: CFD-DEM modeling of recharge events within mush¹²

4.1. Introduction

Injections of new magmas, also called recharge events, are ubiquitous in magmatic systems. They are inferred to cause the formation of long-lived, supersolidus magmatic reservoirs located in the upper crust (Annen et al., 2006; Annen and Sparks, 2002; Karakas et al., 2017). The injection of hotter magma into a cooler resident system is also identified as a common scenario to trigger volcanic eruptions. Caricchi et al. (2014) showed that the long-term supply rate in new magma and time between successive recharge events control the sizes and frequency of eruptions. The associated eruptive products show that the host and the injected materials can either completely mix (e.g. Nakagawa et al., 2002; Pallister et al., 1992), or only display limited or absent mixing (e.g. Bachmann et al., 2002; Eichelberger and Izbekov, 2000; Takahashi and Nakagawa, 2013). The ubiquity of recharge events and the large diversity of possible outcomes raise questions about the link between the dynamic behavior of an intrusion and its ability to trigger a volcanic eruption.

A number of evidences show that shallow silicic reservoirs reside most time in a mush state because of the rapid cooling and crystallization of the emplaced magma (e.g. Bachmann and Huber, 2016; Cashman et al., 2017, and reference therein). A magmatic mush is a crystal-rich magma in which crystals are in frictional contacts, forming a semi-rigid framework that supports force chains (Bergantz et al., 2017), which inhibit the ability of the magma to erupt. Together with the thermal structure of the upper crust and the frequency of recharges, the geometry and mode of emplacement of the intruded magma were identified as having a crucial effect on its cooling rate, which in turn controls the long-term evolution of igneous bodies (Annen et al., 2015). The rock record shows that parts of magmatic systems are regularly fed by both mafic and silicic magmas (e.g. Wiebe, 2016). Intrusion style also has a fundamental role in the way mush rejuvenates (process of recycling the mush to generate an eruptible magma) prior to eruption (Parmigiani et al., 2014, and references

¹² This chapter is currently prepared for submission as a research article to Earth and Planetary Science Letters as: Carrara, A., Burgisser, A., Bergantz, G.W., CFD-DEM modeling of recharge event within mush.

therein). Several rejuvenation scenarios assume that the intruder is emplaced as sills at the base of the mush, and rejuvenate it by supplying heat, and possibly exsolved volatiles, without penetration of the intruded material within the mush except bubbles (Bachmann and Bergantz, 2006; Bergantz, 1989; Burgisser and Bergantz, 2011; Couch et al., 2001; Huber et al., 2011). Other scenarios consider that the injected magma may penetrate the mush, producing various degrees of mixing with the resident mush depending on its buoyant acceleration (e.g. Bergantz and Breidenthal, 2001; Koyaguchi and Kaneko, 2000; Weinberg and Leitch, 1998).

An essential physical process is that the melt and crystals constituting a mush may decouple from each other. Pioneering numerical simulations explicitly accounting for such decoupling as well as the building and destruction of force chains between crystals focused on basaltic mush dynamics (Bergantz et al., 2015; Schleicher et al., 2016; Schleicher and Bergantz, 2017). They have revealed that the local injection of pure melt of the same density and viscosity as the mush interstitial melt may fluidize, penetrate, and mix with the overlying mush. This is restricting the scope of the rejuvenation scenarios based on the emplacement of an underlying mafic gravity current (Snyder and Tait, 1995) by suggesting that underplating may require contrasts in melt densities and/or viscosities to hinder fluidization. As mush dynamics differs from that of pure fluids, previous explorations of the controls of underplating and rejuvenation (e.g. Turner and Campbell, 1986) cannot be directly used to determine the dynamical regimes fostering. It is thus important to identify the parameters controlling the unfolding of an intrusion event in order to improve our understanding of how mush processes are linked to the evolution of magmatic systems.

To constraint the short-term behavior of a recharge event, we performed numerical simulations using a combination of fluid mechanics and discrete elements (Bergantz et al., 2015; Schleicher et al., 2016; Schleicher and Bergantz, 2017) and explored different parameters controlling the dynamics of the intruded material when injected into a mush. We first introduce the numerical model and the modifications we implemented to be able to replicate conditions prevailing in chemically evolved magmas. We define the dimensionless parameters controlling recharge dynamics that are varied in the simulations. Successive runs were performed by varying the contrasts between the physical properties of the two magmas (viscosity and density of the two melts), and injection rate of the intruder. Results of the numerical simulations are then presented in the framework of the dimensionless parameters. Finally, we discuss the assumptions made in

our model and their expected influences on our results as well as the implications of our results on the dynamics of magmatic reservoir and mush rejuvenation.

Symbol (unit)	Definition
d_p (m)	Particle diameter
E (Pa)	Particle Young modulus
\vec{F}_{GPD} (N)	Gravity-Pressure-Drag force
\vec{g} (m s ⁻²)	Gravity acceleration vector
H_{bed} (m)	Particle bed thickness
H_{max} (m)	Intruded layer maximum height above the inlet
H^*	Dimensionless height of the intruded volume
m_p (kg)	Particle mass
P (Pa)	Fluid pressure
R (m)	Intruder batch radius
t^*	Reduced time
U_{inj} (m s ⁻¹)	Injection superficial velocity
U_{mf} (m s ⁻¹)	Minimum fluidization superficial velocity
U^*	Dimensionless injection velocity
\vec{v}_f (m s ⁻¹)	Fluid velocity vector
\vec{v}_p (m s ⁻¹)	Particle velocity vector
W_{inj} (m)	Injection width
ρ_f (kg m ⁻³)	Fluid density
η (Pa s)	Fluid dynamic viscosity
τ_v (s)	Particle viscous response time
β (kg s ⁻¹)	Momentum transfer coefficient
Δt (s)	DEM time step
η (Pa s)	Fluid dynamic viscosity
η_i (Pa s)	Intruder melt dynamic viscosity
η_h (Pa s)	Host melt dynamic viscosity
η^*	Melts dynamic viscosity ratio
μ	Particle friction coefficient
ρ_h (kg m ⁻³)	Host melt density
ρ_i (kg m ⁻³)	Intruder melt density
ρ_p (kg m ⁻³)	Average density of the particles
ρ^*	Melts reduced buoyancy
ρ_b^*	Melts bulk reduced buoyancy
σ	Poisson coefficient
τ_v (s)	Particle viscous response time
Φ	Solid volume fraction

Table 4.1: List of symbols and their meaning

4.2 Method

4.2.1 Numerical method

We performed Computational-Fluid-Dynamic and Discrete-Element-Method (CFD-DEM) numerical simulations by using the MFIX-DEM software (<https://mfix.netl.doe.gov/>). The equations used in this chapter are summarized in the supplementary section S4.1. Details about the theory and implementation of the model can be found in Garg et al. (2010), Syamlal (1998), Syamlal et al. (1993), and validation of the DEM approaches in Garg et al. (2012) and Li et al. (2012). To ensure stability of the simulations, the classical DEM integration scheme imposes to use time steps shorter than the characteristic durations of the physical processes controlling the crystal motions, which are here contact durations and drag characteristic time. When increasing melt viscosity, the particle viscous response time, τ_v (time for the particle to adapt to changes in the fluid velocity) decreases, which results in short DEM time steps and impractically long computations. As the flows simulated are in the laminar regime and the particle Reynolds numbers are also well below the transition to turbulence (Furuichi and Nishiura, 2014), the drag force exerted by the fluid on the particles as well as gravity and pressure forces were calculated using an alternative approach instead of the usual numerical evaluation (Garg et al., 2012).

In the absence of particle contacts, the equation of motion for the solids reads:

$$\frac{d \vec{v}_p}{dt} = -\frac{\nabla P}{\rho_p} + \vec{g} + \frac{\beta}{\Phi \rho_p} (\vec{v}_f - \vec{v}_p), \quad (4.1)$$

where \vec{v}_p is the particle velocity vector, P is the fluid pressure, ρ_p is the crystal density, Φ is the particle volume fraction, β is the momentum exchange coefficient, \vec{v}_f is the fluid velocity vector, and \vec{g} is the gravitational acceleration vector. The first term in the right hand side of Eq. (4.1) is the pressure force, which includes the particle buoyancy. The last term expresses the drag force that depends on the relative motions of the particles compared to the fluid, and on the momentum transfer coefficient, which is parameterized using the Gidaspow drag model (Gidaspow, 1994). For mushy conditions, inertial effects may be neglected, and β reduces to the Kozeny-Carman relationship:

$$\beta = \frac{150 \Phi^2 \eta}{(1-\Phi) d_p^2}, \quad (4.2)$$

where η is the fluid dynamic viscosity, and d_p is the particle diameter. Similarly to Bergantz et al. (2017), the particle response time is defined as $\tau_v = \Phi \rho_p / \beta$. At low Reynolds and Stokes numbers, τ_v is shorter than the fluid characteristic time, which means that the fluid velocity and pressure gradient within Eq. (4.1) may be considered constant during the acceleration of the particle in response to a change in its environment. Consequently, equation (4.1) reduces to a first order ordinary differential equation having as solution:

$$\vec{v}_p(t) = \vec{v}_{p0} e^{-\frac{t}{\tau_v}} + \left(\vec{v}_f + \tau_v \left(\vec{g} - \frac{\nabla P}{\rho_p} \right) \right) \left(1 - e^{-\frac{t}{\tau_v}} \right), \quad (4.3)$$

where \vec{v}_{p0} is an initial particle velocity vector. The effective force, \vec{F}_{GPD} , needed to get from the velocity at time t_0 to that a DEM time step, Δt , later is:

$$\vec{F}_{GPD}(t_0) = \frac{m_p}{\Delta t} \left(\vec{v}_p(t_0 + \Delta t) - \vec{v}_p(t_0) \right), \quad (4.4)$$

where m_p is the mass of the particle. Setting $\vec{v}_{p0} = \vec{v}_p(t)$ in Eq. (4.3), $\vec{F}_{GPD}(t_0)$ becomes:

$$\vec{F}_{GPD}(t_0) = \frac{m_p}{\Delta t} \left(\vec{v}_f(t_0) + \tau_v \left(\vec{g} - \frac{\nabla P(t_0)}{\rho_p} \right) - \vec{v}_p(t_0) \right) \left(1 - e^{-\frac{\Delta t}{\tau_v}} \right). \quad (4.5)$$

Equation (4.5) presents the advantage to depend on the DEM time step instead of on a stability criterion. The DEM time steps are far larger than those stemming from the classical numerical integration of Eq. (4.1), which significantly decreases the computational costs. Our approach represents a compromise between the usual DEM approach that resolves the particles acceleration in time and the approach given in Furuichi and Nishiura, (2014), which assumes that the particles jump to their terminal velocities at the next time step. When $\Delta t \gg \tau_v$, Eq. (4.5) returns the force needed for the particle to jump its terminal velocity at the next time step. When $\Delta t < \tau_v$, Eq (4.5) is able to recover the evolution of the particle velocity in time. We implemented Eq. (4.5) in place of MFIx's classical evaluations of the gravitational, pressure and drag forces, and left unchanged the computations of the contact forces and of the averaging of the drag forces exerted by the particles on the fluid.

4.2.2 Numerical setup and experiments

The computational domain is a 3D medium of $1.6 \times 0.8 \times 0.05$ m (length \times height \times width) filled with a resident melt (Fig. 4.1). We created a mush layer of ~ 0.3 m height with an initial crystal content of ~ 0.64 by simulating the settling of the particles in a vacuum and positioning them at the base of the domain. We used the same density for all particles ($\rho_p = 3300$ kg m⁻³) and three different diameters (4.5, 5, and 5.5 mm) to avoid artificial clustering. All simulations use the same initial particle bed. A crystal-free magma is injected at the base of the mush layer with a superficial vertical velocity, U_{inj} , through an inlet having a width, W_{inj} . The density and the viscosity of the injected melt are kept constant between all the simulations ($\rho_i = 2500$ kg m⁻³; $\eta_i = 1$ Pa s, see table 4.2 for the list of the parameters kept constant in the chapter). We used a conduit of 3.2 cm in height to supply the inlet to ensure that the intruder enters the mush as a Poiseuille flow. At the top of the domain, we used a pressure outflow boundary conditions to ensure the overall mass conservation within the entire domain. The boundary conditions at the front and back of the domain are cyclical, which means that the intruder corresponds to a dyke having one infinite dimension. All the other boundary conditions are non-slip walls (Fig 4.1). For simplicity, thermal effects are ignored.

We performed two sets of numerical simulations to explore the influence of the host melt density, the host melt viscosity, and the injection velocity on the dynamics of a melt intrusion in a mush (See Table 4.3 for a list of all the simulations and the corresponding parameters). The first set of 25 simulations (A1–A25, Table 4.3) explores the influence of the density and the viscosity contrasts between the two magmas. For these simulations, the injection velocities are such that the ratio with the respective minimum fluidization velocity, U_{mf} , remains constant at $U_{inj}/U_{mf}=21.2$. This ratio is chosen to match that used previously in similar works (Schleicher et al., 2016; Schleicher and Bergantz, 2017) according to the formula presented in the supplementary section S4.2. The second set of experiments encompasses 4 simulations and explores the influence of the injection velocity on the intrusion dynamics by varying the ratio U_{inj}/U_{mf} while keeping the same host and intruded materials. We used run A25 as a reference for the physical properties of the host, which is the simulation that presents the largest density and viscosity contrasts between the two melts.

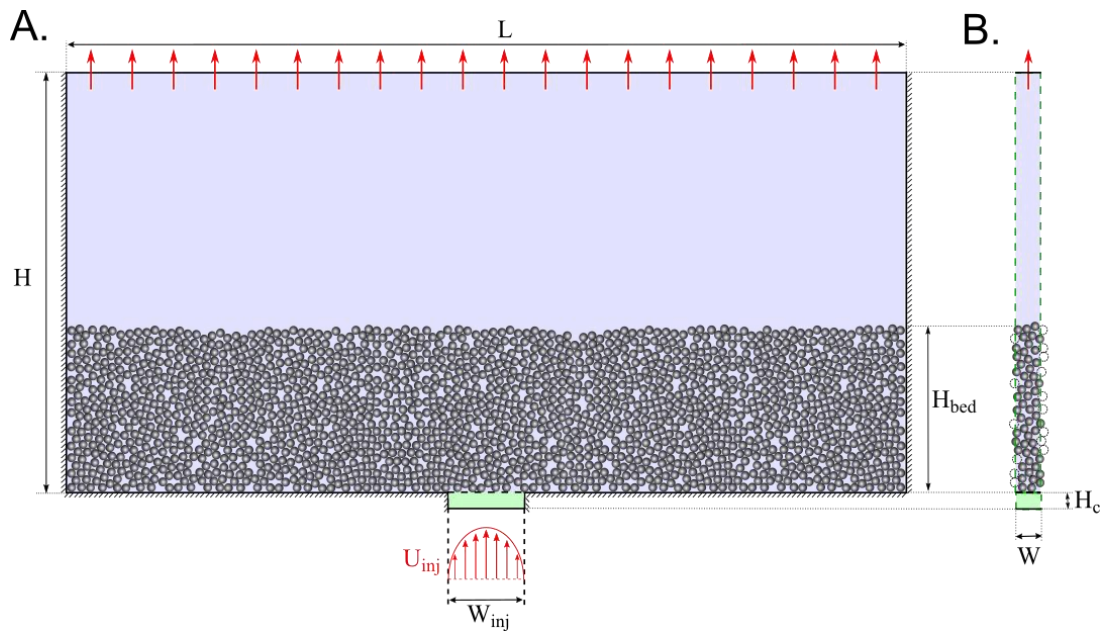


Figure 4.1: Numerical setup. [A] The drawing represents the computational domain viewed from the front. The medium is composed by a rectangular box, which is fed by a conduit at its base. Particles are settled to generate a particle bed having a thickness H_{bed} . The background colors indicates which fluid is present initially in the computational domain. The blue color corresponds to the host melt and the green color to the intruded melt. The red arrows below the conduit represent the velocity profile of the injected fluid (Poiseuille flow). The arrows atop the domain indicate that the boundary condition is a fixed pressure outflow. The hatched walls indicate non-slip boundary conditions. [B] Side view of the computational domain. The green dashed lines indicate that cyclical boundary conditions are used for these walls. The dotted circles indicate particles overlapping with one of the two cyclical boundary conditions and that are also considered to be present on the opposite side.

4.2.3 Dimensionless parameters

In order to compare simulations, we used dimensionless quantities to scale the effects of the contrasts in densities and viscosities, and injection velocities. The injection velocity and melt viscosity control the stress applied by the input of new materials to the mush. These parameters enter the minimum fluidization velocity, U_{mf} (Schleicher et al., 2016, see supplementary material S4.2 for derivation of U_{mf}), which expresses the minimum superficial velocity required for the injection to entrain the host solids and generate the fluidization of the particle bed (Cui et al., 2014; Shi et al., 1984). As the injected melt differs from the host melt, two minimum fluidization velocities can be calculated depending on which melt is considered. For all simulations, we used the minimum of these two velocities, which here always corresponds to that using the host melt properties. The dimensionless injection velocity, U^* , is defined as:

$$U^* = \frac{U_{inj}}{U_{mf}}. \quad (4.5)$$

In simulations having identical U^* , the injection imposes the same stress to the overlying mush. However, the time needed to inject the same new melt volume changes between simulations because U_{mf} varies. We thus used a dimensionless time, t^* , to scale the simulation time (Bergantz et al., 2017):

$$t^* = \frac{t U_{inj}}{H_{bed}}, \quad (4.6)$$

where t is the simulation time. In this way, for identical t^* , the same volumes of intruder are injected and simulation results can be compared directly.

The density contrast between the two materials is scaled using the reduced buoyancy of the intruder. A negative reduced buoyancy indicates that the intruder is buoyant compared to the mush, whereas a positive one indicates a tendency to sink. Two reduced buoyancies may be defined. The first one, ρ^* , expresses the buoyancy contrast between the two melts:

$$\rho^* = \frac{\rho_i - \rho_h}{\rho_i}, \quad (4.7)$$

where ρ_i is the density of the intruded melt, and ρ_h is the host melt density. The second one, ρ_b^* , takes the presence of crystals in the host material into account and scales the bulk densities:

$$\rho_b^* = \frac{\rho_i - (\rho_h (1-\Phi) + \rho_p \Phi)}{\rho_i}, \quad (4.8)$$

Parameter	Value or range
ρ_p	3300 kg m ⁻³
d_p	4.5-5.5 mm
Nb crystals	208495
H_{bed}	0.3 m
W_{inj}	0.1 m
ρ_i	2500 kg m ⁻³
η_i	1 Pa s
E	2 10 ⁷ Pa
σ	0.32
μ	0.3

Table 4.2: Parameters kept constant during the parametric study

where ρ_p is the density of the host solids, and Φ is the particle volume fraction. The viscosity contrast, η^* , between the two melts is expressed as:

$$\eta^* = \frac{\eta_h}{\eta_i}, \quad (4.9)$$

where η_h is the host dynamic viscosity and η_i is that of the injected melt.

Run nb.	ρ_h (kg m ⁻³)	$\rho_b(host)$ (kg m ⁻³)	ρ^*	ρ_b^*	η^*	U_{mf} (m s ⁻¹)	U_{inj} (m s ⁻¹)
A1	2500	3012	0	-0.2048	1	2.956 10 ⁻⁴	6.268 10 ⁻³
A2	2500	3012	0	-0.2048	5	5.913 10 ⁻⁵	1.254 10 ⁻³
A3	2500	3012	0	-0.2048	10	2.957 10 ⁻⁵	6.268 10 ⁻⁴
A4	2500	3012	0	-0.2048	50	5.913 10 ⁻⁶	1.254 10 ⁻⁴
A5	2500	3012	0	-0.2048	100	2.957 10 ⁻⁶	6.268 10 ⁻⁵
A6	2450	2994	0.02	-0.1976	1	3.141 10 ⁻⁴	6.660 10 ⁻³
A7	2450	2994	0.02	-0.1976	5	6.283 10 ⁻⁵	1.332 10 ⁻³
A8	2450	2994	0.02	-0.1976	10	3.141 10 ⁻⁵	6.660 10 ⁻⁴
A9	2450	2994	0.02	-0.1976	50	6.283 10 ⁻⁶	1.332 10 ⁻⁴
A10	2450	2994	0.02	-0.1976	100	3.141 10 ⁻⁶	6.660 10 ⁻⁵
A11	2550	3030	-0.02	-0.212	1	2.772 10 ⁻⁴	5.876 10 ⁻³
A12	2550	3030	-0.02	-0.212	5	5.544 10 ⁻⁵	1.175 10 ⁻³
A13	2550	3030	-0.02	-0.212	10	2.772 10 ⁻⁵	5.876 10 ⁻⁴
A14	2550	3030	-0.02	-0.212	50	5.544 10 ⁻⁶	1.175 10 ⁻⁴
A15	2550	3030	-0.02	-0.212	100	2.772 10 ⁻⁶	5.876 10 ⁻⁵
A16	2200	2904	0.12	-0.1616	1	4.065 10 ⁻⁴	8.618 10 ⁻³
A17	2200	2904	0.12	-0.1616	5	8.130 10 ⁻⁵	1.724 10 ⁻³
A18	2200	2904	0.12	-0.1616	10	4.065 10 ⁻⁵	8.618 10 ⁻⁴
A19	2200	2904	0.12	-0.1616	50	8.130 10 ⁻⁶	1.724 10 ⁻⁴
A20	2200	2904	0.12	-0.1616	100	4.065 10 ⁻⁶	8.618 10 ⁻⁵
A21	2150	2886	0.14	-0.1544	1	4.250 10 ⁻⁴	9.010 10 ⁻³
A22	2150	2886	0.14	-0.1544	5	8.500 10 ⁻⁴	1.802 10 ⁻³
A23	2150	2886	0.14	-0.1544	10	4.250 10 ⁻⁵	9.010 10 ⁻⁴
A24	2150	2886	0.14	-0.1544	50	8.500 10 ⁻⁶	1.802 10 ⁻⁴
A25	2150	2886	0.14	-0.1544	100	4.250 10 ⁻⁶	9.010 10 ⁻⁵
B1	2150	2886	0.14	-0.1544	100	4.250 10 ⁻⁶	4.250 10 ⁻³
B2	2150	2886	0.14	-0.1544	100	4.250 10 ⁻⁶	4.250 10 ⁻²
B3	2150	2886	0.14	-0.1544	100	4.250 10 ⁻⁶	4.250 10 ⁻¹
B4	2150	2886	0.14	-0.1544	100	4.250 10 ⁻⁶	4.250 10 ⁰

Table 4.3: List of the simulation performed for this chapter and corresponding variables.

4.3 Results

4.3.1 Effect of buoyancy and viscosity contrasts

We observed three intrusion regimes at $U^*=21.2$, depending on the host physical properties. The *fluidization* regime was observed in the simulations A1–5, and consists in the development of a fluidized area above the inlet in which the intruded melt rises through the mush (Fig. 4.2), as described previously (Bergantz et al., 2015; Schleicher et al., 2016, Chapter 3). The fluidization of the mush is initiated by the initial overpressure at the inlet that destabilizes locally the force chains and separates the crystals in contact (dark blue regions in Fig. 4.2 that represent small to no particle overlap). The fluidized volume grows vertically above the inlet because of two mechanisms. The first is the upward entrainment of the particles localized above the fluidized cavity, which results in bulging the top surface of the mush layer (Fig. 4.2). The second mechanism is the progressive erosion of the crystals jammed at the boundary between the mush and the fluidized volume, which progressively destabilizes the overlying force chains. Once separated, the crystals start to settle in the fluidized area. Because of this process of mush erosion, the fluidized area ascends faster than the intruded melt (green outline in Fig 4.2). The intruder flows mainly vertically with a minor lateral porous flow. When the fluidized cavity reaches the top of the particles bed, its width progressively decreases to stabilize in the shape of a vertical chimney. At steady state, when $t^*>1$, the crystals located within the chimney show both upward and downward motions whereas the ones located around the chimney flow slowly in the direction of the inlet, forming a ‘mixing bowl’ as a whole (Bergantz et al., 2015).

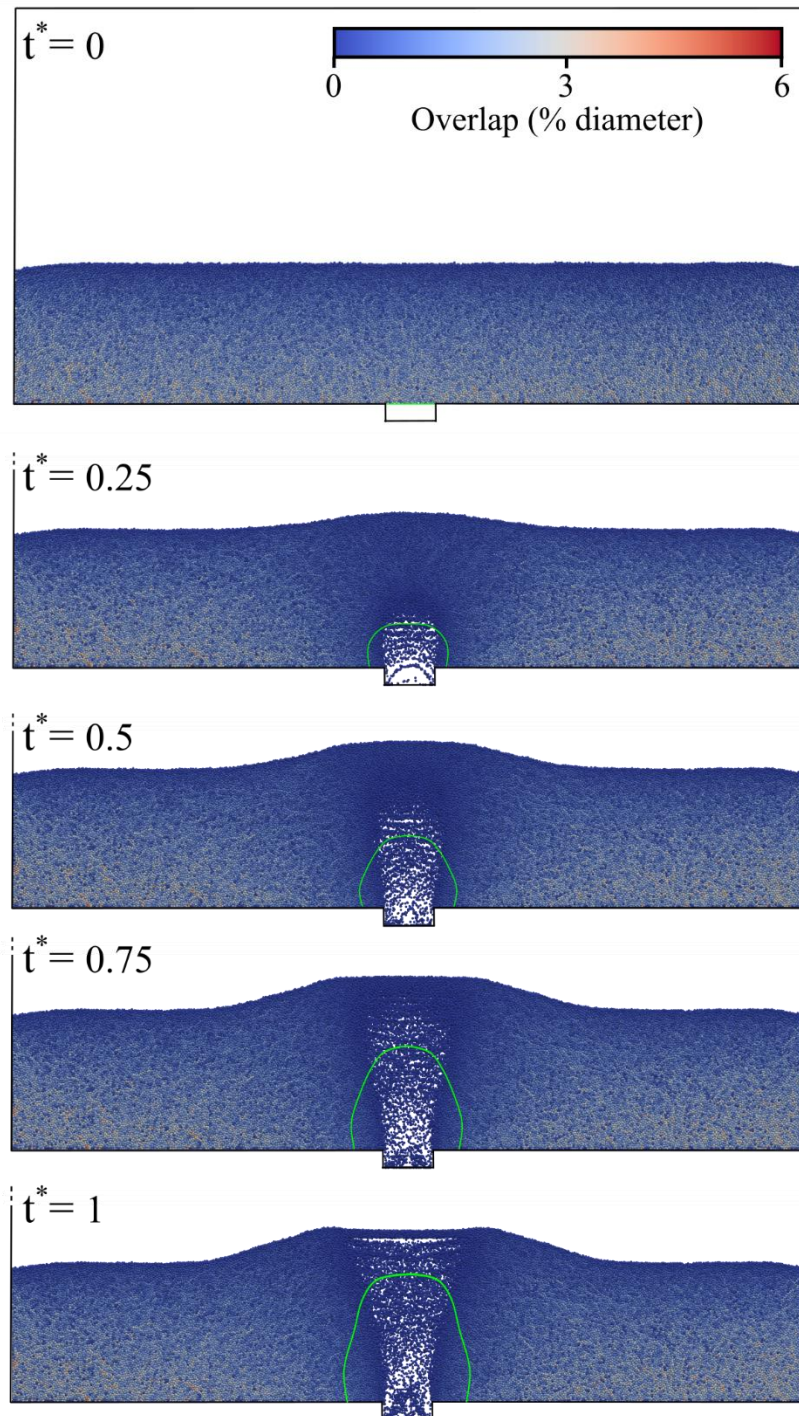


Figure 4.2 Snapshots of simulation A1 illustrating the fluidization regime. Each section represents the particles at different reduced times. For each particle, the color depends on the maximum overlap distance with its neighbors. The green curves represent the boundary between injected and host melts.

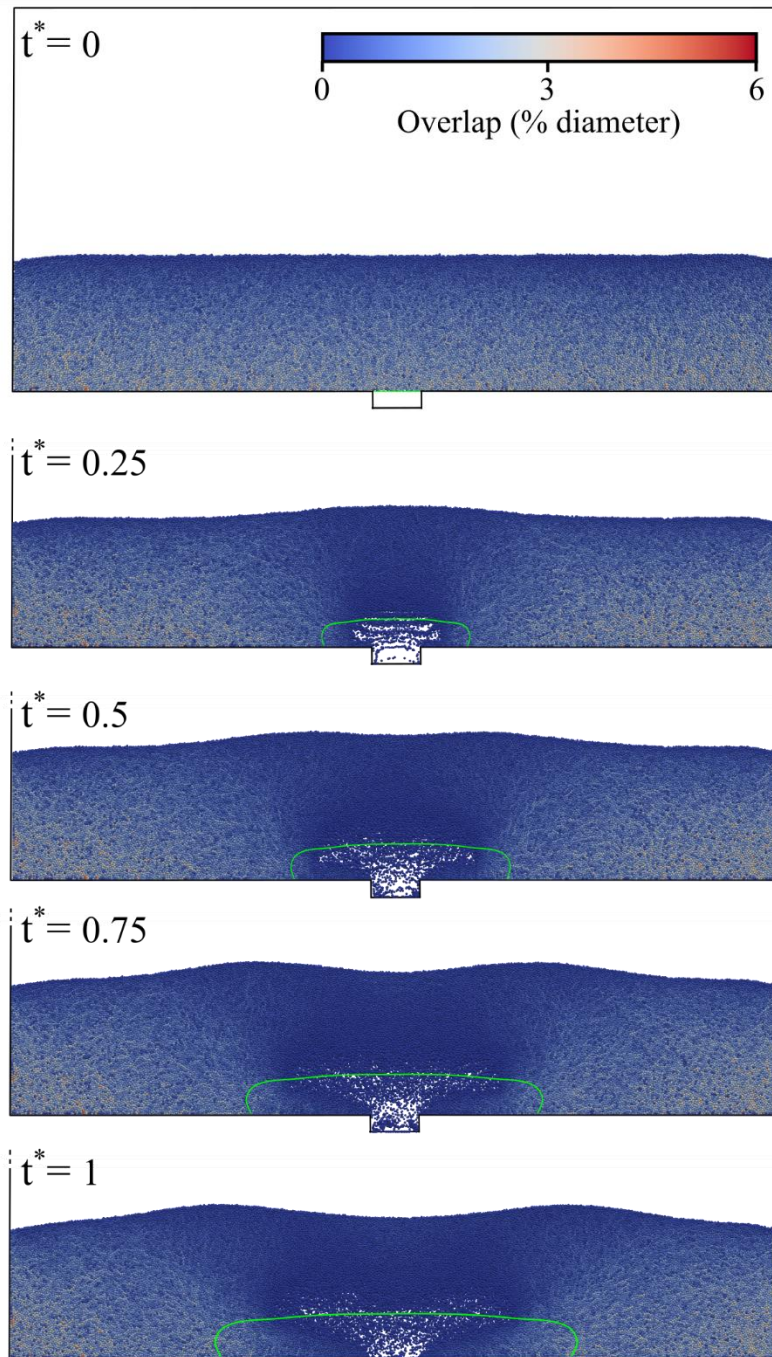


Figure 4.3 Snapshots of simulation A6 illustrating the lateral spreading regime with the same conventions as Fig. 4.2.

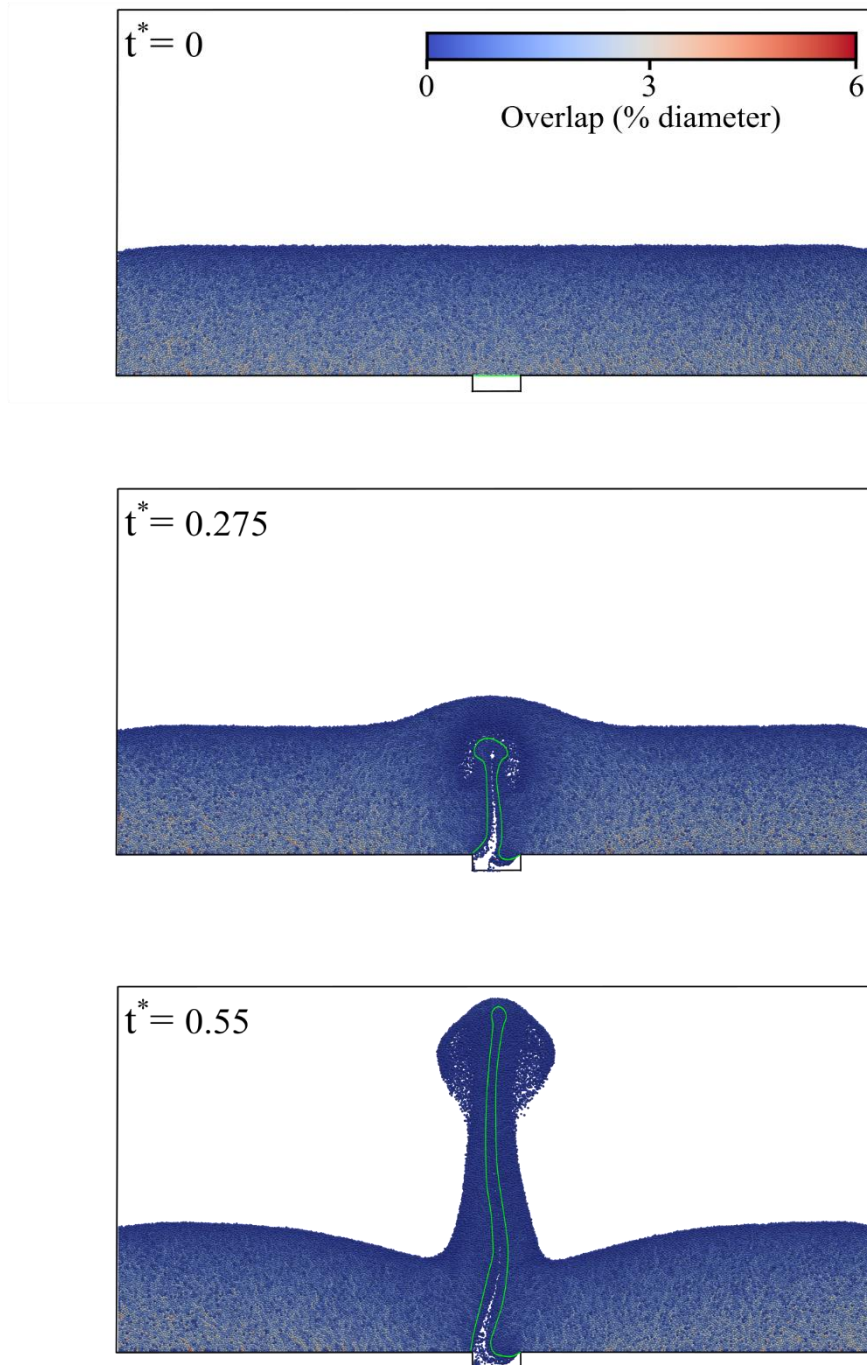


Figure 4.4: Snapshots of simulation A11 illustrating the rising regime with the same conventions as Fig. 4.2.

The *spreading* regime, which prevails in simulations A6–10 and A16–25, is characterized by the lateral spreading of the injected melt similarly to a gravity current hugging the floor of the host reservoir (Fig. 4.3). The flow of the intruded melt is able to entrain laterally the host particles, creating two counter rotating granular vortexes with downward motions above the inlet. The initial overpressure at the inlet and the Reynolds dilatancy (dilation of a granular material when strained; Andreotti et al., 2013, pp 130-131) initiated by the lateral flow of the intruder are both able to destabilize the force chains in the overlying mush (dark blue regions in Fig. 4.3 that represent small to no particle overlap). The fluidized volume grows either predominantly laterally or vertically, depending on the relative importance between the lateral entrainment of the host solids by the intruder and the vertical settling of the mush crystals.

The *rising* regime, or tunneling (Bergantz and Breidenthal, 2001), is characterized by the ascent of the intruded melt within the mush that occurred in simulations A11–15 (Fig. 4.4). Runs start with the initial growth above the inlet of a cavity filled with the intruded fluid. The cavity becomes gravitationally unstable and ascends within the mush. The ascent of the intruder continues above the particle bed, entraining solids from the host. A small fluidized volume is present around the head of the ascending batch (Fig. 4.4). The dimensionless time at which the intrusion reaches the mush top ($t^* \sim 0.3$) is shorter than that of the two other regimes because of the gravitational instability that significantly accelerates the transport of the intruder.

Figure 4.5 plots the simulations with $U^* = 21.2$ as functions of the dimensionless quantities ρ^* , ρ_b^* , and η^* . It shows that the three intrusion regimes can be classified uniquely as a function of the reduced buoyancy between the two melts, ρ^* . When $\rho_i = \rho_h$, the fluidization regime is observed. If $\rho_i > \rho_h$, the spreading regime occurs, whereas if $\rho_i < \rho_h$, the rising regime occurs. Perhaps surprisingly, the bulk buoyancy contrast is not helpful to predict the behavior of the intruder (Fig. 4.5). The amount of viscosity contrasts does not control the intrusion flowing regime, but strengthens its influence on the mush dynamics. Figure 4.6 illustrates how viscosity influences the flow patterns. In the fluidization regime, the increase of the host viscosity enhances the formation of crystal-poor batches at the top of the intruded volume (Fig. 4.6 A–C). Because the minimum fluidization velocity within the intruded melt is lower than for the host, the crystals are not fluidized and sediment in the intruded melt to accumulate atop the inlet (Fig 4.6 A–C). However, in this regime, the increase in the host melt viscosity do not affect the volume of mush showing a decrease in crystal volume fraction and distortion of the forces chains. In the spreading

regime, the viscosity contrast enhances the lateral spreading of the intruder and the entrainment of the host crystals in the two counter rotating vortices (Fig 4.6 D–F). Large host melt viscosity causes the lateral entrainment of the solids to be more efficient than particle settling, which results in the elongation of the fluidized volume in the horizontal direction (Fig 4.6 D–F). In the rising regime, increasing the viscosity contrast enlarges the vortices sizes and the separation distance between their centers (Fig 4.6 G–I). The dimensionless time, t^* , at which the intruder instability occurs decreases with the viscosity of the host. However, the volume of the mush remobilized by the intruder flow does not significantly vary with the host melt viscosity (Fig 4.6 G–I).

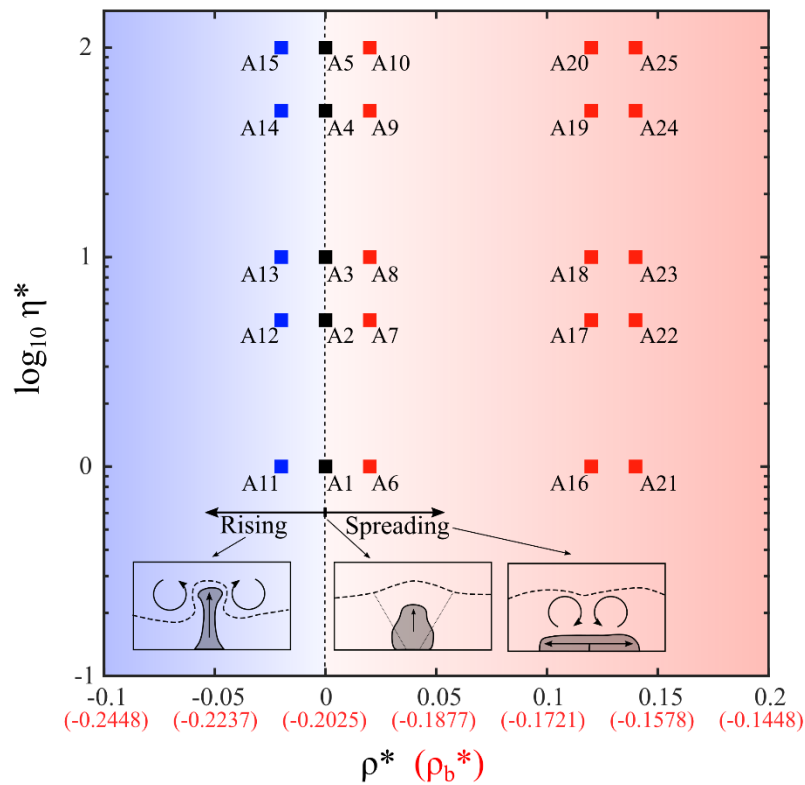


Figure 4.5: Regime diagram of intrusion behavior for low U^* . The diagram represents the positions of the simulations A 1–25 as functions of the reduced buoyancy (abscissa) and viscosity ratios (ordinate). Each square represents a simulation. Square colors depend on the observed regime (blue=rising; black=fluidization; red=lateral spreading). Similarly, the background color interpolates the observed regimes (blue= rising; red=lateral spreading) and the vertical dashed line interpolates where the fluidization is expected to prevail.

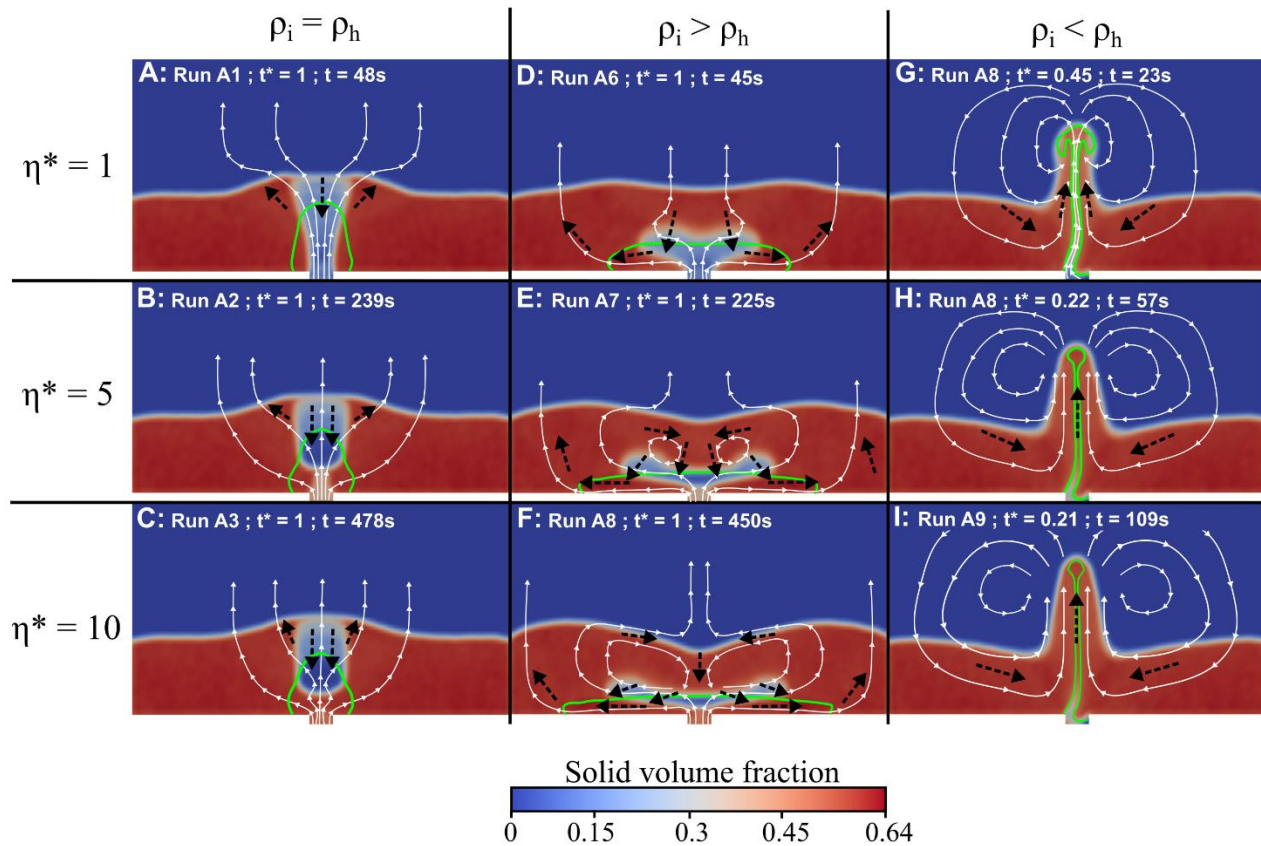


Figure 4.6: Comparison of the effects of buoyancy and viscosity contrasts. Each section represents the advancement of the simulation at $t^*=1$ (or when the rising instability is above the particle bed). The injected melt contours are indicated with green curves. The dashed black arrows indicate the presence and direction of granular flows. The thin white curves indicate the fluid streamlines with small arrowheads indicating flow direction.

4.3.2 Injection velocity

Figure 4.7 displays snapshots of simulations B1–3 for varying t^* and U^* . It shows that at $t^* = 0.1$, all simulations display similar results where the intruder cavity expands mainly vertically (Fig 4.7 A–C). At $t^* = 0.25$, the injection at the lower rate (B1) has started to spread laterally (Fig 4.7 D), whereas the two others rates (B2–B3) grow radially in a similar fashion (Fig 4.7 E–F). Simulations B2 and B3 start to differentiate when $t^* > 0.5$. From this point on, the intruder spreads laterally in simulation B2, which stops its vertical propagation (Fig 4.7 H, K, and N). On the contrary, simulation B3 continues to grow radially without significant lateral spreading (Fig 4.7 I, L, and O). In simulations B1–B2, the maximum height reached by the intruded volume, H_{max} , remains constant once the lateral spreading is fully established (Fig 4.7). Despite the fact that all the simulations share the same intruder shape before the lateral spreading takes place, the sizes of

the regions affected by dilatancy (shown as grey halos surrounding the intruder volume on Fig. 4.7) increase with U^* (Fig. 4.7 A–C and E–F).

When the simulation is dominated by the injection rate, the theoretical maximum height reached by the intruded volume, H_{max} , may be predicted analytically as a function of time. We consider two end-members for the growth of the intrusion volume (vertical or radial). The first end member considers the vertical ascent (dyking) of the intruded melt above the inlet over a width,

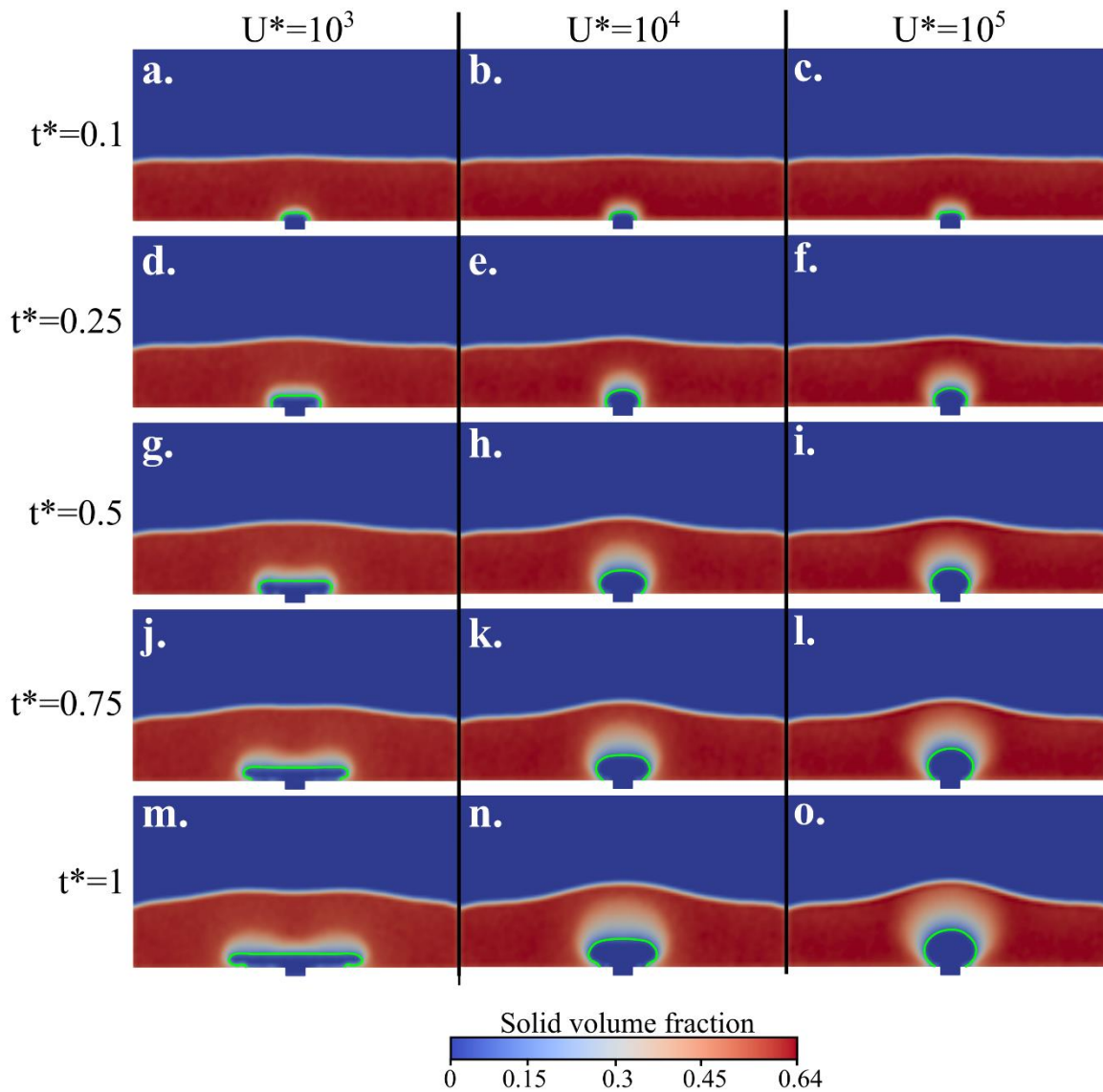


Figure 4.7: Effect of injection velocity on the behavior of the intruder. Snapshots are from simulations B 1–3 ($U^*=10^3$, 10^4 , and 10^5 , respectively) at different t^* . Discrete particles are not represented; colors indicate instead the averaged crystallinity of each fluid cell. Green curves indicate the contour of the intruded melt.

W_{inj} . In this case, the ratio, H^* , between H_{max} and the initial particle bed thickness, H_{bed} ($H^* = H_{max}/H_{bed}$), reads:

$$H^* = t^*. \quad (4.9)$$

For a purely radial growth, H_{max} may be computed as a function of t^* by solving the following system of nonlinear equations (See supplementary section S4.3 for derivation of Eq. 4.10):

$$\begin{cases} 0 = W_{inj} H_{bed} t^* + \frac{2}{3} W_{inj} (2R - H_{max}) + \frac{(2R - H_{max})^3}{2 W_{inj}} - \pi R^2 \\ 0 = (H_{max} - R)^2 + \frac{W_{inj}^2}{4} - R^2 \end{cases}, \quad (4.10)$$

where R is the unknown radius of the spherical batch (note that $2R \neq H_{max}$ because of the presence of the inlet).

Figure 4.8 displays the comparison between the temporal evolution of the theoretical H^* for the two end-member growth scenarios alongside the results of simulations A25 and B1–4. For $t^* < 0.25$, the four simulations B1–4 collapse with the predicted H^* for a vertical intrusion, whereas the simulation A25 spreads purely laterally. Simulation B1 starts to differentiate from B2–4 at $t^* \approx 0.25$ and its height stalls at $H^* \approx 0.2$. Simulation B2 follows a different trend from that of B3–4 after $t^* \approx 0.4$ and its intrusion height stabilizes at $H^* \approx 0.45$. In simulations B3–4, the measured H^* collapse on the same curve as the prediction for a radial growth after $t^* \approx 0.5$. After $t^* = 1.5$, measured and predicted maximum heights start to separate in simulation B3 because of the adverse effect of buoyancy. However, the intrusion is able to reach $H^* = 1$ at $t^* \approx 3.5$. This is unlike simulation B4, which strictly follows the theoretical curve for a radial growth and reaches $H^* = 1$ at $t^* \approx 2.5$, as predicted by Eq. (4.10).

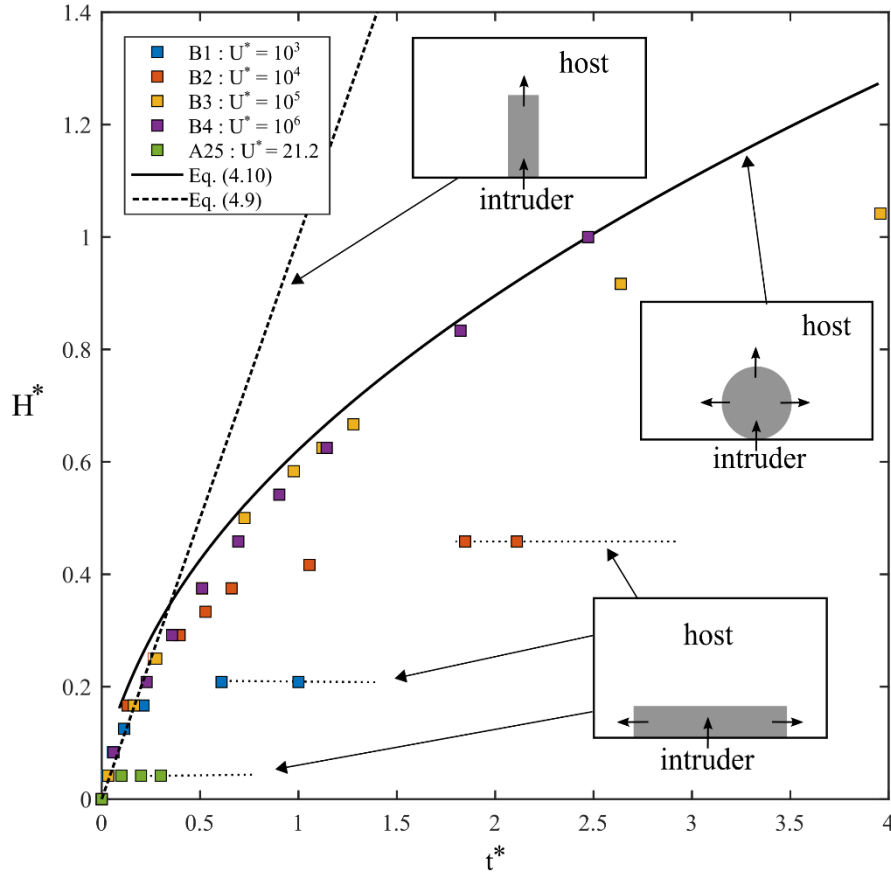


Figure 4.8: Evolution of the height, H^* , of the intruded volume as a function of the dimensionless time t^* . Each square represents the height of the top of the intruded volume measured in the simulations. Square colors depend on the injection rate. Dashed lines indicate the theoretical intruder front height evolution in the case of vertical propagation. The black curve is the theoretical front height for a radial growth, and the horizontal dotted lines indicate the front height evolution during lateral spreading. The three insets illustrate intrusion behaviors.

4.3.3 Results summary

Our results are helpful to predict the behavior of an intrusion within a mush. The dimensionless quantities U^* and ρ^* are the main controls of injection dynamics. When $U^* < \sim 10^5$, buoyancy effects dominate the intruder flow (Fig 4.8). The reduced buoyancy between the two melts, ρ^* , is the key parameters that controls if the intrusion spreads laterally at the base of the mush, or rises through it. On the contrary, the commonly used (e.g. Huppert et al., 1986; Snyder and Tait, 1995) bulk reduced buoyancy results in incorrect predictions of the intruder behavior (Fig. 4.6). This result illustrates that the relative motion existing between the solids and surrounding

melt is of primary importance when studying mush processes. The viscosity contrast, η^* , is found to be a weak control of the intrusion regime. Large viscosity contrasts tend to exacerbate the dynamics present at low viscosity contrasts, such as the formation of crystal-poor batches atop the intrusion or the lateral spreading of the intruder (Fig 4.6).

When $U^* > \sim 10^5$, the behavior of the intruder is dominated by the injection rate, which causes the radial growth of the cavity filled with the intruded melt (Fig. 4.7). At this injection rate and higher, simulations show similar intruder shapes at identical t^* . Even when $U^* < \sim 10^5$, the injection velocity remains an important parameter that controls the thickness of the intruder layer and its lateral spreading rate. It also controls the incorporation of the host solids within the injected melt. When the injection velocity is far above the minimum fluidization velocity computed with the injected melt properties instead of U_{mf} , which is computed with the host melt properties, the intruded melt is emplaced as a crystal-free layer, whereas a significant incorporation of host particles and porous flow occur otherwise.

4.4 Discussion

4.4.1 Model limitations

Our model focuses on some aspects of mush dynamics but neglects others and their possible importance on the dynamics of the intrusion must be discussed. The presence of exsolved volatiles in the melt as isolated bubble or connected channels is beyond the scope of the present model but may exert a strong control on the rejuvenation process because the percolation of exsolved gases in the mush advects heat and buoyant materials (Bachmann and Bergantz, 2006; Parmigiani et al., 2014). The ascent of bubbles, nucleated in the intruder by cooling, within the mush may also advect melt from the intruder into the mush (Wiesmaier et al., 2015), leading to mingling and mixing between the two melts. Similarly, we neglected the chemical reaction and melting of the crystals, which may affect the density of the surrounding melt. Setting thermal exchanges aside means that our simulations focus on the short-term evolution of the intrusion within a mush until steady state is reached but before significant effects of gas percolation and crystal melting can be felt. Alternatively, our simulations may represent the interaction of two magmas that have retained distinct melt properties and crystal contents after having thermally equilibrated (Sparks and

Marshall, 1986). The presence of crystals within the intruded layer is also not explored here. However, our results highlight the ubiquity and importance of the relative motions between the solids and the fluid. Thus, we do not expect that the crystal content of the intruder result in significant differences with our simulations. The melt reduced buoyancy and injection rate still control the behavior of the intruder and location of the boundary between the intruded and host melt.

We do not account for the presence of cohesive forces between crystals. Thereby, the presence of the associated yield stress is neglected here, although the yield stress caused by inter-crystal frictional contacts is present in our simulations. The presence of a bulk yield stress (i.e. due to a combination of friction, anisometric crystal interlocking, and synneusis) was identified as having a control on eruptive style (Karlstrom et al., 2012), and may increase the importance of the mush elasticity. With a significant elastic component in the mush rheology, the transport of the intruder may be modified and controlled by the orientation of the principal stress and overpressure (Pinel et al., 2017), rather than by the injection velocity and buoyancy contrast between the two melts. Thus, our results are valid for a weakly cohesive (frictional) mush with crystallinity close to the jamming transition, but may not be applied to magma transport within partially melted rocks or solidified mush where the elasticity of the solid framework cannot be neglected.

Our results are useful to predict the initial behavior and geometry of the intrusion in the mush and we proposed a simple relationship describing the height evolution of the intruded layer when the injection rate dominates the dynamics. However, these predictions cannot be used to predict the time between the intrusion and chamber-wide overturn or eruption because our simulations represent an open system where the host melt may freely exit the reservoir. When considering natural and closed systems, our results are only relevant for the short-term evolution of the intrusion. Otherwise, the accommodation of the intrusion by the host mush and surrounding crust and geometry of the reservoir has to be accounted for.

Experiments that mimic the replenishment of a felsic reservoir by a more mafic magma show that when a denser fluid is injected in a lighter fluid, it pounds and spread laterally at the base of the reservoir (e.g. Jellinek and Kerr, 1999; Koyaguchi and Kaneko, 2000; Snyder and Tait, 1995), which is in good agreement with our results. Despite the absence of particles, these experiments are able to reproduce the fingering of the intruder and presence of ribbon of felsic

magma (Perugini and Poli, 2005; Snyder et al., 1997; Snyder and Tait, 1995, 1998; Wiebe, 2016a). This contamination of the intruded material by the host results from the interaction between two features generated at the front of the gravity currents. First, a thin layer of host and buoyant material is trapped below the intruded layer that results in the formation of ribbons where the trapped mush percolate the injected layer. The fingering also develop at the front of the gravity current when the intruded fluid is less viscous than the host one because of Saffman-Taylor instabilities. According to Saffman and Taylor (1958), and Snyder et al. (1997), such front instabilities may occurred in all of our simulations holding in lateral spreading regime. However, the minimum theoretical wavelength of the instability is close or larger than the thickness of the intruded layer. Moreover, the thickness of the ribbons and trapped layer of host material are much smaller than the dimension of the fluid lattice. Thereby our model is not able to capture such front instabilities.

4.4.2 Implications on mush dynamics and on the modeling of crystal-bearing magmas

Our results have implications on the processes leading to the rejuvenation of a mush. Many of the current reawakening scenarios involve the emplacement of an intruder sill or gravity current at the base of the mush, supplying heat without mass exchange (Bachmann and Bergantz, 2006; Burgisser and Bergantz, 2011; Couch et al., 2001; Huber et al., 2011). This assumption is consistent with the results obtained when $U^* < 10^5$ and $\rho^* > 0$. In nature, the intruded melt is often the denser because of the chemical evolution and crystallization of the host material (Snyder, 2000). Thereby, the intruders predominantly stall at the floor of the mush. This situation maximizes the remobilized volume of host and entrainment by the intruder. The associated fluidization of the overlying mush decreases the crystal content at range where melt extraction is optimal (Bachmann and Huber, 2019) and exsolved volatiles channels may be formed (Parmigiani et al., 2017). The initial conditions impose that the host crystals and melt are at thermal equilibrium, and the fast processes we simulate results in the incorporation of cold solids within the hotter intrusion that accelerates its cooling and may foster volatile exsolution by second boiling. This result is consistent with geological observations that crystal from the host mush are commonly found in the layer of more mafic magma (Snyder et al., 1997). This particle settling may also incorporate host melt into the intruded material (Laumonier et al., 2015; Renggli et al., 2016; Ubide et al., 2014), inducing

mingling and affecting the cooling rate of the intruder. The lateral spreading of the intruder may generate conditions favorable to the mush reawakening by gas sparging (Bachmann and Bergantz, 2006) by increasing the surface area that may release volatiles. The fluidization of the mush and formation of a mixing bowl/chimney above the inlet (Bergantz et al., 2015; Schleicher et al., 2016; Schleicher and Bergantz, 2017) occurs when no density contrast exist between the host and intruded melts.

Our results show that when the intruder melt is lighter than that of the host, it results in a gravitational instability showing the rise of the injected material through the mush. On the contrary to injection, overturn starts from the absence of momentum and affect the entire mush volume. It results from the presence of small perturbations at the interface between the two magmas that initiate gravitational instabilities forming buoyant Rayleigh-Taylor blobs (Bain et al., 2013). Despite these differences, our results have also implication on the conditions required for overturning. The occurrence of gravitational instabilities in magmatic reservoirs may accelerate its remobilization, and is often addressed by the difference in the bulk density contrast that may exist between the mush and intruder (e.g. Bergantz and Breidenthal, 2001) or between the mush and a thermal boundary layer (e.g. Burgisser and Bergantz, 2011; Couch et al., 2001). However, our results demonstrate that the melt densities control gravitational instabilities rather than the bulk densities. The melting of crystals in a thermal boundary layer, between the intruder and host mush, resulting from the rejuvenation process is expected to increase the density of the surrounding melt, which thereby remains gravitationally stable. The presence of dissolved H₂O and CO₂ have a strong controls on the melt density because its partial specific density is much smaller than for the other constituents (Leshner and Spera, 2015). The amount of dissolved volatiles and their diffusion may thus play a critical role on the occurrence of gravitational instability in magmatic reservoirs.

Our simulations also shed light on the importance of the relative motion between the different phases constituting the magmatic reservoirs. Our results indicates that experiments, or numerical simulations, that account of the presence of the solids or exsolved volatiles as discrete entities (e.g. Barth et al., 2019; Bergantz et al., 2015; Girard and Stix, 2009; Hodge et al., 2012; McIntire et al., 2019; Michioka and Sumita, 2005; Schleicher et al., 2016; Schleicher and Bergantz, 2017) are the most likely to faithfully reproduce mush dynamics. Neglecting phase decoupling by considering the magma as a single-phase fluid having effective properties such as bulk density or

bulk viscosity will not capture the blending of crystal contents between host and intruder and the simultaneous but independent evolution of the melt–melt interface (Fig. 4.6).

4.5 Conclusion

Our simulations show that when the injection velocity is high ($U^* > \sim 10^5$), intrusion dynamics is dominated by the injection momentum. In such conditions, the intruded cavities show radial growth. On the contrary, when the injection velocity is below this threshold, the density contrast between the host and intruded melt phases controls the behavior of the intruder. When the intruded melt is lighter than the host one, it raise through the mush, whereas the contrary shows the lateral spreading of the intruded material. When the two densities are identical, the intruder fluidize the mush and generate a mixing bowl. Bulk buoyancy contrasts appear to have no control on the way the intruder flows. The lateral spreading of the intruder generates two counter rotating granular vortexes showing downward motion above the inlet, which maximizes the volume of the mush entrained by the gravity current. The combined effects of initial overpressure at the inlet and Reynolds dilatancy, resulting from the lateral spreading of the intruder, are able to fluidize the overlying mush. In the nature, the melt density of the intruder is often expected to be higher than in the host, leading to the lateral spreading of the injected materials at the floor of the mushy reservoir, which are conditions favoring mush remobilization. Our results also highlights the importance of considering the crystals or bubbles as discrete entities to mimic faithfully mush dynamics with analogue experiments or numerical simulations.

References:

- Andreotti, B., Forterre, Y., Pouliquen, O., 2013. *Granular Media: Between Fluid and Solid*. Cambridge University Press.
- Annen, C., Blundy, J.D., Leuthold, J., Sparks, R.S.J., 2015. Construction and evolution of igneous bodies: Towards an integrated perspective of crustal magmatism. *Lithos* 230, 206–221. <https://doi.org/10.1016/j.lithos.2015.05.008>
- Annen, C., Blundy, J.D., Sparks, R.S.J., 2006. The Genesis of Intermediate and Silicic Magmas in Deep Crustal Hot Zones. *J. Petrol.* 47, 505–539. <https://doi.org/10.1093/ptrology/egi084>
- Annen, C., Sparks, R.S.J., 2002. Effects of repetitive emplacement of basaltic intrusions on thermal evolution and melt generation in the crust. *Earth Planet. Sci. Lett.* 203, 937–955. [https://doi.org/10.1016/S0012-821X\(02\)00929-9](https://doi.org/10.1016/S0012-821X(02)00929-9)
- Bachmann, O., Bergantz, G.W., 2006. Gas percolation in upper-crustal silicic crystal mushes as a mechanism for upward heat advection and rejuvenation of near-solidus magma bodies. *J. Volcanol. Geotherm. Res.* 149, 85–102. <https://doi.org/10.1016/j.jvolgeores.2005.06.002>
- Bachmann, O., Dungan, M.A., Lipman, P.W., 2002. The Fish Canyon Magma Body, San Juan Volcanic Field, Colorado: Rejuvenation and Eruption of an Upper-Crustal Batholith. *J. Petrol.* 43, 1469–1503. <https://doi.org/10.1093/ptrology/43.8.1469>
- Bachmann, O., Huber, C., 2019. The Inner Workings of Crustal Distillation Columns; the Physical Mechanisms and Rates Controlling Phase Separation in Silicic Magma Reservoirs. *J. Petrol.* 60, 3–18. <https://doi.org/10.1093/ptrology/egy103>
- Bachmann, O., Huber, C., 2016. Silicic magma reservoirs in the Earth's crust. *Am. Mineral.* 101, 2377–2404. <https://doi.org/10.2138/am-2016-5675>
- Bain, A.A., Jellinek, A.M., Wiebe, R.A., 2013. Quantitative field constraints on the dynamics of silicic magma chamber rejuvenation and overturn. *Contrib. Mineral. Petrol.* 165, 1275–1294. <https://doi.org/10.1007/s00410-013-0858-5>
- Barth, A., Edmonds, M., Woods, A., 2019. Valve-like dynamics of gas flow through a packed crystal mush and cyclic strombolian explosions. *Sci. Rep.* 9, 1–9. <https://doi.org/10.1038/s41598-018-37013-8>
- Bergantz, G.W., 1989. Underplating and Partial Melting: Implications for Melt Generation and Extraction. *Science* 245, 1093–1095. <https://doi.org/10.1126/science.245.4922.1093>
- Bergantz, G.W., Breidenthal, R.E., 2001. Non-stationary entrainment and tunneling eruptions: A dynamic link between eruption processes and magma mixing. *Geophys. Res. Lett.* 28, 3075–3078. <https://doi.org/10.1029/2001GL013304>
- Bergantz, G.W., Schleicher, J.M., Burgisser, A., 2017. On the kinematics and dynamics of crystal-rich systems. *J. Geophys. Res. Solid Earth* 122, 2017JB014218. <https://doi.org/10.1002/2017JB014218>
- Bergantz, G.W., Schleicher, J.M., Burgisser, A., 2015. Open-system dynamics and mixing in magma mushes. *Nat. Geosci.* 8, 793–796. <https://doi.org/10.1038/ngeo2534>
- Burgisser, A., Bergantz, G.W., 2011. A rapid mechanism to remobilize and homogenize highly crystalline magma bodies. *Nature* 471, 212–215. <https://doi.org/10.1038/nature09799>
- Caricchi, L., Annen, C., Blundy, J., Simpson, G., Pinel, V., 2014. Frequency and magnitude of volcanic eruptions controlled by magma injection and buoyancy. *Nat. Geosci.* 7, 126–130. <https://doi.org/10.1038/ngeo2041>
- Cashman, K.V., Sparks, R.S.J., Blundy, J.D., 2017. Vertically extensive and unstable magmatic systems: A unified view of igneous processes. *Science* 355, eaag3055. <https://doi.org/10.1126/science.aag3055>
- Couch, S., Sparks, R.S.J., Carroll, M.R., 2001. Mineral disequilibrium in lavas explained by convective self-mixing in open magma chambers. *Nature* 411, 1037–1039. <https://doi.org/10.1038/35082540>
- Cui, X., Li, J., Chan, A., Chapman, D., 2014. Coupled DEM–LBM simulation of internal fluidisation induced by a leaking pipe. *Powder Technol.* 254, 299–306. <https://doi.org/10.1016/j.powtec.2014.01.048>
- Eichelberger, J.C., Izbekov, P.E., 2000. Eruption of andesite triggered by dyke injection: contrasting cases at Karymsky Volcano, Kamchatka and Mt Katmai, Alaska. *Philos. Trans. R. Soc. Lond. Ser. Math. Phys. Eng. Sci.* 358, 1465–1485.
- Furuichi, M., Nishiura, D., 2014. Robust coupled fluid-particle simulation scheme in Stokes-flow regime: Toward the geodynamic simulation including granular media. *Geochem. Geophys. Geosystems* 15, 2865–2882. <https://doi.org/10.1002/2014GC005281>
- Garg, R., Galvin, J., Li, T., Pannala, S., 2012. Open-source MFIx-DEM software for gas–solids flows: Part I—Verification studies. *Powder Technol.* 220, 122–137.
- Garg, R., Galvin, J., Li, T., Pannala, S., 2010. Documentation of open-source MFIx-DEM software for gas-solids flows. URL <https://www.netl.doe.gov/document/demdoc2012-1> Pdf Accessed 31 March 2014.
- Gidaspow, D., 1994. *Multiphase Flow and Fluidization: Continuum and Kinetic Theory Descriptions*. Academic Press.
- Girard, G., Stix, J., 2009. Buoyant replenishment in silicic magma reservoirs: Experimental approach and implications for magma dynamics, crystal mush remobilization, and eruption. *J. Geophys. Res. Solid Earth* 114, B08203. <https://doi.org/10.1029/2008JB005791>
- Hodge, K.F., Carazzo, G., Jellinek, A.M., 2012. Experimental constraints on the deformation and breakup of injected magma. *Earth Planet. Sci. Lett.* 325–326, 52–62. <https://doi.org/10.1016/j.epsl.2012.01.031>
- Huber, C., Bachmann, O., Dufek, J., 2011. Thermo-mechanical reactivation of locked crystal mushes: Melting-induced internal fracturing and assimilation processes in magmas. *Earth Planet. Sci. Lett.* 304, 443–454. <https://doi.org/10.1016/j.epsl.2011.02.022>

- Huppert, H.E., Sparks, R.S.J., Whitehead, J.A., Hallworth, M.A., 1986. Replenishment of magma chambers by light inputs. *J. Geophys. Res. Solid Earth* 6113–6122. [https://doi.org/10.1029/JB091iB06p06113@10.1002/\(ISSN\)2169-9356.OPENSYS1](https://doi.org/10.1029/JB091iB06p06113@10.1002/(ISSN)2169-9356.OPENSYS1)
- Jellinek, A.M., Kerr, R.C., 1999. Mixing and compositional stratification produced by natural convection: 2. Applications to the differentiation of basaltic and silicic magma chambers and komatiite lava flows. *J. Geophys. Res. Solid Earth* 104, 7203–7218. <https://doi.org/10.1029/1998JB900117>
- Karakas, O., Degruyter, W., Bachmann, O., Dufek, J., 2017. Lifetime and size of shallow magma bodies controlled by crustal-scale magmatism. *Nat. Geosci.* 10, 446–450. <https://doi.org/10.1038/ngeo2959>
- Karlstrom, L., Rudolph, M.L., Manga, M., 2012. Caldera size modulated by the yield stress within a crystal-rich magma reservoir. *Nat. Geosci.* 5, 402–405. <https://doi.org/10.1038/ngeo1453>
- Koyaguchi, T., Kaneko, K., 2000. Thermal evolution of silicic magma chambers after basalt replenishments. *Earth Environ. Sci. Trans. R. Soc. Edinb.* 91, 47–60. <https://doi.org/10.1017/S0263593300007288>
- Laumonier, M., Scaillet, B., Arbaret, L., Andújar, J., Champallier, R., 2015. Experimental mixing of hydrous magmas. *Chem. Geol.* 418, 158–170. <https://doi.org/10.1016/j.chemgeo.2015.10.031>
- Leshner, C.E., Spera, F.J., 2015. Chapter 5 - Thermodynamic and Transport Properties of Silicate Melts and Magma, in: Sigurdsson, H. (Ed.), *The Encyclopedia of Volcanoes (Second Edition)*. Academic Press, Amsterdam, pp. 113–141. <https://doi.org/10.1016/B978-0-12-385938-9.00005-5>
- Li, T., Garg, R., Galvin, J., Pannala, S., 2012. Open-source MFIX-DEM software for gas-solids flows: Part II—Validation studies. *Powder Technol.* 220, 138–150.
- McIntire, M.Z., Bergantz George W., Schleicher Jillian M., 2019. On the hydrodynamics of crystal clustering. *Philos. Trans. R. Soc. Math. Phys. Eng. Sci.* 377, 20180015. <https://doi.org/10.1098/rsta.2018.0015>
- Michioka, H., Sumita, 2005. Rayleigh-Taylor instability of a particle packed viscous fluid: Implications for a solidifying magma. *Geophys. Res. Lett.* 32. <https://doi.org/10.1029/2004GL021827>
- Nakagawa, M., Wada, K., Wood, C.P., 2002. Mixed Magmas, Mush Chambers and Eruption Triggers: Evidence from Zoned Clinopyroxene Phenocrysts in Andesitic Scoria from the 1995 Eruptions of Ruapehu Volcano, New Zealand. *J. Petrol.* 43, 2279–2303. <https://doi.org/10.1093/petrology/43.12.2279>
- Pallister, J.S., Hoblitt, R.P., Reyes, A.G., 1992. A basalt trigger for the 1991 eruptions of Pinatubo volcano? *Nature* 356, 426–428. <https://doi.org/10.1038/356426a0>
- Parmigiani, A., Degruyter, W., Leclaire, S., Huber, C., Bachmann, O., 2017. The mechanics of shallow magma reservoir outgassing. *Geochem. Geophys. Geosystems* 18, 2887–2905. <https://doi.org/10.1002/2017GC006912>
- Parmigiani, A., Huber, C., Bachmann, O., 2014. Mush microphysics and the reactivation of crystal-rich magma reservoirs. *J. Geophys. Res. Solid Earth* 119, 6308–6322. <https://doi.org/10.1002/2014JB011124>
- Perugini, D., Poli, G., 2005. Viscous fingering during replenishment of felsic magma chambers by continuous inputs of mafic magmas: Field evidence and fluid-mechanics experiments. *Geology* 33, 5–8. <https://doi.org/10.1130/G21075.1>
- Pinel, V., Carrara, A., Maccaferri, F., Rivalta, E., Corbi, F., 2017. A two-step model for dynamical dike propagation in two dimensions: Application to the July 2001 Etna eruption. *J. Geophys. Res. Solid Earth* 122, 1107–1125. <https://doi.org/10.1002/2016JB013630>
- Renggli, C.J., Wiesmaier, S., De Campos, C.P., Hess, K.-U., Dingwell, D.B., 2016. Magma mixing induced by particle settling. *Contrib. Mineral. Petrol.* 171, 96. <https://doi.org/10.1007/s00410-016-1305-1>
- Saffman, P.G., Taylor, G.I., 1958. The penetration of a fluid into a porous medium or Hele-Shaw cell containing a more viscous liquid. *Proc. R. Soc. Lond. Ser. Math. Phys. Sci.* 245, 312–329. <https://doi.org/10.1098/rspa.1958.0085>
- Schleicher, J.M., Bergantz, G.W., 2017. The Mechanics and Temporal Evolution of an Open-system Magmatic Intrusion into a Crystal-rich Magma. *J. Petrol.* 58, 1059–1072. <https://doi.org/10.1093/petrology/egx045>
- Schleicher, J.M., Bergantz, G.W., Breidenthal, R.E., Burgisser, A., 2016. Time scales of crystal mixing in magma mushes. *Geophys. Res. Lett.* 43, 1543–1550. <https://doi.org/10.1002/2015GL067372>
- Shi, Y.F., Yu, Y.S., Fan, L.T., 1984. Incipient fluidization condition for a tapered fluidized bed. 484–489.
- Snyder, D., 2000. Thermal effects of the intrusion of basaltic magma into a more silicic magma chamber and implications for eruption triggering. *Earth Planet. Sci. Lett.* 175, 257–273. [https://doi.org/10.1016/S0012-821X\(99\)00301-5](https://doi.org/10.1016/S0012-821X(99)00301-5)
- Snyder, D., Crambes, C., Tait, S., Wiebe, R.A., 1997. Magma Mingling in Dikes and Sills. *J. Geol.* 105, 75–86. <https://doi.org/10.1086/606148>
- Snyder, D., Tait, S., 1998. The imprint of basalt on the geochemistry of silicic magmas. *Earth Planet. Sci. Lett.* 160, 433–445. [https://doi.org/10.1016/S0012-821X\(98\)00102-2](https://doi.org/10.1016/S0012-821X(98)00102-2)
- Snyder, D., Tait, S., 1995. Replenishment of magma chambers: comparison of fluid-mechanics experiments with field relations. *Contrib. Mineral. Petrol.* 122, 230–240. <https://doi.org/10.1007/s004100050123>
- Sparks, R.S.J., Marshall, L.A., 1986. Thermal and mechanical constraints on mixing between mafic and silicic magmas. *J. Volcanol. Geotherm. Res.* 29, 99–124. [https://doi.org/10.1016/0377-0273\(86\)90041-7](https://doi.org/10.1016/0377-0273(86)90041-7)
- Syamlal, M., 1998. MFIX documentation numerical technique. EG and G Technical Services of West Virginia, Inc., Morgantown, WV (United States).
- Syamlal, M., Rogers, W., O'Brien, T.J., 1993. MFIX documentation theory guide. USDOE Morgantown Energy Technology Center, WV (United States).
- Takahashi, R., Nakagawa, M., 2013. Formation of a Compositionally Reverse Zoned Magma Chamber: Petrology of the ad 1640 and 1694 Eruptions of Hokkaido-Komagatake Volcano, Japan. *J. Petrol.* 54, 815–838. <https://doi.org/10.1093/petrology/egs087>

- Turner, J.S., Campbell, I.H., 1986. Convection and mixing in magma chambers. *Earth-Sci. Rev.* 23, 255–352. [https://doi.org/10.1016/0012-8252\(86\)90015-2](https://doi.org/10.1016/0012-8252(86)90015-2)
- Ubide, T., Galé, C., Larrea, P., Arranz, E., Lago, M., Tierz, P., 2014. The Relevance of Crystal Transfer to Magma Mixing: a Case Study in Composite Dykes from the Central Pyrenees. *J. Petrol.* 55, 1535–1559. <https://doi.org/10.1093/petrology/egu033>
- Weinberg, R.F., Leitch, A.M., 1998. Mingling in mafic magma chambers replenished by light felsic inputs: fluid dynamical experiments. *Earth Planet. Sci. Lett.* 157, 41–56. [https://doi.org/10.1016/S0012-821X\(98\)00025-9](https://doi.org/10.1016/S0012-821X(98)00025-9)
- Wiebe, R.A., 2016. Mafic replenishments into floored silicic magma chambers. *Am. Mineral.* 101, 297–310. <https://doi.org/10.2138/am-2016-5429>
- Wiesmaier, S., Morgavi, D., Renggli, C.J., Perugini, D., Campos, C.P. de, Hess, K.-U., Ertel-Ingrisch, W., Lavallée, Y., Dingwell, D.B., 2015. Magma mixing enhanced by bubble segregation. *Solid Earth* 1007–1023. <https://doi.org/10.5194/se-6-1007-2015>

Supplementary Section S4.1: List of the model equations

This Supplementary section includes two tables summarizing the equation system solved in our numerical simulations (Tables S4.1.1–S4.1.2).

Equation names	Equations	Ref.
Mass conservation	$\frac{\partial \varepsilon_f}{\partial t} + \nabla \cdot (\varepsilon_f \vec{v}_f) = 0$	1
Momentum conservation	$\rho_f \left(\frac{\partial}{\partial t} (\varepsilon_f \vec{v}_f) + \nabla \cdot (\varepsilon_f \vec{v}_f \otimes \vec{v}_f) \right) = \nabla \cdot (\vec{\sigma}_f) + \varepsilon_f \rho_f \vec{g} + \vec{I}_f$	1
Stress tensor	$\vec{\sigma}_f = P_f \delta_{ij} + \frac{2}{3} \eta_f \text{tr}(\vec{\varepsilon}_f) \delta_{ij} + 2 \eta_f \vec{\varepsilon}_f$	1
Euler velocity integration	$\vec{v}_p^{(k)}(t + \Delta t) = \vec{v}_p^{(k)}(t) + \Delta t \frac{\vec{F}_{GPD}^{(k)}(t) + \sum_{l=1}^{N_t^{(k)}} \left(\vec{F}_C^{N(k,l)}(t) + \vec{F}_C^T(k,l)(t) \right)}{m^{(k)}}$	Eq. (4.4)
Euler displacement integration	$\vec{X}_p^{(k)}(t + \Delta t) = \vec{X}_p^{(k)}(t) + \Delta t \vec{v}_p^{(k)}(t + \Delta t)$	2
Euler rotation integration	$\vec{\omega}_p^{(k)}(t + \Delta t) = \vec{\omega}_p^{(k)}(t) + \Delta t \frac{\sum_{l=1}^{N_t^{(k)}} \left(\vec{T}_C^{(k,l)} + \vec{T}_L^{(k,l)}(t) \right)}{I^{(k)}}$	2
Normal contact force	$\vec{F}_c^N^{(i,j)}(t) = \left(-k_n^{(i,j)}(t) \delta_n^{(i,j)}(t) + \eta_n^{(i,j)}(t) \Delta V_p^{N(i,j)}(t) \right) \vec{n}_{ij}$	2 5
Tangential contact force	$\vec{F}_c^T^{(i,j)}(t) = -k_t^{(i,j)}(t) \delta_t^{(i,j)}(t) + \eta_t^{(i,j)}(t) \Delta V_p^T(i,j)(t)$	2 5
Collisional torque	$\vec{T}_c^{(i,j)}(t) = \frac{d_p^{(i)} - \delta_n^{(i,j)}(t)}{2} \vec{F}_c^T(i,j)(t) ; \vec{T}_c^{(j,i)}(t) = \frac{d_p^{(j)} - \delta_n^{(i,j)}(t)}{2} \vec{F}_c^T(i,j)(t)$	2
normal spring (Hertzian model)	$k_n^{(i,j)}(t) = \frac{4}{3} \frac{E^{(i)} E^{(j)} \sqrt{R_{eff}^{(i,j)}}}{E^{(i)}(1 - \sigma^{(i)^2}) + E^{(j)}(1 - \sigma^{(j)^2})} \delta_n^{(i,j)\frac{1}{2}}(t)$	2
tangential spring (Hertzian model)	$k_t^{(i,j)}(t) = \frac{16}{3} \frac{G^{(i)} G^{(j)} \sqrt{R_{eff}^{(i,j)}}}{G^{(i)}(2 - \sigma^{(i)}) + G^{(j)}(2 - \sigma^{(j)})} \delta_t^{(i,j)\frac{1}{2}}(t)$	2

Equation names	Equations	Ref.
Elastic modulus	$G = \frac{E}{2(1+\sigma)}$	2
Normal damping coefficient	$\eta_n^{(i,j)}(t) = \frac{2\sqrt{m_{eff}^{(i,j)} k_n^{(i,j)}(t) \ln e_n }}{\sqrt{\pi^2 + \ln^2 e_n}} \delta_n^{(i,j)}(t)^{\frac{1}{4}}$	2 5
Tangential damping coefficient	$\eta_t^{(i,j)} = \frac{2\sqrt{m_{eff}^{(i,j)} k_t^{(i,j)}(t) \ln e_t }}{\sqrt{\pi^2 + \ln^2 e_t}} \delta_t^{(i,j)}(t)^{\frac{1}{4}}$	2 5
effective radius	$R_{eff}^{(i,j)} = \frac{2(d_p^{(i)} + d_p^{(j)})}{d_p^{(i)} d_p^{(j)}}$	2
Effective mass	$m_{eff}^{(i,j)} = \frac{m^{(i)} + m^{(j)}}{m^{(i)} m^{(j)}}$	2
Solids/Fluid momentum exchange on REV	$\vec{I}_f(t) = \frac{1}{V_{REV}} \sum_{k=1}^{N_k} \vec{F}_D^{(k)}(t) K_{REV}(X_p^{(k)})$	2
Drag forces (for the fluid)	$\vec{F}_D^{(k)}(t) = -\nabla P_f(t) \left(\frac{\pi}{6} d_p^{(k)3}\right) + \frac{\beta_{fs}^{(k)}(t)}{(1-\varepsilon_f(t))} \left(\frac{\pi}{6} d_p^{(k)3}\right) (\vec{v}_f(t) - \vec{v}_p^{(k)}(t))$	2
Local fluid/solid momentum transfer	$\beta_{fs}^{(k)}(t) = \begin{cases} \frac{3}{4} C_D^{(k)}(t) \frac{\rho_f \varepsilon_f(t) (1-\varepsilon_f)}{d_p^{(k)}} \ \vec{v}_f - \vec{v}_s^{(k)}\ \varepsilon_f^{-2.65} & \varepsilon_f \geq 0.8 \\ \frac{150 (1-\varepsilon_f(t))^2 \eta_f}{\varepsilon_f(t) d_p^{(k)2} + \frac{1.75 \rho_f (1-\varepsilon_f(t)) \ \vec{v}_f(t) - \vec{v}_s^{(k)}(t)\ }{d_p^{(k)}}} & \varepsilon_f < 0.8 \end{cases}$	3 4
Drag coefficient	$C_D^{(k)}(t) = \begin{cases} \frac{24}{Re^{(k)}(t)(1+0.15 Re^{(k)}(t)^{0.687})} & Re^{(k)}(t) < 1000 \\ 0.44 & Re^{(k)}(t) \geq 1000 \end{cases}$	3 4
Particle Gravity-Drag-Pressure force	$\vec{F}_{GPD}(t) = \frac{m_p}{\Delta t} \left(\vec{v}_f + \tau_v \left(\vec{g} - \frac{\nabla P}{\rho_p} \right) - \vec{v}_p(t) \right) \left(1 - e^{-\frac{\Delta t}{\tau_v}} \right)$	Eq. (4.5)
Reynolds number	$Re^{(k)}(t) = \frac{d_m^{(k)} \ \vec{v}_f(t) - \vec{v}_s^{(k)}(t)\ \rho_f}{\eta_f}$	3

Table S4.1.1: List of the equations implemented in the CFD-DEM model

¹ Syamlal et al., (1993)

² Garg et al., (2010)

³ Benyahia et al., (2012)

⁴ Gidaspow, (1986)

Symbol	Definition
$C_D^{(k)}$	Drag coefficient of the k^{th} particle
$d_p^{(i)}$	i^{th} particle diameter
e_n	Particle normal restitution coefficient
e_t	Particle tangential restitution coefficient
$E^{(i)}$	i^{th} particle Young modulus
$\vec{F}_C^{N(k,l)}$	Normal contact force between k^{th} particle and its l^{th} neighbor
$\vec{F}_C^{T(k,l)}$	Tangential contact forces between k^{th} particle and its l^{th} neighbor
$\vec{F}_D^{(k)}$	Drag force on k^{th} particle
\vec{g}	Gravitational vector (m s^{-2})
$G^{(k)}$	k^{th} particle shear moduli
$h^{(i,j)}$	Distance between i^{th} and j^{th} particles edges
\vec{I}_f	Fluid-solid momentum exchange
$I^{(k)}$	k^{th} particle moment of inertia
K_{REM}	Generic kernel to determine the influence of a particle located at $\vec{X}_p^{(k)}$ on the REV
$k_n^{(i,j)}$	Normal spring coefficient between i^{th} and j^{th} particles contact
$k_t^{(i,j)}$	Tangential spring coefficient between i^{th} and j^{th} particles contact
l	Neighbors index
$m^{(k)}$	k^{th} particle mass
$m_{eff}^{(i,j)}$	i^{th} and j^{th} particles effective radius
$N_l^{(k)}$	Number of neighbors of the k^{th} particle
N_k	Number of particles
\vec{n}_{ij}	Normal vector between i^{th} and j^{th} particles
P_f	Fluid pressure (Pa)
REV	Representative elementary volume
$Re^{(k)}$	i^{th} particle Reynolds number
$R_{eff}^{(i,j)}$	i^{th} and j^{th} particles effective radius
$R_c^{(i,j)}$	Contact area radius between i^{th} and j^{th} particles
$\vec{T}_C^{(k,l)}$	Contact torque between k^{th} particle and its l^{th} neighbor
$\vec{T}_L^{(k,l)}$	Lubrication torque between k^{th} particle and its l^{th} neighbor
\vec{v}_f	Fluid velocity vector (m s^{-1})
$\vec{v}_p^{(k)}$	k^{th} particle velocity vector (m s^{-1})
$\vec{X}_p^{(k)}$	k^{th} particle position (m)
$\beta_{fs}^{(k)}$	k^{th} particle – fluid momentum transfer coefficient
$\Delta V_p^{N(i,j)}$	Normal relative velocity between i^{th} and j^{th} particles
$\Delta V_p^{T(i,j)}$	Tangential relative velocity between i^{th} and j^{th} particles
δ_{ij}	Kronecker tensor
$\delta_n^{(i,j)}$	Normal overlap between i^{th} and j^{th} particles
$\delta_t^{(i,j)}$	Tangential displacement during the contact between i^{th} and j^{th} particles contact
ε	Roughness distance below which lubrication is ineffective (m)
ε_f	Fluid volume fraction
$\bar{\varepsilon}_f$	Fluid strain rate tensor
η_f	Fluid viscosity (Pa s)
$\eta_n^{(i,j)}$	Normal damping coefficient between i^{th} and j^{th} particles
$\eta_t^{(i,j)}$	Tangential damping coefficient between i^{th} and j^{th} particles
v	Domain volume (m^3)
ρ_f	Fluid density (kg m^{-3})
$\sigma^{(i)}$	i^{th} particle Poisson coefficient
$\bar{\sigma}_f$	Fluid stress tensor
$\vec{\omega}_p^{(k)}$	k^{th} particle rotation vector (rad s^{-1})
∇	Nabla operator
\otimes	Outer product

Table S4.1.2 : Symbols used in Table S4.1.1.

Supplementary Section S4.2: Derivation of the minimum fluidization velocity

This supplementary section presents an updated derivation of the minimum fluidization velocity compared to those used in the literature.

The onset of fluidization of a crystal bed occurs when the upward drag force exerted by the injected fluid exceed its net weight. Shi et al. (1984) proposed a formula to predict the minimum fluidization velocity of a random packed bed due to a localized injection of fluid. These authors made the assumption that the fluid velocity is only vertical and uniformly distributed on horizontal cross-sectional area (Fig. S4.2.1). The total upward drag force is computed with the Ergun's formula (Ergun, 1952) for a bed fluidized uniformly. Later, Cui et al. (2014) adapted this formula by considering the fluid velocity uniform along a semi-circular cross sectional area. Here, we modify the approach of Cui et al. (2014) to predict the minimum fluidization velocity in the experimental apparatus geometry because the original derivation incorrectly assumed the distance between the injection point and center of the inlet, r_0 , and the boundaries of the integral in their Eq. (13).

The total upward drag force applied by the inlet on the particle bed is computed as:

$$F_D = \int_{r_0}^{H+r_0} (AU_r + BU_r^2) S(r) dr, \quad (\text{S4.2.1})$$

where r_0 correspond of the vertical coordinates of the bottom and $H + r_0$ is the position of the top of the particle bed. The variable r corresponds to the radial distance from a hypothetic injection point (Fig. S4.2.1). A and B are given by Ergun (1952):

$$A = 150 \frac{\phi^2}{(1-\phi)^3} \frac{\eta_f}{d_p^2}, \quad (\text{S4.2.2})$$

$$B = 1.75 \frac{\phi}{(1-\phi)^3} \frac{\rho_f}{d_p}. \quad (\text{S4.2.3})$$

$S(r)$ represents the area of the curved surface on which the fluid velocity is uniform, and it is computed as a function of r as:

$$S(r) = 2\alpha(r + r_0)W_l. \quad (\text{S4.2.4})$$

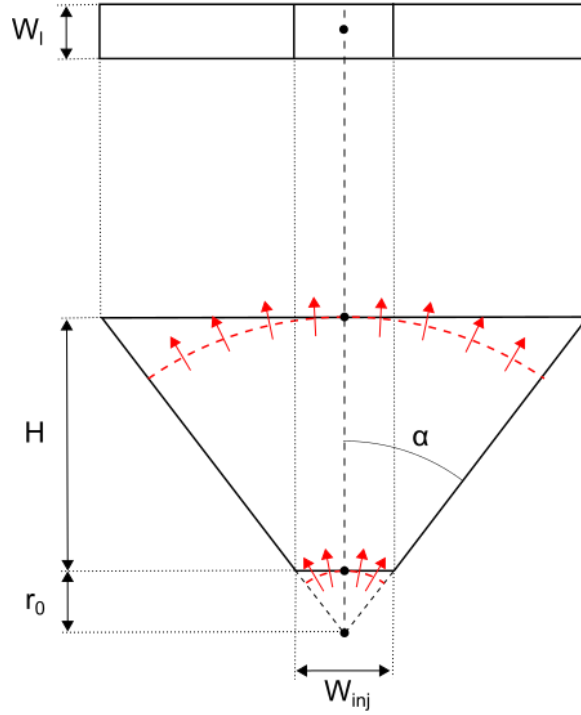


Figure S4.2.1: Conceptual framework to derive the minimum fluidization velocity. The top draw is a view from the top. The bottom draw is a front view. On both draws, the thick black lines represent the boundaries of the volume of the particle bed, which is fluidized. The red dashed curves indicate the cross sectional areas where the magnitude of the fluid velocity is uniform. The arrows represent the direction of the fluid flow. The black dots represent the positions of the theoretical injections point and intersections between the cross sectional areas where the fluid velocity is uniform and the vertical boundary of the fluidized particle bed.

U_r is the fluid velocity at a radial distance r . U_r may be computed by considering that the injected flux is conserved through the particle bed height, which yields:

$$Q_{inj} = U_r S(r), \quad (\text{S4.2.5})$$

and, with (S4.2.4):

$$U_r = \frac{Q_{inj}}{2\alpha(r+r_0)W_l} \quad (\text{S4.2.6})$$

Substituting Eqs. (S4.2.6) and (S4.2.4) into Eq. (S4.2.1) yields:

$$F = AQ_{inj}H_0 + \frac{B Q_{inj}^2}{2\alpha W_l} \ln\left(\frac{H_0+2r_0}{2r_0}\right) \quad (\text{S4.2.7})$$

In this geometry, the net weight of the bed, W , is given by:

$$W = \left[(r_0 + H_0)^2 \tan \alpha - \frac{W_{inj} r_0}{2} \right] W_l (\rho_p - \rho_f) g \phi. \quad (S4.2.8)$$

Introducing $r_0 = W_{inj} / (2 \tan \alpha)$, the onset of fluidization occurred when $F = W$, which yields:

$$A Q_{inj} H_0 + \frac{B Q_{inj}^2}{2 \alpha W_l} \ln \left(\frac{2 \tan \alpha}{W_{inj}} + 1 \right) - [H_0 (W_{inj} + H_0 \tan \alpha)] W_l (\rho_p - \rho_f) g \phi = 0 \quad (S4.2.9)$$

Figure S4.2.2 displays comparison of the minimum fluidization velocities computed with formulas from Ergun (1952), Shi et al. (1984), Cui et al., (2014), and Eq. (S4.2.9), function of the particle bed height. It shows that Eq (S4.2.9) is closer to the result predicted with the formulas from Ergun (1952) and Shi et al. (1984). The incorrect formula derived by Cui et al., (2014) results in the significant overestimations of the minimum fluidization velocity.

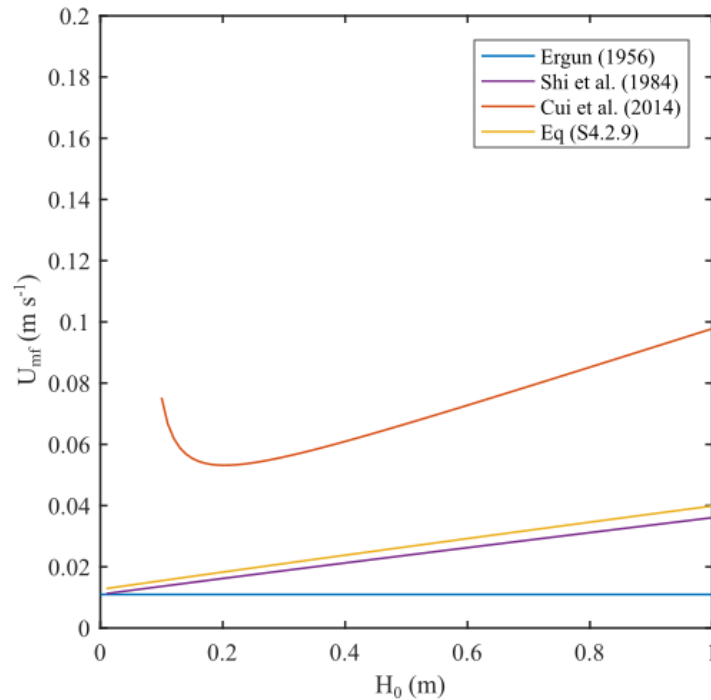


Figure S4.2.2: Comparison of the minimum fluidization velocities function of the initial particle bed height. The curves represent the minimum fluidization velocities derived by authors and the one given here.

Supplementary Section S4.3: Approximation of the intruder height during a spherical growth

This supplementary section presents the derivation of the equations used to compute the maximum height of a magma batch that grows radially above the inlet.

We consider as spherical intrusion having a unknown radius, R , and fed by an inlet of width W_{inj} (Fig. S4.3.1). The inlet truncates the sphere at a vertical distance, h , which depends on both R and W_{inj} . The objective is to compute the distance from the inlet to the top of the sphere, H , knowing the area A and injection width W_{inj} . The total area, A_{tot} , of the sphere is the sum of the area A , where the intruded fluid is present and the truncated area B as:

$$A_{tot} = A + B. \quad (S4.3.1)$$

The area A depends on injection velocity and time. The area A_{tot} may be expressed using the sphere radius R . Replacing A and A_{tot} in equation (S4.3.1) and rearranging yields:

$$\pi R^2 = W_{inj} H_{bed} t^* + A_B. \quad (S4.3.2)$$

The area B may be approximated with a good accuracy as (Harris and Stöcker, 1998, pp 92-93):

$$A_B \approx \frac{2}{3} W_{inj} h + \frac{h^3}{2 W_{inj}}. \quad (S4.3.3)$$

Inserting Eq. (S4.3.3) in Eq. (S4.3.2) gives:

$$0 = W_{inj} H_{bed} t^* + \frac{2}{3} W_{inj} h + \frac{h^3}{2 W_{inj}} - \pi R^2. \quad (S4.3.4)$$

Equation (S4.3.4) contains two unknowns, R and h , which can be related to each other tanks to geometry:

$$0 = \frac{W_{inj}^2}{4} + (R - h)^2 - R^2. \quad (S4.3.5)$$

Finally, H reads:

$$H = 2R - h \quad (S4.3.6)$$

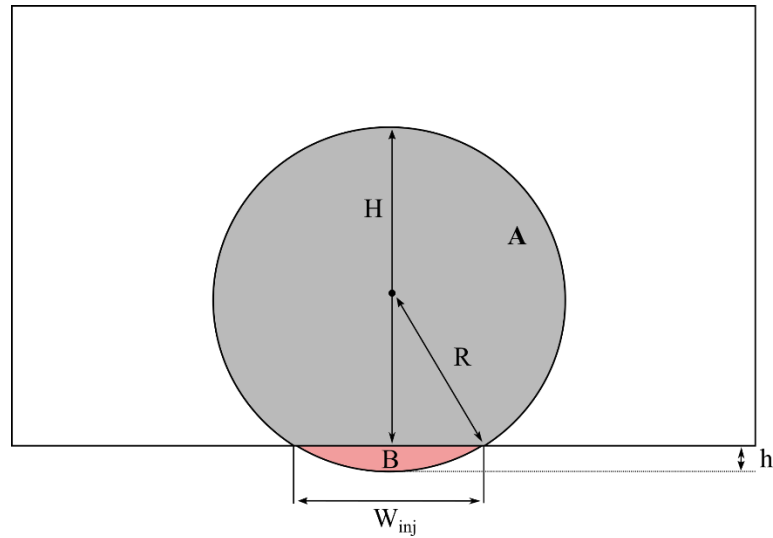


Figure S4.3.1: Schematics of the geometrical setup. The drawing represents a vertical section of the intrusion. The area covered by the injected melt is in gray and the area truncated from the circle of radius R is in red.

Supplementary References

- Benyahia, S., Syamlal, M., O'Brien, T.J., 2012. Summary of MFIX equations 2012-1. URL <https://www.nsl.doe.gov/documentation/MFIXEquations2012-1> Pdf.
- Ergun, S., 1952. Fluid flow through packed columns. *Chem Eng Prog* 48, 89–94.
- Gidaspow, D., 1986. Hydrodynamics of Fluidization and Heat Transfer: Supercomputer Modeling. *Appl. Mech. Rev.* 39, 1–23. <https://doi.org/10.1115/1.3143702>
- Harris, J.W., Stöcker, H., 1998. *Handbook of Mathematics and Computational Science*. Springer-Verlag, New York.

Chapter 5: Numerical simulations of the mixing caused by a magma intruding a resident mush¹³

5.1 Introduction

The replenishments of magmatic reservoirs with hotter and more mobile magmas are ubiquitous in nature. These events may trigger volcanic eruptions (Bachmann and Bergantz, 2006; Burgisser and Bergantz, 2011; Huber et al., 2011), and their repetitions are inferred to result in forming mushy magmatic reservoirs in the upper crust (Annen et al., 2015, 2006; Karakas et al., 2017). The products of eruptions triggered by a recharge in new magma evidence either significant (e.g., Murphy et al., 2000; Nakagawa et al., 2002; Pallister et al., 1992; Pichavant et al., 2018), or limited (e.g., Bachmann et al., 2014, 2002; Eichelberger and Izbekov, 2000; Hildreth, 1979; Takahashi and Nakagawa, 2013) mixing between the two end members involved. In chapter 4, we have shown that, when intruded at a gentle rate, a denser melt spreads laterally at the base of the mush, whereas it flows radially from the inlet at high injection velocities. The lateral spreading of the intrusion appears to be common in long-lived magmatic systems as exemplified by silicic-mafic layers complexes observed at the root of plutons (e.g. Bain et al., 2013; Wiebe, 2016). The efficiency of mixing in such a scenario was previously explored with experiments mimicking the mush and intruded magma as pure fluids having equivalent effective properties (e.g. Jellinek and Kerr, 1999; Snyder and Tait, 1996, 1995). This approach neglects the relative motion between crystals and the surrounding melt, and relies on the bulk densities of the constituents, which may result in discrepancies compared to the expected behavior of real magmas (Chapter 4). The efficiency of mixing accounting for granular dynamics was explored previously in the context of mush fluidization with both injected and resident melts having equal density and viscosity (Bergantz et al., 2015; Schleicher et al., 2016; Schleicher and Bergantz, 2017). It now requires to

¹³ This chapter is currently prepared for submission as a research article to *Geology* as: Carrara, A., Burgisser, A., Bergantz, G.W., Numerical simulations of the mixing caused by a magma intruding a resident mush

be constrained in the context of the injection of a denser melt with a different viscosity to extend our understanding of the magma reservoir processes that may result in eruptions.

The mixing between two materials having different viscosities has been addressed by imposing the stirring with the more viscous materials on inclusions or intrusions of less viscous ones (e.g. Bergantz and Breidenthal, 2001; Couch et al., 2001; Manga, 1996). As a result, the convective nature of the host material is the key parameter controlling the efficiency of the hybridization between the two magmas. The thermal interactions between the host mush and the intruder are able to generate thermal and compositional convections and greatly impact the mixing and hybridizations between the two end-member materials (Bain et al., 2013; Jellinek and Kerr, 1999; Snyder and Tait, 1996; Tait and Jaupart, 1992). In chapter 4, we focused on the short-term behavior of the injection and neglected thermal effects. A description of mixing requires accounting for the heat exchange between the magmas and for the dependence of the melts properties (density and viscosity) on temperature (e.g. Montagna et al., 2017). It also requires modeling the dynamics of the magmatic reservoir after the injection ceases (Schleicher and Bergantz, 2017) to account for the thermal interactions that take place over durations longer than that of injection.

In the present chapter, we performed Computational Fluid Dynamics and Discrete Element Method (CFD-DEM) simulations to explore the thermal effects and evolution of the interactions between a host mush and an intruded magma of different composition. First, we present the modifications made on the numerical model with respect to chapter 4 and the initial conditions and compositions of the magmas. Then, we describe the results of the simulations and the differences resulting from including thermal effects. One simulation is then used to explore the evolution of the interactions between the host and intruder materials after the injection shuts off. Finally, we discuss the limitations and implications of our results.

Symbol (unit)	Definition
ρ_f (kg m ⁻³)	Fluid density
T (K)	Fluid temperature
C_{pf} (J K ⁻¹)	Isobar heat capacity of the fluid
k_f (W m ⁻¹ K ⁻¹)	Fluid heat conductivity
α_f (K ⁻¹)	Fluid expansion coefficient
η (Pa s)	Fluid dynamic viscosity
ρ_s (kg m ⁻³)	Particle density
t^*	Reduced time
U_{inj} (m s ⁻¹)	Injection superficial velocity
U_{mf} (m s ⁻¹)	Minimum fluidization superficial velocity
U^*	Dimensionless injection velocity
Q_{fs} (w m ⁻²)	Fluid-solid heat transfer
Q_{ss} (w m ⁻²)	Solid-solid heat transfer
Q_{sfs} (w m ⁻²)	Solid-fluid-solid heat transfer
C_{ps} (J K ⁻¹)	Isobar heat capacity of the solids
k_s (W m ⁻¹ K ⁻¹)	Solids heat conductivity

Table 5.1: List of symbols and their meaning

5.2 Method

We performed CFD-DEM numerical simulations by using the MFIX-DEM software (<https://mfix.netl.doe.gov/>), with the modifications introduced in the chapter 4 that allowed us to use viscosities relevant for magmatic melts. As thermal effects are accounted for, we consider the energy equations of the two phases in the set of conservation equations. For the fluid, the energy equation reads (see chapter 2):

$$(1 - \Phi)\rho_f C_{pf} \left(\frac{\partial T_f}{\partial t} + \vec{v}_f \cdot \nabla T_f \right) + k_f \nabla \cdot \left((1 - \Phi) \cdot \nabla T_f \right) - Q_{fs} = 0, \quad (5.1)$$

where ρ_f is the fluid density, C_{pf} is the isobar heat capacity of the fluid, Φ is the volume fraction of solids, T_f is the fluid temperature, \vec{v}_f is the fluid velocity vector, k_f is the heat conductivity in the fluid, and Q_{fs} is the heat flux between the solids and the fluid. For the solids, the discrete equation that controls the evolution of temperature is (see chapter 2):

$$m_s(i) C_{ps}(i) \frac{\partial T_s(i)}{\partial t} = Q_{fs}(i) + \sum_{j=1}^N \left(Q_{ss}(i, j) + Q_{sfs}(i, j) \right) + \sum_{j=1}^M Q_{sfs}(i, j), \quad (5.2)$$

where m_s is the mass of the i^{th} particle, C_{ps} is the isobar heat capacity of the solid, T_s is the temperature of the solid, $Q_{ss}(i, j)$ is the heat flux between particles i and j in contact, and $Q_{sfs}(i, j)$

is the heat flux between particles i and j through the thin fluid layer located between them (Rong and Horio, 1999). In the bounds of the sums in Eq. (5.2), the index N indicates the number of particles that are in contact with particle i , and the index M is the number of neighboring particles that are close to but separated from the i^{th} particle. In a mush, the heat transfer between close solids through the fluid film separating them, Q_{sf} , is the dominant heat transfer mode (see chapter 2). The overall heat transfer in magmas and mush is mainly controlled by the fluid conductivity (Delvosalle and Vanderschuren, 1985). We do not account of the melting and crystallization of the solids here.

Changes in fluid temperature induce thermal dilatation and contraction and affect the fluid dynamic viscosity. The thermal expansion of the fluid causes density changes, which may induce convection. The equation of state linking the temperature of the melt phase to its density is:

$$\frac{\partial \rho_f}{\partial T_f} = \alpha_f, \quad (5.3)$$

where α_f is the thermal expansion of the melt. The characteristic thermal expansion of crystals is much smaller than that of the melt, which allowed us to neglect the effects of the solids dilatations and contractions. The viscosity of a magmatic melt depends on its chemical composition, dissolved water content, and temperature as (Giordano et al., 2008):

$$\text{Log}_{10} \eta = -4.55 + \frac{B}{C+T_f} \quad (5.4)$$

where B and C are constants that depend on the chemical composition of the melt phase. Because we consider two melts having different chemical compositions that mix during the simulations, we used the chemical composition of the two end-member magmas and an ideal mixture relationship to compute the local coefficients B and C .

To account for the diversity in chemical compositions of magmas and mush that are encountered in arc magmatism, we explored two different scenarios. The first one (A) considers the presence of a basaltic mush in which a hotter basaltic melt is injected. The second scenario (B) mimics the replenishment of a dacitic reservoir by a basaltic melt. For simulation A, we computed the physical properties of the melts and solid contents by computing the cooling and crystallization of a basaltic magma using the MELTS model (Ghiorso, 2004; Ghiorso and Kress, 2004) in the software PELE (Boudreau, 1999), at a pressure of 250 MPa using the QFM buffer. The initial

chemical compositions of the basaltic melt is taken from Dufek and Bachmann (2010) (see Table 5.2 for the initial composition and physical properties of the constituents). For simulation B, the chemical compositions and crystal contents of the end-member materials were taken from Caricchi and Blundy (2015) and Melekhova et al. (2013).

We employed the same 3D computational domain, thickness of the mush layer, and boundary conditions as used previously in chapter 4. The crystal-free melt is injected at the base of the mush layers through an inlet. We scale the injection velocity by computing the minimum fluidization velocities as in chapter 4. The two simulations use the same dimensionless injection velocity for which the injection momentum is dominant (see chapter 4). In both simulations, the density contrasts between the two melts are such that the intruded material will spread laterally if the injection momentum is negligible. The two simulations are compared for the same dimensionless time, t^* (chapter 4), for which the same volumes are injected. The short computational duration (~ 1.5 h on 128 cores) required to reach this dimensionless time in simulation A allows us to continue the simulation and explore the evolution of the interaction between host and intruded materials. In this way, we turn off the injection after $t^*=1.17$ ($t=7$ s) and continue the simulation until $t^*=83.9$ ($t=527$ s). Reaching the same dimensionless duration in simulation B would have required a calculation time too costly to be easily performed ($t\sim 14$ h and approximately 1.5 year of computation on 128 cores).

To quantify the mixing efficiency in the discrete phase, we computed the Initial Neighbor Distance (IND) mixing index employed by Schleicher et al. (2016). The IND is computed as the ratio of the sum of the distances that separates each particles with its initial nearest neighbor over the sum of the distances separating each particle and a random one (Schleicher et al., 2016). The IND is close to zero when particles remains ordered and close to unity when they are fully mixed.

Parameter	Host Sim. A ²	Intrusion Sim. A ²	Host Sim. B ¹	Intrusion Sim. B ³
SiO ₂ (% wt)	54.69	48.39	74.97	45.37
TiO ₂ (% wt)	0.6	0.98	0.14	0.7
Al ₂ O ₃ (% wt)	18.85	16.93	14.23	13.88
FeO(T) (% wt)	5.41	10.07	0.93	7.30
MnO (% wt)	0.48	0.18	0.08	0.34
MgO (% wt)	1.12	5.96	0.24	13.63
CaO (% wt)	4.77	10.46	1.29	10.30
Na ₂ O (% wt)	4.78	2.67	2.68	2.23
K ₂ O (% wt)	3.32	1.20	5.44	0.14
P ₂ O ₅ (% wt)	0.59	0.22	0	0.08
H ₂ O (% wt)	5.39	1.95	6.08	4.5
T (°C)	925	1150	800	1200
Φ_0	0.64	0.0	0.64	0.0
Mineral phases (% vol cryst.)	53-20-27 (pl-ol-cpx)	-	75-17-8 (pl-bi-cpx)	-
ρ_f (kg m ⁻³)	2305.1	2570.0	2036.97	2429.96
ρ_s (kg m ⁻³)	2700-3300-3400 (pl-ol-cpx)	-	2700-3500-3400 (pl-bi-cpx)	-
B	7005.9	5460	9690.5	4913.8
C	213.4	448.1	33.6	452.3
η (Pa s)	366.52	11.21	5.912 10 ⁴	1.835
α_f (K ⁻¹)	1 10 ⁻⁴	1 10 ⁻⁴	1 10 ⁻⁴	1 10 ⁻⁴
k_f (W m ² K ⁻¹)	1.5286	1.5286	1.5286	1.5286
Cp_f (J kg ⁻¹ K ⁻¹)	1367.4	1367.4	1367.4	1367.4
k_s (W m ² K ⁻¹)	2.4863	-	2.4863	-
Cp_s (J kg ⁻¹ K ⁻¹)	11146	-	11146	-
U_{inj} (m s ⁻¹)	-	4.839 10 ⁻² m s ⁻¹	-	5 10 ⁻⁴ m s ⁻¹
U^*	-	93470	-	93470

Table 5.2: Chemical compositions and physical properties of the magmas considered. Abbreviations pl, ol, cpx, and bi represent the plagioclase, olivine, clinopyroxene, and biotite mineral groups, respectively. Initial compositions were taken from ¹Caricchi and Blundy (2015), ²Dufek and Bachmann (2010), and ³Melekhova et al. (2013).

5.3 Results

Figure 5.1 displays snapshots of simulation A at a dimensionless time $t^*=1.17$ ($t=7s$). The intruded volume growth radially (Fig. 5.1 B) as expected with the dimensionless superficial injection velocity we imposed. The relaxation of the initial overpressure imposed by the initiation of mass inflow at the inlet (~ 1000 Pa above the injected material, after 1s of injection) results in the dilation of the crystal framework in a halo surrounding the injected volume (Fig. 5.1 A). The fluid flow is radial with velocities that are maximum above the inlet and that decrease away from it (Fig. 5.1 C). The intruded material diffuses its heat to the host and cools down. The temperature of the melt decreases radially from the inlet and shows a diffusive pattern (Fig. 5.1 D). Except near the interface between the intruded and host melts at the floor of the tank, no host crystals were present in the intruded volume at that time (Fig. 5.1 E). The solids located above the intruded volume have upward motions in their vertical component, whereas the ones located on the side of this volume do not show significant vertical motion.

Simulation B with the dacitic mush presents a similar radial growth of the intruded volume (Fig. 5.2). The location of the intruded material is similar to the one observed in simulation A. The shape of the dacitic mush intruder is nevertheless a little more elongated horizontally (Fig. 5.2 B) than the basaltic mush intruder (Fig. 5.1 B). The flow pattern of the melts is significantly different from that of the basaltic mush (Fig. 5.2 C). The intruded material starts to convect once $t^*>0.5$. The convective cells are restricted to the intruded volume and are not able to stir the overlying mush. Within the mush, the flow pattern of the melt is radial from the boundary between the host and intruded materials and it is similar to the one observed in simulation A. The distribution of temperature within the intrusion is affected by thermal convection. It shows the ascent of hot material and the downward flow of colder melt above the left bound of the inlet (Fig. 5.2 D). Thermal convection also concentrates the temperature gradients at the margin of the intruded volume. Host particles are found within the intruded melt (Fig. 5.2 F). The host solids are introduced because of the progressive erosion of the crystal framework above the intruded volume. The crystals located in the intruder have downward motions and tend to accumulate at the inlet. Around the intruded volume, the granular flow shows either upward or negligible vertical motions, as observed in simulation A.

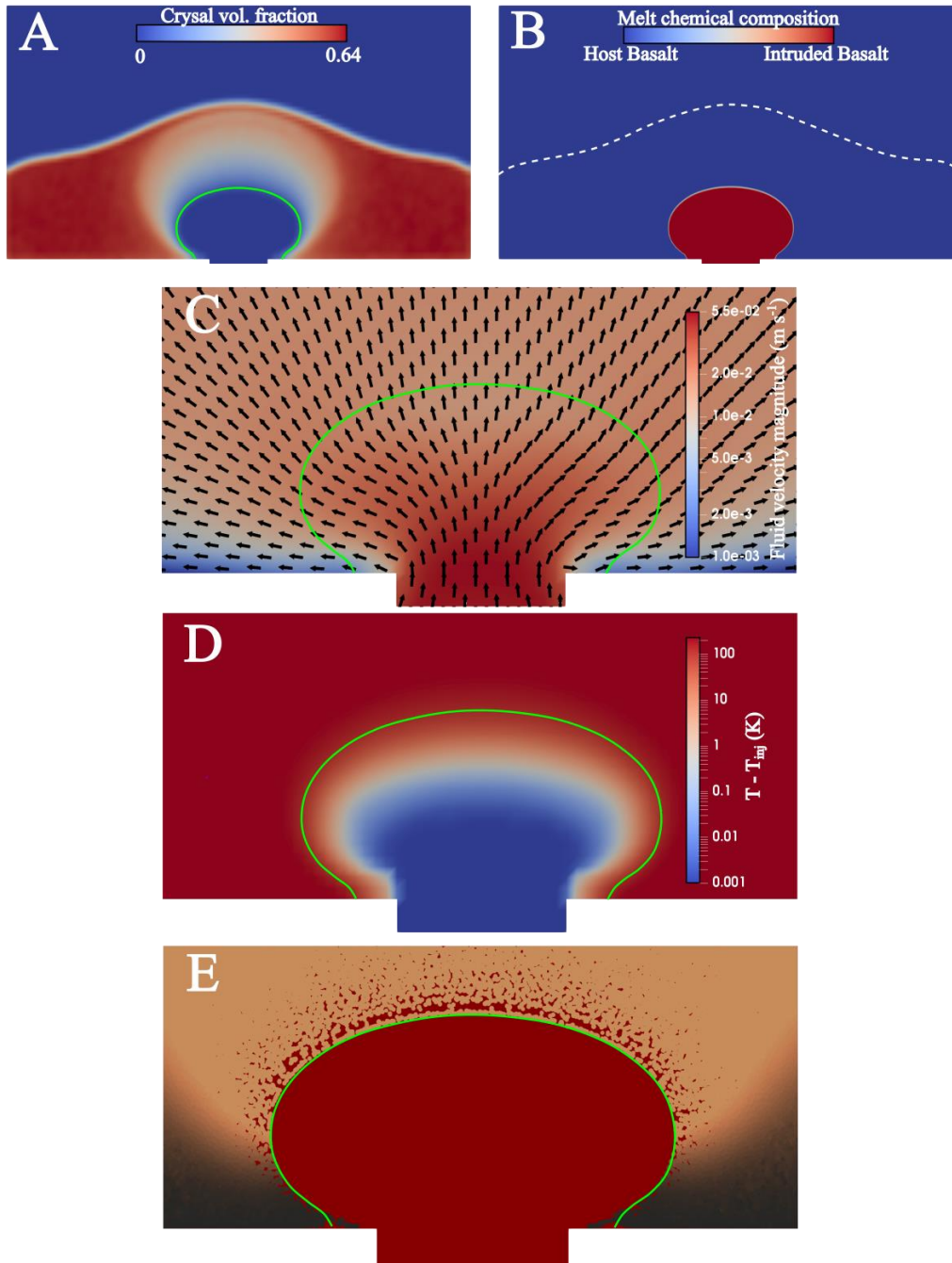


Figure 5.1: Results of simulation A at $t^*=1.17$ ($t=7$ s) viewed from the front of the tank. In A and C–E, the green curves represent the boundary between the host and intruded melts given by snapshot B. [A] Distribution of crystal content. [B] Chemical composition of the melt. The white dashed curve is the location of the top of the mush layer, taken at $\Phi=0.4$ in snapshot A. [C] Velocity field of the melt phase. The black arrows indicate the direction of the flow and are unscaled. The magnitude of the flow velocity is given by the background color with a logarithm scale. [D] Difference of the local temperature with respect to the intrusion temperature. Note that the scale is logarithmic and chosen to reflect the evolution of the temperature in the intrusion. The diffusion of the heat of the host into the mush is not visible here. [E] Vertical velocity of the crystals. Each disc represents a particle. Particles colored in beige move upward and particles displayed in black have negligible vertical velocities. No particle having a downward motion is present.

Figure 5.3 displays snapshots of the evolution of the distribution of crystal content, chemical composition, and temperature of simulation A after stopping the injection and until $t^*=83.9$ ($t=527$ s). It shows that once the injection stops, the evolution of the intruded layer is controlled by the buoyancy contrast between the host and introduced melts. The intruded volume starts to pond at the base of the mush (Fig. 5.3 B, H, and N). The thickness of the intruded layer decreases as the lateral spreading progresses (Fig. 5.3 A–F). Importantly, materials (crystals and melt) from the host are trapped below the intrusion. The host melt that is trapped is buoyant with respect to the intrusion and forms Rayleigh-Taylor instabilities, entraining the solids through the ponding intrusion and sometimes forming isolated crystal-rich pockets (Fig. 5.3 C–F). Once the lateral spreading becomes slower, host crystals surrounding the intrusion may settle and penetrate the intruder. At $t^*=83.9$, the intruder crystal volume fraction range from 5% to 15% at the fronts, and between 0% and 2-3% in the body, on a width of approximately 3 times the inlet centered around the inlet (Fig. 5.3 F). The crystal content in the rising blobs of host materials is characterized by higher volume fraction in solids (~30–40%).

We observe the progressive decrease of the crystals content of the entire mush layer once injection stops. At $t^*=1.12$, the crystal content of the mush is typically >60%, whereas at $t^*=83.9$, the maximum concentrations in solids are <60% (at most ~58%). The overlap distances, which are proxies for the force chains strength, show a significant decrease in their magnitude (from ~3.5% particle diameters at the end of the injection phase to ~0.1% at $t^*=83.9$). A strong decrease in crystal content is observed in the mush above the inlet. It artificially results from the finite size of the particle bed that cannot supply the downward granular motions above the inlet with crystals. Above the body of the intruded layer away from the inlet, the mush has a region of lower crystal content (~40% vol. fraction in solids) that tends to grow vertically with time (Fig. 5.3 D–F).

The distribution of the chemical composition shows the progressive hybridization of the melt located in the body of intruded layer away from the inlet (Fig. 5.3 G–L). On the contrary, the composition of the intruded melt located above the inlet remains unchanged. The progressive cooling of the intrusion (Fig. 5.3 M–R) results from the diffusion of heat into the mush, the incorporation of crystals at thermal equilibrium with the host melt, and the advection of the colder material trapped below the intruder (Fig. 5.3 O–R).

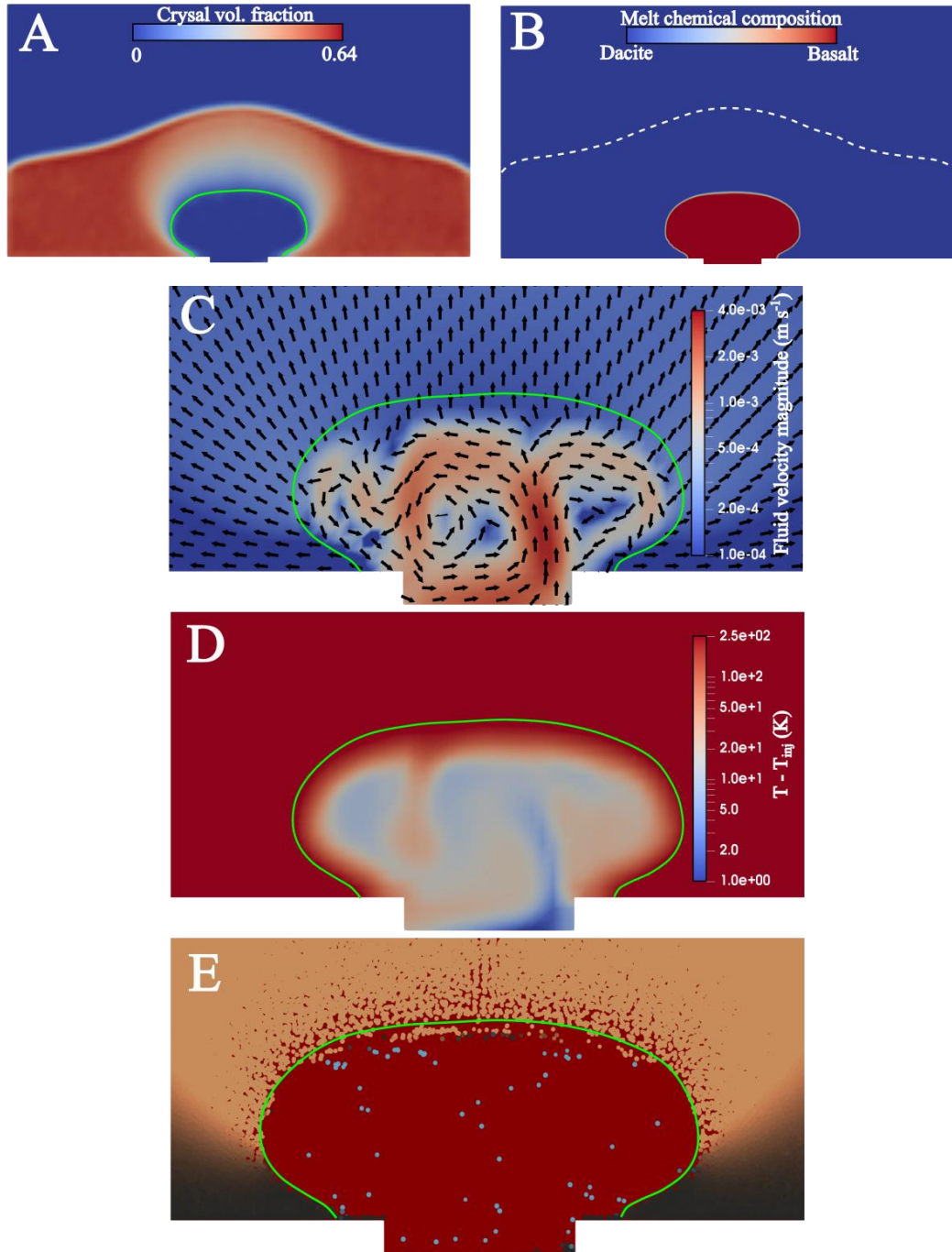


Figure 5.2: Results of simulation B at $t^*=1.17$ ($t=699$ s) viewed from the front. In snapshots A and C–E, the green curves represent the boundary between the host and intruded melts given by snapshot B. [A] Distribution of crystal content. [B] Chemical composition of the melt. The white dashed curve is the location of the top of the mush layer, taken at $\Phi=0.4$ in snapshot A. [C] Velocity field of the melt phase. Black arrows indicate the directions of the flow and are unscaled. The magnitude of the flow velocity is given by the background color with a logarithmic scale. [D] Difference of the local temperature with respect to the intrusion temperature. Note that the scale is logarithmic and chosen to reflect the evolution of the temperature in the intrusion. The diffusion of the heat of the host into the mush is not visible here. [E] Vertical velocity of the crystals. Each disc represents a particle. Particles colored in beige and cyan move upward and downward, respectively. Particles displayed in black have negligible vertical velocities.

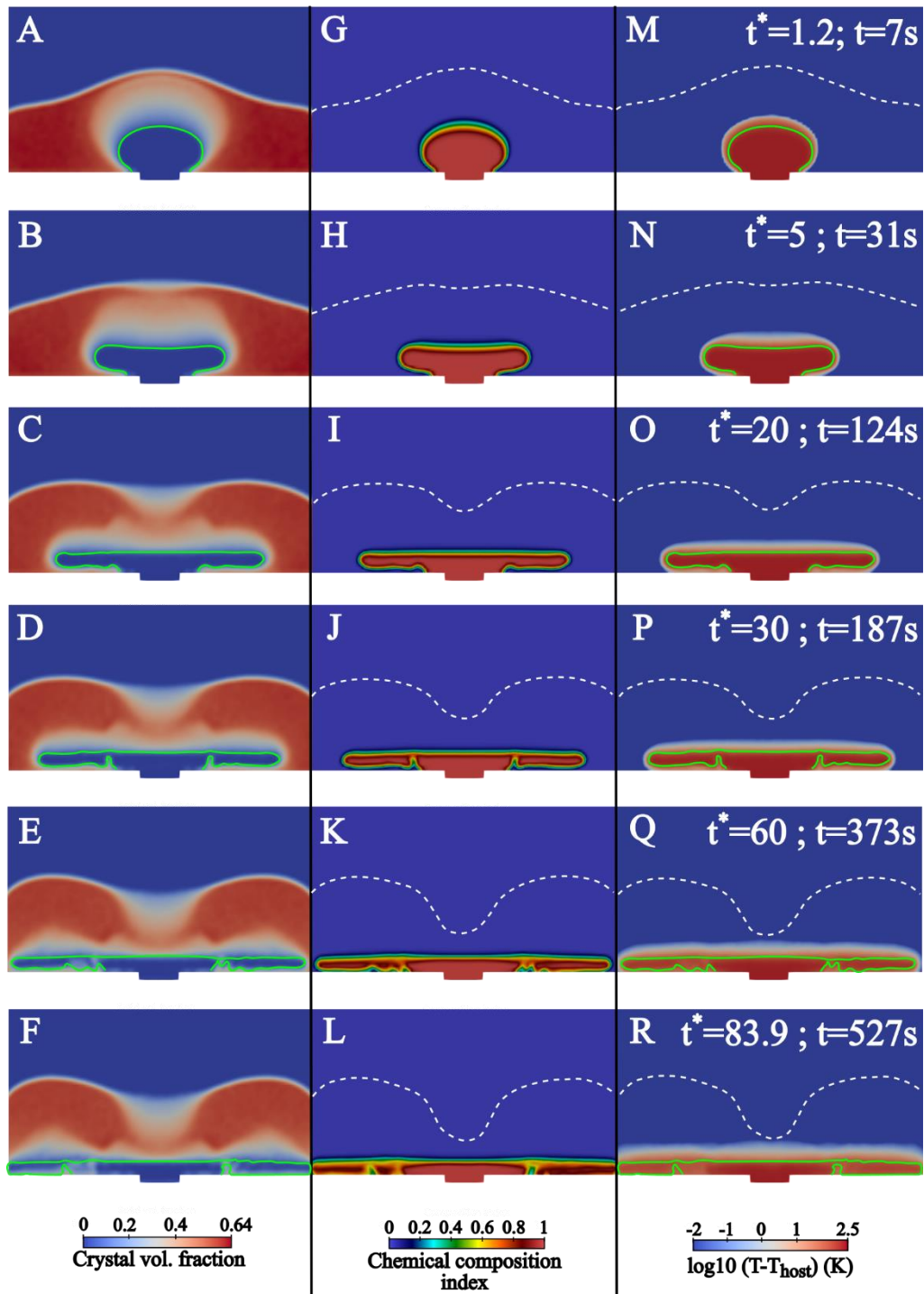


Figure 5.3: Interactions between the intruded and host materials after shutting off the injection. The solid green curve and dashed white curves have the same meanings as in Fig. 5.2. [A]–[F] Distribution of the content in crystals. The background color indicates the crystal volume fraction. The green curves correspond to the boundary where the melt is composed by equal parts of the host and introduced melts. [G]–[L] Chemical composition of the melt phase. [M]–[R] Evolution of the difference of local temperature compared to the host initial temperature. Note that the temperature scale is logarithmic and chosen to highlight the evolution of temperature of the host melt. The cooling of the host melt is visible after $t^*=60$.

Figure 5.4 displays snapshots of the granular dynamics at $t^*=83.9$. It shows that two counter-rotating granular vortexes are present within the mush overlying the intrusion (Fig. 5.4 A–B), resulting from the lateral spreading of the intruder (see chapter 4). Even if the lateral spreading rate of the intruder is weak at $t^*=83.9$, the granular vortexes of the solids are still present. Despite the decrease of volume fraction in solids, contacts are still present within the mush and restricted to two regions near the top of the mush layer (Fig. 5.4 C). We also observe the presence of contacts between the particles in the host material that is rising through the intrusion. In the volumes located above the intrusion where the crystal contents decrease to $\sim 40\%$ (Fig. 5.3 F), most solid–solid contacts vanished. Some force chains are present in these volumes, but their strength (proportional to the square root of the particle overlap) are negligible compared to the ones at $t^*=1.17$ when the injection stops. The Initial Neighbor Distance at $t^*=83.9$ is 0.0114 for the entire bed. However, the spatial distribution of the initial neighbor separation shows that most of the mixing in the solids occurs in the intruded layer (Fig. 5.4 D). In the mush layer that surrounds the intruded layer, the two granular vortexes are not able to mix the host crystals. Restricting the computation of the IND to the crystals located in the intruded melt (where the composition index is above or equal to 0.5) is 0.106, while the IND of the crystals in the mush is 0.0083. Even deformed and entrained by the granular vortexes, mush crystals remain poorly mixed.

5.4 Discussion

The IND is useful to quantify the overall amount of crystal mixing, and the initial closest neighbor separation distance is useful to visualize where the mixing is located. During the lateral spreading of intruder, the efficiency of the solids mixing is small compared to the case of fluidization explored in Schleicher et al. (2016). Even when computed only into the intruded layer, the IND remains low, indicating the low efficiency of the spreading layer in generating mixing. This result is in agreement with the experimental observations from Jellinek and Kerr (1999), who have addressed mixing using pure fluids of contrasting densities and viscosities. Ideally, one should consider separately the mixing of the solids and that of the melts. Quantifying the mixing between the host and injected melts in our simulations is challenging because of numerical diffusion. The thickness of the spreading layer encompasses only 3 grid cells that are visibly affected by numerical

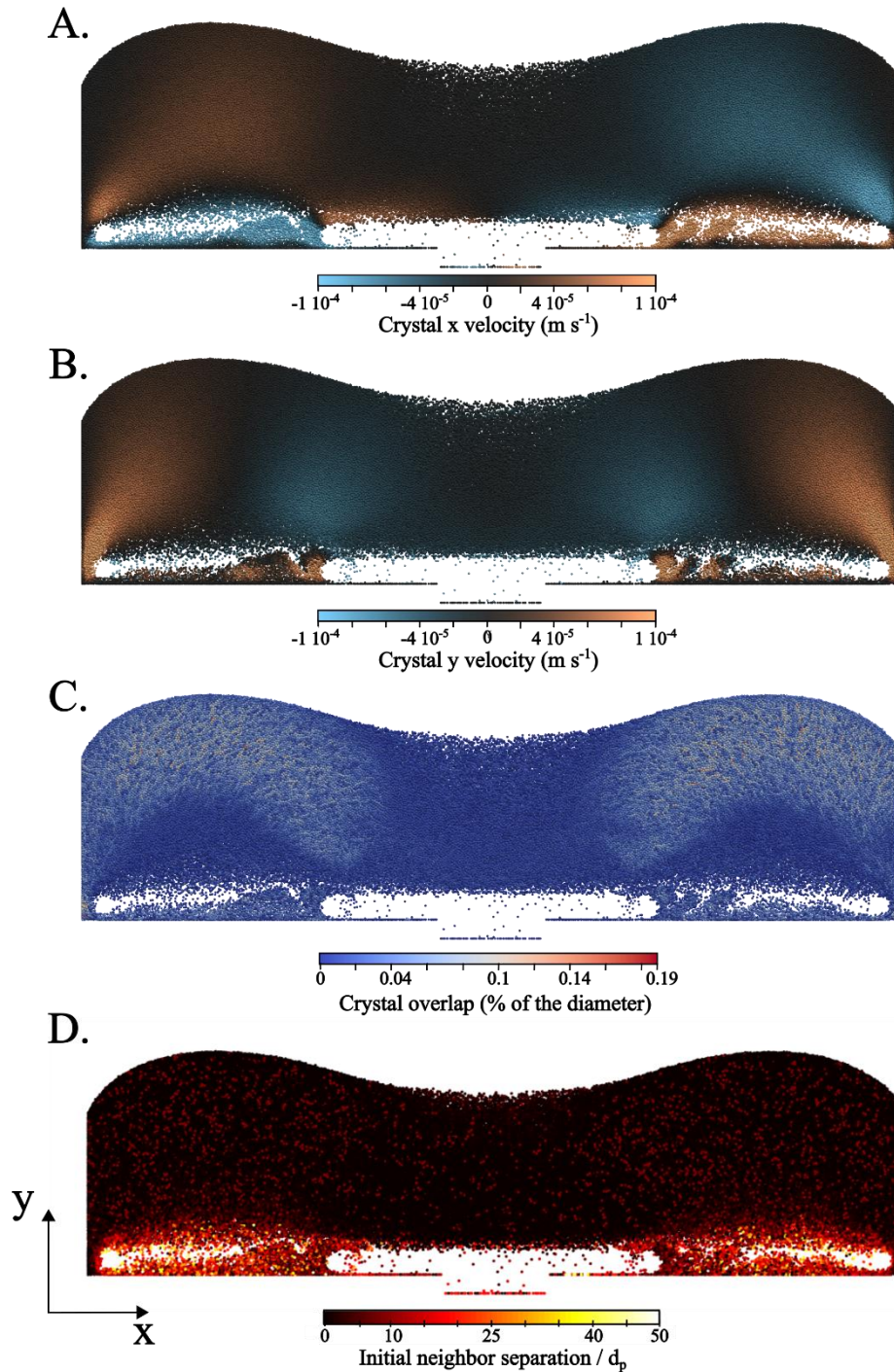


Figure 5.4: Dynamics of the granular phase at $t^*=83.9$ for simulation A. [A] Velocity field of the crystals in the x direction. Note that the color scale saturates for the solids located in the intruded layer. [B] Velocity of the crystals in the y direction. [C] Percentage of the overlap distance with respect to particle diameter. [D] Dimensionless initial neighbor separation. For each particle, it is the distance that separates it from its closest neighbor at the beginning of the simulation.

diffusion near the intrusion fronts (Fig. 5.3 L). Chemical diffusion, which is ignored in our simulations, exists in magmas but each element (e.g., SiO_2 , Al_2O_3 , H_2O) has a different diffusivity coefficient (Morgavi et al., 2013). Therefore, a reliable quantification of the hybridization between two melts requires performing simulations on a larger scale to increase the number of fluid cells composing the intruded layer, and to track the diffusion of the each element with a transport/diffusion equation.

Although we considered the difference in temperature between the two melts, it does not have significant effects on the behavior of the injection of simulation A, which could have been deduced from the results of chapter 4. This is because the growth of the intruded volume is too fast for the intruder to convect and because the injection shut-off stops the heat supply. During the lateral spreading, the thinning of the intruded layer and ensuing heat diffusion into the overlying and underlying mush reduces the likelihood of convection. Because simulation B takes a longer time to reach $t^*=1.17$ (699 s) and because of the lower viscosity of the injected melt, simulation B features convection within the intruded volume, a result that none of the simulations of chapter 4 shows. The excessive computation duration of this simulation did not allow us to explore the effects of this convection on the evolution of the mush–intrusion interaction. Convection within the intruder is expected to increase mixing efficiency between the two magmas because the goodness of mixing is a function of the vigor of convection (Bergantz and Ni, 1999; Jellinek and Kerr, 1999). The convective cells tend to homogenize the temperature of the melt with the intruded volume and to concentrate the temperature gradient to the margin of this volume, which both increase the cooling rate of the intrusion (Huber et al., 2009b). The rapid cooling of the host accelerates the crystallization process, which, to first order, increases the effective viscosity of the magma, possibly hindering convection. We thus expect that the presence of convection within the intruder will initially enhance granular mixing after the intrusion is turned off, before eventually hindering convection. In neither simulations is the heat supplied by the intruder able to generate convection in the host mush. The Rayleigh number in the host thermal boundary layer that surrounds the intrusion (i.e. the mush that is affected by heat diffusion) is on the order of 10^{-2} , far below the critical Rayleigh number at which convection starts ($\sim 10^3$). According to the scaling relationship given in Snyder (2000) for a continuous heat supply, the activation time of convection in the host material of simulation A is ~ 1150 s, which is longer than the full duration of our simulations and much longer than the time at which injection interruption cancels heat supply. We thus do not

expect convection in the host for $t^* > 83.9$, nor the vertical entrainment of intruded material by convection as observed in the experiments of Snyder and Tait (1996). It follows that the triggering of mush convection requires the injection of a sufficiently large volume of magma to supply enough heat to the mush.

Because of the cooling of the intruded material and the heating of the overlying mush, crystallization and melting of the solids may occur. In this study, we do not consider these processes. According to the crystal growth rate considered in Ruprecht et al. (2008), the maximum growth or melting in our simulations represents $\sim 10^{-4}$ % of the crystal diameter, which suggests that neglecting crystallization and melting of crystals is valid in our case. Over longer times, the formation and growth of crystals in the basalt withdraws the ferromagnesian elements from the surrounding melt, reducing its density and possibly generating compositional convection (Tait and Jaupart, 1992).

Even if the injection of the hot basalt was not able to induce host convection in our simulations, the injection generated important dynamical effects that affected the physical state of the surrounding mush. In chapter 4, we have shown that the lateral spreading of the intrusion entrained the formation of granular vortexes in the overlying mush. Here, the joint effects of the settling of the host crystals and Reynolds dilatancy (see chapter 4) are able to decrease locally the solid volume fraction of the overlying mush. In simulation A, the average crystal volume fraction in the mush layer decreases from 0.64 at the end of the injection to 0.58 at $t^* = 83.9$ (the mush immediately surrounding the intruded volume was not taken into account in this averaging) (Fig. 5.3 A–F). The initial stress generated by the on-going intrusion is accommodated by both the bulging of the particle bed and the loading of force chains throughout the mush. Once the injection stops, the stress relaxes by the progressive dilation of the mush layer. The accommodation done by bulging is not expected to occur when the magmatic reservoir is entirely composed of mush. The elastic loading of the force chains, however, is expected. Thus, in a mush-filled reservoir, the combined effects of the relaxation of the injection stress, Reynolds dilatancy, and settling of the host particle in the intruder decrease the solid volume fraction of the host to a range at which the extraction of the interstitial melt by repacking of the crystals framework is optimal (Bachmann and Huber, 2019).

In simulation A, once the lateral spreading of the intruded volume becomes negligible, the two regions of the mush with a lowered crystallinity of 40% propagate upward (Fig. 5.3 E–F). We thus expect that if simulation A were run further in time, these more dilute volumes would continue to progress upward, maybe in the fashion described experimentally by Shibano et al. (2012). The injection of a denser magma in an open mush thus appears to be an efficient trigger for the extraction of the mush interstitial melt. The decrease of the crystal content also affects the behavior of exsolved volatiles if present. Whereas in mushy conditions, the gas phase may channelize and ascends effectively through the mush, at the crystal contents we obtained, the exsolved volatiles are likely to be found as isolated bubbles (Parmigiani et al., 2017, 2014), which reduces their ability to advect heat through the overlying mush and to rejuvenate the mush by gas sparging (Bachmann and Bergantz, 2006).

Our simulations are able to reproduce some features observed in plutons where the interactions between the host mush and injected material can be observed. Well-preserved mafic-felsic interfaces often present gravitational instabilities and mingling features (e.g. Bain et al., 2013; Wiebe, 2016, and references therein) (Fig 5.5 A). These outcrops show sharp transitions between the two lithologies (Bain et al., 2013), which suggests that chemical diffusion has a weak effect prior to the solidification and the preservation of the mafic-felsic complex. The instabilities are inferred to be generated by the buoyant rise of the underlying felsic mush within a layer of basalt. The presence of the felsic mush below the intruder has been interpreted to be the result of a yield stress within the mush that then supports the vertical flow of basalt (Jellinek and Kerr, 1999). In this scenario, the negatively buoyant intrusion spreads laterally when a weaker region of the magmatic reservoir is encountered. The underlying strong mush is progressively weakened because of the warming imposed by the intruder. It results in gravitationally instabilities at the basal silicic-mafic interface, and in the rise of buoyant felsic magma through the newly emplaced mafic magma, sometimes forming pipes (Bain et al., 2013). Experiments mimicking the replenishment of a reservoir with a denser fluid showed that resident materials may be trapped beneath such a laterally spreading layer (Snyder and Tait, 1995).

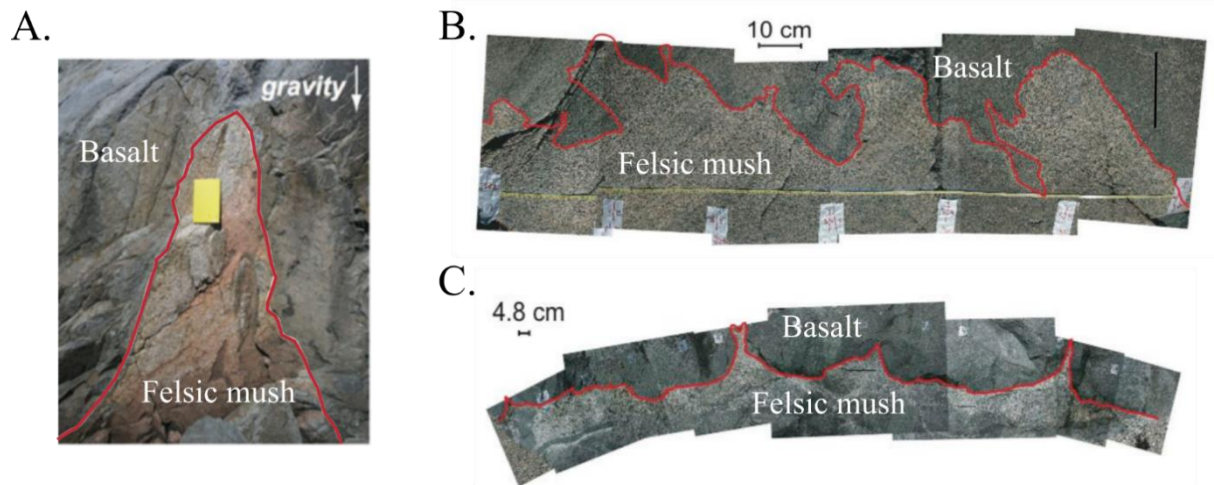


Figure 5.5: Silicic-mafic interfaces, redrawn from Bain et al. (2013). [A] Example of unstable silicic-mafic interface observed at the Coastal Maine Magmatic Province. [B] Outcrop from the Pleasant Bay, Ray point, Maine USA. [C] Outcrop from Mount Desert Island, Stewart Head, Maine, USA. Each red curve indicates the silicic-mafic interface and was drawn by Bain et al. (2013).

Under low injection rates, the trapped layer is very thin (see chapter 4) and has probably a negligible effect on the intruder. Simulation A has shown that when the injection of the basalt is short and dies off rapidly, a significant thickness of the host mush may be trapped below the intrusion (Fig. 5.3). The trapped layer is weak enough to flow and rise through the spreading layer. Our results suggest that the rise of buoyant mush through the intruded layer may also be initiated by an alternative scenario to the one proposed by Bain et al. (2013) and Jellinek and Kerr (1999) because the occurrence of instabilities does not necessarily implies a thermal origin but a contrast in melt densities (Snyder and Tait, 1998) and a short but intense injection event. In our scenario, the rise of the host mush occurs while the intruder spread. The rising blobs of mush are progressively tilted and deformed along the flow direction (Fig. 5.3 D–F). In some of the outcrops reported in Bain et al. (2013), the mafic-felsic interfaces show a preferential orientation in the tilt of the rising blobs of resident mush (Fig. 5.5 B). We speculate that the preferential lateral deformation of the rising blobs may reflect the direction of the intrusion flow. Analyzing the spatial distribution of such deformations may help to locate the feeding point of the intrusion. Some outcrops displayed in Bain et al. (2013) do not show significant lateral deformation of the rising blobs (Fig. 5.5 C), suggesting either that the mafic layer was at rest during the rise of the mush, or that the direction of the flow was perpendicular to the outcrop.

5.5 Conclusions

In this chapter, we modeled the injection of a hot and mobile magma into a mush and their interactions during and after emplacement while accounting for the heat exchange and thermal effects on the melts physical properties. We implemented the thermal expansion and viscosity variations of the melts with respect to temperature in the CFD-DEM model employed in chapter 4. Two cases were explored, the intrusions of two basaltic melts in a basaltic mush and a dacitic mush, respectively. The two simulations used the same dimensionless intrusion speed for which the injection momentum controls the intruder behavior. During the injections, the shape of the two intruded volumes had similar shapes but the dynamics of the intruded melts were different. With the basaltic mush (simulation A), melts flows were radial from the inlet and the temperature was transferred by conduction to the mush. The higher viscosity of the dacitic mush (simulation B) lengthens the duration of the injection, enhancing the cooling of the intruded volume compared to simulation A for the same dimensionless time. The temperature contrast between the margin of the intrusion and the inlet causes convection in the intrusion. Because of the rheological contrast between the host and intruded materials, convection was restricted to the intrusion.

In simulation A, when the injection was stopped, the intruded material ponded to the base of the mush and spread laterally, trapping host material below it. The buoyant underlying melt ascended through the intruded layer, entraining host crystals. Other crystals from the overlying mush also penetrated the intrusion by settling. Crystals mixing was restricted within the intruded layer and in its vicinity. The presence of convection in the intruded volume increased the efficiency of mixing in the intrusion, but the overall mixing efficiency was lower than in the fluidization regime explored by Schleicher et al., (2016, 2017). The amount of heat injected in the mush was not able to trigger mush convection. Overall, our simulations replicate most of the textures of magma mixing and mingling observed in rocks (e.g., enclaves, isolated crystals in disequilibrium with their host) despite strong density and viscosity contrasts, which suggests that magma mixing is a fundamentally two-phase process that can be captured by CFD-DEM simulations. More specifically, our results also reproduce the gravitational instabilities observed in outcrops featuring silicic-mafic interfaces, which suggests that the rise of the host mush in an intruded layer does not necessarily require thermal activation and may be triggered instead by a rapid and short injection event.

References:

- Annen, C., Blundy, J.D., Leuthold, J., Sparks, R.S.J., 2015. Construction and evolution of igneous bodies: Towards an integrated perspective of crustal magmatism. *Lithos* 230, 206–221. <https://doi.org/10.1016/j.lithos.2015.05.008>
- Annen, C., Blundy, J.D., Sparks, R.S.J., 2006. The Genesis of Intermediate and Silicic Magmas in Deep Crustal Hot Zones. *J. Petrol.* 47, 505–539. <https://doi.org/10.1093/petrology/egi084>
- Bachmann, O., Bergantz, G.W., 2006. Gas percolation in upper-crustal silicic crystal mushes as a mechanism for upward heat advection and rejuvenation of near-solidus magma bodies. *J. Volcanol. Geotherm. Res.* 149, 85–102. <https://doi.org/10.1016/j.jvolgeores.2005.06.002>
- Bachmann, O., Deering, C.D., Lipman, P.W., Plummer, C., 2014. Building zoned ignimbrites by recycling silicic cumulates: insight from the 1,000 km³ Carpenter Ridge Tuff, CO. *Contrib. Mineral. Petrol.* 167, 1025. <https://doi.org/10.1007/s00410-014-1025-3>
- Bachmann, O., Dungan, M.A., Lipman, P.W., 2002. The Fish Canyon Magma Body, San Juan Volcanic Field, Colorado: Rejuvenation and Eruption of an Upper-Crustal Batholith. *J. Petrol.* 43, 1469–1503. <https://doi.org/10.1093/petrology/43.8.1469>
- Bachmann, O., Huber, C., 2019. The Inner Workings of Crustal Distillation Columns; the Physical Mechanisms and Rates Controlling Phase Separation in Silicic Magma Reservoirs. *J. Petrol.* 60, 3–18. <https://doi.org/10.1093/petrology/egy103>
- Bain, A.A., Jellinek, A.M., Wiebe, R.A., 2013. Quantitative field constraints on the dynamics of silicic magma chamber rejuvenation and overturn. *Contrib. Mineral. Petrol.* 165, 1275–1294. <https://doi.org/10.1007/s00410-013-0858-5>
- Bergantz, G.W., Breidenthal, R.E., 2001. Non-stationary entrainment and tunneling eruptions: A dynamic link between eruption processes and magma mixing. *Geophys. Res. Lett.* 28, 3075–3078. <https://doi.org/10.1029/2001GL013304>
- Bergantz, G.W., Ni, J., 1999. A numerical study of sedimentation by dripping instabilities in viscous fluids. *Int. J. Multiph. Flow* 25, 307–320. [https://doi.org/10.1016/S0301-9322\(98\)00050-0](https://doi.org/10.1016/S0301-9322(98)00050-0)
- Bergantz, G.W., Schleicher, J.M., Burgisser, A., 2015. Open-system dynamics and mixing in magma mushes. *Nat. Geosci.* 8, 793–796. <https://doi.org/10.1038/ngeo2534>
- Boudreau, A.E., 1999. PELE—a version of the MELTS software program for the PC platform. *Comput. Geosci.* 25, 201–203.
- Burgisser, A., Bergantz, G.W., 2011. A rapid mechanism to remobilize and homogenize highly crystalline magma bodies. *Nature* 471, 212–215. <https://doi.org/10.1038/nature09799>
- Caricchi, L., Blundy, J., 2015. Experimental petrology of monotonous intermediate magmas. *Geol. Soc. Lond. Spec. Publ.* 422, 105–130. <https://doi.org/10.1144/SP422.9>
- Couch, S., Sparks, R.S.J., Carroll, M.R., 2001. Mineral disequilibrium in lavas explained by convective self-mixing in open magma chambers. *Nature* 411, 1037–1039. <https://doi.org/10.1038/35082540>
- Delvosalle, C., Vanderschuren, J., 1985. Gas-to-particle and particle-to-particle heat transfer in fluidized beds of large particles. *Chem. Eng. Sci.* 40, 769–779. [https://doi.org/10.1016/0009-2509\(85\)85030-2](https://doi.org/10.1016/0009-2509(85)85030-2)
- Dufek, J., Bachmann, O., 2010. Quantum magmatism: Magmatic compositional gaps generated by melt-crystal dynamics. *Geology* 38, 687–690. <https://doi.org/10.1130/G30831.1>
- Eichelberger, J.C., Izbekov, P.E., 2000. Eruption of andesite triggered by dyke injection: contrasting cases at Karymsky Volcano, Kamchatka and Mt Katmai, Alaska. *Philos. Trans. R. Soc. Lond. Ser. Math. Phys. Eng. Sci.* 358, 1465–1485.
- Ghiorso, M.S., 2004. An equation of state for silicate melts. I. Formulation of a general model. *Am. J. Sci.* 304, 637–678. <https://doi.org/10.2475/ajs.304.8-9.637>
- Ghiorso, M.S., Kress, V.C., 2004. An equation of state for silicate melts. II. Calibration of volumetric properties at 105 Pa. *Am. J. Sci.* 304, 679–751. <https://doi.org/10.2475/ajs.304.8-9.679>
- Giordano, D., Russell, J.K., Dingwell, D.B., 2008. Viscosity of magmatic liquids: A model. *Earth Planet. Sci. Lett.* 271, 123–134. <https://doi.org/10.1016/j.epsl.2008.03.038>
- Hildreth, W., 1979. The Bishop Tuff: Evidence for the origin of compositional zonation in silicic magma chambers. *Geol. Soc. Am. Spec. Pap.* 180, 43–75.
- Huber, C., Bachmann, O., Dufek, J., 2011. Thermo-mechanical reactivation of locked crystal mushes: Melting-induced internal fracturing and assimilation processes in magmas. *Earth Planet. Sci. Lett.* 304, 443–454. <https://doi.org/10.1016/j.epsl.2011.02.022>
- Huber, C., Bachmann, O., Manga, M., 2009. Homogenization processes in silicic magma chambers by stirring and mushification (latent heat buffering). *Earth Planet. Sci. Lett.* 283, 38–47. <https://doi.org/10.1016/j.epsl.2009.03.029>
- Jellinek, A.M., Kerr, R.C., 1999. Mixing and compositional stratification produced by natural convection: 2. Applications to the differentiation of basaltic and silicic magma chambers and komatiite lava flows. *J. Geophys. Res. Solid Earth* 104, 7203–7218. <https://doi.org/10.1029/1998JB900117>
- Karakas, O., Degruyter, W., Bachmann, O., Dufek, J., 2017. Lifetime and size of shallow magma bodies controlled by crustal-scale magmatism. *Nat. Geosci.* 10, 446–450. <https://doi.org/10.1038/ngeo2959>
- Manga, M., 1996. Mixing of heterogeneities in the mantle: Effect of viscosity differences. *Geophys. Res. Lett.* 23, 403–406. <https://doi.org/10.1029/96GL00242>
- Melekhova, E., Annen, C., Blundy, J., 2013. Compositional gaps in igneous rock suites controlled by magma system heat and water content. *Nat. Geosci.* 6, 385–390. <https://doi.org/10.1038/ngeo1781>

- Montagna, C.P., Papale, P., Longo, A., Bagagli, M., 2017. Magma Chamber Rejuvenation: Insights from Numerical Models, in: Gottsmann, J., Neuberg, J., Scheu, B. (Eds.), *Volcanic Unrest : From Science to Society*, Advances in Volcanology. Springer International Publishing, Cham, pp. 111–122. https://doi.org/10.1007/11157_21
- Morgavi, D., Perugini, D., De Campos, C.P., Ertel-Ingrisch, W., Dingwell, D.B., 2013. Time evolution of chemical exchanges during mixing of rhyolitic and basaltic melts. *Contrib. Mineral. Petrol.* 166, 615–638. <https://doi.org/10.1007/s00410-013-0894-1>
- Murphy, M.D., Sparks, R.S.J., Barclay, J., Carroll, M.R., Brewer, T.S., 2000. Remobilization of Andesite Magma by Intrusion of Mafic Magma at the Soufriere Hills Volcano, Montserrat, West Indies. *J. Petrol.* 41, 21–42. <https://doi.org/10.1093/petrology/41.1.21>
- Nakagawa, M., Wada, K., Wood, C.P., 2002. Mixed Magmas, Mush Chambers and Eruption Triggers: Evidence from Zoned Clinopyroxene Phenocrysts in Andesitic Scoria from the 1995 Eruptions of Ruapehu Volcano, New Zealand. *J. Petrol.* 43, 2279–2303. <https://doi.org/10.1093/petrology/43.12.2279>
- Pallister, J.S., Hoblitt, R.P., Reyes, A.G., 1992. A basalt trigger for the 1991 eruptions of Pinatubo volcano? *Nature* 356, 426–428. <https://doi.org/10.1038/356426a0>
- Parmigiani, A., Degruyter, W., Leclaire, S., Huber, C., Bachmann, O., 2017. The mechanics of shallow magma reservoir outgassing. *Geochem. Geophys. Geosystems* 18, 2887–2905. <https://doi.org/10.1002/2017GC006912>
- Parmigiani, A., Huber, C., Bachmann, O., 2014. Mush microphysics and the reactivation of crystal-rich magma reservoirs. *J. Geophys. Res. Solid Earth* 119, 6308–6322. <https://doi.org/10.1002/2014JB011124>
- Pichavant, M., Poussineau, S., Lesne, P., Solaro, C., Bourdier, J.-L., 2018. Experimental Parametrization of Magma Mixing: Application to the ad 1530 Eruption of La Soufrière, Guadeloupe (Lesser Antilles). *J. Petrol.* 59, 257–282. <https://doi.org/10.1093/petrology/egy030>
- Rong, D., Horio, M., 1999. DEM simulation of char combustion in a fluidized bed. *Second Int. Conf. CFD Miner. Process Ind.* CSIRO Melb. Aust. 1999 65–70.
- Ruprecht, P., Bergantz, G.W., Dufek, J., 2008. Modeling of gas-driven magmatic overturn: Tracking of phenocryst dispersal and gathering during magma mixing. *Geochem. Geophys. Geosystems* 9. <https://doi.org/10.1029/2008GC002022>
- Schleicher, J.M., Bergantz, G.W., 2017. The Mechanics and Temporal Evolution of an Open-system Magmatic Intrusion into a Crystal-rich Magma. *J. Petrol.* 58, 1059–1072. <https://doi.org/10.1093/petrology/egx045>
- Schleicher, J.M., Bergantz, G.W., Breidenthal, R.E., Burgisser, A., 2016. Time scales of crystal mixing in magma mushes. *Geophys. Res. Lett.* 43, 1543–1550. <https://doi.org/10.1002/2015GL067372>
- Shibano, Y., Namiki, A., Sumita, I., 2012. Experiments on upward migration of a liquid-rich layer in a granular medium: Implications for a crystalline magma chamber. *Geochem. Geophys. Geosystems* 13. <https://doi.org/10.1029/2011GC003994>
- Snyder, D., 2000. Thermal effects of the intrusion of basaltic magma into a more silicic magma chamber and implications for eruption triggering. *Earth Planet. Sci. Lett.* 175, 257–273. [https://doi.org/10.1016/S0012-821X\(99\)00301-5](https://doi.org/10.1016/S0012-821X(99)00301-5)
- Snyder, D., Tait, S., 1998. The imprint of basalt on the geochemistry of silicic magmas. *Earth Planet. Sci. Lett.* 160, 433–445. [https://doi.org/10.1016/S0012-821X\(98\)00102-2](https://doi.org/10.1016/S0012-821X(98)00102-2)
- Snyder, D., Tait, S., 1996. Magma mixing by convective entrainment. *Nature* 379, 529–531. <https://doi.org/10.1038/379529a0>
- Snyder, D., Tait, S., 1995. Replenishment of magma chambers: comparison of fluid-mechanic experiments with field relations. *Contrib. Mineral. Petrol.* 122, 230–240. <https://doi.org/10.1007/s004100050123>
- Tait, S., Jaupart, C., 1992. Compositional convection in a reactive crystalline mush and melt differentiation. *J. Geophys. Res. Solid Earth* 97, 6735–6756. <https://doi.org/10.1029/92JB00016>
- Takahashi, R., Nakagawa, M., 2013. Formation of a Compositionally Reverse Zoned Magma Chamber: Petrology of the ad 1640 and 1694 Eruptions of Hokkaido-Komagatake Volcano, Japan. *J. Petrol.* 54, 815–838. <https://doi.org/10.1093/petrology/egs087>
- Wiebe, R.A., 2016. Mafic replenishments into floored silicic magma chambers. *Am. Mineral.* 101, 297–310. <https://doi.org/10.2138/am-2016-5429>

Chapter 6: The seismic properties of eruptible magmas¹⁴

6.1 Introduction

The ubiquity of replenishment of the magmatic reservoir with mobile magma (see chapter 4), the crystal contents of eruptive products (e.g. Takahashi and Nakagawa, 2013), and the occurrence of mechanisms that lead to the extraction of melt from a mush (e.g. Bachmann and Huber, 2019) indicate the episodic presence in upper crustal magmatic reservoirs of volumes dominated by melt. These magma bodies correspond to the eruptible volume of a magmatic reservoir. The rheology of eruptible magmas has a strong control on eruptive style (e.g. Cassidy et al., 2018; Karlstrom et al., 2012). The detection of melt-dominated volumes and the estimation of their physical properties are of paramount importance to enhance our ability to predict eruptive styles and to best assess volcanic hazards. The presence of eruptible magma is expected to cause the sharp decrease of the compressional wave velocity and to suppress shear waves (Caricchi et al., 2008). Tomographic images of seismic wave velocities and attenuations show the presence of partially molten rocks and crystal mush, but they have never evidenced the presence of melt-dominated bodies (e.g. De Siena et al., 2014; Kiser et al., 2016; Paulatto et al., 2012; Waite and Moran, 2009). Tomographic images are computed with the first wave arrivals at the stations, which corresponds to the fastest travel from the source. Because of the lower velocities of the compressional waves in magmas, the ray paths of the first arrivals may avoid melt volume, which undersample them in the resulting image, effectively hiding them. The spatial averaging of the seismic properties resulting from tomography may also smooth the effects of the presence of small melt-dominated bodies, which are then interpreted as partially molten rocks. Finally, it is possible that seismic waves are attenuated during their propagation across magmatic systems.

A comprehensive interpretation of the results of seismic velocities and attenuation tomography requires a good knowledge of the acoustic properties of the materials constituting the magmatic system. Models exist to compute the compressional and shear waves velocities and attenuation

¹⁴ This chapter is currently prepared for submission as a research article to Acoustical Society of America as: Carrara, A., , Lesage, P., Burgisser, A., The seismic properties of eruptible magmas

coefficients in partially molten rocks (e.g. Mavko, 2012), in pure melts (e.g. Kress and Carmichael, 1991), or in bubbly melts (e.g. Collier et al., 2006; Neuberg and O’Gorman, 2002). Caricchi et al. (2008) studied experimentally the velocities of P and S waves in eruptible magmas. Some seismic properties of crystal-bearing magmas remain, however, poorly constrained. It is the case of intrinsic attenuation, which is one focus of this chapter.

In the acoustic literature, the acoustic properties of suspensions of solids in fluids have been widely studied because of industrial interests (Challis et al., 2005). Authors used two main approaches. The scattering approach is based on the harmonic decomposition of the waves radiated by the solids in the suspension, and presents the advantage to be reliable at any frequency, but is not able to account for the relative motion between the constituents (Berryman, 1980; Kuster and Toksöz, 1974; Kuster and Toksoz, 1974; Valier-Brasier et al., 2015). On the contrary, the coupled phase approach is based on the constitutive equations that control the dynamic of the carrier and suspended phases. It is limited to the long wavelength regime (seismic wavelengths much larger than the solid sizes), but it can take into account complex physical phenomena such as the relative motions that exist between the constituents (Atkinson and Kytömaa, 1992; Evans and Attenborough, 2002, 1997; Gibson and Toksöz, 1989; Hacker et al., 2003; Valier-Brasier et al., 2015). Application of the coupled phase approach to constrain the seismic properties of magmas at seismic frequencies is promising because the long wavelength assumption is always valid. However, some modifications of the coupled phase method are required in order to be applied for magmas. The large viscosities of magmatic melt imply that the viscous stress tensor of the fluid cannot be discarded. Moreover, the effect of lubrication forces may become significant in crystal-bearing magmas during transient dynamics and oscillatory motions (see chapter 2). These two effects have never been considered before in the coupled phase approach.

The aim of this chapter is to adapt and use the coupled phase approach to constrain the acoustic properties of crystal-bearing magmas. We first describe the assumptions made on the considered suspensions. Then we introduce the coupled phase method used to compute the seismic properties of magmas as a function of the chemical compositions of the considered magmas. The third part presents the modifications made to the equation system to compute the velocities and attenuation coefficients of seismic waves. The model is then applied to a representative suspension and to typical magmas in order to estimate the mechanical wave velocities and attenuation coefficients. In the last part, we discuss about the validation and limitations of the model to mimic

real magmas, before exploring the implications of our results on the detection of melt dominated volumes.

Symbol (unit)	Definition
A	Lubrication geometrical parameter
d_p (m)	Particle diameter
\vec{F}_D (kg m ⁻¹ s ⁻²)	Drag force
\vec{F}_{VM} (kg m ⁻¹ s ⁻²)	Virtual mass force
\vec{F}_B (kg m ⁻¹ s ⁻²)	Basset force
\vec{F}_{lub} (kg m ⁻¹ s ⁻²)	Lubrication force
f (Hz)	Frequency
\vec{g} (m s ⁻²)	Gravitational acceleration
\vec{I}_{fs} (kg m s ⁻¹)	Momentum exchange coefficient
\vec{I}_{ss} (kg m s ⁻¹)	Solid-Solid momentum transfer
\vec{I}_{sfs} (kg m s ⁻¹)	Solid-Fluid-Solid momentum transfer
j	Lubrication dimensionless separation distance
K_f (Pa)	Fluid bulk modulus
K_s (Pa)	Solid bulk modulus
K^* (Pa)	Effective bulk modulus of the suspension
k_p (m ⁻¹)	Compressional wave wavenumber
P (Pa)	Pressure
Re_Ω	Oscillatory Reynolds number
V_p (m s ⁻¹)	Compressional wave velocity
\vec{v}_f (m s ⁻¹)	Fluid velocity
\vec{v}_s (m s ⁻¹)	Solids velocity
α_p (Np m ⁻¹)	Attenuation coefficient of the compressional waves
β (rad)	Incidence angle
β_{fs}	Momentum exchange coefficient
Δx (m)	Distance between the particle center of mass in the x direction
η (Pa s)	Fluid dynamic viscosity
ρ_f (kg m ⁻³)	Fluid density
ρ_s (kg m ⁻³)	Solids density
ρ^* (kg m ⁻³)	Effective density of the suspension
$\vec{\sigma}_f$ (kg m ⁻¹ s ⁻²)	Fluid stress tensor
Φ	Solid volume fraction
Φ_{max}	Maximum packing fraction
ω (rad s ⁻¹)	Angular frequency

Table 6.1: List of symbols and their meaning

6.2 Theoretical assumptions

We consider an infinite 3D suspension of spheres in a viscous fluid. Particles are organized regularly in space, forming a 3D lattice of face-centered cubic structure (Fig. 6.1), in which all particles are separated by the same distance. Particles are organized as imbricated layers aligned along the x direction. The particle densities are identical and the fluid density and viscosity are uniform in space. The medium is initially static before the propagation of the acoustic perturbation. We only consider the translational motions of the constituents and neglected rotations. Mechanical (small amplitude) plane waves (compressional and shear waves) are propagating along the x direction. The long wavelength approximation allow us to neglect the resonance of the waves in the solids. For simplicity, we do not include thermal effects and the direct contacts between neighboring particles, which restrict the scope of the present study to fluidized suspension and eruptible magmas.

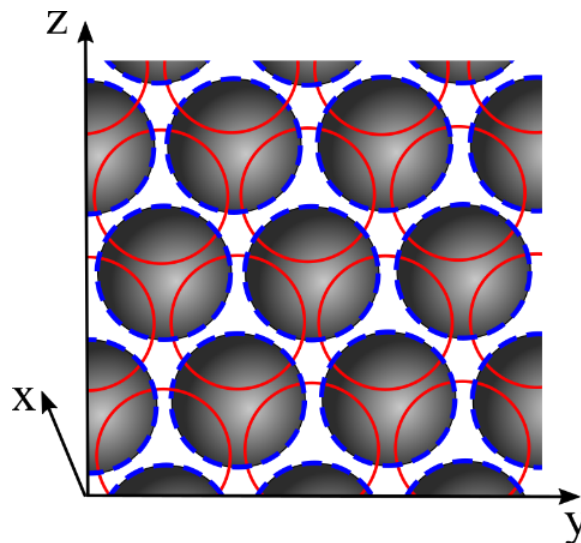


Figure 6.1: Conceptual medium considered in the present study viewed parallel to the x direction. The medium is composed by a suspension of spheres organized regularly in a cubic face-centered 3D lattice. 3 layers of particles along the x axis are represented in the drawing. The first layer is displayed as shaded spheres. The particles located on the second layer (above layer 1) are indicated with red open circles. The particles located on the third layer (above layer 2) are plotted with open and blue dashed circles.

6.3 Method

6.3.1 Conservative equations of the phases

The propagation of acoustic perturbation in suspension may be described with the continuum conservation equation of both the melt and the particulate phase (e.g. Atkinson and Kytömaa, 1992; Harker and Temple, 1988; Valier-Brasier et al., 2015). Contrary to chapters 3 and 4, the present approach requires to use a Two-Fluids model in which the two phases are considered as two interpenetrating continua (e.g. Dufek and Bachmann, 2010; Molina et al., 2012). The conservation equations for the solid phase have to be derived in Eulerian formulations rather than in discrete notations. The mass conservation for the carrier compressible fluid reads (Ishii and Hibiki, 2011):

$$\frac{\partial (1-\phi) \rho_f}{\partial t} + \nabla \cdot ((1-\phi) \rho_f \vec{v}_f) = 0, \quad (6.1)$$

where ϕ is the solids volume fraction, ρ_f is the fluid density, and \vec{v}_f is the fluid velocity vector (see table 6.1 for a list of the chapter symbols and their meaning). Similarly, the mass conservation of the compressible solid phase is expressed as (Ishii and Hibiki, 2011):

$$\frac{\partial \phi \rho_s}{\partial t} + \nabla \cdot (\phi \rho_s \vec{v}_s) = 0, \quad (6.2)$$

where ρ_s is the solid density, and \vec{v}_s is the solids velocity vector. The compressible momentum conservation of the fluid phase is (Ishii and Hibiki, 2011):

$$\frac{D((1-\phi) \rho_f \vec{v}_f)}{Dt} + (1-\phi) \cdot \nabla P - \nabla \cdot \overline{\overline{\sigma}}_f + \overline{\overline{I}}_{fs} - \rho_f \vec{g} = 0, \quad (6.3)$$

where the first term in the right hand side is the material derivative, P is the fluid pressure, $\overline{\overline{\sigma}}_f$ is the viscous stress tensor, $\overline{\overline{I}}_{fs}$ expresses the momentum coupling between the fluid and the solids, and \vec{g} is the gravitational acceleration vector. For the solids, the momentum conservation reads (Ishii and Hibiki, 2011):

$$\frac{D(\phi \rho_s \vec{v}_s)}{Dt} + \phi \cdot \nabla P - \vec{I}_{fs} - \vec{I}_{ss} - \rho_s \vec{g} = 0, \quad (6.4)$$

where \vec{I}_{ss} is the solid-solid momentum coupling term. As we neglected the collisional and frictional contacts between the particles, we do not include the granular phase stress tensor usually used in a two fluid model (e.g. Molina et al., 2012; Syamlal and O'Brien, 1988). To close the equation system, we used the equation of state of both phases that describe the coupling between the pressure and density oscillations (Harker and Temple, 1988):

$$\frac{\partial \rho_f}{\partial P} = \frac{\rho_f}{K_f} \quad (6.5a)$$

$$\frac{\partial \rho_s}{\partial P} = \frac{\rho_s}{K_s} \quad (6.5b)$$

where K_f is the bulk modulus of the fluid, and K_s is the bulk modulus of the solids.

6.3.2 Fluid-solid and solid-solid momentum couplings

The momentum transfer term between the solids and the surrounding fluid generally includes both the effects of steady and unsteady relative motions between the phases, and is expressed as:

$$\vec{I}_{fs} = \vec{F}_D + \vec{F}_{VM} + \vec{F}_B, \quad (6.6)$$

where \vec{F}_D is the drag force, \vec{F}_{VM} is the virtual mass force, and \vec{F}_B is the Basset force. The drag expresses the steady viscous forces applied by the fluid on the particles (or vice versa) because of their relative motions. The virtual mass and Basset forces are the inertial terms and both depend on the relative acceleration between the particles and the fluid. The virtual mass describes the effect of the force needed to move a volume of fluid when a particle is accelerating. The Basset term expresses the effect of the variation in the size of the viscous boundary layers that surround the particles. The relative importance between the viscous and inertial effects may be expressed as a function of the oscillatory Reynolds number (Atkinson and Kytömaa, 1992):

$$Re_\Omega = \sqrt{\frac{\rho_f \omega d_p^2}{8 \eta}}, \quad (6.7)$$

where ω is the angular frequency of the plane wave, d_p is the particle diameter, and η is the fluid dynamic viscosity. The transition between viscously to inertially dominated momentum exchanges occurs when (Atkinson and Kytömaa, 1992):

$$\omega = \frac{16 \eta}{d_p^2 \rho_f} \left(\frac{(\Phi/\Phi_{max})^{2/3}}{(1-(\Phi/\Phi_{max})^{1/3})^2} \right), \quad (6.8)$$

where Φ_{max} is the maximum solid volume fraction at which crystals touch each other. Combining equation (6.7) and (6.8) gives the critical oscillatory Reynolds number at which the transition between viscous and inertial interactions occurs:

$$Re_{\Omega}^{crit} = \sqrt{2 \left(\frac{(\Phi/\Phi_{max})^{2/3}}{(1-(\Phi/\Phi_{max})^{1/3})^2} \right)}. \quad (6.9)$$

The incorporation of the drag force in the two-fluid model requires to identify the forces that may be neglected and to determine the appropriate momentum transfer term for the present application.

In the absence of contacts between the solids, the momentum exchange coefficient is reduced to the lubrication forces. In a Lagrangian framework, both normal and tangential lubrication forces (rolling and twisting motions may be neglected, Marzougui et al., 2015) may be expressed as (see chapter 3):

$$\overrightarrow{F}_{lub} = - \frac{3 \eta \Delta \overrightarrow{v}_s}{\rho_p d_p^2} A, \quad (6.10)$$

where $\Delta \overrightarrow{v}_s$ is the relative velocity vector between the particles. The coefficient A is a geometrical parameter that relates to the normal and tangential components of the lubrication force:

$$A = \frac{3 \cos(\beta)}{2 j} - \ln(j) \sin(\beta), \quad (6.11)$$

where β is an incidence angle representing the angle between the direction that links the particle centers of mass and the relative velocity vector (see chapter 3). The index j is the ratio of the distance separating the particle and their radius, which may be approximated as a function of the solid volume fraction and maximum packing fraction ($\Phi_{max} \approx 0.64$ here) as (Ancy et al., 1999):

$$j = 1 - \left(\frac{\Phi}{\Phi_{max}} \right)^{1/3}. \quad (6.12)$$

The incorporation of the lubrication forces in Eq. (6.4) requires expressing the lubrication forces in a continuous formulation.

6.3.3 Calculation of the acoustical properties of the suspension

Once the conservative equations of the constituents are expressed, we compute the velocities and attenuation coefficients of compressional and shear waves with the coupled phase approach, using the same mathematical steps as in previous works (Atkinson and Kytömaa, 1992; Evans and Attenborough, 1997; Harker and Temple, 1988; Kytömaa, 1995; Margulies and Schwarz, 1994; Valier-Brasier et al., 2015). This requires to linearize the conservative equations (Eq 6.1–6.4) and to impose perturbations around the static conditions of the variables that are affected by the wave propagation (here the pressure and the constituent densities, velocities and concentrations) with wave-like solutions (here for a quantity \mathcal{A} : $\mathcal{A} = \bar{\mathcal{A}}e^{i(kx-\omega t)}$). These oscillatory terms depend on the angular frequency and the complex wavenumber, k (noted here for compressional waves, P):

$$k_P = \frac{\omega}{V_P} + i \alpha_P \quad (6.13)$$

where V_P is the compressional wave velocity and α_P the attenuation coefficient. The method consists in finding k_P that satisfies Eqs. (6.1–6.4), knowing ω and the physical properties of the constituents. Then, the propagation velocities and attenuation coefficients of the suspension may be deduced from the real and imaginary parts of k_P , respectively.

Species (wt%)	Basalt	Andesite	Dacite
SiO ₂	48.854	60.231	67.652
TiO ₂	0.985	1.152	0.448
Al ₂ O ₃	17.145	16.950	15.550
Fe ₂ O ₃	1.416	1.166	0.706
FeO	8.737	4.549	2.677
MnO	0.177	0.098	0.070
MgO	6.017	1.211	0.925
CaO	10.557	4.361	2.965
Na ₂ O	2.698	4.114	3.761
K ₂ O	1.211	3.593	4.079
P ₂ O ₅	0.217	0.600	0.189
H ₂ O	1.970	1.969	0.977
Pressure	250 MPa	250 MPa	250 MPa
Initial temperature	1250 °C	1200 °C	1100 °C

Table 6.2: Initial composition, pressure and temperature of the three magmas used in the present study

6.3.4 Magmas under consideration

We consider three magmas representative of the different compositions that may be encountered in arc magmatic systems (basalt, andesite, and dacite). We simulated the isobaric cooling and crystallization of magmas using the MELTS model (Ghiorso, 2004; Ghiorso and Kress, 2004) in the software PELE (Boudreau, 1999) at a pressure of 250 MPa using the Ni-NiO buffer for the andesitic and dacitic magmas and the QFM (Quartz-Fayalite-Magnetite) buffer for the basaltic melt. The initial melt compositions are taken from Dufek and Bachmann (2010) (see table 6.2). However, we decreased the initial content in dissolved H₂O to ensure that the concentration in dissolved water remains below the saturation threshold, and avoid bubble exsolution by second boiling. To compute the compressional wave velocities and attenuation coefficients in our model, we used the melt density and bulk modulus computed during these crystallization simulations. The melt viscosities were determined using the model from Giordano et al. (2008), with the chemical compositions and temperatures of the residual melts computed

Mineral species	K_p (GPa)
Olivine	132
Pyroxene	114.2
Plagioclase	75
Feldspar	58.3
Quartz	57

Table 6.3: Bulk modulus of the mineral phases. Data from Hacker et al. (2003).

during the crystallization simulations. For the solids, we used the averaged densities of the crystals that is output during the simulations. The average bulk modulus of the solids is computed with the relative proportions of the mineral species and the representative values reported by Hacker et al. (2003) (see table 6.3).

6.4 Results

The physical properties of the magmas are required to develop the wave model because they justify simplifying assumptions a priori. Thereby, this section first presents the results of the simulation of the cooling and crystallization of the magma before describing the model and its application.

6.4.1 Magmas physical properties

Figure 6.2 displays the evolution of the properties of the basaltic, andesitic and dacitic magmas with temperature and crystal content. During cooling, the melt densities and bulk moduli decrease with the decrease in temperature (Fig 6.2 A–B), and increase in crystal content (Fig. 6.2 G–H), whereas melt viscosities decrease with temperature (Fig 6.2 C). The dacitic and andesitic melts show similar bulk modulus in a wide range of temperature and crystal content (Fig 6.2 B and H). The density of the basaltic melt changes more steeply with temperature or crystal content than the andesitic and dacitic melts because olivine plus pyroxene crystallization withdraws Fe from the melt.

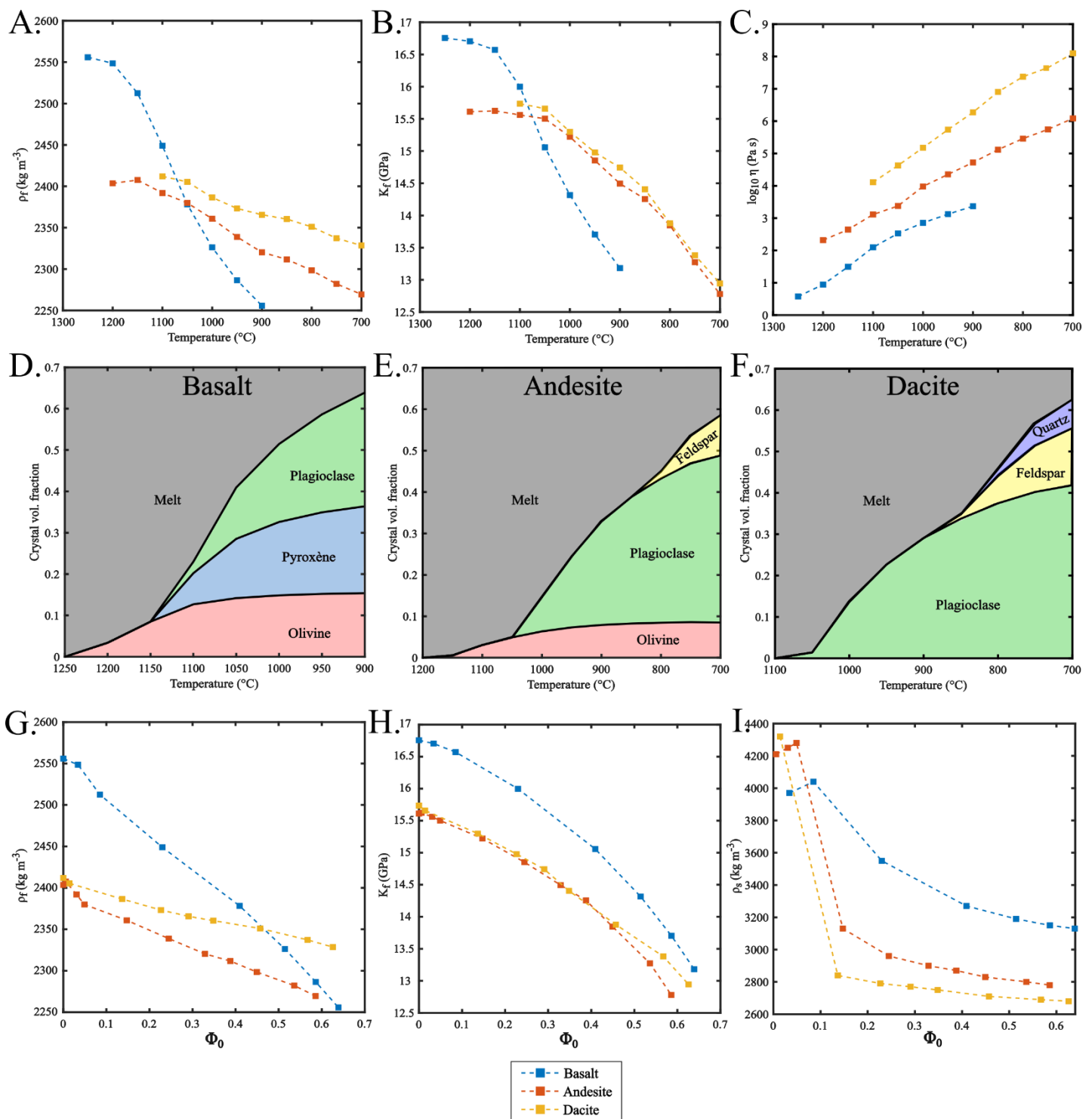


Figure 6.2: Modeling of the cooling and crystallization of the three magmas using the PELE software. [A] Evolution of the melt densities as a function of temperature. [B] Melt bulk moduli with temperature. [C] Dynamic viscosities of the melts as a function of temperature. Graphs [D], [E] and [F] represent the proportions of melt and crystal species during the cooling of the basalt (D), andesite (E), and dacite (F). [G] Evolution of the melt density respect to the crystal volume fraction. [H] Melt bulk moduli as a function of the crystals content. [I] Density of the solids computed with PELE as a function of crystal content. In the graphs [A]–[C] and [G]–[I], the squares represent the PELE simulation outputs that are used to compute the velocities and attenuation coefficient of compressional waves.

6.4.2 Fluid-solid momentum coupling

Figure 6.3 displays the oscillatory Reynolds numbers computed during the cooling of the magmas as functions of crystal content and frequency. Except for the basalt below 10% volume fraction of crystals, it shows that at seismic frequencies (<100 Hz) $Re_\Omega \ll Re_\Omega^{crit}$, which means that for most magmatic conditions, the unsteady inertial forces may be neglected compared to the steady viscous term (Atkinson and Kytömaa, 1992). Thereby, the momentum exchange term is simply expressed as:

$$\overline{I}_{fs} = \beta_{fs} (\overline{v}_f - \overline{v}_s), \quad (6.14)$$

where β_{fs} is the momentum exchange coefficient. To compute β_{fs} , the Gidaspow's drag correlation, which is widely used in multiphase flow modeling, may be simplified for the present application by combining a Stokes drag law at low particle volume fraction and a Kozeny-Carman relationship for high concentrations in solids (see supplementary section 6.1):

$$\beta_{fs} = \begin{cases} \frac{18 \eta \Phi}{d_p^2} & \Phi \leq \frac{3}{28} \\ \frac{150 \Phi^2 \eta}{(1-\Phi) d_p^2} & \Phi > \frac{3}{28} \end{cases} \quad (6.15)$$

Equation (6.15) is suitable for a coupled phase approach because both the Stokes and Kozeny-Carman relationships depend linearly on the relative velocity between the particles and the fluid.

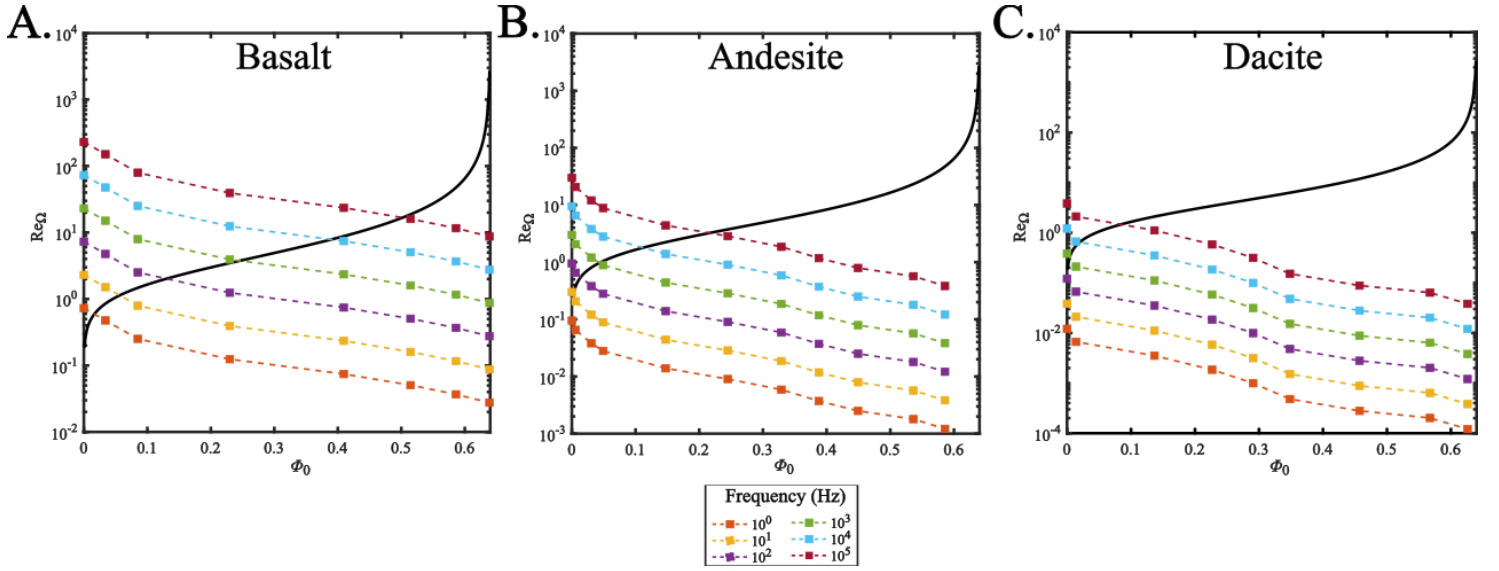


Figure 6.3: Oscillatory Reynolds numbers as a function of crystal content and perturbation frequency. In each graph, the solid black curve is the critical Reynolds number that separates inertial conditions (above the curve) from viscous conditions (below the curve). The three graphs represent the cooling of a basalt [A], an andesite [B], and a dacite [C]. In each graph, the squares represent the PELE outputs.

6.4.3 Solids-solids momentum coupling

To incorporate lubrication forces into the solids momentum equation, we focus on one particle of the system (displayed with a red boundary on layer 2 in Fig. 6.4 A). All the particles located on the same layer have the same velocity because the oscillations are perpendicular to the particle layers. The oscillating nature of the flow imposes that a velocity gradient exists in space within the solids phase. Thereby, the particle of interest experiences relative motions and lubricated interactions with its neighbors located in layers 1 and 3: $\vec{v}_s(1) > \vec{v}_s(2) > \vec{v}_s(3)$ (Fig. 6.4 B). The total lubrication force experienced by the target particle is the sum of all the individual lubricated forces with its neighbors:

$$\vec{F}_{lub}(2) = \frac{9\eta_f A}{\rho_p d_p^2} (\vec{v}_s(1) + \vec{v}_s(3) - 2\vec{v}_s(2)), \quad (6.16)$$

The sum in the parenthesis of Eq. (6.16) may be approximated by the second derivative in space of the solids velocity as:

$$\Delta x^2 \frac{\partial^2 \vec{v}_s}{\partial x^2} \cong \vec{v}_s(1) + \vec{v}_s(3) - 2\vec{v}_s(2), \quad (6.17)$$

where Δx is the distance in the x direction between the center of mass of particles located in successive layers. By geometrical relationship, this distance can be expressed as:

$$\Delta x = \sqrt{\frac{2}{3}} \left(d_p \left(1 + \frac{j}{2} \right) \right). \quad (6.18)$$

Combining Eqs. (6.16), (6.17), and (6.18) gives the momentum exchange term between the solids:

$$\vec{T}_{ss} = \vec{F}_{lub} = \frac{6 \eta_f \left(1 + \frac{j}{2} \right)^2 A}{\rho_p} \frac{\partial^2 \vec{v}_p}{\partial x^2}. \quad (6.19)$$

From geometrical arguments, the incidence angle β may be deduced and gives $\beta = \cos^{-1}(\sqrt{2/3})$ for compressional waves (relative motion in the x direction), and $\beta = \pi/2 - \cos^{-1}(\sqrt{2/3})$ for shear waves (relative motion in the y direction).

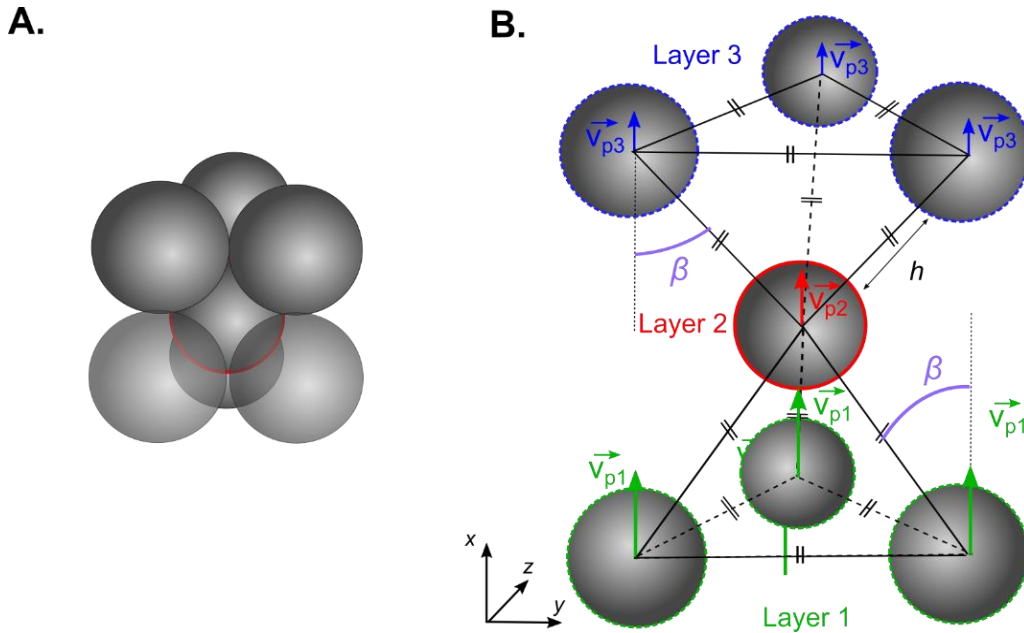


Figure 6.4. Conceptual model used to derive the solids-solids momentum transfer term. [A] Schematic representation of the particle organization around a target particle (indicated with a red boundary), viewed from the side. [B] Schematic zoom on the lubricated interactions between the target particles and its neighbors (For a compressional wave propagating in the x direction here). The color of the particle boundaries depend on the layer in which the particles are located (green for layer 1, red for layer 2 and target particle, and blue for layer 3). Arrows represent the particle velocity vectors. The incidence angle β is represented in purple.

6.4.4 Wave velocities and attenuation coefficients in suspensions

6.4.4.a Compressional waves

According to Dingwell and Webb (1989), the melt volume viscosity, λ , may be assumed as equal to a third of the shear viscosity, η . Thereby, for a plane wave travelling in the x direction, the viscous stress tensor of the fluid phase may be expressed for a compressional wave as:

$$\bar{\sigma}_f = \frac{7}{3} (1 - \phi) \eta \frac{\partial v_{f_x}}{\partial x}, \quad (6.20)$$

Following the common derivation of the acoustical properties of a suspension (e.g. Atkinson and Kytömaa, 1992; Harker and Temple, 1988), the propagation of a compressional wave in a material imposes the oscillation of variables around their static values. The dynamic variables are defined as:

$$\rho_f = \rho_{f_0} + \rho_f', \quad (6.21a)$$

$$\rho_s = \rho_{s_0} + \rho_s', \quad (6.21b)$$

$$v_{f_x} = v_{f_x}', \quad (6.21c)$$

$$v_{s_x} = v_{s_x}', \quad (6.21d)$$

$$P = P_0 + P', \quad (6.21e)$$

$$\phi = \phi_0 + \phi', \quad (6.21f)$$

where ρ_{f_0} , ρ_{s_0} , P_0 , and ϕ_0 , are the static fluid density, solid density, pressure, and crystal content, respectively. Variables ρ_f' , ρ_s' , v_{f_x}' , v_{s_x}' , P' , and ϕ' are the oscillation of the fluid density, solids density, fluid velocity, solids velocity, pressure, and crystal content (the indices x in the velocity symbols indicate flow directions). Incorporating Eqs. (6.14), (6.19), (6.20), and (6.21a–f) into Eqs. (6.1)–(6.6) and linearizing the resulting equations yields to the following system that describes the motion of a two-phase compressible flow imposed by a compressional wave propagating in the x direction:

$$(1 - \phi_0) \frac{\partial \rho_f'}{\partial t} - \rho_{f_0} \frac{\partial \phi'}{\partial t} + (1 - \phi_0) \rho_{f_0} \nabla \cdot (v_{f_x}') = 0, \quad (6.22a)$$

$$\phi_0 \frac{\partial \rho_s'}{\partial t} + \rho_{s0} \frac{\partial \phi'}{\partial t} + \phi_0 \rho_{s0} \nabla \cdot (v_{sx}') = 0, \quad (6.22b)$$

$$(1 - \phi_0) \rho_{f0} \frac{\partial v_{fx}'}{\partial t} + (1 - \phi_0) \nabla \cdot P' - B \nabla \cdot \left(\frac{\partial v_{fx}'}{\partial x} \right) + \beta_{fs} (v_{fx}' - v_{sx}') = 0, \quad (6.22c)$$

$$\phi_0 \rho_{s0} \frac{\partial v_{sx}'}{\partial t} + \phi_0 \nabla \cdot P' - C \frac{\partial^2 v_{fx}'}{\partial x^2} - \beta_{fs} (v_{fx}' - v_{sx}') = 0, \quad (6.22d)$$

$$\frac{\partial \rho_f'}{\partial P'} - \frac{\rho_{f0}}{K_f} = 0, \quad (6.22e)$$

$$\frac{\partial \rho_s'}{\partial P'} - \frac{\rho_{s0}}{K_s} = 0, \quad (6.22f)$$

with,

$$B = \frac{7}{3} (1 - \phi) \eta, \quad (6.23)$$

$$C = \frac{6 \eta_f \left(1 + \frac{j}{2}\right)^2 A}{\rho_p}. \quad (6.24)$$

Each oscillating term is replaced by a wave like solution following:

$$\rho_f' = \bar{\rho}_f e^{i(k_px - \omega t)}, \quad (6.25a)$$

$$\rho_s' = \bar{\rho}_s e^{i(k_px - \omega t)}, \quad (6.25b)$$

$$v_{fx}' = \bar{v}_f e^{i(k_px - \omega t)}, \quad (6.25c)$$

$$v_{sx}' = \bar{v}_s e^{i(k_px - \omega t)}, \quad (6.25d)$$

$$P' = \bar{P} e^{i(k_px - \omega t)}, \quad (6.25e)$$

$$\phi' = \bar{\phi} e^{i(k_px - \omega t)}, \quad (6.25f)$$

where $\bar{\rho}_f$, $\bar{\rho}_s$, \bar{v}_f , \bar{v}_s , \bar{P} , and $\bar{\phi}$ are the amplitudes of the oscillations of the fluid density, solid density, fluid velocity, solid velocity, pressure, and particle volume fraction, respectively. Merging Eqs (6.25a–f) and Eqs (6.22a–f) gives the following matrix equation:

$$M_p \begin{bmatrix} \bar{\rho}_f \\ \bar{\rho}_s \\ \bar{v}_f \\ \bar{v}_s \\ \bar{\phi} \\ \bar{P} \end{bmatrix} = 0 \quad (6.26)$$

with

$$M_p = \begin{bmatrix} -i\omega(1-\phi_0) & 0 & ik_p(1-\phi_0)\rho_{f_0} & 0 & i\omega\rho_{f_0} & 0 \\ 0 & -i\omega\phi_0 & 0 & ik_p\phi_0\rho_{s_0} & -i\omega\rho_{s_0} & 0 \\ 0 & 0 & (\beta_{fs} - i\omega(1-\phi_0)\rho_{f_0} + k_p^2 B) & -\beta & 0 & ik_p(1-\phi_0) \\ 0 & 0 & -\beta & (\beta_{fs} - i\omega\phi_0\rho_{s_0} + k_p^2 C) & 0 & ik_p\phi_0 \\ 1 & 0 & 0 & 0 & 0 & -\frac{\rho_{f_0}}{K_f} \\ 0 & 1 & 0 & 0 & 0 & -\frac{\rho_{s_0}}{K_s} \end{bmatrix} \quad (6.27)$$

The non-trivial solution of Eq. (6.26) implies to find the complex wavenumbers, k_p , for which $\det\|M_p\| = 0$ as functions of the angular frequency, the proportions of each constituent, and their material properties. Then the compressional wave velocity and attenuation coefficient, α_p , are deduced from the real and imaginary parts of k_p , respectively.

6.4.4.b Shear waves

For a shear wave, no compression of the constituents occurs and the effect of volume viscosity vanish because the trace of the strain rate tensor of the fluid is null. The viscous stress tensor may be expressed as:

$$\bar{\bar{\sigma}}_f = (1 - \phi) \eta \frac{\partial v_{fy}}{\partial x}. \quad (6.28)$$

The absence of compression also reduces the number of oscillating variables to the two constituent velocities:

$$v_f = v_f', \quad (6.29a)$$

$$v_s = v_s', \quad (6.29b)$$

For the same reason, the two remaining conservative equations are:

$$(1 - \phi_0) \rho_{f_0} \frac{\partial v_{fy}'}{\partial t} - B \nabla \cdot \left(\frac{\partial v_{fy}'}{\partial x} \right) + \beta_{fs} (v_{fy}' - v_{sy}') = 0 \quad (6.30a)$$

$$\phi_0 \rho_{s0} \frac{\partial v_{sy}'}{\partial t} - C \frac{\partial^2 v_{fy}'}{\partial x^2} - \beta_{fs} (v_{fy}' - v_{sy}') = 0 \quad (6.30b)$$

As for compressional waves, the oscillatory terms in Eqs. (6.29a–b) are replaced by:

$$v_{fy}' = \overline{v_{fy}} e^{i(k_s x - \omega t)}, \quad (6.31a)$$

$$v_{sy}' = \overline{v_{sy}} e^{i(k_s x - \omega t)}, \quad (6.31b)$$

Plugging Eqs (6.31a–b) into Eqs (6.30a–b) yields:

$$M_s \begin{bmatrix} \overline{v_{fy}} \\ \overline{v_{sy}} \end{bmatrix} = 0, \quad (6.32)$$

with

$$M_s = \begin{bmatrix} \beta_{fs} + k_s^2 (1 - \Phi_0) \eta - i \omega (1 - \Phi_0) \rho_{f0} & -\beta_{fs} \\ -\beta_{fs} & \beta_{fs} + k_s^2 C - i \omega \Phi_0 \rho_{s0} \end{bmatrix} \quad (6.33)$$

After finding k_s so that $\det \|M_s\| = 0$, the shear wave velocity and attenuation coefficient are deduced from the real and imaginary part of k_s , respectively.

6.4.5 Compressional waves in suspensions

To explore the effect of each physical parameter of the suspension on the seismic wave velocities and attenuation coefficients, we define reference conditions for which the densities and bulk moduli of the constituents are identical. Then each parameter is varied in turn independently from the others. Figure 6.5 displays the velocities of compressional waves in a suspension as functions of the concentration, density, and bulk modulus of the solids. The velocities of compressional waves computed by solving Eq. (6.26) are identical to the low frequency limit and may be computed with the Reuss bound (Reuss, 1929), in which the compressional wave velocity is $V_p = \sqrt{K^*/\rho^*}$, where K^* and ρ^* are the effective bulk modulus and density of the suspension given by:

$$\frac{1}{K^*} = \frac{(1-\Phi_0)}{K_f} + \frac{\Phi_0}{K_p}, \quad (6.34)$$

and:

$$\rho^* = (1 - \Phi_0) \rho_{f_0} + \Phi_0 \rho_{s_0}. \quad (6.35)$$

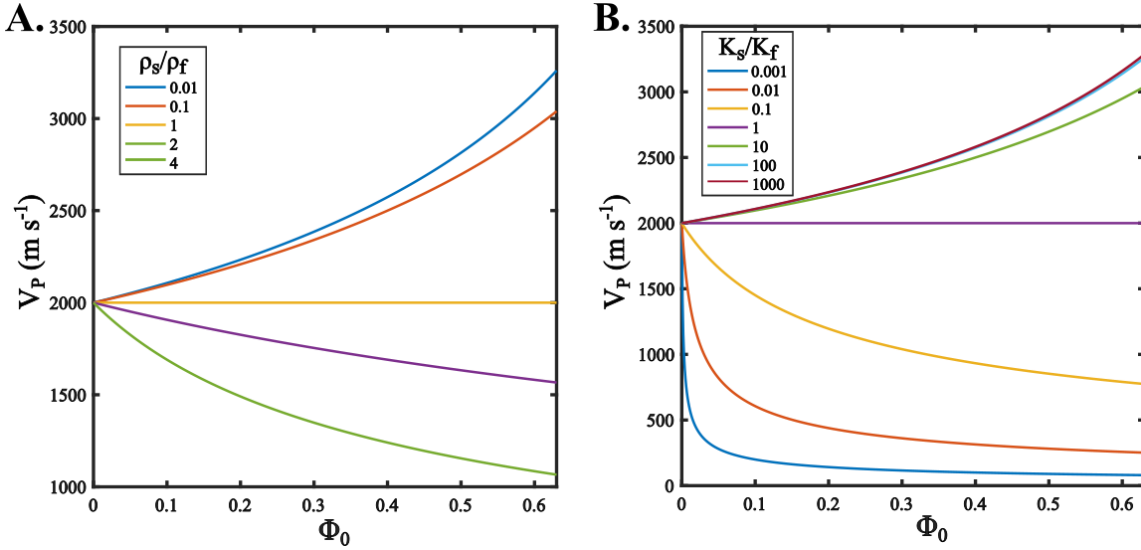


Figure 6.5: Compressional wave velocity as a function of the solid volume fraction. [A] Effect of the ratio between the solid and fluid densities. [B] Effect of the ratio between the solid and fluid bulk moduli. For the two graphs, the constant physical parameters used were $\rho_{s_0} = 2500 \text{ kg m}^{-3}$, $\rho_{f_0} = 2500 \text{ kg m}^{-3}$, $K_f = 10 \text{ GPa}$, $K_s = 10 \text{ GPa}$, $f = 100 \text{ Hz}$, $d_p = 1 \text{ mm}$, $\eta = 1000 \text{ Pa s}$. We varied ρ_{s_0} in (A) and K_s in (B).

Parameter	Value
ρ_f	2500 kg m^{-3}
ρ_s	2500 kg m^{-3}
K_f	10 Gpa
K_s	10 Gpa
d_p	1 mm
η	1000 Pa s
f	100 Hz

Table 6.4: Reference parameters used to compute the seismic properties of the suspension.

Figure 6.6 displays the variations of compressional wave attenuation as a function of the crystal volume fraction by varying separately different physical parameters of the suspension. The wave frequency, fluid viscosity, and contrast between the bulk modulus of the carrier and suspended phases are the main parameters that control the attenuation coefficients (Fig 6.6 A and C–D). The attenuation coefficient increases as the square of the frequency and linearly with the melt viscosity because of the dissipation imposed by the viscous stress tensor. The contrast between the bulk modulus of the constituents greatly increases α_p when the suspended phase is more compressible than the carrier (Fig 6.6 D). The attenuation is minimum when $K_s > 100 K_f$. The difference between the density of the fluid and that of the suspended phase has a weaker effect on the attenuation coefficients, which are minimized when the density ratio approaches unity (Fig. 6.6 E). In the range of magmatic crystal sizes, particle diameter has no effect on α_p (Fig. 6.6 B). All the curves display a sharp increase in attenuation when the concentration in solids approaches the maximum packing fraction (0.64) because of the short-range lubrication forces.

Figure 6.7 displays the relative importance of the three main dissipation mechanisms (the relative motion between the constituents, the viscous dissipation, and the lubrication forces) in magmas as functions of melt viscosity and crystal content. The other physical properties of the constituents are kept at representative values (Table 6.5). At low viscosity ($\eta = 10$ Pa s), the attenuation of compressional waves is dominated by the relative motion between the solids and the fluid. Both viscous dissipation and lubrication have negligible effects on the attenuation coefficient. At a viscosity of 100 Pa s, while the effect of relative motion is still dominant, the viscous and lubrication effects are significant (Fig. 6.7 B). The amount of dissipation resulting from lubrication reaches 10% in the vicinity of the maximum packing fraction (~ 0.64). At the maximum viscosity ($\eta = 1000$ Pa s), viscous dissipation dominates the effects of the relative motion between the two phases and of the lubrication forces (Fig. 6.7 C). The dissipation resulting from lubrication reaches 15% of the total attenuation close to the maximum packing fraction of the solids.

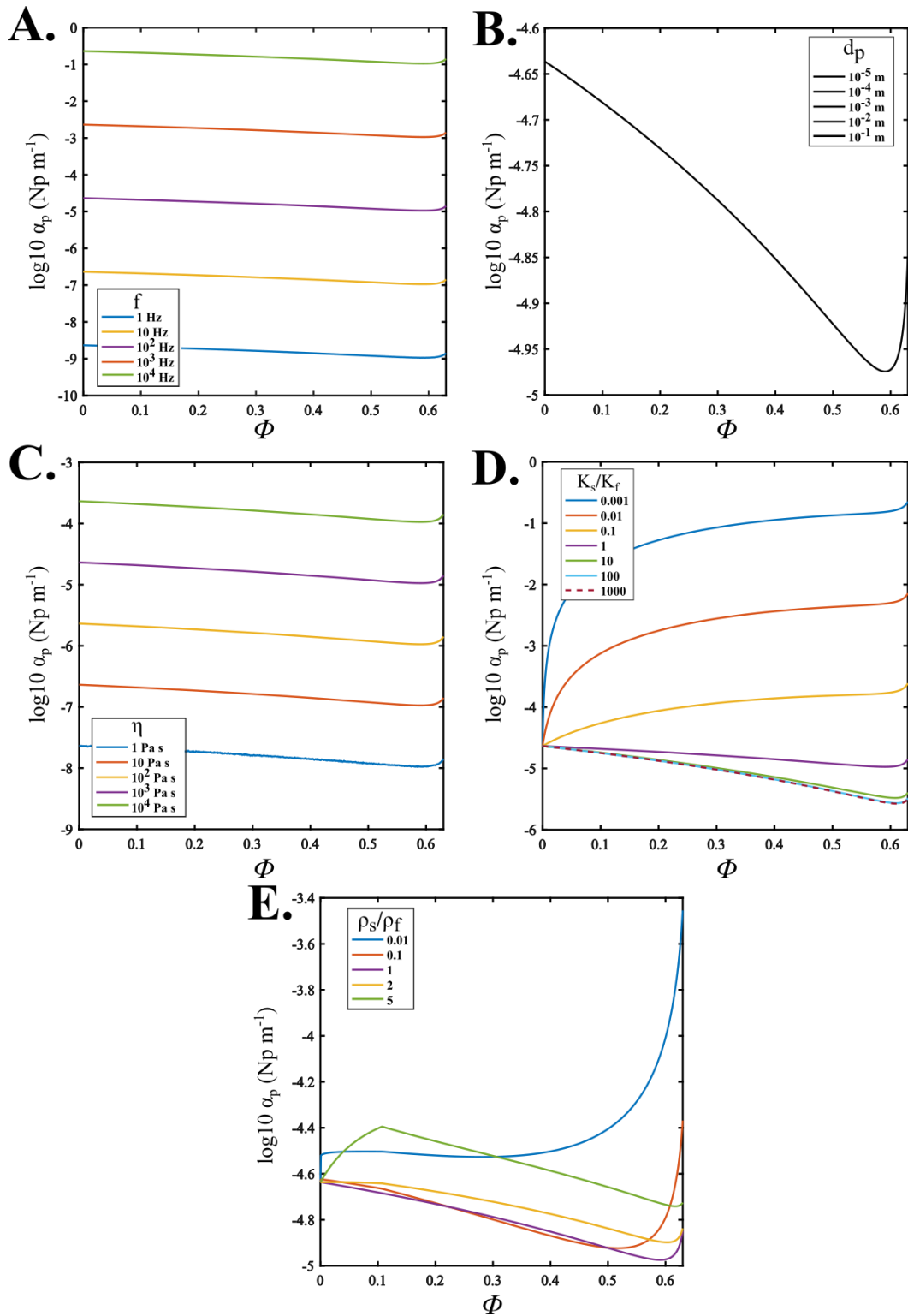


Figure 6.6: Compressional wave velocity as functions of solid volume fraction and physical properties of the constituents. For all graphs, the constant physical parameters used were $\rho_{s0} = 2500 \text{ kg m}^{-3}$, $\rho_{f0} = 2500 \text{ kg m}^{-3}$, $K_f = 10 \text{ GPa}$, $K_s = 10 \text{ GPa}$, $f = 100 \text{ Hz}$, $d_p = 1 \text{ mm}$, $\eta = 1000 \text{ Pa s}$. Each parameter was varied independently from the others. The effect of the perturbation frequency [A], particle diameter [B], fluid viscosity [C], bulk modulus contrast [D], and density contrast [E] were explored. Results are presented in neper per meter, which is the natural logarithm between the initial amplitude and amplitude after 1 m of propagation.

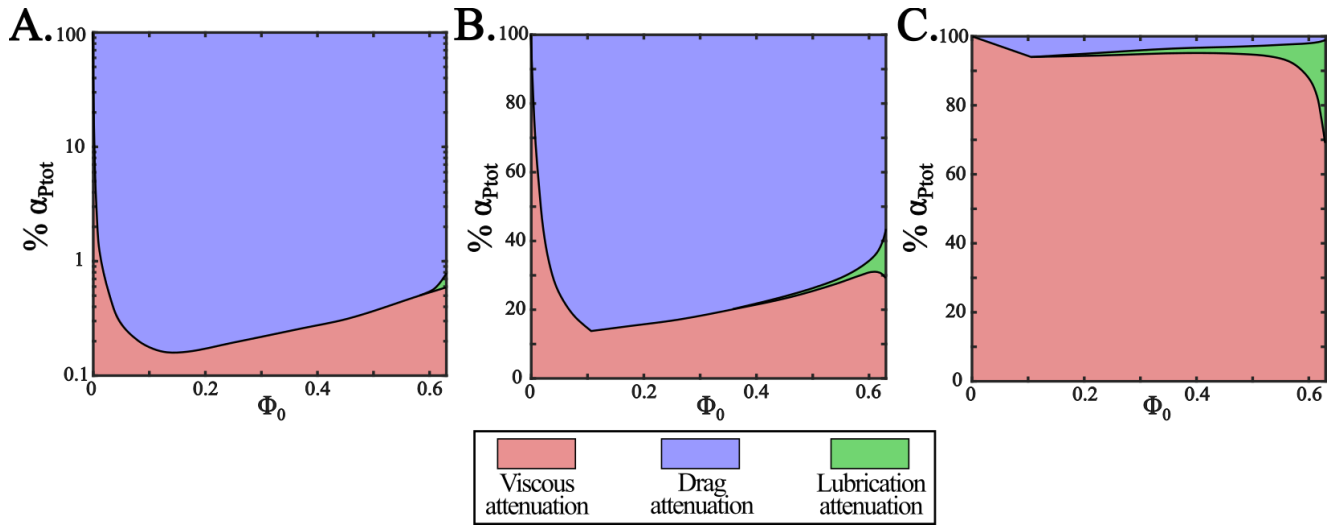


Figure 6.7: Relative importance of dissipation mechanisms of compressional waves in suspensions as a function of the solid volume fraction. For all graphs, the constant physical parameters used were $\rho_{s0} = 3300 \text{ kg m}^{-3}$, $\rho_{f0} = 2500 \text{ kg m}^{-3}$, $K_f = 10 \text{ GPa}$, $K_s = 100 \text{ GPa}$, $f = 100 \text{ Hz}$, $d_p = 1 \text{ mm}$. The viscosities used were $\eta = 10 \text{ Pa s}$ [A], $\eta = 100 \text{ Pa s}$ [B], $\eta = 1000 \text{ Pa s}$ [C]. Note the logarithmic scale of the ordinate axis of (A)

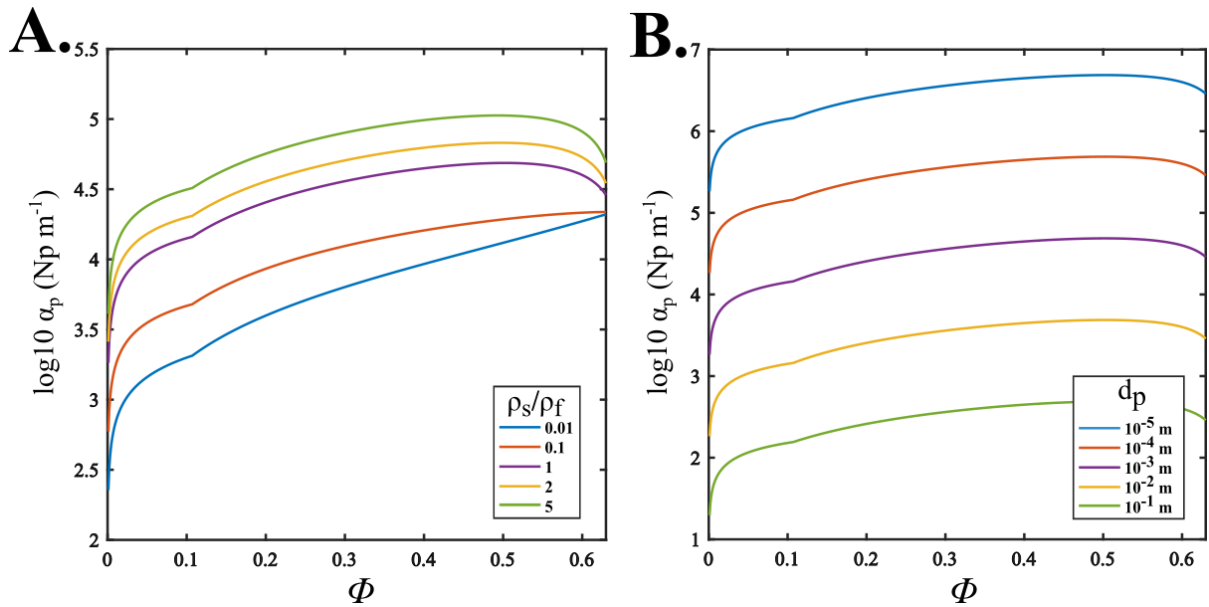


Figure 6.8: Attenuation coefficient of shear wave in suspensions as a function of the solid volume fraction. [A] Effect of the density difference between the solids and the fluid. [B] Effect of the particle diameter.

Parameter	Value
ρ_f	2500 kg m ⁻³
ρ_s	3300 kg m ⁻³
K_f	10 Gpa
K_s	100 Gpa
d_p	1 mm
η	10-1000-1000 Pa s
f	100 Hz

Table 6.5: Physical parameters used to discriminate the relative importance of each dissipation mechanism.

6.4.6 Shear waves in suspensions

Figure 6.8 displays the evolution of the attenuation coefficient for a shear wave as a function of the solid volume fraction for the two parameters that affect α_s : the density ratio between the two constituents and the particle diameter. The attenuation increases with the density ratio and decreases with the particle diameter. The attenuation coefficient for S waves is very large, which means that shear waves rapidly vanish. Unlike compressional waves, the lubrication forces decrease the attenuation of S waves close to the maximum packing fraction.

6.4.7 Application to magmas

We used the simulations of the cooling and crystallizations of the basalt, andesite, and dacite, to compute the compressional wave velocities (Fig. 6.9). The solids densities are set to the averaged densities computed during the PELE simulations (Fig. 6.2 I). The solids bulk moduli are set to the weighted averages computed with the proportions of different mineral species and their individual bulk modulus (see Table 6.3; Hacker et al., 2003). The dacitic and andesitic magmas have similar compressional wave velocities at a given temperature, whereas the basalt has higher velocities (Fig. 6.9 A). When the compressional wave velocities in the magmas are compared as a function of the respective crystal contents, the three curves merge (Fig. 6.9 B).

Contrary to the velocities, the intrinsic attenuation coefficients of compressional waves depend on the chemical composition of the magmas (Fig. 6.10). The dacite has the highest attenuations and the basalt the smallest. The curves computed for the andesitic and dacitic magmas have the same trends, showing an increase of the compressional wave attenuation coefficients with

a decrease in temperature and the concurrent increase in crystal content. On the contrary, the basalt shows initially a decrease in attenuation at the beginning of crystallization before an attenuation increase as crystallization progresses. The trends of the curves are opposed to the ones computed in Fig 6.6 because of the increase in the melt viscosities resulting from cooling and the ensuing chemical evolution during crystallization. For each composition, the increase in frequency causes a vertical translation of the curves. At a given frequency, the attenuation coefficients of the three magmas are different because of the differences in melt viscosities.

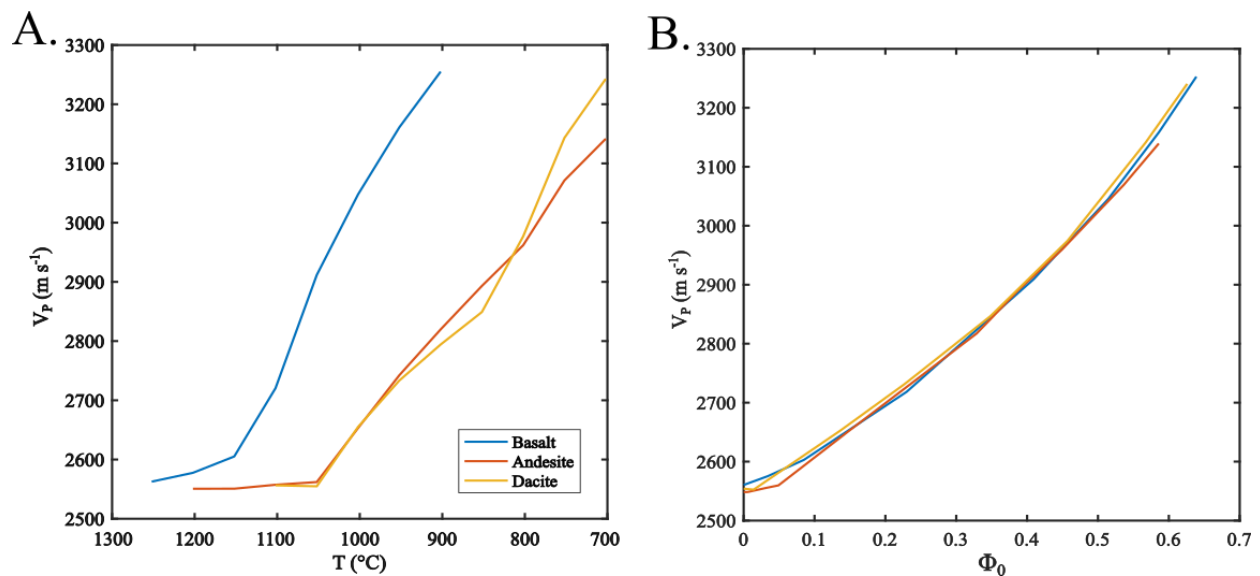


Figure 6.9: Compressional wave velocities in three magmas. [A] Comparison of the velocities of P waves in the basaltic, andesitic and dacitic magmas as a function of temperature. [B] Comparison of the compressional wave velocities in the three magmas as a function of the solid volume fraction.

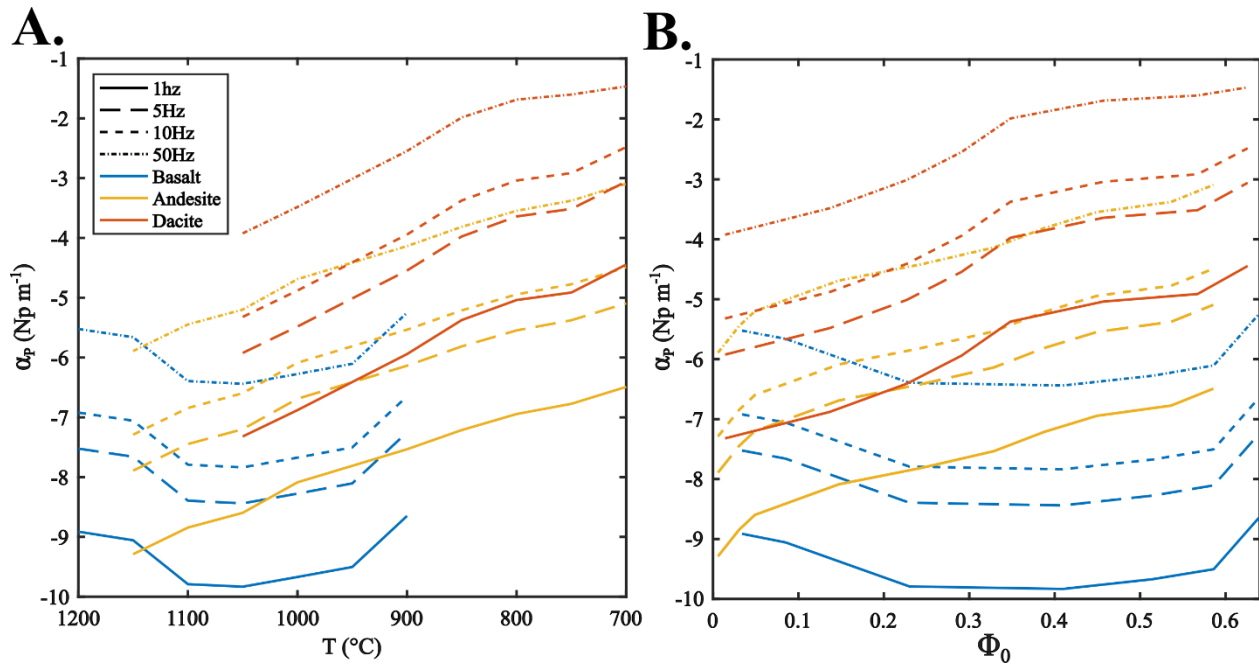


Figure 6.10: Attenuation coefficients as functions of magma composition, temperature and crystallinity. [A] Evolution of the attenuation coefficients with respect to the temperature. The colors of the curves indicate the compositions of the magmas (blue, yellow, and orange for the basalt, andesite, and dacite, respectively). The dash patterns depend on the frequency of the perturbation. [B] Same as A) as a function of the crystal content, Φ_0 .

6.5 Discussion

6.5.1 Limitations

To compute the acoustical properties of magmas, we used a conceptual suspension in which smooth spheres of identical diameters are organized regularly in space. In magmas, the crystal size distribution is often polydisperse and polymodal, and crystals are not spherical (Higgins, 2006; Higgins and Roberge, 2003; Marsh, 1988; Picard et al., 2011). Particle shape affects both the solids Poisson coefficient and Young modulus, which depend on the orientation of the elongated axes (Ahuja and Hendee, 1978; Banks-Sills et al., 1997). It also affects the drag between the carrier and suspended phases, which also becomes non uniform and dependent on the elongated axis orientation (Bergantz et al., 2017; Dellino et al., 2005; Dioguardi et al., 2014). Similarly, the shape and curvature of particles affect lubrication forces (Bergantz et al., 2017; Claeys and Brady, 1993; Janoschek et al., 2013). Both particle size distribution and particle shapes affect the solid volume fraction at which solids begin to touch each other (Bergantz et al., 2017; Faroughi and Huber, 2014b; Robert S. Farr and Groot, 2009; Nolan and Kavanagh, 1995; Ouchiyaama and Tanaka, 2002;

Zou and Yu, 1996), controlling the critical crystallinity above which the suspension has a rigidity modulus and can transmit shear waves. All these effects may break the isotropic nature of both acoustic wave velocities and attenuation coefficients, depending on the preferential orientation of the crystals. Strong preferential orientations may be induced by strain localization when magma are strained (Picard et al., 2011). The length scales of the bands of strain localization, however, are smaller than the perturbation wavelengths, and the randomness of the crystal orientation over the wave length scales averages out and reduces these anisotropic effects.

The chemical composition of the crystals affects their bulk modulus (Hacker et al., 2003). For simplicity, we considered each mineral species as having a constant bulk modulus that is independent from the solid state solution exact compositions, which are computed as the averaged composition of each species during the simulation. For example, the relative proportion between anortite (An) and albite (Ab) minerals composing the plagioclases group is not constant. For the basalt, the relative content between An and Ab of the plagioclases group varies from 0.87-0.13, at the beginning of the crystallization, to 0.67-0.32 near the end of the simulation. For a given group of minerals, however, the difference inherent to a given solid state solution is small compared to their averaged values (Hacker et al., 2003). Thus, we do not expect that the evolution of the chemical composition of the precipitated minerals has a significant impact on the seismic velocities we predict (Fig. 6.9). Also, the ratio between the bulk modulus of the solids and the fluid has a weak effect on the attenuation coefficients once the solids have a bulk modulus larger than that of the fluid (Fig. 6.6 D). We thus do not expect noticeable differences in the attenuation coefficients we estimated in Fig. 6.10 if the evolution of the chemical composition of the mineral phases were accounted for.

In our model, the fluid phase is characterized by its dynamic viscosity, bulk modulus and density, and is considered to behave as a Newtonian fluid. This assumption is perfectly valid at low frequency, in a relaxed state (Dingwell and Webb, 1990). When the frequency of the perturbation increases, however, a transition occurs in the response of the melt phase to stress, which behaves as an elastic material in unrelaxed conditions (Caricchi et al., 2008). At low frequency, the melt phase presents a vanishing shear modulus, whereas at high frequency, its shear modulus is no more null and its viscosity decreases with frequency (Bagdassarov et al., 1994; Caricchi et al., 2008; Dingwell and Webb, 1990, 1989). This transition changes the velocities of compressional and shear waves in the suspension (Caricchi et al., 2008; Kress and Carmichael, 1991). Because of the

decrease in melt viscosity, the relaxed/unrelaxed nature of the melt also influences the attenuation of perturbations. According to a Maxwell model, the transition between relaxed and unrelaxed behavior occurs when the product of the angular frequency and relaxation time is close to one (Dingwell and Webb, 1990, 1989). Thereby, the transition between the relaxed and unrelaxed states is proportional to the frequency of the perturbation and to the inverse of fluid viscosity. In our computations, we ensured that the melt phases were in a relaxed state in which melt viscosity and bulk modulus remain constant. Applying this model to experimental data obtained on magmas with ultrasounds (e.g. Caricchi et al., 2008; Kress and Carmichael, 1991), however, requires the addition of the increase in bulk and rigidity moduli and the decrease of melt viscosity caused by an increase in frequency to give reliable estimations of velocity and attenuation.

Our model neglects the thermal dissipation of acoustic energy. Even if the two phases are in thermal equilibrium before the perturbation propagates, the contrasts in heat conductivities, heat capacities, and thermal expansion coefficients of the constituents result in thermal dissipation of the energy of the wave and heat transfer between the phases. The cycle of heating and cooling of the materials during the compression and decompression results in a thermal wave that decays rapidly and that has a velocity depending on the thermal diffusivity of the constituents (Challis et al., 2005). The difference in thermal expansion coefficients results in the relative compression and extension of the particles compared to the fluid, which behave as secondary perturbation sources (Challis et al., 2005). The thermal dissipation resulting from the cyclical heating and cooling of the constituents may be incorporated in our model by adding the energy equations of both phases and by adding thermal expansion terms in the two equations of state (Eqs. 6.5a–b) (Evans and Attenborough, 2002, 1997). Because of the typically high viscosities of magmatic melts, we considered that viscous dissipations were dominant over thermal ones. Neglecting thermal dissipations result in slightly underestimating the attenuation coefficients in magmas. Similarly to thermal effects, the contrast between the bulk moduli of the suspended and carrier phases may also result in the relative contraction and dilatation of the particles with respect to the fluid, which results in the re-radiation of the acoustic perturbation. These effects are induced by the dynamic oscillation of the diameter of the suspended particles. Such behavior may be accounted for in a coupled phase approach (Valier-Brasier et al., 2015) but it is neglected here. When the discrete phase is less

compressible than the carrier, however, these effects may be neglected (Challis et al., 2005; Valier-Brasier et al., 2015; Fig 6.6 D).

Our aim was to compute the seismic properties of magmas in which crystal are suspended. However, both petrological (Wallace, 2005) and field (Wallace, 2001) evidences showed that magma bodies may contain a significant proportion (~10% tot vol.; Wallace et al., 1999) of exsolved volatiles even at upper crustal depths (up to ~20km). For the crystal contents we consider here, the gas phase is most likely to be present as isolated bubbles (Parmigiani et al., 2017, 2014). Models exist to predict the compressional wave velocities and attenuation coefficients in bubbly magmas (e.g. Collier et al., 2006; Neuberg and O’Gorman, 2002). Treating a mixture of three phases is, however, beyond the scope of the coupled phase approach. The compressional wave velocities of three-phase magmas may be computed accurately using the mixture equation and the Reuss bound (Eqs. 6.34 and 6.35). To compute the attenuation coefficient, however, it is doubtful that the gas and solid suspended phases may be lumped together as a single discrete phase having effective properties depending on the two constituents properties and the gas–solid ratio. The effect of the oscillation of the radius of gas bubbles, for instance, may contribute significantly to the attenuation coefficient of the suspension. Considering solids and bubbles as one single, discrete phase having averaged properties would thus probably underestimate this phenomenon and the attenuation coefficients.

In summary, despite the differences between our conceptual framework of suspensions and real magmas, we expect that our model is suitable to predict the seismic velocities of compressional waves and gives correct estimates of the order of magnitude of the attenuation coefficient in gas-free eruptible magmas. The presence of exsolved gas may significantly increase the attenuation factors. The estimations given with the present model must thus be viewed as lower bounds of the intrinsic attenuation coefficient in bubbly magmas because the presence of exsolved volatiles increases attenuation.

6.5.2 Model validation

Few experiments have been performed to measure acoustic wave velocities and attenuation coefficients within suspensions in conditions relevant for magmas. Because of the industrial interest in characterizing suspension properties with ultrasound, most experiments use frequencies and particle sizes for which assumptions made in our model do not hold (e.g. Atkinson and Kytömaa, 1992; Kuster and Toksoz, 1974). The experiments performed by Hampton (1967) on the suspension of kaolinite in water with moderate frequencies (100 kHz) and small particle sizes ($\sim 1.13 \mu\text{m}$), are an exception because they fulfill the long wavelength approximation. The comparison of our model results with these experimental results shows good agreement in both the propagation velocities and attenuation coefficients (Fig. 6.11). The sharp changes in the variation of the attenuation close to $\Phi_0 = 0.1$ results from the drag model we used (Fig. 6.11 B). With a more accurate drag model (e.g. Gidaspow, 1994), the slope change is smoother but the same bound is reached at $\Phi_0 = 0$ (see supplementary Fig. S6.1). Sadly, the viscosity of the fluid and the range of particle content explored experimentally do not allow us to validate our implementation of the lubrication forces or the way we account for the viscous attenuation imposed by the fluid.

Caricchi et al. (2008) performed wave propagation experiments on synthetic magmas. Their results, however, may not be directly compared with our model because the frequency used (3 MHz) causes the melt phase to be unrelaxed (Caricchi et al., 2008), and put the suspensions in conditions where the long wavelength approximation is not valid (the wavelength, $\lambda_p = \sim 1 \text{ mm}$, and $d_p = \sim 0.1 \text{ mm}$). Performing experiments on magmas at seismic frequencies is very challenging because the size of the sample has to be as large as one seismic wavelength. At seismic frequencies ($< 50 \text{ Hz}$), wavelengths are comprised between hundreds of meters to several kilometers. Our model thus has to be modified to handle high frequencies and unrelaxed melts so that its outputs can be compared with experiments.

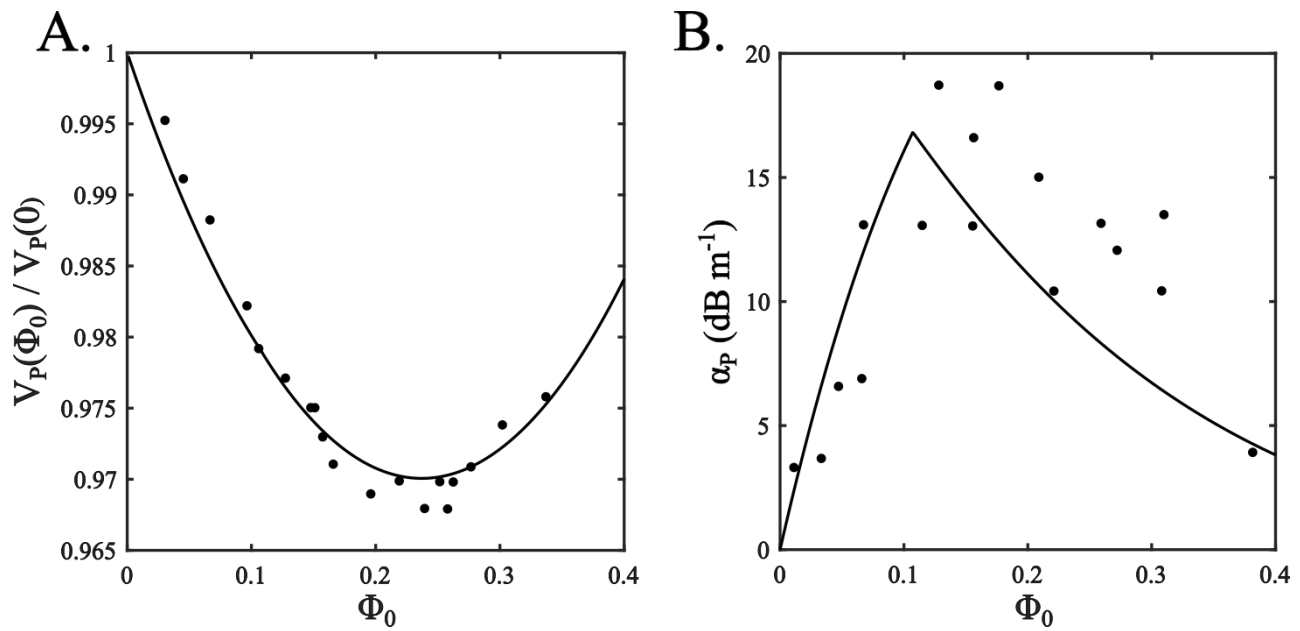


Figure 6.11: Comparison of the estimations of the model and experimental results from Hampton (1967) for a suspension of kaolinite ($d_p = 1.13 \mu\text{m}$, $K_p = 12.5 \text{ Gpa}$; $\rho_s = 2360 \text{ kg m}^{-3}$) in water at 100 kHz. The physical parameters of the constituents are reported in Gibson and Toksöz (1989). [A] Evolution of the phase velocity as a function of the concentration in solids. [B] Evolution of the attenuation coefficients as a function of the solid volume fraction. The ordinate scale is in dB m^{-1} ($1 \text{ Np} = 8.67 \text{ dB}$). Black curves correspond to the results of our model and the dots to the experimental results from Hampton (1967).

6.5.3 Implications for magmas

Our model is aimed at predicting seismic wave velocities and attenuation coefficients in magmas where crystals are not in contact. Our theoretical results have shown that for the three magmas, the velocities depended only on the crystal contents and not on the chemical composition of the magmas. At a pressure of 250 MPa, the seismic velocities of the magmas range from 2550 m s^{-1} to 3250 m s^{-1} (Fig 6.9 B). The attenuation coefficients we computed may be used to estimate the distance after which the compressional waves are fully attenuated (Fig. 6.12). For instance, a compressional wave having a frequency of 50 Hz is totally attenuated after 1 km in a dacite having 50 vol.% crystals. A wave travelling in basalt at the same frequency, however, is not fully attenuated after 100 km. Below 1 Hz, P waves are weakly attenuated in all magmas. The presence of exsolved volatiles in the magma result in an increased attenuation (Neuberg and O’Gorman, 2002), which highly depends on bubble size (Collier et al., 2006).

Experiments performed on magmas have shown that a sharp change occurs in the velocities of compressional waves once solids are in contact (Caricchi et al., 2008). This transition is also associated with the vanishing of the shear waves once particles are separated. These changes were

observed along mid-ocean ridges (Singh et al., 1998). Our results also predict the rapid attenuation of shear waves in magmas when crystals are not in contact, which is consistent with these observations. The attenuation coefficient we computed for shear waves (Fig 6.8) indicates that the maximum penetration distance of shear waves in magma is ~10 cm (Fig 6.12). The lubrication force may reduce the attenuation of shear waves but are not able to maintain a rigidity modulus of the suspension when particles are at close but finite distance of each other.

The rejuvenation of a mushy magmatic reservoir is expected to result from the emplacement of horizontal layer of a hot and crystal-poor magma that destabilizes the force chains and dilates the overlying mush (see chapter 4 and 5). The velocity of a compressional wave depends mainly on the crystal content of the magma (Fig. 6.9) and presents a sharp decrease once crystals are separated. The rejuvenation of a mush is thus expected to result in the rapid attenuation of shear waves in the freshly eruptible magma. However, because of the presumably small size of such eruptible volumes with respect to the seismic wavelengths and to the vertical resolution of tomographic images, we expect that the detection of the rejuvenation of a mush would be difficult to perform with one velocity tomographic image because of smoothing effects. Even if a volume dominated by the presence of melt is accurately detected, to interpret it in terms of the physical properties of the constituents requires the knowledge of the temperature at which the magma is stored. Storage temperatures in the upper crust depend on several parameters such as the frequency of the recharge in new magmas, the volume and shape of the intrusion, and the presence of a mature reservoir in the lower crust (Annen et al., 2015, 2006; Karakas et al., 2017). When the temperature is unknown, the joint interpretation of velocity and attenuation tomographic images (e.g. De Siena et al., 2014) may help to estimate the physical properties of the magmas. One more difficulty is that the total attenuation coefficient measured in seismic signals is the sum of the intrinsic and scattering contributions (e.g. Lesage and Surono, 1995; Prudencio et al., 2018). The two may be discriminated by using a diffusion model (e.g. Sato et al., 2012). While the intrinsic attenuation coefficient may be computed with our model, it is not the case of the scattering coefficient although it generally represents the main part of the total attenuation (Prudencio et al., 2018). Thus, estimating the physical properties of the magma from a single snapshot of subsurface total attenuation is very challenging.

Unlike intrinsic attenuations, the scattering attenuations are not expected to vary greatly during the rejuvenation process. This opens a promising way to detect an unrest event by measuring the time evolution of the tomographic images of wave velocity (e.g. Patanè et al., 2006) and attenuation. While our model adds to the existing models addressing seismic properties of eruptible magmas and partially molten rocks (Collier et al., 2006; Mavko, 1980), the seismic signatures of magmatic mush remains poorly known. This is an issue because interpreting the evolution of wave attenuation in magmatic systems requires the ability to address the full spectrum of crystallinity, from liquidus to solidus. The seismic properties of mushes depends on the strength of the force chains, and the non-linear effects arising from the frictional contacts contribute to wave attenuation (Brunet et al., 2008). These effects require further considerations.

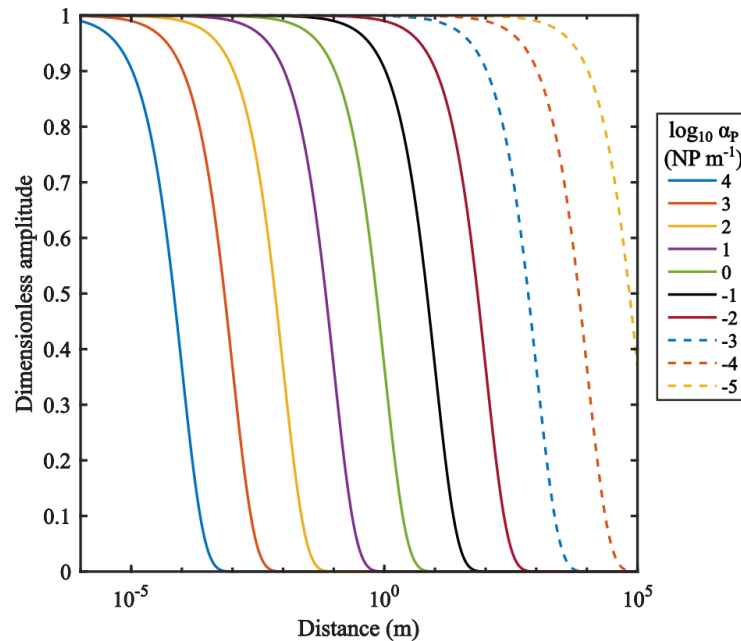


Figure 6.12: Dimensionless decay of the acoustic wave amplitude as a function of distance. Each curve represents the decay in amplitude of an acoustic wave for a given attenuation coefficient.

6.6 Conclusions

In this study, we computed the velocities and attenuation coefficients of seismic waves in crystal-bearing magmas. We employed and modified the coupled-phase approach. We notably incorporated the effects of the viscous dissipation in the melt phase and lubrication forces. Our model reproduces experimental results of wave velocities and attenuation that fulfill the long wavelength approximation. To our knowledge, there are no experimental data to test our model predictions on the role of lubrication forces or that of the fluid viscous attenuation. Our results suggest that for low frequencies, the velocities of compressional wave depend on the bulk modulus, densities and respective concentration between the carrier and discrete phases, and are independent of frequency in the seismic range. The attenuation coefficients of compressional waves depend mainly on the viscosity of the fluid, the frequency of the perturbation, and the ratio between the bulk moduli of the constituents.

We applied this model to eruptible magmas using input data from simulations mimicking magma cooling and crystallization and showed that, for three magma compositions (basalt, andesite, and dacite), the velocity of compressional waves are functions of the crystallinity. The chemical composition of the magmas has no effect on wave velocity other than controlling the temperature at which these crystallinities are reached. Differences in chemical compositions, however, result in orders of magnitude of differences in the attenuation coefficients of compressional waves. Despite the simplifications compared to real magma, our model produces the first results in predicting the attenuation coefficients of compressional waves in crystal-bearing magmas. We neglected thermal effect and the presence of bubble. Both may result in an excess of attenuation compared to our results. Therefore our results must be viewed as lower-bound estimates of wave attenuation in magmas.

References:

- Ahuja, A.S., Hende, W.R., 1978. Effects of particle shape and orientation on propagation of sound in suspensions. *J. Acoust. Soc. Am.* 63, 1074–1080. <https://doi.org/10.1121/1.381814>
- Ancey, C., Coussot, P., Evesque, P., 1999. A theoretical framework for granular suspensions in a steady simple shear flow. *J. Rheol.* 43, 1673–1699. <https://doi.org/10.1122/1.551067>
- Annen, C., Blundy, J.D., Leuthold, J., Sparks, R.S.J., 2015. Construction and evolution of igneous bodies: Towards an integrated perspective of crustal magmatism. *Lithos* 230, 206–221. <https://doi.org/10.1016/j.lithos.2015.05.008>
- Annen, C., Blundy, J.D., Sparks, R.S.J., 2006. The Genesis of Intermediate and Silicic Magmas in Deep Crustal Hot Zones. *J. Petrol.* 47, 505–539. <https://doi.org/10.1093/ptrology/egi084>
- Atkinson, C.M., Kytömaa, H.K., 1992. Acoustic wave speed and attenuation in suspensions. *Int. J. Multiph. Flow* 18, 577–592. [https://doi.org/10.1016/0301-9322\(92\)90053-J](https://doi.org/10.1016/0301-9322(92)90053-J)
- Bachmann, O., Huber, C., 2019. The Inner Workings of Crustal Distillation Columns; the Physical Mechanisms and Rates Controlling Phase Separation in Silicic Magma Reservoirs. *J. Petrol.* 60, 3–18. <https://doi.org/10.1093/ptrology/egy103>
- Bagdassarov, N.S., Dingwell, D.B., Webb, S.L., 1994. Viscoelasticity of crystal-and bubble-bearing rhyolite melts. *Phys. Earth Planet. Inter.* 83, 83–99.
- Banks-Sills, L., Leiderman, V., Fang, D., 1997. On the effect of particle shape and orientation on elastic properties of metal matrix composites. *Compos. Part B Eng.* 28, 465–481. [https://doi.org/10.1016/S1359-8368\(96\)00068-6](https://doi.org/10.1016/S1359-8368(96)00068-6)
- Bergantz, G.W., Schleicher, J.M., Burgisser, A., 2017. On the kinematics and dynamics of crystal-rich systems. *J. Geophys. Res. Solid Earth* 122, 2017JB014218. <https://doi.org/10.1002/2017JB014218>
- Berryman, J.G., 1980. Long-wavelength propagation in composite elastic media I. Spherical inclusions. *J. Acoust. Soc. Am.* 68, 1809–1819. <https://doi.org/10.1121/1.385171>
- Boudreau, A.E., 1999. PELE—a version of the MELTS software program for the PC platform. *Comput. Geosci.* 25, 201–203.
- Brunet, Th., Jia, X., Mills, P., 2008. Mechanisms for Acoustic Absorption in Dry and Weakly Wet Granular Media. *Phys. Rev. Lett.* 101, 138001. <https://doi.org/10.1103/PhysRevLett.101.138001>
- Caricchi, L., Burlini, L., Ulmer, P., 2008. Propagation of P and S-waves in magmas with different crystal contents: Insights into the crystallinity of magmatic reservoirs. *J. Volcanol. Geotherm. Res., Evolution, Transfer and Release of Magmas and Volcanic Gases* 178, 740–750. <https://doi.org/10.1016/j.jvolgeoes.2008.09.006>
- Cassidy, M., Manga, M., Cashman, K., Bachmann, O., 2018. Controls on explosive-effusive volcanic eruption styles. *Nat. Commun.* 9, 1–16. <https://doi.org/10.1038/s41467-018-05293-3>
- Challis, R.E., Povey, M.J.W., Mather, M.L., Holmes, A.K., 2005. Ultrasound techniques for characterizing colloidal dispersions. *Rep. Prog. Phys.* 68, 1541.
- Claeys, I.L., Brady, J.F., 1993. Suspensions of prolate spheroids in Stokes flow. Part 1. Dynamics of a finite number of particles in an unbounded fluid. *J. Fluid Mech.* 251, 411–442. <https://doi.org/10.1017/S0022112093003465>
- Collier, L., Neuberg, J.W., Lensky, N., Lyakhovsky, V., Navon, O., 2006. Attenuation in gas-charged magma. *J. Volcanol. Geotherm. Res., MULTIMO: Multi-Parameter Monitoring, Modelling and Forecasting of Volcanic Hazard* 153, 21–36. <https://doi.org/10.1016/j.jvolgeoes.2005.08.009>
- Dellino, P., Mele, D., Bonasia, R., Braia, G., Volpe, L.L., Sulpizio, R., 2005. The analysis of the influence of pumice shape on its terminal velocity. *Geophys. Res. Lett.* 32. <https://doi.org/10.1029/2005GL023954>
- De Siena, L., Thomas, C., Waite, G.P., Moran, S.C., Klemme, S., 2014. Attenuation and scattering tomography of the deep plumbing system of Mount St. Helens. *J. Geophys. Res. Solid Earth* 119, 8223–8238. <https://doi.org/10.1002/2014JB011372>
- Dingwell, D.B., Webb, S.L., 1990. Relaxation in silicate melts. *Eur. J. Mineral.* 427–449.
- Dingwell, D.B., Webb, S.L., 1989. Structural relaxation in silicate melts and non-Newtonian melt rheology in geologic processes. *Phys. Chem. Miner.* 16, 508–516. <https://doi.org/10.1007/BF00197020>
- Dioguardi, F., Dellino, P., Mele, D., 2014. Integration of a new shape-dependent particle–fluid drag coefficient law in the multiphase Eulerian–Lagrangian code MFIX-DEM. *Powder Technol.* 260, 68–77. <https://doi.org/10.1016/j.powtec.2014.03.071>
- Dufek, J., Bachmann, O., 2010. Quantum magmatism: Magmatic compositional gaps generated by melt-crystal dynamics. *Geology* 38, 687–690. <https://doi.org/10.1130/G30831.1>
- Ergun, S., 1952. Fluid flow through packed columns. *Chem Eng Prog* 48, 89–94.
- Evans, J.M., Attenborough, K., 2002. Sound propagation in concentrated emulsions: Comparison of coupled phase model and core-shell model. *J. Acoust. Soc. Am.* 112, 1911–1917.
- Evans, J.M., Attenborough, K., 1997. Coupled phase theory for sound propagation in emulsions. *J. Acoust. Soc. Am.* 102, 278–282. <https://doi.org/10.1121/1.419745>
- Faroughi, S.A., Huber, C., 2014. Crowding-based rheological model for suspensions of rigid bimodal-sized particles with interfering size ratios. *Phys. Rev. E* 90, 052303. <https://doi.org/10.1103/PhysRevE.90.052303>
- Farr, R.S., Groot, R.D., 2009. Close packing density of polydisperse hard spheres. *J. Chem. Phys.* 131, 244104. <https://doi.org/10.1063/1.3276799>
- Ghiorso, M.S., 2004. An equation of state for silicate melts. I. Formulation of a general model. *Am. J. Sci.* 304, 637–678. <https://doi.org/10.2475/ajs.304.8-9.637>
- Ghiorso, M.S., Kress, V.C., 2004. An equation of state for silicate melts. II. Calibration of volumetric properties at 105 Pa. *Am. J. Sci.* 304, 679–751. <https://doi.org/10.2475/ajs.304.8-9.679>
- Gibson, R.L., Toksöz, M.N., 1989. Viscous attenuation of acoustic waves in suspensions. *J. Acoust. Soc. Am.* 85, 1925–1934.

-
- Gidaspow, D., 1994. *Multiphase Flow and Fluidization: Continuum and Kinetic Theory Descriptions*. Academic Press.
- Giordano, D., Russell, J.K., Dingwell, D.B., 2008. Viscosity of magmatic liquids: A model. *Earth Planet. Sci. Lett.* 271, 123–134. <https://doi.org/10.1016/j.epsl.2008.03.038>
- Hacker, B.R., Abers, G.A., Peacock, S.M., 2003. Subduction factory 1. Theoretical mineralogy, densities, seismic wave speeds, and H₂O contents. *J. Geophys. Res. Solid Earth* 108. <https://doi.org/10.1029/2001JB001127>
- Hampton, L.D., 1967. Acoustic Properties of Sediments. *J. Acoust. Soc. Am.* 42, 882–890. <https://doi.org/10.1121/1.1910662>
- Harker, A.H., Temple, J.A.G., 1988. Velocity and attenuation of ultrasound in suspensions of particles in fluids. *J. Phys. Appl. Phys.* 21, 1576–1588. <https://doi.org/10.1088/0022-3727/21/11/006>
- Higgins, M.D., 2006. Verification of ideal semi-logarithmic, lognormal or fractal crystal size distributions from 2D datasets. *J. Volcanol. Geotherm. Res., Modern Trends in Petrography*: 154, 8–16. <https://doi.org/10.1016/j.jvolgeores.2005.09.015>
- Higgins, M.D., Roberge, J., 2003. Crystal Size Distribution of Plagioclase and Amphibole from Soufrière Hills Volcano, Montserrat: Evidence for Dynamic Crystallization–Textural Coarsening Cycles. *J. Petrol.* 44, 1401–1411. <https://doi.org/10.1093/petrology/44.8.1401>
- Ishii, M., Hibiki, T., 2011. *Thermo-Fluid Dynamics of Two-Phase Flow*. Springer Science+Business Media, LLC.
- Janoschek, F., Harting, J., Toschi, F., 2013. Accurate lubrication corrections for spherical and non-spherical particles in discretized fluid simulations. *ArXiv13086482 Cond-Mat Physicsphysics*.
- Karakas, O., Degruyter, W., Bachmann, O., Dufek, J., 2017. Lifetime and size of shallow magma bodies controlled by crustal-scale magmatism. *Nat. Geosci.* 10, 446–450. <https://doi.org/10.1038/ngeo2959>
- Karlstrom, L., Rudolph, M.L., Manga, M., 2012. Caldera size modulated by the yield stress within a crystal-rich magma reservoir. *Nat. Geosci.* 5, 402–405. <https://doi.org/10.1038/ngeo1453>
- Kiser, E., Palomeras, I., Levander, A., Zelt, C., Harder, S., Schmandt, B., Hansen, S., Creager, K., Ulberg, C., 2016. Magma reservoirs from the upper crust to the Moho inferred from high-resolution V_p and V_s models beneath Mount St. Helens, Washington State, USA. *Geology* 44, 411–414. <https://doi.org/10.1130/G37591.1>
- Kress, V.C., Carmichael, I.S.E., 1991. The compressibility of silicate liquids containing Fe₂O₃ and the effect of composition, temperature, oxygen fugacity and pressure on their redox states. *Contrib. Mineral. Petrol.* 108, 82–92. <https://doi.org/10.1007/BF00307328>
- Kuster, G., Toksöz, M., 1974. Velocity and attenuation of seismic waves in two-phase media: part i. theoretical formulations. *GEOPHYSICS* 39, 587–606. <https://doi.org/10.1190/1.1440450>
- Kuster, G.T., Toksoz, M.N., 1974. Velocity and attenuation of seismic waves in two-phase media; Part II, Experimental results. *Geophysics* 39, 607–618. <https://doi.org/10.1190/1.1440451>
- Kytömaa, H.K., 1995. Theory of sound propagation in suspensions: a guide to particle size and concentration characterization. *Powder Technol.* 82, 115–121. [https://doi.org/10.1016/0032-5910\(94\)02901-Y](https://doi.org/10.1016/0032-5910(94)02901-Y)
- Lesage, Ph., Surono, 1995. Seismic precursors of the February 10, 1990 eruption of Kelut volcano, Java. *J. Volcanol. Geotherm. Res.* 65, 135–146. [https://doi.org/10.1016/0377-0273\(94\)00051-H](https://doi.org/10.1016/0377-0273(94)00051-H)
- Margulies, T.S., Schwarz, W.H., 1994. A multiphase continuum theory for sound wave propagation through dilute suspensions of particles. *J. Acoust. Soc. Am.* 96, 319–331.
- Marsh, B.D., 1988. Crystal size distribution (CSD) in rocks and the kinetics and dynamics of crystallization. *Contrib. Mineral. Petrol.* 99, 277–291. <https://doi.org/10.1007/BF00375362>
- Marzougui, D., Chareyre, B., Chauchat, J., 2015. Microscopic origins of shear stress in dense fluid–grain mixtures. *Granul. Matter* 17, 297–309. <https://doi.org/10.1007/s10035-015-0560-6>
- Mavko, G.M., 1980. Velocity and attenuation in partially molten rocks. *J. Geophys. Res. Solid Earth* 5173–5189. [https://doi.org/10.1029/JB085iB10p05173@10.1002/\(ISSN\)2169-9356.STANFORD1](https://doi.org/10.1029/JB085iB10p05173@10.1002/(ISSN)2169-9356.STANFORD1)
- Molina, I., Burgisser, A., Oppenheimer, C., 2012. Numerical simulations of convection in crystal-bearing magmas: A case study of the magmatic system at Erebus, Antarctica. *J. Geophys. Res. Solid Earth* 117. <https://doi.org/10.1029/2011JB008760>
- Neuberg, J., O’Gorman, C., 2002. A model of the seismic wavefield in gas-charged magma: application to Soufrière Hills Volcano, Montserrat. *Geol. Soc. Lond. Mem.* 21, 603–609. <https://doi.org/10.1144/GSL.MEM.2002.021.01.29>
- Nolan, G.T., Kavanagh, P.E., 1995. Random packing of nonspherical particles. *Powder Technol.* 84, 199–205. [https://doi.org/10.1016/0032-5910\(95\)98237-S](https://doi.org/10.1016/0032-5910(95)98237-S)
- Ouchiyama, N., Tanaka, T., 2002. Porosity estimation for random packings of spherical particles [WWW Document]. <https://doi.org/10.1021/i100016a019>
- Parmigiani, A., Degruyter, W., Leclaire, S., Huber, C., Bachmann, O., 2017. The mechanics of shallow magma reservoir outgassing. *Geochem. Geophys. Geosystems* 18, 2887–2905. <https://doi.org/10.1002/2017GC006912>
- Parmigiani, A., Huber, C., Bachmann, O., 2014. Mush microphysics and the reactivation of crystal-rich magma reservoirs. *J. Geophys. Res. Solid Earth* 119, 6308–6322. <https://doi.org/10.1002/2014JB011124>
- Patanè, D., Barberi, G., Cocina, O., De Gori, P., Chiarabba, C., 2006. Time-resolved seismic tomography detects magma intrusions at Mount Etna. *Science* 313, 821–823.
- Paulatto, M., Annen, C., Henstock, T.J., Kiddle, E., Minshull, T.A., Sparks, R.S.J., Voight, B., 2012. Magma chamber properties from integrated seismic tomography and thermal modeling at Montserrat. *Geochem. Geophys. Geosystems* 13. <https://doi.org/10.1029/2011GC003892>
- Picard, D., Arbaret, L., Pichavant, M., Champallier, R., Launeau, P., 2011. Rheology and microstructure of experimentally deformed plagioclase suspensions. *Geology* 39, 747–750. <https://doi.org/10.1130/G32217.1>
-

-
- Prudencio, J., Manga, M., Taira, T., 2018. Subsurface Structure of Long Valley Caldera Imaged With Seismic Scattering and Intrinsic Attenuation. *J. Geophys. Res. Solid Earth* 123, 5987–5999. <https://doi.org/10.1029/2017JB014986>
- Reuss, A., 1929. Berechnung der fließgrenze von mischkristallen auf grund der plastizitätsbedingung für einkristalle. *ZAMM-Journal Appl. Math. Mech. Für Angew. Math. Mech.* 9, 49–58.
- Sato, H., Fehler, M.C., Maeda, T., 2012. Seismic wave propagation and scattering in the heterogeneous earth. Springer.
- Singh, S.C., Kent, G.M., Collier, J.S., Harding, A.J., Orcutt, J.A., 1998. Melt to mush variations in crustal magma properties along the ridge crest at the southern East Pacific Rise. *Nature* 394, 874–878. <https://doi.org/10.1038/29740>
- Syamlal, M., O'Brien, T.J., 1988. Simulation of granular layer inversion in liquid fluidized beds. *Int. J. Multiph. Flow* 14, 473–481. [https://doi.org/10.1016/0301-9322\(88\)90023-7](https://doi.org/10.1016/0301-9322(88)90023-7)
- Takahashi, R., Nakagawa, M., 2013. Formation of a Compositionally Reverse Zoned Magma Chamber: Petrology of the ad 1640 and 1694 Eruptions of Hokkaido-Komagatake Volcano, Japan. *J. Petrol.* 54, 815–838. <https://doi.org/10.1093/petrology/egs087>
- Valier-Brasier, T., Conoir, J.-M., Coulouvrat, F., Thomas, J.-L., 2015. Sound propagation in dilute suspensions of spheres: Analytical comparison between coupled phase model and multiple scattering theory. *J. Acoust. Soc. Am.* 138, 2598–2612. <https://doi.org/10.1121/1.4932171>
- Waite, G.P., Moran, S.C., 2009. VP Structure of Mount St. Helens, Washington, USA, imaged with local earthquake tomography. *J. Volcanol. Geotherm. Res.* 182, 113–122. <https://doi.org/10.1016/j.jvolgeores.2009.02.009>
- Wallace, P.J., 2005. Volatiles in subduction zone magmas: concentrations and fluxes based on melt inclusion and volcanic gas data. *J. Volcanol. Geotherm. Res.* 140, 217–240.
- Wallace, P.J., 2001. Volcanic SO₂ emissions and the abundance and distribution of exsolved gas in magma bodies. *J. Volcanol. Geotherm. Res.* 108, 85–106.
- Wallace, P.J., Anderson Jr, A.T., Davis, A.M., 1999. Gradients in H₂O, CO₂, and exsolved gas in a large-volume silicic magma system: Interpreting the record preserved in melt inclusions from the Bishop Tuff. *J. Geophys. Res. Solid Earth* 104, 20097–20122.
- Zou, R.P., Yu, A.B., 1996. Evaluation of the packing characteristics of mono-sized non-spherical particles. *Powder Technol., Research of Powder Technology in Australia* 88, 71–79. [https://doi.org/10.1016/0032-5910\(96\)03106-3](https://doi.org/10.1016/0032-5910(96)03106-3)

Supplementary section 6.1:

This supplementary section presents the drag law used in chapter 6.

The momentum transfer term (Eqs. 6.14) includes a momentum exchange coefficient, β_{fs} . Several formulations were proposed by authors based on either experimental or theoretical results. The simplest formulation is the Stokes drag, which considers isolated spheres. After a procedure of volume averaging, it yields:

$$\beta_{stokes} = \frac{18 \eta \Phi}{d_p^2} \quad (\text{S6.1.1})$$

The presence of neighboring particles influences the fluid flow around a given particle and may be captured by the Gidaspow drag model (Gidaspow, 1994), which combines a Wen-Yu's drag law at low concentrations in solids, and an Ergun's relationship (Ergun, 1952) at high particle volume fraction. The Gidaspow momentum exchange coefficient, $\beta_{gidaspow}$, is:

$$\beta_{gidaspow} = \begin{cases} \frac{3}{4} C_D \frac{\rho_f \Phi (1-\Phi) \|\vec{v}_f - \vec{v}_s\|}{d_p} (1-\Phi)^{-2.65} & \Phi < 0.2 \\ \frac{150 \Phi^2 \eta}{(1-\Phi) d_p^2} + \frac{1.75 \Phi \rho_f \|\vec{v}_f - \vec{v}_s\|}{d_p} & \Phi \geq 0.2 \end{cases} \quad (\text{S6.1.2})$$

where C_D is the drag coefficient that depends on the particle Reynolds number, Re_p , as:

$$C_D = \begin{cases} \frac{24}{Re_p} (1 + 0.15 Re_p^{0.687}) & Re_p < 1000 \\ 0.44 & Re_p \geq 1000 \end{cases} \quad (\text{S6.1.3})$$

The first line of Eq. (6.1.2) is the Wen-Yu momentum coefficient. The second line is the Ergun drag law, in which the first term is a Kozeny-Karman relationship capturing the viscous effects, and the second term is a Burk-Plummer equation including the inertial effects. Alternatively, simpler momentum coupling terms exist but are only valid over a certain range of concentrations in particles (e.g., Bergantz et al., 2017).

Comparison of the magnitude of the different drag laws shows that for magmatic conditions, the Ergun law may be reduced to the Kozeny-Carman relationship by neglecting inertial effects (Fig. S6.1). At very low particle volume fraction ($\Phi \ll 0.05$), the Wen-Yu and Stokes drag merge. The Stokes and Kozeny-Carman laws present the advantage to be linearly dependent on the

relative velocity between the solids and the fluid, and are thus suitable for a coupled phase approach. Thereby, we decided to combine a Stokes law at low concentrations in solids and a Kozeny-Carman relationship at higher concentrations to keep a linear dependence over the whole range of particle volume fraction. The momentum transfer coefficient β_{fs} is thus:

$$\beta_{fs} = \begin{cases} \frac{18 \eta \phi}{d_p^2} & \phi \leq 0.10715 \\ \frac{150 \phi^2 \eta}{(1-\phi) d_p^2} & \phi > 0.10715 \end{cases} \quad (\text{S6.1.4})$$

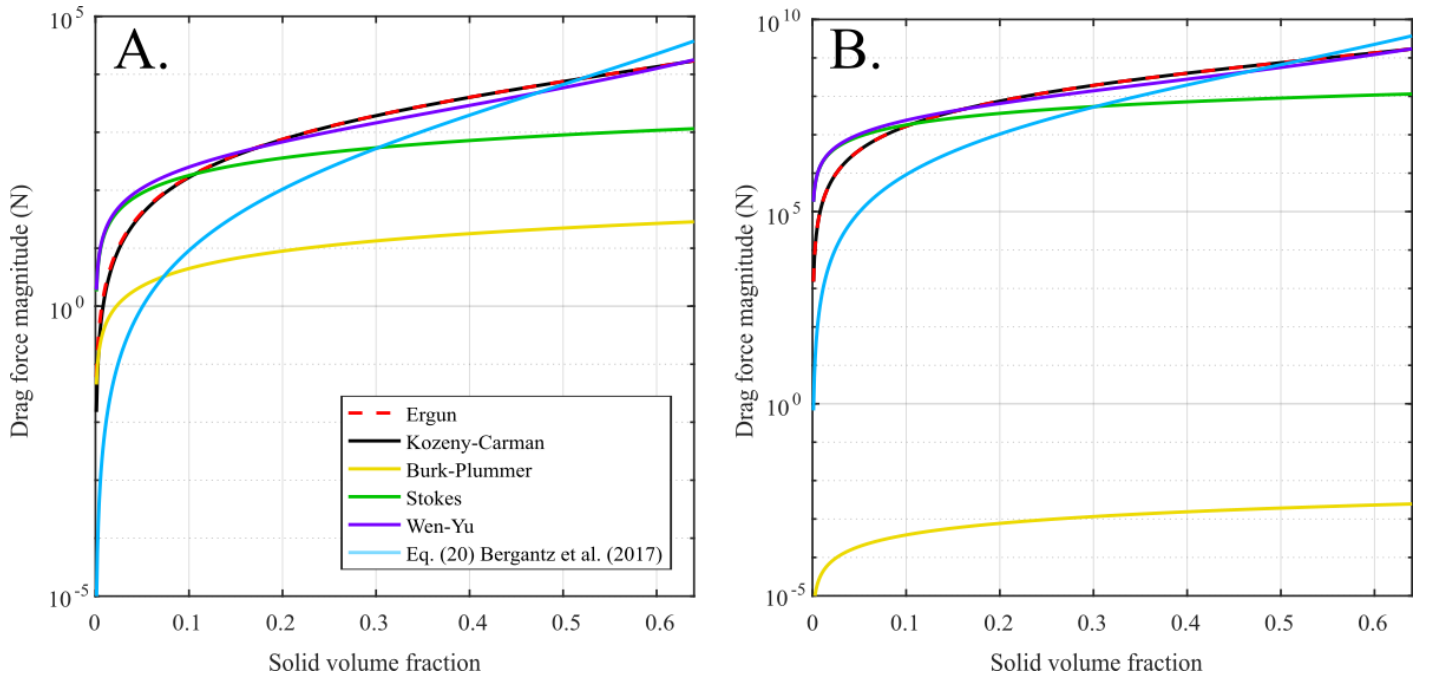


Figure S6.1: Comparison of drag laws as function of the solid volume fraction. [A] $d_p = 0.01 \text{ m}$, $\Delta v = 0.01 \text{ m s}^{-1}$, $\rho_f = 2550 \text{ kg m}^{-3}$, $\eta = 1 \text{ Pa s}$. [B] $d_p = 0.0001 \text{ m}$, $\Delta v = 0.00001 \text{ m s}^{-1}$, $\rho_f = 2250 \text{ kg m}^{-3}$, $\eta = 1000 \text{ Pa s}$.

Chapter 7: General conclusions

This thesis, which is based on CFD-DEM numerical modeling and fluid mechanics, aimed at improving our understanding of the physical processes leading to the reawakening of a magmatic reservoir and the associated effects on geophysical signals. We explored the rheology of mush and crystal-bearing magmas to identify and quantify the relevant physical processes that control the motion of the crystals. Our investigation focused on the importance and effects of lubrication forces, which were not explicitly considered in previous models. We then performed series of numerical simulations of injection of a mobile magma into a mush. Once the expected behaviors of intrusions in natural conditions were identified, we focused our modeling on the interactions between the mush and the intruded magma and on how the intrusion affects the physical properties of the materials located in the magmatic reservoir. Finally, to explore the effect of magma input on seismic signals, we computed the seismic wave velocities and attenuation coefficients in eruptible magmas by improving the coupled phase approach for wave propagation.

The rheologies of mush and crystal-bearing magmas are complex and their description requires to account for several physical processes such as the viscous drag exerted by the melt and the presence of frictional forces chains (Bergantz et al., 2017). The influence and effects of the lubrication forces, however, were not fully constrained in previous works. We developed in Chapter 3 scaling relationships and performed CFD-DEM numerical simulations to address the importance and effects of lubrication in mush dynamics. Our results showed that lubrication is important at the initiation or dying-off of motion in the mush, and protracts the duration of these transient dynamics. Lubrication, however, has a negligible importance in steady-state conditions. This is why lubrication was weakly visible in experiments aimed at constraining the rheology of magma and mush (e.g. Caricchi et al., 2007; Lavallée et al., 2007; Mueller et al., 2010). These studies used measurements acquired during the steady-state straining of magmas, for which lubrication may be neglected. Highlighting experimentally lubrication is thus challenging using steady shearing experiments. Oscillatory rheometry seems the most promising approach to evidence the influence of lubrication forces and study transient dynamics in magmas.

CFD-DEM numerical simulations exploring the intrusion of magmas in mush (Bergantz et al., 2015; Schleicher et al., 2016; Schleicher and Bergantz, 2017) have revealed many interesting

features and highlighted the importance of the dynamics of the granular phase. In these studies, the differences existing between the physical properties of the mush and those of the intruded magma were restricted to the crystal content. The contrasts between the densities and viscosities of the two melt phases expected to occur in nature required further considerations. This CFD-DEM model required modifications to be able to simulate the dynamics of chemically evolved mush (i.e. with high melt viscosity). After implementing modifications to the CFD-DEM model that allowed us to address the dynamics of any magma, we performed in Chapter 4 series of numerical simulations by varying the physical properties of the resident melt. Our results show that, for gentle injection velocities, three regimes exist depending on the density contrast between the two melts. When the two melts have the same density, the formation of a mixing bowl occurs as described in Bergantz et al. (2015), Schleicher et al. (2016), and Schleicher and Bergantz (2017). When the intruded melt is lighter than the resident one, the injection rises through the mush as described in Girard and Stix (2009). On the contrary, when the intruded melt is the densest, the intrusion ponds at the base of the mush in the same fashion as presented in Jellinek and Kerr (1999) and Snyder and Tait (1995). At high injection rate, the effect of the density contrast between the two melts is dominated by the injection momentum and the intrusion grows radially. We found that, under most natural conditions, the intrusion is expected to spread at the base of the mush and to be emplaced as a horizontal layer. The relevant parameter controlling the behavior of the intrusion is the density contrast between the melts of the mush and intruded materials, contrary to the assumptions made in many studies, which considered the bulk density contrast as being the relevant parameter (e.g. Bain et al., 2013; Jellinek and Kerr, 1999; Snyder, 2000; Snyder and Tait, 1995). This result also suggests that mimicking mush and magma dynamics in experiments or numerical modeling requires solids to be accounted for explicitly as a discrete phase.

This thesis highlights the importance of accounting for the relative motion between melt and crystals. The role of the exsolved volatiles was not explored in this work and remains unclear. Some authors consider that the upward motion of bubbles may drive the ascent of the overlying magma (e.g. Ruprecht et al. 2008). Identify the parameters that control the motion of a magma in which liquid, solid, and gas phases coexist requires to account for the complex physics of exsolved volatiles (Parmigiani et al., 2017, 2014) as well as the dynamics of the granular phase. Such exploration is only beginning.

The interactions and mixing between the intruded magma and resident mush was previously explored using a CFD-DEM approach in the context of mush fluidization (Schleicher et al., 2016; Schleicher and Bergantz, 2017) and required further considerations for scenarios where the intrusion ponds at the base of the mush. Improving the description of the interactions between the two materials required to account for the thermal exchanges between them and for their effects on the density and viscosity of the melts. Using the results of Chapter 4, we built in Chapter 5 two simulations in which the intrusion is expected to spread at the base of the mush and for which the dimensionless injection velocities are identical. The initial injection velocities were chosen to impose the initial radial growth of the intrusion volumes. The two simulations reproduced the intrusion of a basaltic melt in a basaltic mush and the injection of a basaltic melt in a dacitic mush, respectively. We took advantage of the short computational time of the first simulation to explore the dynamics of the intrusion after shutting off the injection. Our results show that during the growth of the intruded volumes, thermal effects may significantly affect the dynamics of the intruded magma. For the simulation mimicking a basaltic mush, the melt flowed radially from the inlet, whereas it convected in that using a dacitic mush. This difference resulted mainly from the longer duration required in the second simulation to inject the same volume as in the first one.

After stopping the injection, the intrusion ponded at the base of the reservoir, trapping a layer of the resident basaltic mush beneath it. The trapped resident melt was buoyant compared to that of the intruder and rose through the intrusion, forming Rayleigh-Taylor instabilities and entraining trapped mush crystals. Some crystals from the overlying host invaded the intrusion by settling. These two features are commonly observed in plutonic rocks (e.g. Bain et al., 2013; Wiebe, 2016). Our results suggest that these processes do not need a thermal activation, as often considered (Bain et al., 2013; Jellinek and Kerr, 1999), and may instead result from a short, but intense, injection. Crystal mixing was restricted to the intrusion layer and it was less efficient than for the fluidization regime described in Schleicher et al. (2016). The amount of heat supplied by the injection was not able to trigger convection in the mush, which is in agreement with the theoretical predictions of Snyder (2000). The injection, however, generated conditions for which repacking occurs within the mush, which may trigger the extraction of the interstitial melt (Bachmann and Huber, 2019). Fully describing mixing between the intrusion and the host requires to perform

simulations on a larger scale with a resolution that allows to capture front instabilities such as those described in Snyder and Tait (1995), and accounting of the chemical diffusion.

The detection of mush reawakening in seismic signals requires constraining the seismic properties of eruptible magmas. We used and adapted the coupled-phase approach to compute the seismic wave velocities and attenuation coefficients in magmas where crystals are not in contact. Results show that the velocity of compressional waves in eruptible magmas depends on their crystal content. This decouples any link between wave velocity and magma composition because magma chemical composition and ambient pressure affect the temperature at which these crystallinities are reached. A given crystal content (and thus wave velocity) can be shared by magmas of different compositions and temperatures. A sharp increase of the compressional waves velocity and appearance of shear waves is expected once crystals are in contact, as highlighted in Caricchi et al. (2008). On the contrary, the intrinsic attenuation coefficients depend greatly on the chemical compositions of the magmas in a way that is not uniquely related to crystal content. The joint interpretation of the wave velocities and damping coefficients is thus necessary to estimate the physical properties of the eruptible magmas. It follows that the monitoring of the joint evolution of seismic velocities and attenuation seems the most suitable method to detect the unrest of a magmatic reservoir.

Magmatic reservoirs spend most of their time as mush. Therefore, the understanding of the seismic properties of mush where the crystals are in contact is also required to identify the best method to detect unrest events. CFD-DEM simulations could be an appropriate tool to that end, but it requires to couple the DEM and fluid phase numerical solvers in an iterative way for each time step so that the motions of the two phases are solved jointly. The actual implementation of the CFD-DEM model solves for each phase motion successively by considering the velocity of the other phase as constant during the time step of one phase. Such assumption is not valid for modeling wave propagation because of the wave rapid and transient dynamics.

Perspectives

Our results have shed light on the physical processes that may initiate the reawakening of a mush. These results allow us to sketch a large-scale picture of mush reawakening (Fig. 7.1) that highlight scenarios that are supported by these newly established physical processes and scenarios that our findings hint at but that need to be explored further. In many natural conditions, the melt phase of the injected magma is denser than that of the mush. Our results show that, in such situation, the intruder is expected to be emplaced as a horizontal layer (Fig. 7.1 A–B). The contamination of the intrusion occurs because of the settling of host crystals from the overlying mush and because buoyant host materials beneath the intrusion rise through it (Fig. 7.1 C). The presence material having the ability to flow beneath the emplaced layer may result from the thermal reactivation of a strong mush presenting initially a yield stress (Bain et al., 2013; Jellinek and Kerr, 1999), or from a short but intense injection trapping a layer of weak mush that does not need thermal reactivation (Chapter 5).

We speculate that this situation may evolve in two distinct ways. We have shown that the occurrence of gravitational instabilities in a magmatic system is dominated by the density contrast of the melt phases involved. Thereby, the evolution of the densities of the intruded and host melts during the thermal evolution that follows emplacement has a critical importance on the initiation of a large-scale instability of the intruded material. In the simulations of the cooling and crystallization of the magmas in Chapter 6, the density of the basaltic melt is smaller than the andesitic and dacitic ones once the temperature is below 1050°C (Fig. 6.2). We expect that the cooling and crystallization of a basaltic intrusion in a dacitic mush may lead to the density inversion of the two melts. The same process as observed at small scale between the trapped mush and the intrusion (Fig 7.1 C) may then occur at large scale, causing the rise of this intrusion from the floor of the reservoir (Fig 7.1 D). If an eruption ensues, the large-scale rise of this material will entrain uncontaminated host mush in the eruption. The eruptive sequence of such an eruption is expected to start with the deposition of materials showing the mingling or mixing between the basalt and host materials, and then the emission of mush material. This eruptive sequence is in agreement with observed ones (e.g., Pinatubo 1991, Pallister et al., 1992).

Because it requires to be thermally activated (i.e. the intruded material needs to cool sufficiently to cause density inversion), the scenario depicted in Fig. 7.1 D does not explain the

rapid transport of basalt through the magmatic reservoir with limited hybridization with the host material (e.g. Komagatake, 1640; Takahashi and Nakagawa, 2013). Such a rapid transport must result from an intense injection or from the presence of a yield stress in the mush that then supports the vertical ascent of the basalt (Fig 7.1 E). When the cooling of the intrusion does not lead to unstable conditions, the intruder is expected to stay near the base of the mush. This situation may initiate the extraction of the mush interstitial melt by repacking (Chapter 5, Bachmann and Huber, 2019), possibly leading to its eventual accumulation at the top of the reservoir (Fig 7.1 F) (Bachmann and Bergantz, 2004). An accurate prediction of the occurrence of a large-scale instability of the intrusion thus requires exploring further the consequences of the evolution of the host and intruded melt densities after an intrusive event while accounting for chemical diffusion, melting, and crystallization.

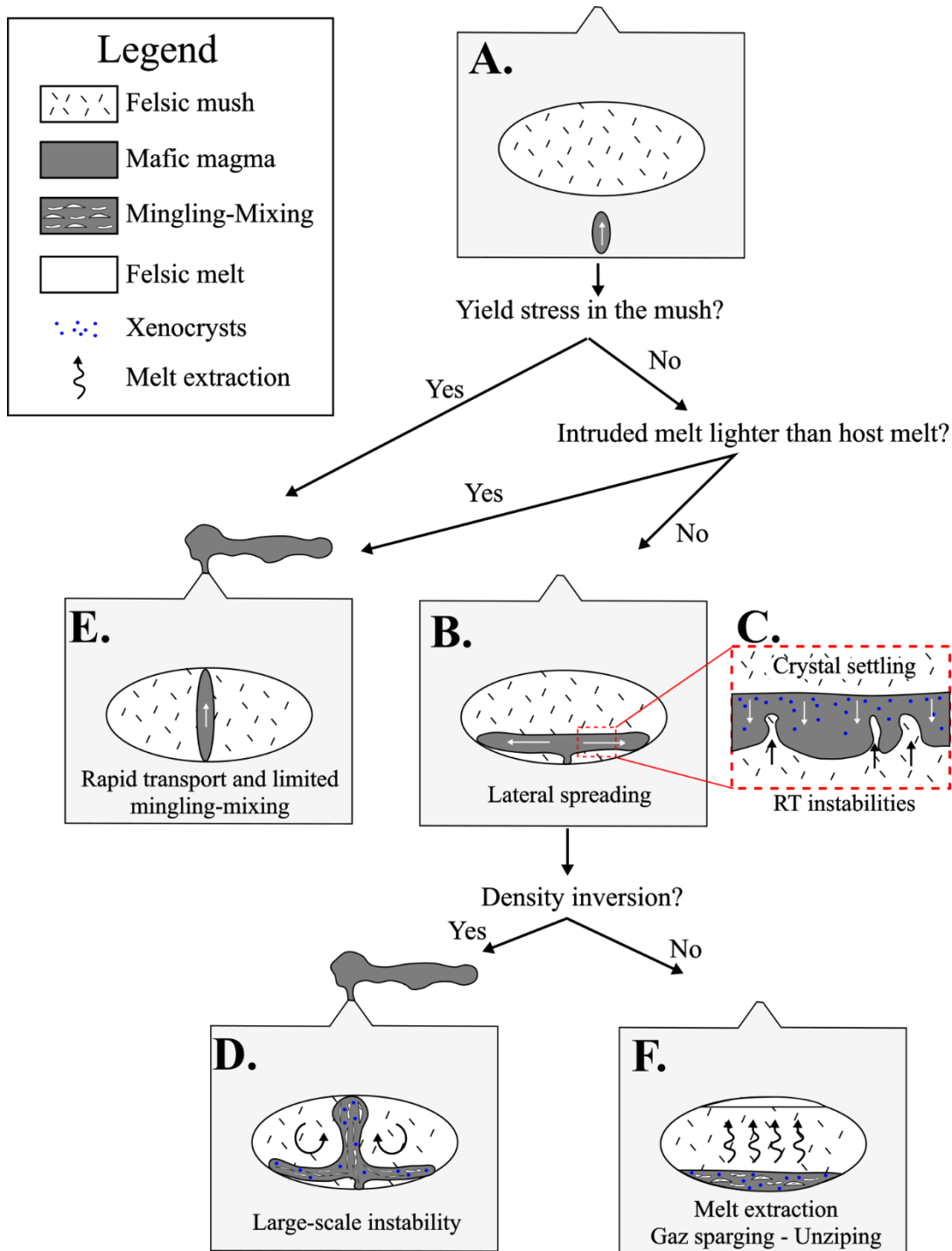


Figure 7.1: Scenarios of mush reawakening. [A] Initial conditions. The drawing represents a crustal section in which a mushy reservoir is present. A basalt arriving from below is introducing the mush. [B] The intrusion is emplaced as a horizontal layer. [C] Zoom on the interfaces at the top and bottom of the intrusion layer. White arrows represent the crystals settling from the top of the intrusion, and the black ones the upward migration of the host mush from the trapped layer of mush below the intrusion. [D] Large-scale instability of the intrusion in which mingling and mixing with the resident material occurs. Black arrows indicate the entrainment of the mush in the eruption. [E] Rapid transport of the intrusion within the mush. [F] Melt extraction induced by the emplacement of an intrusion. Wiggling arrows indicate the processes of melt extraction.

Manuscript references

- Ahuja, A.S., Hendee, W.R., 1978. Effects of particle shape and orientation on propagation of sound in suspensions. *J. Acoust. Soc. Am.* 63, 1074–1080. <https://doi.org/10.1121/1.381814>
- Ancey, C., Coussot, P., Evesque, P., 1999. A theoretical framework for granular suspensions in a steady simple shear flow. *J. Rheol.* 43, 1673–1699. <https://doi.org/10.1122/1.551067>
- Andreotti, B., Forterre, Y., Pouliquen, O., 2013. *Granular Media: Between Fluid and Solid*. Cambridge University Press.
- Annen, C., Blundy, J.D., Leuthold, J., Sparks, R.S.J., 2015. Construction and evolution of igneous bodies: Towards an integrated perspective of crustal magmatism. *Lithos* 230, 206–221. <https://doi.org/10.1016/j.lithos.2015.05.008>
- Annen, C., Blundy, J.D., Sparks, R.S.J., 2006. The Genesis of Intermediate and Silicic Magmas in Deep Crustal Hot Zones. *J. Petrol.* 47, 505–539. <https://doi.org/10.1093/petrology/egi084>
- Annen, C., Sparks, R.S.J., 2002. Effects of repetitive emplacement of basaltic intrusions on thermal evolution and melt generation in the crust. *Earth Planet. Sci. Lett.* 203, 937–955. [https://doi.org/10.1016/S0012-821X\(02\)00929-9](https://doi.org/10.1016/S0012-821X(02)00929-9)
- Atkinson, C.M., Kytömaa, H.K., 1992. Acoustic wave speed and attenuation in suspensions. *Int. J. Multiph. Flow* 18, 577–592. [https://doi.org/10.1016/0301-9322\(92\)90053-J](https://doi.org/10.1016/0301-9322(92)90053-J)
- Bachmann, O., Bergantz, G., 2008. The Magma Reservoirs That Feed Supereruptions. *Elements* 4, 17–21. <https://doi.org/10.2113/GSELEMENTS.4.1.17>
- Bachmann, O., Bergantz, G.W., 2006. Gas percolation in upper-crustal silicic crystal mushes as a mechanism for upward heat advection and rejuvenation of near-solidus magma bodies. *J. Volcanol. Geotherm. Res.* 149, 85–102. <https://doi.org/10.1016/j.jvolgeores.2005.06.002>
- Bachmann, O., Bergantz, G.W., 2004. On the origin of crystal-poor rhyolites: extracted from batholithic crystal mushes. *J. Petrol.* 45, 1565–1582.
- Bachmann, O., Deering, C.D., Lipman, P.W., Plummer, C., 2014. Building zoned ignimbrites by recycling silicic cumulates: insight from the 1,000 km³ Carpenter Ridge Tuff, CO. *Contrib. Mineral. Petrol.* 167, 1025. <https://doi.org/10.1007/s00410-014-1025-3>
- Bachmann, O., Dungan, M.A., Lipman, P.W., 2002. The Fish Canyon Magma Body, San Juan Volcanic Field, Colorado: Rejuvenation and Eruption of an Upper-Crustal Batholith. *J. Petrol.* 43, 1469–1503. <https://doi.org/10.1093/petrology/43.8.1469>
- Bachmann, O., Huber, C., 2019. The Inner Workings of Crustal Distillation Columns; the Physical Mechanisms and Rates Controlling Phase Separation in Silicic Magma Reservoirs. *J. Petrol.* 60, 3–18. <https://doi.org/10.1093/petrology/egy103>
- Bachmann, O., Huber, C., 2016. Silicic magma reservoirs in the Earth's crust. *Am. Mineral.* 101, 2377–2404. <https://doi.org/10.2138/am-2016-5675>
- Bagdassarov, N.S., Dingwell, D.B., Webb, S.L., 1994. Viscoelasticity of crystal-and bubble-bearing rhyolite melts. *Phys. Earth Planet. Inter.* 83, 83–99.
- Bain, A.A., Jellinek, A.M., Wiebe, R.A., 2013. Quantitative field constraints on the dynamics of silicic magma chamber rejuvenation and overturn. *Contrib. Mineral. Petrol.* 165, 1275–1294. <https://doi.org/10.1007/s00410-013-0858-5>
- Banks-Sills, L., Leiderman, V., Fang, D., 1997. On the effect of particle shape and orientation on elastic properties of metal matrix composites. *Compos. Part B Eng.* 28, 465–481. [https://doi.org/10.1016/S1359-8368\(96\)00068-6](https://doi.org/10.1016/S1359-8368(96)00068-6)
- Barboni, M., Boehnke, P., Schmitt, A.K., Harrison, T.M., Shane, P., Bouvier, A.-S., Baumgartner, L., 2016. Warm storage for arc magmas. *Proc. Natl. Acad. Sci.* 201616129. <https://doi.org/10.1073/pnas.1616129113>
- Barth, A., Edmonds, M., Woods, A., 2019. Valve-like dynamics of gas flow through a packed crystal mush and cyclic strombolian explosions. *Sci. Rep.* 9, 1–9. <https://doi.org/10.1038/s41598-018-37013-8>
- Batchelor, K.G., O'Brien, W.R., 1977. Thermal or electrical conduction through a granular material. *Proc. R. Soc. Lond. Math. Phys. Sci.* 355, 313–333. <https://doi.org/10.1098/rspa.1977.0100>
- Bergantz, G.W., 2000. On the dynamics of magma mixing by reintrusion: implications for pluton assembly processes. *J. Struct. Geol.* 22, 1297–1309. [https://doi.org/10.1016/S0191-8141\(00\)00053-5](https://doi.org/10.1016/S0191-8141(00)00053-5)
- Bergantz, G.W., 1989. Underplating and Partial Melting: Implications for Melt Generation and Extraction. *Science* 245, 1093–1095. <https://doi.org/10.1126/science.245.4922.1093>

- Bergantz, G.W., Breidenthal, R.E., 2001. Non-stationary entrainment and tunneling eruptions: A dynamic link between eruption processes and magma mixing. *Geophys. Res. Lett.* 28, 3075–3078. <https://doi.org/10.1029/2001GL013304>
- Bergantz, G.W., Ni, J., 1999. A numerical study of sedimentation by dripping instabilities in viscous fluids. *Int. J. Multiph. Flow* 25, 307–320. [https://doi.org/10.1016/S0301-9322\(98\)00050-0](https://doi.org/10.1016/S0301-9322(98)00050-0)
- Bergantz, G.W., Schleicher, J.M., Burgisser, A., 2017. On the kinematics and dynamics of crystal-rich systems. *J. Geophys. Res. Solid Earth* 122, 2017JB014218. <https://doi.org/10.1002/2017JB014218>
- Bergantz, G.W., Schleicher, J.M., Burgisser, A., 2015. Open-system dynamics and mixing in magma mushes. *Nat. Geosci.* 8, 793–796. <https://doi.org/10.1038/ngeo2534>
- Berryman, J.G., 1980. Long-wavelength propagation in composite elastic media I. Spherical inclusions. *J. Acoust. Soc. Am.* 68, 1809–1819. <https://doi.org/10.1121/1.385171>
- Boudreau, A.E., 1999. PELE—a version of the MELTS software program for the PC platform. *Comput. Geosci.* 25, 201–203.
- Boyer, F., Guazzelli, É., Pouliquen, O., 2011. Unifying Suspension and Granular Rheology. *Phys. Rev. Lett.* 107, 188301. <https://doi.org/10.1103/PhysRevLett.107.188301>
- Breard, E.C.P., Dufek, J., Lube, G., 2018. Enhanced Mobility in Concentrated Pyroclastic Density Currents: An Examination of a Self-Fluidization Mechanism. *Geophys. Res. Lett.* 45, 654–664. <https://doi.org/10.1002/2017GL075759>
- Brunet, Th., Jia, X., Mills, P., 2008. Mechanisms for Acoustic Absorption in Dry and Weakly Wet Granular Media. *Phys. Rev. Lett.* 101, 138001. <https://doi.org/10.1103/PhysRevLett.101.138001>
- Burgisser, A., Bergantz, G.W., 2011. A rapid mechanism to remobilize and homogenize highly crystalline magma bodies. *Nature* 471, 212–215. <https://doi.org/10.1038/nature09799>
- Burgisser, A., Bergantz, G.W., Breidenthal, R.E., 2005. Addressing complexity in laboratory experiments: the scaling of dilute multiphase flows in magmatic systems. *J. Volcanol. Geotherm. Res.* 141, 245–265. <https://doi.org/10.1016/j.jvolgeores.2004.11.001>
- Caricchi, L., Annen, C., Blundy, J., Simpson, G., Pinel, V., 2014. Frequency and magnitude of volcanic eruptions controlled by magma injection and buoyancy. *Nat. Geosci.* 7, 126–130. <https://doi.org/10.1038/ngeo2041>
- Caricchi, L., Blundy, J., 2015a. The temporal evolution of chemical and physical properties of magmatic systems. *Geol. Soc. Lond. Spec. Publ.* 422, 1–15. <https://doi.org/10.1144/SP422.11>
- Caricchi, L., Blundy, J., 2015b. Experimental petrology of monotonous intermediate magmas. *Geol. Soc. Lond. Spec. Publ.* 422, 105–130. <https://doi.org/10.1144/SP422.9>
- Caricchi, L., Burlini, L., Ulmer, P., 2008. Propagation of P and S-waves in magmas with different crystal contents: Insights into the crystallinity of magmatic reservoirs. *J. Volcanol. Geotherm. Res., Evolution, Transfer and Release of Magmas and Volcanic Gases* 178, 740–750. <https://doi.org/10.1016/j.jvolgeores.2008.09.006>
- Caricchi, L., Burlini, L., Ulmer, P., Gerya, T., Vassalli, M., Papale, P., 2007. Non-Newtonian rheology of crystal-bearing magmas and implications for magma ascent dynamics. *Earth Planet. Sci. Lett.* 264, 402–419. <https://doi.org/10.1016/j.epsl.2007.09.032>
- Cashman, K.V., Giordano, G., 2014. Calderas and magma reservoirs. *J. Volcanol. Geotherm. Res.* 288, 28–45. <https://doi.org/10.1016/j.jvolgeores.2014.09.007>
- Cashman, K.V., Sparks, R.S.J., Blundy, J.D., 2017. Vertically extensive and unstable magmatic systems: A unified view of igneous processes. *Science* 355, eaag3055. <https://doi.org/10.1126/science.aag3055>
- Cassidy, M., Manga, M., Cashman, K., Bachmann, O., 2018. Controls on explosive-effusive volcanic eruption styles. *Nat. Commun.* 9, 1–16. <https://doi.org/10.1038/s41467-018-05293-3>
- Challis, R.E., Povey, M.J.W., Mather, M.L., Holmes, A.K., 2005. Ultrasound techniques for characterizing colloidal dispersions. *Rep. Prog. Phys.* 68, 1541.
- Champallier, R., Bystricky, M., Arbaret, L., 2008. Experimental investigation of magma rheology at 300 MPa: From pure hydrous melt to 76 vol.% of crystals. *Earth Planet. Sci. Lett.* 267, 571–583. <https://doi.org/10.1016/j.epsl.2007.11.065>
- Chen, X., Wang, J., 2014. A comparison of two-fluid model, dense discrete particle model and CFD-DEM method for modeling impinging gas–solid flows. *Powder Technol.* 254, 94–102. <https://doi.org/10.1016/j.powtec.2013.12.056>
- Chiarabba, C., Moretti, M., 2006. An insight into the unrest phenomena at the Campi Flegrei caldera from Vp and Vp/Vs tomography. *Terra Nova* 18, 373–379. <https://doi.org/10.1111/j.1365-3121.2006.00701.x>

- Cimarelli, C., Costa, A., Mueller, S., Mader, H.M., 2011. Rheology of magmas with bimodal crystal size and shape distributions: Insights from analog experiments. *Geochem. Geophys. Geosystems* 12. <https://doi.org/10.1029/2011GC003606>
- Cioni, R., Civetta, L., Marianelli, P., Metrich, N., Santacroce, R., Sbrana, A., 1995. Compositional layering and syn-eruptive mixing of a periodically refilled shallow magma chamber: the AD 79 Plinian eruption of Vesuvius. *J. Petrol.* 36, 739–776.
- Claeys, I.L., Brady, J.F., 1993. Suspensions of prolate spheroids in Stokes flow. Part 1. Dynamics of a finite number of particles in an unbounded fluid. *J. Fluid Mech.* 251, 411–442. <https://doi.org/10.1017/S0022112093003465>
- Collier, L., Neuberg, J.W., Lensky, N., Lyakhovsky, V., Navon, O., 2006. Attenuation in gas-charged magma. *J. Volcanol. Geotherm. Res.*, MULTIMO: Multi-Parameter Monitoring, Modelling and Forecasting of Volcanic Hazard 153, 21–36. <https://doi.org/10.1016/j.jvolgeores.2005.08.009>
- Cooper, K.M., Kent, A.J.R., 2014. Rapid remobilization of magma crystals kept in cold storage. *Nature* 506, 480–483.
- Cordonnier, B., Caricchi, L., Pistone, M., Castro, J., Hess, K.-U., Gottschaller, S., Manga, M., Dingwell, D.B., Burlini, L., 2012. The viscous-brittle transition of crystal-bearing silicic melt: Direct observation of magma rupture and healing. *Geology* 40, 611–614. <https://doi.org/10.1130/G3914.1>
- Costa, A., Caricchi, L., Bagdassarov, N., 2009. A model for the rheology of particle-bearing suspensions and partially molten rocks. *Geochem. Geophys. Geosystems* 10. <https://doi.org/10.1029/2008GC002138>
- Couch, S., Sparks, R.S.J., Carroll, M.R., 2001. Mineral disequilibrium in lavas explained by convective self-mixing in open magma chambers. *Nature* 411, 1037–1039. <https://doi.org/10.1038/35082540>
- Courrech du Pont, S., Gondret, P., Perrin, B., Rabaud, M., 2003. Wall effects on granular heap stability. *EPL Europhys. Lett.* 61, 492. <https://doi.org/10.1209/epl/i2003-00156-5>
- Coussot, P., Ancey, C., 1999. Rheophysical classification of concentrated suspensions and granular pastes. *Phys. Rev. E* 59, 4445–4457. <https://doi.org/10.1103/PhysRevE.59.4445>
- Crowe, C.T., Schwarzkopf, J.D., Sommerfeld, M., Tsuji, Y., 1997. *Multiphase Flows with Droplets and Particles*. CRC Press.
- Cui, X., Li, J., Chan, A., Chapman, D., 2014. Coupled DEM–LBM simulation of internal fluidisation induced by a leaking pipe. *Powder Technol.* 254, 299–306. <https://doi.org/10.1016/j.powtec.2014.01.048>
- Davis, M., Koenders, M.A., Petford, N., 2007. Vibro-agitation of chambered magma. *J. Volcanol. Geotherm. Res.*, Large Silicic Magma Systems 167, 24–36. <https://doi.org/10.1016/j.jvolgeores.2007.07.012>
- Deubelbeiss, Y., Kaus, B.J.P., Connolly, J.A.D., Caricchi, L., 2011. Potential causes for the non-Newtonian rheology of crystal-bearing magmas. *Geochemistry Geophys. Geosystems* 12, Q05007
- Deen, N.G., Annaland, M. van S., Hoef, M.A. van der, Kuipers, J. a. M., 2007. Review of discrete particle modeling of fluidized beds. *Chem. Eng. Sci.* 62, 28–44. <https://doi.org/10.1016/j.ces.2006.08.014>
- Dellino, P., Mele, D., Bonasia, R., Braia, G., Volpe, L.L., Sulpizio, R., 2005. The analysis of the influence of pumice shape on its terminal velocity. *Geophys. Res. Lett.* 32. <https://doi.org/10.1029/2005GL023954>
- Delvosalle, C., Vanderschuren, J., 1985. Gas-to-particle and particle-to-particle heat transfer in fluidized beds of large particles. *Chem. Eng. Sci.* 40, 769–779. [https://doi.org/10.1016/0009-2509\(85\)85030-2](https://doi.org/10.1016/0009-2509(85)85030-2)
- De Siena, L., Thomas, C., Waite, G.P., Moran, S.C., Klemme, S., 2014. Attenuation and scattering tomography of the deep plumbing system of Mount St. Helens. *J. Geophys. Res. Solid Earth* 119, 8223–8238. <https://doi.org/10.1002/2014JB011372>
- Dingwell, D.B., Webb, S.L., 1990. Relaxation in silicate melts. *Eur. J. Mineral.* 427–449.
- Dingwell, D.B., Webb, S.L., 1989. Structural relaxation in silicate melts and non-Newtonian melt rheology in geologic processes. *Phys. Chem. Miner.* 16, 508–516. <https://doi.org/10.1007/BF00197020>
- Dioguardi, F., Dellino, P., Mele, D., 2014. Integration of a new shape-dependent particle–fluid drag coefficient law in the multiphase Eulerian–Lagrangian code MFIX-DEM. *Powder Technol.* 260, 68–77. <https://doi.org/10.1016/j.powtec.2014.03.071>
- Dufek, J., Bachmann, O., 2010. Quantum magmatism: Magmatic compositional gaps generated by melt-crystal dynamics. *Geology* 38, 687–690. <https://doi.org/10.1130/G30831.1>
- Dufek, J., Bergantz, G.W., 2005. Lower Crustal Magma Genesis and Preservation: a Stochastic Framework for the Evaluation of Basalt–Crust Interaction. *J. Petrol.* 46, 2167–2195. <https://doi.org/10.1093/petrology/egi049>
- Džugys, A., Peters, B., 2001. An approach to simulate the motion of spherical and non-spherical fuel particles in combustion chambers. *Granul. Matter* 3, 231–266. <https://doi.org/10.1007/PL00010918>
- Edmonds, Cashman Katharine V., Holness Marian, Jackson Matthew, 2019. Architecture and dynamics of magma reservoirs. *Philos. Trans. R. Soc. Math. Phys. Eng. Sci.* 377, 20180298. <https://doi.org/10.1098/rsta.2018.0298>
- Eichelberger, J.C., Izbekov, P.E., 2000. Eruption of andesite triggered by dyke injection: contrasting cases at Karymsky Volcano, Kamchatka and Mt Katmai, Alaska. *Philos. Trans. R. Soc. Lond. Ser. Math. Phys. Eng. Sci.* 358, 1465–1485.

-
- Ergun, S., 1952. Fluid flow through packed columns. *Chem Eng Prog* 48, 89–94.
- Evans, J.M., Attenborough, K., 2002. Sound propagation in concentrated emulsions: Comparison of coupled phase model and core-shell model. *J. Acoust. Soc. Am.* 112, 1911–1917.
- Evans, J.M., Attenborough, K., 1997. Coupled phase theory for sound propagation in emulsions. *J. Acoust. Soc. Am.* 102, 278–282. <https://doi.org/10.1121/1.419745>
- Faroughi, S.A., Huber, C., 2014a. Crowding-based rheological model for suspensions of rigid bimodal-sized particles with interfering size ratios. *Phys. Rev. E* 90, 052303.
- Faroughi, S.A., Huber, C., 2014b. Crowding-based rheological model for suspensions of rigid bimodal-sized particles with interfering size ratios. *Phys. Rev. E* 90, 052303. <https://doi.org/10.1103/PhysRevE.90.052303>
- Farr, R.S., Groot, R.D., 2009. Close packing density of polydisperse hard spheres. *J. Chem. Phys.* 131, 244101.
- Farr, Robert S., Groot, R.D., 2009. Close packing density of polydisperse hard spheres. *J. Chem. Phys.* 131, 244104. <https://doi.org/10.1063/1.3276799>
- Fernandez, N., Mani, R., Rinaldi, D., Kadau, D., Mosquet, M., Lombois-Burger, H., Cayer-Barrioz, J., Herrmann, H.J., Spencer, N.D., Isa, L., 2013. Microscopic Mechanism for Shear Thickening of Non-Brownian Suspensions. *Phys. Rev. Lett.* 111, 108301. <https://doi.org/10.1103/PhysRevLett.111.108301>
- Frankel, N.A., Acrivos, A., 1967. On the viscosity of a concentrated suspension of solid spheres. *Chem. Eng. Sci.* 22, 847–853. [https://doi.org/10.1016/0009-2509\(67\)80149-0](https://doi.org/10.1016/0009-2509(67)80149-0)
- Furuichi, M., Nishiura, D., 2014. Robust coupled fluid-particle simulation scheme in Stokes-flow regime: Toward the geodynamic simulation including granular media. *Geochem. Geophys. Geosystems* 15, 2865–2882. <https://doi.org/10.1002/2014GC005281>
- Garg, R., Galvin, J., Li, T., Pannala, S., 2012. Open-source MFIx-DEM software for gas–solids flows: Part I—Verification studies. *Powder Technol.* 220, 122–137.
- Garg, R., Galvin, J., Li, T., Pannala, S., 2010. Documentation of open-source MFIx-DEM software for gas–solids flows. URL <Httpsmfix.Net1DoeGovdocumentationdemdoc2012-1Pdf> Accessed 31 March 2014.
- Garg, R., Narayanan, C., Lakehal, D., Subramaniam, S., 2007. Accurate numerical estimation of interphase momentum transfer in Lagrangian–Eulerian simulations of dispersed two-phase flows. *Int. J. Multiph. Flow* 33, 1337–1364. <https://doi.org/10.1016/j.ijmultiphaseflow.2007.06.002>
- Gear, C., 1971. Simultaneous Numerical Solution of Differential-Algebraic Equations. *IEEE Trans. Circuit Theory* 18, 89–95. <https://doi.org/10.1109/TCT.1971.1083221>
- Gelman, S.E., Gutiérrez, F.J., Bachmann, O., 2013. On the longevity of large upper crustal silicic magma reservoirs. *Geology* 41, 759–762. <https://doi.org/10.1130/G34241.1>
- Ghiorso, M.S., 2004. An equation of state for silicate melts. I. Formulation of a general model. *Am. J. Sci.* 304, 637–678. <https://doi.org/10.2475/ajs.304.8-9.637>
- Ghiorso, M.S., Kress, V.C., 2004. An equation of state for silicate melts. II. Calibration of volumetric properties at 105 Pa. *Am. J. Sci.* 304, 679–751. <https://doi.org/10.2475/ajs.304.8-9.679>
- Gibson, R.L., Toksöz, M.N., 1989. Viscous attenuation of acoustic waves in suspensions. *J. Acoust. Soc. Am.* 85, 1925–1934. <https://doi.org/10.1121/1.397846>
- Gidaspow, D., 1994. *Multiphase Flow and Fluidization: Continuum and Kinetic Theory Descriptions*. Academic Press.
- Giordano, D., Russell, J.K., Dingwell, D.B., 2008. Viscosity of magmatic liquids: A model. *Earth Planet. Sci. Lett.* 271, 123–134. <https://doi.org/10.1016/j.epsl.2008.03.038>
- Girard, G., Stix, J., 2009. Buoyant replenishment in silicic magma reservoirs: Experimental approach and implications for magma dynamics, crystal mush remobilization, and eruption. *J. Geophys. Res. Solid Earth* 114, B08203. <https://doi.org/10.1029/2008JB005791>
- Girona, T., Costa, F., Schubert, G., 2015. Degassing during quiescence as a trigger of magma ascent and volcanic eruptions. *Sci. Rep.* 5, 18212. <https://doi.org/10.1038/srep18212>
- Gondret, P., Lance, M., Petit, L., 2002. Bouncing motion of spherical particles in fluids. *Phys. Fluids* 14, 643–652. <https://doi.org/10.1063/1.1427920>
- Gori, P.D., Chiarabba, C., Patanè, D., 2005. Qp structure of Mount Etna: Constraints for the physics of the plumbing system. *J. Geophys. Res. Solid Earth* 110. <https://doi.org/10.1029/2003JB002875>
- Gottsmann, J., Lavallée, Y., Martí, J., Aguirre-Díaz, G., 2009. Magma–tectonic interaction and the eruption of silicic batholiths. *Earth Planet. Sci. Lett.* 284, 426–434. <https://doi.org/10.1016/j.epsl.2009.05.008>
- Hacker, B.R., Abers, G.A., Peacock, S.M., 2003. Subduction factory 1. Theoretical mineralogy, densities, seismic wave speeds, and H₂O contents. *J. Geophys. Res. Solid Earth* 108. <https://doi.org/10.1029/2001JB001127>

- Hampton, L.D., 1967. Acoustic Properties of Sediments. *J. Acoust. Soc. Am.* 42, 882–890. <https://doi.org/10.1121/1.1910662>
- Harker, A.H., Temple, J.A.G., 1988. Velocity and attenuation of ultrasound in suspensions of particles in fluids. *J. Phys. Appl. Phys.* 21, 1576–1588. <https://doi.org/10.1088/0022-3727/21/11/006>
- Hertz, H., 1896. Miscellaneous papers by H. Hertz. Transl. Jones Schott GA MacMillan Co Ltd Lond. 146–183.
- Higgins, M.D., 2006. Verification of ideal semi-logarithmic, lognormal or fractal crystal size distributions from 2D datasets. *J. Volcanol. Geotherm. Res., Modern Trends in Petrography*: 154, 8–16. <https://doi.org/10.1016/j.jvolgeores.2005.09.015>
- Higgins, M.D., Roberge, J., 2003. Crystal Size Distribution of Plagioclase and Amphibole from Soufrière Hills Volcano, Montserrat: Evidence for Dynamic Crystallization–Textural Coarsening Cycles. *J. Petrol.* 44, 1401–1411. <https://doi.org/10.1093/petrology/44.8.1401>
- Hildreth, W., 2004. Volcanological perspectives on Long Valley, Mammoth Mountain, and Mono Craters: several contiguous but discrete systems. *J. Volcanol. Geotherm. Res.* 136, 169–198.
- Hildreth, W., 1979. The Bishop Tuff: Evidence for the origin of compositional zonation in silicic magma chambers. *Geol. Soc. Am. Spec. Pap.* 180, 43–75.
- Hodge, K.F., Carazzo, G., Jellinek, A.M., 2012. Experimental constraints on the deformation and breakup of injected magma. *Earth Planet. Sci. Lett.* 325–326, 52–62. <https://doi.org/10.1016/j.epsl.2012.01.031>
- Holohan, E.P., Sudhaus, H., Walter, T.R., Schöpfer, M.P.J., Walsh, J.J., 2017. Effects of Host-rock Fracturing on Elastic-deformation Source Models of Volcano Deflation. *Sci. Rep.* 7, 1–12. <https://doi.org/10.1038/s41598-017-10009-6>
- Huber, C., Parmigiani, A., Chopard, B., Manga, M., and Bachmann, O., 2008, Lattice Boltzmann model for melting with natural convection: *International Journal of Heat and Fluid Flow*, v. 29, no. 5, p. 1469–1480.
- Huber, C., Bachmann, O., Dufek, J., 2011. Thermo-mechanical reactivation of locked crystal mushes: Melting-induced internal fracturing and assimilation processes in magmas. *Earth Planet. Sci. Lett.* 304, 443–454. <https://doi.org/10.1016/j.epsl.2011.02.022>
- Huber, C., Bachmann, O., Manga, M., 2009. Homogenization processes in silicic magma chambers by stirring and mushification (latent heat buffering). *Earth Planet. Sci. Lett.* 283, 38–47. <https://doi.org/10.1016/j.epsl.2009.03.029>
- Huppert, H.E., Sparks, R.S.J., Whitehead, J.A., Hallworth, M.A., 1986. Replenishment of magma chambers by light inputs. *J. Geophys. Res. Solid Earth* 6113–6122. [https://doi.org/10.1029/JB091iB06p06113@10.1002/\(ISSN\)2169-9356.OPENSYS1](https://doi.org/10.1029/JB091iB06p06113@10.1002/(ISSN)2169-9356.OPENSYS1)
- Huppert, H.E., Stephen, R., Sparks, J., Turner, J.S., 1984. Some effects of viscosity on the dynamics of replenished magma chambers. *J. Geophys. Res. Solid Earth* 89, 6857–6877. <https://doi.org/10.1029/JB089iB08p06857>
- Indrastuti, N., Nugraha, A.D., McCausland, W.A., Hendrasto, M., Gunawan, H., Kusnandar, R., Kasbani, Kristianto, 2019. 3-D Seismic Tomographic study of Sinabung Volcano, Northern Sumatra, Indonesia, during the inter-eruptive period October 2010–July 2013. *J. Volcanol. Geotherm. Res.* <https://doi.org/10.1016/j.jvolgeores.2019.03.001>
- Ishii, M., Hibiki, T., 2011. *Thermo-Fluid Dynamics of Two-Phase Flow*. Springer Science+Business Media, LLC, .
- Janoschek, F., Harting, J., Toschi, F., 2013. Accurate lubrication corrections for spherical and non-spherical particles in discretized fluid simulations. *ArXiv13086482 Cond-Mat Physicsphysics*.
- Jeffrey, D.J., Onishi, Y., 1984. The forces and couples acting on two nearly touching spheres in low-Reynolds-number flow. *Z. Für Angew. Math. Phys. ZAMP* 35, 634–641. <https://doi.org/10.1007/BF00952109>
- Jellinek, A.M., Kerr, R.C., 1999. Mixing and compositional stratification produced by natural convection: 2. Applications to the differentiation of basaltic and silicic magma chambers and komatiite lava flows. *J. Geophys. Res. Solid Earth* 104, 7203–7218. <https://doi.org/10.1029/1998JB900117>
- Jellinek, A.M., Kerr, R.C., Griffiths, R.W., 1999. Mixing and compositional stratification produced by natural convection: 1. Experiments and their application to Earth’s core and mantle. *J. Geophys. Res. Solid Earth* 104, 7183–7201. <https://doi.org/10.1029/1998JB900116>
- Karakas, O., Degruyter, W., Bachmann, O., Dufek, J., 2017. Lifetime and size of shallow magma bodies controlled by crustal-scale magmatism. *Nat. Geosci.* 10, 446–450. <https://doi.org/10.1038/ngeo2959>
- Karlstrom, L., Rudolph, M.L., Manga, M., 2012. Caldera size modulated by the yield stress within a crystal-rich magma reservoir. *Nat. Geosci.* 5, 402–405. <https://doi.org/10.1038/ngeo1453>
- Kelfoun, K., Druitt, T.H., 2005. Numerical modeling of the emplacement of Socompa rock avalanche, Chile. *J. Geophys. Res. Solid Earth* 110. <https://doi.org/10.1029/2005JB003758>
- Keller, T., and Suckale, J., 2019, A continuum model of multi-phase reactive transport in igneous systems: *Geophysical Journal International*, v. 219, no. 1, p. 185–222.

-
- Kendrick, J.E., Lavallée, Y., Hess, K.-U., Heap, M.J., Gaunt, H.E., Meredith, P.G., Dingwell, D.B., 2013. Tracking the permeable porous network during strain-dependent magmatic flow. *J. Volcanol. Geotherm. Res.* 260, 117–126. <https://doi.org/10.1016/j.jvolgeores.2013.05.012>
- Kiser, E., Palomeras, I., Levander, A., Zelt, C., Harder, S., Schmandt, B., Hansen, S., Creager, K., Ulberg, C., 2016. Magma reservoirs from the upper crust to the Moho inferred from high-resolution Vp and Vs models beneath Mount St. Helens, Washington State, USA. *Geology* 44, 411–414. <https://doi.org/10.1130/G37591.1>
- Koyaguchi, T., Kaneko, K., 2000. Thermal evolution of silicic magma chambers after basalt replenishments. *Earth Environ. Sci. Trans. R. Soc. Edinb.* 91, 47–60. <https://doi.org/10.1017/S0263593300007288>
- Kress, V.C., Carmichael, I.S.E., 1991. The compressibility of silicate liquids containing Fe₂O₃ and the effect of composition, temperature, oxygen fugacity and pressure on their redox states. *Contrib. Mineral. Petrol.* 108, 82–92. <https://doi.org/10.1007/BF00307328>
- Kumagai, H., Chouet, B.A., 2000. Acoustic properties of a crack containing magmatic or hydrothermal fluids. *J. Geophys. Res. Solid Earth* 105, 25493–25512. <https://doi.org/10.1029/2000JB900273>
- Kuster, G., Toksöz, M., 1974a. Velocity and attenuation of seismic waves in two-phase media: part i. theoretical formulations. *GEOPHYSICS* 39, 587–606. <https://doi.org/10.1190/1.1440450>
- Kuster, G.T., Toksoz, M.N., 1974b. Velocity and attenuation of seismic waves in two-phase media; Part II, Experimental results. *Geophysics* 39, 607–618. <https://doi.org/10.1190/1.1440451>
- Kytömaa, H.K., 1995. Theory of sound propagation in suspensions: a guide to particle size and concentration characterization. *Powder Technol.* 82, 115–121. [https://doi.org/10.1016/0032-5910\(94\)02901-Y](https://doi.org/10.1016/0032-5910(94)02901-Y)
- Laumonier, M., Scaillet, B., Arbaret, L., Andújar, J., Champallier, R., 2015. Experimental mixing of hydrous magmas. *Chem. Geol.* 418, 158–170. <https://doi.org/10.1016/j.chemgeo.2015.10.031>
- Laumonier, M., Scaillet, B., Arbaret, L., Champallier, R., 2014. Experimental simulation of magma mixing at high pressure. *Lithos* 196–197, 281–300. <https://doi.org/10.1016/j.lithos.2014.02.016>
- Laumonier, M., Scaillet, B., Pichavant, M., Champallier, R., Andújar, J., Arbaret, L., 2013. On the conditions of magma mixing and its bearing on andesite production in the crust. *Nat. Commun.* 5, 12 p. <https://doi.org/10.1038/ncomms6607>
- Lavallée, Y., Benson, P.M., Heap, M.J., Hess, K.-U., Flaws, A., Schillinger, B., Meredith, P.G., Dingwell, D.B., 2013. Reconstructing magma failure and the degassing network of dome-building eruptions. *Geology* 41, 515–518. <https://doi.org/10.1130/G33948.1>
- Lavallée, Y., Hess, K.-U., Cordonnier, B., Dingwell, D.B., 2007. Non-Newtonian rheological law for highly crystalline dome lavas. *Geology* 35, 843–846. <https://doi.org/10.1130/G23594A.1>
- Lavallée, Y., Varley, N., Alatorre-Ibargüengoitia, M., Hess, K.-U., Kueppers, U., Mueller, S., Richard, D., Scheu, B., Spieler, O., Dingwell, D., 2012. Magmatic architecture of dome-building eruptions at Volcán de Colima, Mexico. *Bull. Volcanol.* 74, 249–260.
- Lees, J.M., 1992. The magma system of Mount St. Helens: non-linear high-resolution P-wave tomography. *J. Volcanol. Geotherm. Res.* 53, 103–116. [https://doi.org/10.1016/0377-0273\(92\)90077-Q](https://doi.org/10.1016/0377-0273(92)90077-Q)
- Lesage, Ph., Surono, 1995. Seismic precursors of the February 10, 1990 eruption of Kelut volcano, Java. *J. Volcanol. Geotherm. Res.* 65, 135–146. [https://doi.org/10.1016/0377-0273\(94\)00051-H](https://doi.org/10.1016/0377-0273(94)00051-H)
- Leshner, C.E., Spera, F.J., 2015. Chapter 5 - Thermodynamic and Transport Properties of Silicate Melts and Magma, in: Sigurdsson, H. (Ed.), *The Encyclopedia of Volcanoes (Second Edition)*. Academic Press, Amsterdam, pp. 113–141. <https://doi.org/10.1016/B978-0-12-385938-9.00005-5>
- Li, T., Garg, R., Galvin, J., Pannala, S., 2012. Open-source MFI-X-DEM software for gas-solids flows: Part II—Validation studies. *Powder Technol.* 220, 138–150.
- Li, T., Pannala, S., Shahnam, M., 2014. Reprint of "CFD simulations of circulating fluidized bed risers, part II, evaluation of differences between 2D and 3D simulations. *Powder Technol., Selected Papers from the 2012 NETL Multiphase Flow Workshop* 265, 13–22. <https://doi.org/10.1016/j.powtec.2014.04.007>
- Longo, A., Papale, P., Vassalli, M., Saccorotti, G., Montagna, C.P., Cassioli, A., Giudice, S., Boschi, E., 2012. Magma convection and mixing dynamics as a source of Ultra-Long-Period oscillations. *Bull. Volcanol.* 74, 873–880. <https://doi.org/10.1007/s00445-011-0570-0>
- Longo, A., Vassalli, M., Papale, P., Barsanti, M., 2006. Numerical simulation of convection and mixing in magma chambers replenished with CO₂-rich magma. *Geophys. Res. Lett.* 33. <https://doi.org/10.1029/2006GL027760>

- Lube, G., Breard, E.C.P., Jones, J., Fullard, L., Dufek, J., Cronin, S.J., Wang, T., 2019. Generation of air lubrication within pyroclastic density currents. *Nat. Geosci.* 12, 381–386. <https://doi.org/10.1038/s41561-019-0338-2>
- MacDonald, M.J., Chu, C.-F., Guilloit, P.P., Ng, K.M., 1991. A generalized Blake-Kozeny equation for multisized spherical particles. *AIChE J.* 37, 1583–1588.
- Mader, H.M., Llewellyn, E.W., Mueller, S.P., 2013. The rheology of two-phase magmas: A review and analysis. *J. Volcanol. Geotherm. Res.* 257, 135–158. <https://doi.org/10.1016/j.jvolgeores.2013.02.014>
- Manga, M., 1996. Mixing of heterogeneities in the mantle: Effect of viscosity differences. *Geophys. Res. Lett.* 23, 403–406. <https://doi.org/10.1029/96GL00242>
- Margulies, T.S., Schwarz, W.H., 1994. A multiphase continuum theory for sound wave propagation through dilute suspensions of particles. *J. Acoust. Soc. Am.* 96, 319–331.
- Mari, R., Seto, R., Morris, J.F., Denn, M.M., 2014. Shear thickening, frictionless and frictional rheologies in non-Brownian suspensions. *J. Rheol.* 58, 1693–1724. <https://doi.org/10.1122/1.4890747>
- Marsh, B.D., 1981. On the crystallinity, probability of occurrence, and rheology of lava and magma. *Contr. Mineral. and Petrol.* 78, 85–98. <https://doi.org/10.1007/BF00371146>
- Marsh, B.D., 1988. Crystal size distribution (CSD) in rocks and the kinetics and dynamics of crystallization. *Contrib. Mineral. Petrol.* 99, 277–291. <https://doi.org/10.1007/BF00375362>
- Marzougui, D., Chareyre, B., Chauchat, J., 2015. Microscopic origins of shear stress in dense fluid–grain mixtures. *Granul. Matter* 17, 297–309. <https://doi.org/10.1007/s10035-015-0560-6>
- Mavko, G.M., 1980. Velocity and attenuation in partially molten rocks. *J. Geophys. Res. Solid Earth* 5173–5189. [https://doi.org/10.1029/JB085iB10p05173@10.1002/\(ISSN\)2169-9356.STANFORD1](https://doi.org/10.1029/JB085iB10p05173@10.1002/(ISSN)2169-9356.STANFORD1)
- McIntire, M.Z., Bergantz George W., Schleicher Jillian M., 2019. On the hydrodynamics of crystal clustering. *Philos. Trans. R. Soc. Math. Phys. Eng. Sci.* 377, 20180015. <https://doi.org/10.1098/rsta.2018.0015>
- Melekhova, E., Annen, C., Blundy, J., 2013. Compositional gaps in igneous rock suites controlled by magma system heat and water content. *Nat. Geosci.* 6, 385–390. <https://doi.org/10.1038/ngeo1781>
- Michioka, H., Sumita, 2005. Rayleigh-Taylor instability of a particle packed viscous fluid: Implications for a solidifying magma. *Geophys. Res. Lett.* 32. <https://doi.org/10.1029/2004GL021827>
- Miller, D.S., Smith, R.B., 1999. P and S velocity structure of the Yellowstone volcanic field from local earthquake and controlled-source tomography. *J. Geophys. Res. Solid Earth* 104, 15105–15121. <https://doi.org/10.1029/1998JB900095>
- Moitra, P., Gonnermann, H.M., 2015. Effects of crystal shape- and size-modality on magma rheology. *Geochem. Geophys. Geosystems* 16, 1–26. <https://doi.org/10.1002/2014GC005554>
- Molina, I., Burgisser, A., Oppenheimer, C., 2012. Numerical simulations of convection in crystal-bearing magmas: A case study of the magmatic system at Erebus, Antarctica. *J. Geophys. Res. Solid Earth* 117. <https://doi.org/10.1029/2011JB008760>
- Montagna, C.P., Papale, P., Longo, A., 2015. Timescales of mingling in shallow magmatic reservoirs. *Geol. Soc. Lond. Spec. Publ.* 422, 131–140. <https://doi.org/10.1144/SP422.6>
- Montagna, C.P., Papale, P., Longo, A., Bagagli, M., 2017. Magma Chamber Rejuvenation: Insights from Numerical Models, in: Gottsmann, J., Neuberg, J., Scheu, B. (Eds.), *Volcanic Unrest: From Science to Society, Advances in Volcanology*. Springer International Publishing, Cham, pp. 111–122. https://doi.org/10.1007/11157_2017_21
- Morgan, J.K., McGovern, P.J., 2005. Discrete element simulations of gravitational volcanic deformation: 1. Deformation structures and geometries. *J. Geophys. Res. Solid Earth* 110. <https://doi.org/10.1029/2004JB003252>
- Morgavi, D., Perugini, D., De Campos, C.P., Ertel-Ingrisch, W., Dingwell, D.B., 2013. Time evolution of chemical exchanges during mixing of rhyolitic and basaltic melts. *Contrib. Mineral. Petrol.* 166, 615–638. <https://doi.org/10.1007/s00410-013-0894-1>
- Mueller, S., Llewellyn, E.W., Mader, H.M., 2011. The effect of particle shape on suspension viscosity and implications for magmatic flows. *Geophys. Res. Lett.* 38. <https://doi.org/10.1029/2011GL047167>
- Mueller, S., Llewellyn, E.W., Mader, H.M., 2010. The rheology of suspensions of solid particles. *Proc. R. Soc. Lond. Math. Phys. Eng. Sci.* 466, 1201–1228. <https://doi.org/10.1098/rspa.2009.0445>
- Murphy, M.D., Sparks, R.S.J., Barclay, J., Carroll, M.R., Brewer, T.S., 2000. Remobilization of Andesite Magma by Intrusion of Mafic Magma at the Soufriere Hills Volcano, Montserrat, West Indies. *J. Petrol.* 41, 21–42. <https://doi.org/10.1093/petrology/41.1.21>
- Murphy, M.D., Sparks, R.S.J., Barclay, J., Carroll, M.R., Lejeune, A.-M., Brewer, T.S., Macdonald, R., Black, S., Young, S., 1998. The role of magma mixing in triggering the current eruption at the Soufriere Hills Volcano, Montserrat, West Indies. *Geophys. Res. Lett.* 25, 3433–3436. <https://doi.org/10.1029/98GL00713>
- Mutabaruka, P., Delenne, J.-Y., Soga, K., Radjai, F., 2014. Initiation of immersed granular avalanches. *Phys. Rev. E* 89, 052203. <https://doi.org/10.1103/PhysRevE.89.052203>

-
- Nakagawa, M., Wada, K., Wood, C.P., 2002a. Mixed Magmas, Mush Chambers and Eruption Triggers: Evidence from Zoned Clinopyroxene Phenocrysts in Andesitic Scoria from the 1995 Eruptions of Ruapehu Volcano, New Zealand. *J. Petrol.* 43, 2279–2303. <https://doi.org/10.1093/petrology/43.12.2279>
- Nakagawa, M., Wada, K., Wood, C.P., 2002b. Mixed Magmas, Mush Chambers and Eruption Triggers: Evidence from Zoned Clinopyroxene Phenocrysts in Andesitic Scoria from the 1995 Eruptions of Ruapehu Volcano, New Zealand. *J. Petrol.* 43, 2279–2303. <https://doi.org/10.1093/petrology/43.12.2279>
- Nakajima, J., Matsuzawa, T., Hasegawa, A., Zhao, D., 2001. Three-dimensional structure of Vp, Vs, and Vp/Vs beneath northeastern Japan: Implications for arc magmatism and fluids. *J. Geophys. Res. Solid Earth* 106, 21843–21857. <https://doi.org/10.1029/2000JB000008>
- Ness, C., Sun, J., 2015. Flow regime transitions in dense non-Brownian suspensions: Rheology, microstructural characterization, and constitutive modeling. *Phys. Rev. E* 91, 012201. <https://doi.org/10.1103/PhysRevE.91.012201>
- Neuberg, J., O’Gorman, C., 2002. A model of the seismic wavefield in gas-charged magma: application to Soufrière Hills Volcano, Montserrat. *Geol. Soc. Lond. Mem.* 21, 603–609. <https://doi.org/10.1144/GSL.MEM.2002.021.01.29>
- Nolan, G.T., Kavanagh, P.E., 1995. Random packing of nonspherical particles. *Powder Technol.* 84, 199–205. [https://doi.org/10.1016/0032-5910\(95\)98237-S](https://doi.org/10.1016/0032-5910(95)98237-S)
- Oppenheimer, J., Rust, A.C., Cashman, K.V., Sandnes, B., 2015. Gas migration regimes and outgassing in particle-rich suspensions. *Front. Phys.* 3, 60.
- Ouchiyama, N., Tanaka, T., 2002. Porosity estimation for random packings of spherical particles [WWW Document]. <https://doi.org/10.1021/i100016a019>
- Pallister, J.S., Hoblitt, R.P., Reyes, A.G., 1992. A basalt trigger for the 1991 eruptions of Pinatubo volcano? *Nature* 356, 426–428. <https://doi.org/10.1038/356426a0>
- Parmigiani, A., Degruyter, W., Leclaire, S., Huber, C., Bachmann, O., 2017. The mechanics of shallow magma reservoir outgassing. *Geochem. Geophys. Geosystems* 18, 2887–2905. <https://doi.org/10.1002/2017GC006912>
- Parmigiani, A., Faroughi, S., Huber, C., Bachmann, O., Su, Y., 2016. Bubble accumulation and its role in the evolution of magma reservoirs in the upper crust. *Nature* 532, 492–495. <https://doi.org/10.1038/nature17401>
- Parmigiani, A., Huber, C., Bachmann, O., 2014. Mush microphysics and the reactivation of crystal-rich magma reservoirs. *J. Geophys. Res. Solid Earth* 119, 6308–6322. <https://doi.org/10.1002/2014JB011124>
- Parmigiani, A., Huber, C., Bachmann, O., and Chopard, B., 2011. Pore-scale mass and reactant transport in multiphase porous media flows: *Journal of Fluid Mechanics*, v. 686, p. 40-76.
- Patanè, D., Barberi, G., Cocina, O., De Gori, P., Chiarabba, C., 2006. Time-resolved seismic tomography detects magma intrusions at Mount Etna. *Science* 313, 821–823.
- Patankar, S.V., 1980. Numerical heat transfer and fluid flow. Hemisphere Pub. Corp.
- Paulatto, M., Annen, C., Henstock, T.J., Kiddle, E., Minshull, T.A., Sparks, R.S.J., Voight, B., 2012. Magma chamber properties from integrated seismic tomography and thermal modeling at Montserrat. *Geochem. Geophys. Geosystems* 13. <https://doi.org/10.1029/2011GC003892>
- Peirano, E., Delloume, V., Leckner, B., 2001. Two- or three-dimensional simulations of turbulent gas–solid flows applied to fluidization. *Chem. Eng. Sci.* 56, 4787–4799. [https://doi.org/10.1016/S0009-2509\(01\)00141-5](https://doi.org/10.1016/S0009-2509(01)00141-5)
- Perugini, D., Poli, G., 2005. Viscous fingering during replenishment of felsic magma chambers by continuous inputs of mafic magmas: Field evidence and fluid-mechanics experiments. *Geology* 33, 5–8. <https://doi.org/10.1130/G21075.1>
- Petford, N., 2009. Which effective viscosity? *Mineral. Mag.* 73, 167–191. <https://doi.org/10.1180/minmag.2009.073.2.167>
- Picard, D., Arbaret, L., Pichavant, M., Champallier, R., Launeau, P., 2011. Rheology and microstructure of experimentally deformed plagioclase suspensions. *Geology* 39, 747–750. <https://doi.org/10.1130/G32217.1>
- Pichavant, M., Poussineau, S., Lesne, P., Solaro, C., Bourdier, J.-L., 2018. Experimental Parametrization of Magma Mixing: Application to the ad 1530 Eruption of La Soufrière, Guadeloupe (Lesser Antilles). *J. Petrol.* 59, 257–282. <https://doi.org/10.1093/petrology/egy030>
- Pinel, V., Carrara, A., Maccaferri, F., Rivalta, E., Corbi, F., 2017. A two-step model for dynamical dike propagation in two dimensions: Application to the July 2001 Etna eruption. *J. Geophys. Res. Solid Earth* 122, 1107–1125. <https://doi.org/10.1002/2016JB013630>
-

- Pistone, M., Caricchi, L., Ulmer, P., Burlini, L., Ardia, P., Reusser, E., Marone, F., Arbaret, L., 2012. Deformation experiments of bubble- and crystal-bearing magmas: Rheological and microstructural analysis. *J. Geophys. Res. Solid Earth* 117. <https://doi.org/10.1029/2011JB008986>
- Prudencio, J., Manga, M., Taira, T., 2018. Subsurface Structure of Long Valley Caldera Imaged With Seismic Scattering and Intrinsic Attenuation. *J. Geophys. Res. Solid Earth* 123, 5987–5999. <https://doi.org/10.1029/2017JB014986>
- Qin, Z., Alison, K., Suckale, J., 2019. Rotation matters - Direct numerical simulations of rectangular particles in suspensions at low to intermediate solid fraction. *ArXiv190308167 Phys.*
- Qin, Z., Suckale, J., 2017. Direct numerical simulations of gas–solid–liquid interactions in dilute fluids. *Int. J. Multiph. Flow* 96, 34–47.
- Ranz, W.E., Marshall, W.R., 1952. Evaporation from droplets. *Chem. Eng. Prog.* 48, 141–146.
- Renggli, C.J., Wiesmaier, S., De Campos, C.P., Hess, K.-U., Dingwell, D.B., 2016. Magma mixing induced by particle settling. *Contrib. Mineral. Petrol.* 171, 96. <https://doi.org/10.1007/s00410-016-1305-1>
- Reuss, A., 1929. Berechnung der fließgrenze von mischkristallen auf grund der plastizitätsbedingung für einkristalle. *ZAMM-Journal Appl. Math. Mech. Für Angew. Math. Mech.* 9, 49–58.
- Rong, D., Horio, M., 1999. DEM simulation of char combustion in a fluidized bed. *Second Int. Conf. CFD Miner. Process Ind.* CSIRO Melb. Aust. 1999 65–70.
- Ruprecht, P., Bergantz, G.W., Dufek, J., 2008. Modeling of gas-driven magmatic overturn: Tracking of phenocryst dispersal and gathering during magma mixing. *Geochem. Geophys. Geosystems* 9. <https://doi.org/10.1029/2008GC002022>
- Ryerson, F.J., Weed, H.C., Piwinski, A.J., 1988. Rheology of subliquidus magmas: 1. Picritic compositions. *J. Geophys. Res. Solid Earth* 93, 3421–3436. <https://doi.org/10.1029/JB093iB04p03421>
- Saffman, P.G., Taylor, G.I., 1958. The penetration of a fluid into a porous medium or Hele-Shaw cell containing a more viscous liquid. *Proc. R. Soc. Lond. Ser. Math. Phys. Sci.* 245, 312–329. <https://doi.org/10.1098/rspa.1958.0085>
- Sato, H., Fehler, M.C., Maeda, T., 2012. *Seismic wave propagation and scattering in the heterogeneous earth.* Springer.
- Schleicher, J.M., Bergantz, G.W., 2017. The Mechanics and Temporal Evolution of an Open-system Magmatic Intrusion into a Crystal-rich Magma. *J. Petrol.* 58, 1059–1072. <https://doi.org/10.1093/petrology/egx045>
- Schleicher, J.M., Bergantz, G.W., Breidenthal, R.E., Burgisser, A., 2016. Time scales of crystal mixing in magma mushes. *Geophys. Res. Lett.* 43, 1543–1550. <https://doi.org/10.1002/2015GL067372>
- Shi, Y.F., Yu, Y.S., Fan, L.T., 1984. Incipient fluidization condition for a tapered fluidized bed. 484–489.
- Shibano, Y., Namiki, A., Sumita, I., 2012. Experiments on upward migration of a liquid-rich layer in a granular medium: Implications for a crystalline magma chamber. *Geochem. Geophys. Geosystems* 13. <https://doi.org/10.1029/2011GC003994>
- Silbert, L.E., Ertaş, D., Grest, G.S., Halsey, T.C., Levine, D., Plimpton, S.J., 2001. Granular flow down an inclined plane: Bagnold scaling and rheology. *Phys. Rev. E* 64, 051302.
- Singh, S.C., Kent, G.M., Collier, J.S., Harding, A.J., Orcutt, J.A., 1998. Melt to mush variations in crustal magma properties along the ridge crest at the southern East Pacific Rise. *Nature* 394, 874–878. <https://doi.org/10.1038/29740>
- Snyder, D., 2000. Thermal effects of the intrusion of basaltic magma into a more silicic magma chamber and implications for eruption triggering. *Earth Planet. Sci. Lett.* 175, 257–273. [https://doi.org/10.1016/S0012-821X\(99\)00301-5](https://doi.org/10.1016/S0012-821X(99)00301-5)
- Snyder, D., Crambes, C., Tait, S., Wiebe, R.A., 1997. Magma Mingling in Dikes and Sills. *J. Geol.* 105, 75–86. <https://doi.org/10.1086/606148>
- Snyder, D., Tait, S., 1998. The imprint of basalt on the geochemistry of silicic magmas. *Earth Planet. Sci. Lett.* 160, 433–445. [https://doi.org/10.1016/S0012-821X\(98\)00102-2](https://doi.org/10.1016/S0012-821X(98)00102-2)
- Snyder, D., Tait, S., 1996. Magma mixing by convective entrainment. *Nature* 379, 529–531. <https://doi.org/10.1038/379529a0>
- Snyder, D., Tait, S., 1995. Replenishment of magma chambers: comparison of fluid-mechanic experiments with field relations. *Contrib. Mineral. Petrol.* 122, 230–240. <https://doi.org/10.1007/s004100050123>
- Sparks, R.S.J., 2003. Forecasting volcanic eruptions. *Earth Planet. Sci. Lett.* 210, 1–15. [https://doi.org/10.1016/S0012-821X\(03\)00124-9](https://doi.org/10.1016/S0012-821X(03)00124-9)
- Sparks, R.S.J., Annen, C., Blundy, J.D., Cashman, K.V., Rust, A.C., Jackson, M.D., 2019. Formation and dynamics of magma reservoirs. *Philos. Trans. R. Soc. A.* <https://doi.org/10.1098/rsta.2018.0019>
- Sparks, R.S.J., Marshall, L.A., 1986. Thermal and mechanical constraints on mixing between mafic and silicic magmas. *J. Volcanol. Geotherm. Res.* 29, 99–124. [https://doi.org/10.1016/0377-0273\(86\)90041-7](https://doi.org/10.1016/0377-0273(86)90041-7)
- Suckale, J., Keller, T., Cashman, K.V., Persson, P.-O., 2016. Flow-to-fracture transition in a volcanic mush plug may govern normal eruptions at Stromboli. *Geophys. Res. Lett.* 43, 12,071–12,081.

-
- Suckale, J., Sethian, J.A., Yu, J., Elkins-Tanton, L.T., 2012. Crystals stirred up: 1. Direct numerical simulations of crystal settling in nondilute magmatic suspensions. *J. Geophys. Res. Planets* 117. <https://doi.org/10.1029/2012JE004066>
- Sundaram, S., Collins, L.R., 1996. Numerical Considerations in Simulating a Turbulent Suspension of Finite-Volume Particles. *J. Comput. Phys.* 124, 337–350. <https://doi.org/10.1006/jcph.1996.0064>
- Syamlal, 1998. MFIX documentation numerical technique (No. DOE/MC/31346-01). EG and G Technical Services of West Virginia, Inc., Morgantown, WV (United States). <https://doi.org/10.2172/656644>
- Syamlal, M., 1998. MFIX documentation numerical technique. EG and G Technical Services of West Virginia, Inc., Morgantown, WV (United States).
- Syamlal, M., O'Brien, T.J., 1988. Simulation of granular layer inversion in liquid fluidized beds. *Int. J. Multiph. Flow* 14, 473–481. [https://doi.org/10.1016/0301-9322\(88\)90023-7](https://doi.org/10.1016/0301-9322(88)90023-7)
- Syamlal, M., Rogers, W., O'Brien, T.J., 1993. MFIX documentation theory guide. USDOE Morgantown Energy Technology Center, WV (United States).
- Tait, S., Jaupart, C., 1992. Compositional convection in a reactive crystalline mush and melt differentiation. *J. Geophys. Res. Solid Earth* 97, 6735–6756. <https://doi.org/10.1029/92JB00016>
- Takahashi, R., Nakagawa, M., 2013. Formation of a Compositionally Reverse Zoned Magma Chamber: Petrology of the ad 1640 and 1694 Eruptions of Hokkaido-Komagatake Volcano, Japan. *J. Petrol.* 54, 815–838. <https://doi.org/10.1093/petrology/egs087>
- Tomiya, A., Takeuchi, S., 2009. Two-Stage Magma Mixing and Initial Phase of the 1667 Plinian Eruption of Tarumai Volcano. AGU Fall Meet. Abstr. 51.
- Tsuji, Y., Kawaguchi, T., Tanaka, T., 1993. Discrete particle simulation of two-dimensional fluidized bed. *Powder Technol.* 77, 79–87. [https://doi.org/10.1016/0032-5910\(93\)85010-7](https://doi.org/10.1016/0032-5910(93)85010-7)
- Turner, J.S., Campbell, I.H., 1986. Convection and mixing in magma chambers. *Earth-Sci. Rev.* 23, 255–352. [https://doi.org/10.1016/0012-8252\(86\)90015-2](https://doi.org/10.1016/0012-8252(86)90015-2)
- Ubide, T., Galé, C., Larrea, P., Arranz, E., Lago, M., Tierz, P., 2014. The Relevance of Crystal Transfer to Magma Mixing: a Case Study in Composite Dykes from the Central Pyrenees. *J. Petrol.* 55, 1535–1559. <https://doi.org/10.1093/petrology/egu033>
- Valier-Brasier, T., Conoir, J.-M., Coulouvrat, F., Thomas, J.-L., 2015. Sound propagation in dilute suspensions of spheres: Analytical comparison between coupled phase model and multiple scattering theory. *J. Acoust. Soc. Am.* 138, 2598–2612. <https://doi.org/10.1121/1.4932171>
- Waite, G.P., Moran, S.C., 2009. VP Structure of Mount St. Helens, Washington, USA, imaged with local earthquake tomography. *J. Volcanol. Geotherm. Res.* 182, 113–122. <https://doi.org/10.1016/j.jvolgeores.2009.02.009>
- Wallace, P.J., 2005. Volatiles in subduction zone magmas: concentrations and fluxes based on melt inclusion and volcanic gas data. *J. Volcanol. Geotherm. Res.* 140, 217–240.
- Wallace, P.J., 2001. Volcanic SO₂ emissions and the abundance and distribution of exsolved gas in magma bodies. *J. Volcanol. Geotherm. Res.* 108, 85–106.
- Wallace, P.J., Anderson Jr, A.T., Davis, A.M., 1999. Gradients in H₂O, CO₂, and exsolved gas in a large-volume silicic magma system: Interpreting the record preserved in melt inclusions from the Bishop Tuff. *J. Geophys. Res. Solid Earth* 104, 20097–20122.
- Weinberg, R.F., Leitch, A.M., 1998. Mingling in mafic magma chambers replenished by light felsic inputs: fluid dynamical experiments. *Earth Planet. Sci. Lett.* 157, 41–56. [https://doi.org/10.1016/S0012-821X\(98\)00025-9](https://doi.org/10.1016/S0012-821X(98)00025-9)
- Wiebe, R.A., 2016a. Mafic replenishments into floored silicic magma chambers. *Am. Mineral.* 101, 297–310. <https://doi.org/10.2138/am-2016-5429>
- Wiebe, R.A., 2016b. Mafic replenishments into floored silicic magma chambers. *Am. Mineral.* 101, 297–310. <https://doi.org/10.2138/am-2016-5429>
- Wiesmaier, S., Morgavi, D., Renggli, C.J., Perugini, D., Campos, C.P. de, Hess, K.-U., Ertel-Ingrisch, W., Lavallée, Y., Dingwell, D.B., 2015. Magma mixing enhanced by bubble segregation. *Solid Earth* 1007–1023. <https://doi.org/10.5194/se-6-1007-2015>
- Zou, R.P., Yu, A.B., 1996. Evaluation of the packing characteristics of mono-sized non-spherical particles. *Powder Technol., Research of Powder Technology in Australia* 88, 71–79. [https://doi.org/10.1016/0032-5910\(96\)03106-3](https://doi.org/10.1016/0032-5910(96)03106-3)